Quasicrystalline-Generated Phononic Crystals for Advanced Engineering Applications

Thesis submitted in fulfilment of the requirement for the degree of

Doctor of Philosophy

By

Zhijiang CHEN

September 2022

School of Engineering

Cardiff University

Acknowledgements

In the journey towards submitting this thesis, I am indebted to many intelligent, patient and encouraging people who have helped me through the course of my PhD research. I would like to take this opportunity to acknowledge their supports.

I want to express my most profound appreciation and gratitude to my supervisors Prof. Massimiliano Gei and Dr Lorenzo Morini, for their tremendous guidance, patience, encouragement and wisdom, and for being the friendliest supervisors during the past four years. Their valuable feedback and constructive comments helped me in all my time of research and writing of this thesis, for instance, preparing scientific publications, attending conferences and correct English writing. I also would like to thank Dr Iulia Mihai for allowing me to become a teaching assistant in Finite Element method.

I want to thank China Scholarship Council and Cardiff University, who funded my PhD project. I am also quite thankful to my colleagues and friends whom I have worked within the office W 2.13, in Queen's Building over the years for their thoughtful suggestions and accompany. Special thanks to my friends working in BIM for smart engineering, who kindly gave me valuable advice and offered me generous support during my life. Besides, during the difficulty I met in the past three years, I also want to thank Dr Xindong Chen, Dr Yulin Luo, Dr Yu Wang, Xiaofeng Zhu, Xiaoyu Liu, Feiqiang Lin, Xintong Yang and other cronies to comfort and help me.

I wish to thank my wife, Shuang Chen, for her immense and endless emotional supports throughout my thesis writing stage. Without her love and care, it would have been much more stressful during difficult times. Finally, I would like to thank my family for their endless love, support, and motivation. I will remember it forever.

Abstract

Quasicrystalline phononic crystals structures have attracted intensive attention due to their outstanding capability in manipulating acoustic and elastic waves. They are rationally designed composites made of tailored building blocks, which are composed of one or more constituent bulk materials. As a main contribution to the research field, the concept of canonical configuration is here introduced as a novel tool to design quasicrystalline-generated structures.

A periodic one-dimensional quasicrystalline-generated rod can be used to minimise system noise and vibration acting as a wave filter. It can be composed of repeated elementary cells devised by adopting generalised Fibonacci substitution rules. We apply the concept of canonical configuration into it, for which the orbits predicted by the trace map at the specific frequencies, which we call canonical frequencies, are periodic. This theory reveals that (i): the frequency spectrum is periodic and symmetric, (ii): a set of multiple periodic orbits exist at frequencies, and (iii): scaling exists in the frequency spectra that can be explained rigorously.

Negative refraction effect can be used for wave focusing as a perfect lens. This effect in quasicrystalline laminate is governed by three particular frequencies. Canonical configurations for laminates and canonical frequencies can be used as a rule to investigate the effect of variation of those frequencies with different phases of the laminate. Three main conclusions can be drawn: (i): the effects of pure negative refraction following variation of canonical ratio and two-phase material are analysed, (ii): the three mentioned frequencies show some local peaks that can be analysed, in some cases analytically, (iii): under certain conditions, the expression of the Poynting vector can be simplified to calculate explicitly the transmission angle and to formulate an 'inverse problem' to design the laminate to achieve a particular pair of frequency and wavenumber.

The interface state in periodic structures is formed in the interfacial region at two one-dimensional structures with different surface impedance, which can be determined by the symmetric properties of band-edge mode on lower or upper bandgap or, otherwise, properties of the Zak phase. It can be used as an amplifier leading an increasing of sensitivity at the target frequency. Three results are obtained: (i): the surface impedance of band-edge mode is periodically associated with canonical frequencies with canonical configuration, (ii): the representation based on the universal torus can be used as a new tool for designing quasicrystalline waveguides with the sign of surface impedance determined without Zak phase integral, (iii): the frequency of interface state is determined under two particular configurations.

Contents

List of Figures

List of Tables

Nomenclature

A_L, A_S	the cross-section of area for elementary rod L and S
A	scatter coefficients for incident wave
A	Jacobians for saddle points
a, b	amplitude for wave left and right propagation
B	Jacobians for other periodic orbits
C_1, C_2	constants in the solution of governing equation
C_g	general coordinate in linear space
$C^{(1)}, C^{(2)}, C^{(3)}$	the canonical ratio for families 1, 2, 3
c_L, c_S	longitudinal wave phase speed for elementary rod L and S or shear wave phase speed for elementary laminate L and S
c_0	shear wave phase speed in substrate
[**c**]	vector for scattering coefficients
D	general first derivatives for periodic orbits
$\bar{D}$	eigenvector in Newton iteration
D	Jacobians for periodic orbits
d	vector for derivatives of initial three traces
det()	determination function
[**d**]	vector for the special integral of size
E_L, E_S	young's modulus for the material of elementary rod L and S

E	mean energy flux
E	identity matrix
e	natural constant
exp()	exponent function
F_i	Fibonacci sequence with i-order
F	second type transmission matrix
$\mathbf{F}_t$	second type global transfer matrix for finite $\mathcal{N}$ cells
$f_i^{1st}, f_i^{1bg}, \tilde{f}_i$	three edge frequencies associated with first passband, first bandgap, and second passband with Fibonacci i order
f_i^{min}	the minimum frequency to let the wave number entering the second Brillouin zone with Fibonacci i order
$\tilde{f}_{iu}, \tilde{f}_{il}$	the frequency at the intersection of the upper boundary line and lower one with flow line in i-order laminate
f	elements in second type transfer matrix
G	vector associated with second derivatives of multi-variables
H_1, H_2	the condition for band-edge mode symmetric or asymmetric for canonical ratio C
h_L, h_S	the thickness for the elementary laminate L and S
I	Kohmotos invariant
i	imaginary unit
J	Jacobians for nonlinear map
j, q, k	parameters in the canonical ratio
j_ω, k_ω	parameters in canonical frequency
K	normalised Bloch wave number
K_x, K_y, K_0	wavenumber in x and y direction and the substrate

$\bar{K}$, $\bar{k}$	imaginary part of wave number K and k
$\tilde{K}$, $\tilde{k}$	other wave number compare with K and k
$\overline{K}_x L_i$	initial $K_x L_i$ associate with $K_y = 0$ in laminate
$k_y^{(m)}$	y direction wave number for a reflected wave in m mode
L_t	the total length for one elementary rod or total thickness for one elementary laminate
L_i	the total length for rod or total thickness for laminate with Fibonacci sequence i-order
l_L, l_S	the length for the elementary rod L and S
$\overline{\mathcal{M}}$, $\overline{\mathcal{N}}$	blocks with certain permutation elements
M_L, M_S	transmission matrix for laminate L and S
M_i, trM_i	transmission matrix and trace of this matrix for Fibonacci sequence with i-order in laminate
$\mathcal{M}$, $\mathcal{N}$, m, n	natural number
mt, nr	total number of transmission wave and reflected wave
$\overline{m}_1$, $\overline{m}_2$, $\bar{L}$, $\bar{S}$	natural numbers
mod()	modulo operation function
N	axial force for rods
$\bar{N}$	dynamic axial force in rod
$\tilde{n}_i$	generalised Fibonacci i-order number
$\hat{n}$	substitution for $n^{(L)} q_L h_L + n^{(S)} q_S h_S$
$n_i^{(L)}, n_i^{(S)}$	the number of elements L and S contained in the laminates or rods with i-order
P_k	saddle points on Kohmoto's surface
$\mathcal{P}_x$, $\mathcal{P}_y$	Poynting vector in x and y direction

Q_L, Q_S	substitution for $\sqrt{1/c_L^2 - \kappa^2}$ and $\sqrt{1/c_S^2 - \kappa^2}$
q_L, q_S	substitution for $\sqrt{(\omega/c_L)^2 - K_y^2}$ and $\sqrt{(\omega/c_S)^2 - K_y^2}$
R_i	the point with periodic orbit on Kohmoto's surface
R_m	scatter coefficients for reflection wave in m mode
Re, Im	real and imaginary part calculation
r	reflection coefficient
$r_{\mathcal{N}}$	reflection coefficient for finite $\mathcal{N}$ cells rods
$\mathbf{r}$	vector difference between saddle points and perturbation
$\mathcal{S}$	substitutional rule
$S^{(i)}$	other state vector in elementary cell i phase
sgn()	sign function
T_L, T_S	first type transmission matrix for rods L and S
T_i, trT_i	first type transmission matrix and trace of this matrix for
T_l	scatter coefficients for transmission wave in l mode
$\mathcal{T}_{g,s,b}$	trace recursion rule for the Fibonacci golden, silver and bronze mean sequence
$t_{\mathcal{N}}$	transmission coefficient for finite $\mathcal{N}$ cells rods
t	time coefficient
$\bar{U}$	dynamic axial displacement in rod
$\mathbf{U}$	state vector covering displacement and force
u	axial displacement field along the rods
u_z	displacement along z direction in laminates
U_m	mode shape for reflected wave in m mode
V	velocity for calculation impedance
v_x^g, v_y^g	wave group speed in x and y direction

W_1, W_2	the condition for band-edge mode symmetric or asymmetric for canonical ratio $1/C$
$\mathcal{W}_{n,K}$	periodic part with Bloch number K in n band
w_l	mode shape in laminate for transmission wave in l mode
$\tilde{x}_i, \tilde{y}_i, \tilde{z}_i$	coordinates in Kohmoto's surface associated with traces
Y_1, Y_2	expressions concerning dispersion relation and H_1, H_2
Y_3, Y_4	expressions concerning dispersion relation and W_1 and W_2
$Z_{\text{rhs}}, Z_{\text{lhs}}$	impedance for right and left periodic rods
Z_0	reference impedance
Z_L, Z_S	substitution for $A_L\sqrt{E_L\rho_L}$ and $A_S\sqrt{E_S\rho_S}$ (impedance)
α, ζ, o, ι	number of permutation elements
$\bar{\alpha}$	rational number
β	mismatch impedance for rod or laminates
γ	substitution for $q_L\mu_L = q_S\mu_S = \gamma$
Γ^+, Γ^-	substitution for $\beta/2 \pm \sqrt{(\beta/2)^2 - 1}$
δ	a small perturbation
ϵ_1, ϵ_2	material parameters
η	coefficients in Newton iteration
$\theta^{\text{inc}}, \theta^{\text{trans}}, \theta^{\text{ref}}$	incident, transmission and reflection wave angle
θ^{Zak}	Zak phase
ϑ_g, λ_g	the eigenvalue of Jacobians
κ	substitution $\sqrt{(\mu_L\rho_L - \mu_S\rho_S)/(\mu_L^2 - \mu_S^2)}$
λ	bulk modulus
$\bar{\lambda}$	coefficient in auxiliary function
μ_L, μ_S, μ_0	shear modulus for elementary laminate L, S and substrate

$\bar{\mu}$	average shear modulus along the one elementary laminate
ν	substitution for $(n_i^{(L)}\sqrt{1-c_L^2\kappa^2}+Cn_i^{(S)}\sqrt{1-c_S^2\kappa^2})/(c_L n_i^{(;)}+Cc_S n_i^{(S)})$
ξ_L, ξ_S	substitution for $\sqrt{\rho_L/E_L}\omega l_L$ and $\sqrt{\rho_S/E_S}\omega l_S$ in rods or $q_L h_L$ and $q_S h_S$ in laminates also is dimensionless frequency
ξ_L', ξ_S'	other ξ_L, ξ_S for easy to theocratical deducing
π	ratio of a circle's circumference
ρ_L, ρ_S	density per unit volume for elementary rod or laminate L and S
ρ_0	density per unit volume for substrate
ϱ	constant in eigenvector problem
σ	stress
ς	the imaginary part of surface impedance
ϕ	the limit for Fibonacci golden mean sequence
φ	reflection phase
ψ	the eigenvector of Jacobians
ω, f	circular frequency and frequency $f=\omega/(2\pi)$
ω_c, f_c	circular canonical frequency and canonical frequency
ω_t, f_t	canonical period circular frequency and frequency
ϖ	structure parameter $\varpi=\zeta o-\alpha\iota$

Chapter 1- Introduction

1.1 Motivation and Background

Walser (2001) used the term 'metamaterial' for the first time in a publication (the prefix meta- is the ancient Greek word for beyond), but there is not yet a definition of metamaterial that is consistently used by all. The majority of scholars concur with the following rough definition: metamaterials are tailor-made composites comprised of one or more bulk component material possessing properties that are not usually found in nature. Metamaterials are macroscopic composites of periodic or non-periodic structures (even though the vast majority of metamaterials created to date are periodic), whose function is attributable to both the underlying cell architecture and the chemical composition (Cui et al. 2010; Milton 1995; Kenneth et al. 2012). Rational design of metamaterials with the help of both theoretical and numerical approaches is a long-held goal of applied physics to avoid trial-and-error procedures and excessive experimentation. Reasonable design enables metamaterial properties to go beyond those of the ingredient materials, qualitatively or quantitatively, or to what was previously believed to be impossible in nature. Metamaterials can be used in electromagnetism, acoustic or elastic dynamic applications (Kadic et al. 2019). Typical metamaterials and elementary cells are depicted in Figure 1.1.

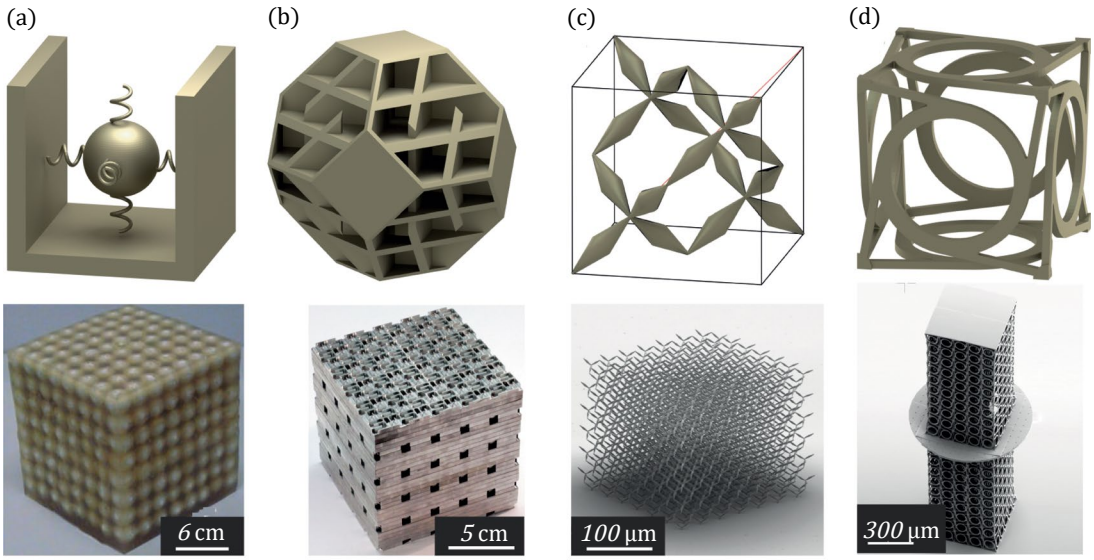

Figure 1.1. Some 3D acoustical and mechanical metamaterial unit cells (upper) and corresponding experimental realizations (lower). (a). Unit cells with internal mass-spring resonance that leads to negative mass density. (b). Labyrinthine channel system that leads to an isotropic slowing down of sound propagation. (c). Pentamode cell that gives rise to a small shear modulus. (d). Chiral mechanical metamaterials that give rise to small bulk modulus. Figure reproduced from Kadic et al. (2019)

The idea in Figure 1.1 (a) states that a strong periodic modulation in density and sound velocity can create spectral gaps (bandgap) that forbid wave propagation. By varying the size and geometry of the structural unit, the frequency ranges for bandgaps can be tuned (Liu et al. 2000). Extension to lower and higher frequency elastic wave systems may lead to applications in seismic wave reflection. Frenzel et al. (2013) find positive phase and group velocities of sound slower than in air by a factor of about eight over a large range of relevant acoustic frequencies. The losses are very significant though, making these labyrinthine structures an interesting option for sub-wavelength broadband all-angle acoustic absorbers for acoustic-noise suppression as shown in Figure 1.1 (b). Pushing on an ordinary linearly elastic bar can cause it to be deformed in many ways. However, within Cauchy continuum mechanics, a twist is strictly zero and the stiffness constant as shown in Figure 1.1 (d), which could be used to steer force or mechanical waves around obstacles using static or dynamic cloaking structures, respectively (Frenzel et al. 2017).

Controlling waves with mechanical metamaterials is a well-established topic of study that has attained a certain level of maturity. Two methods are mainly followed to achieve this aim: the first one is based on the investigation of dispersion properties of periodic structures that compose specially designed units or elementary cells (Kushwaha et al. 1993; Lin 1962; Sigalas and Economou 1992); the second relies on mathematical transformations dictating local features of the metamaterial, such as guiding waves along predetermined paths (Brun et al. 2009; Colquitt et al. 2014; Colquitt et al. 2017; Farhat et al. 2009; Maldovan 2013; Milton et al. 2006; Norris 2008; Parnell et al. 2012). Thus, mechanical metamaterials possess a large capacity to influence waves and energy being able to filter waves, induce negative refraction and exploit topological interface properties. A metamaterial can block frequency ranges corresponding to wave propagation (bandgap structure), create a state with only evanescent wave propagation, and might be utilised to minimise system noise and vibration acting as a wave filter. Veselago pioneered the concept of negative refraction (1964). As depicted in Figure 1.2, Veselago (1964) utilised negative permittivity and permeability to create a "left-handed structure" in which a negative group velocity with positive phase velocity existed, allowing a perfect flat lens for an optical wave to be obtained for focusing energy from point source radiation. This is not a lens in the conventional sense, as it does not focus on a single point, but rather a jumble of rays emanating from infinity. As for real lenses, Figure 1.3 depicts the beam propagation paths of left-handed lens materials. Convex and concave lenses are inherently opposed because the convex lens has a diverging ray effect and the concave lens has a converging ray impact.

Although 3D microstructures and nanostructures have more potential applications for metamate-

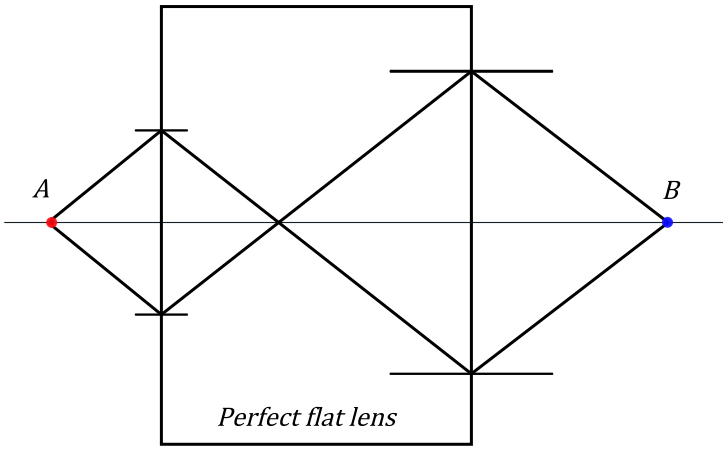

Figure 1.2. Propagation of rays of light through the flat lens with negative refraction, the wave will be focusing on another side of the lens, A - a source of radiation; B - detector of radiation, figure reproduced from Veselogo (1964)

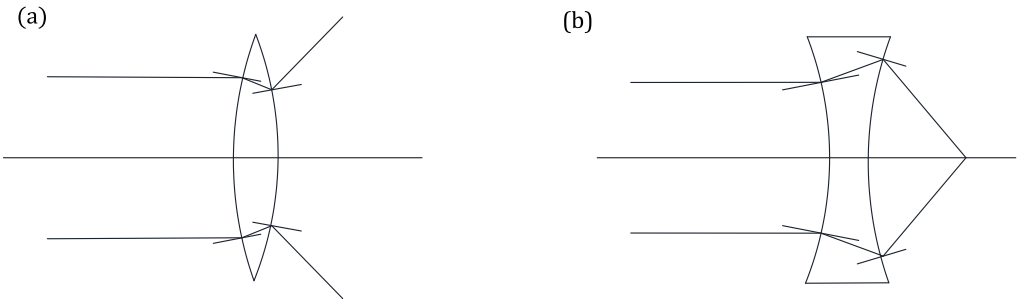

Figure 1.3. Paths of rays through lenses made of left-handed material, figure reproduced from Veselogo (1964)

rials, the 1D model is easier to fabricate and design complexity is limited such that closed-form solutions can be found. Thus, in this research thesis, 1D periodic structures will be considered.

Periodic phononic crystals/materials are a subclass of metamaterials (Srivastava and Willis, 2017) with bandgaps in the dispersion diagram. This notable feature can be attributed to Bragg scattering (Kushwaha et al. 1993), local resonance (Liu 2000), and inertial amplification (Yilmaz et al. 2007), as the unit cell operates as an insulator or filter for waves while permitting other frequencies to pass through. Quasiperiodic sequences may be used to conceptualise the unit cell. The sequences are generated by the combination of two homogeneous pieces to create non-periodic patterns, which may be described in general terms by deterministic laws (commonly known as generation or substitution rules detailed in Chapter 2). Two separate groups of quasiperiodic structured media may be recognised based on the features of these laws: quasicrystalline structures (Levine and Steinhardt 1984) and non-quasicrystalline deterministic systems (Huang et al. 1992). Kolar (1993) developed a precise categorization for one dimension quasiperiodic structural patterns. The aperiodic deterministic structures of quasicrystalline media are midway between those of crystalline and amorphous substances (Poddubny and Ivchenko 2010). Figure 1.4 is a typ-

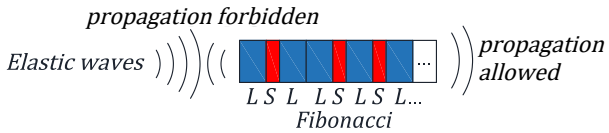

Figure 1.4. Fibonacci quasicrystalline rod as a wave filter

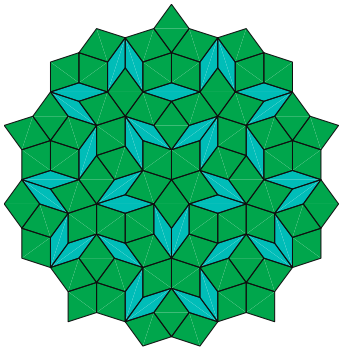

Figure 1.5. Penrose tiling, figure reproduced from Penrose (1974)

ical example of a one-dimensional quasicrystalline structure represented by the Fibonacci golden mean sequence. Figure 1.5 depicts the Penrose tiling (Penrose, 1974) with rotational symmetry and quasicrystalline tessellation in two dimensions.

Dispersion spectra of quasicrystalline generated waveguides display self-similarity that can be explained through a scaling factor. It is an exciting phenomenon because the range of passband and bandgap layout can be scaled (predicted) with different Fibonacci order in acoustic, elastic and optical waves. This phenomenon could be related to the properties of a certain nonlinear map that can be defined on the trace of the transfer matrix (Poddubny et al. 2009; Kohmoto 1987). In general periodic media, scaling and self-similarity in the dispersion spectrum cannot be detected (Steurer 2004; Steurer and Deloudi 2008; Fan and Huang 2021). Typical self-similar and scaling effects are shown in Figure 1.6 (Gei 2010). Morini and Gei (2018) investigated traces of the transfer matrix associated with the precious mean sequence at increasing of Fibonacci order. The trace of consecutive elements of the sequence follows a nonlinear recursive relationships. An invariant is obtained through an algebraic technique, that can be mapped as a surface in a three-dimensional space with a Cartesian system. This surface was first introduced by Kohmoto and Oono (1984) while investigating the spectrum of Schrödinger's equations in quasicrystalline potential wells. Thus, the surface and invariant are called Kohmoto's surface and Kohmoto's invariant, respectively. The nonlinear map defines points that describe a discrete orbit on the Kohmoto's surface. Periodic orbits can be detected. Kohmoto's invariant is introduced in Chapter 2.

Scaling and self-similarity phenomena can be studied as perturbations of periodic orbits through a linearisation of the nonlinear map introduced previously. The 'direction' of the perturbation

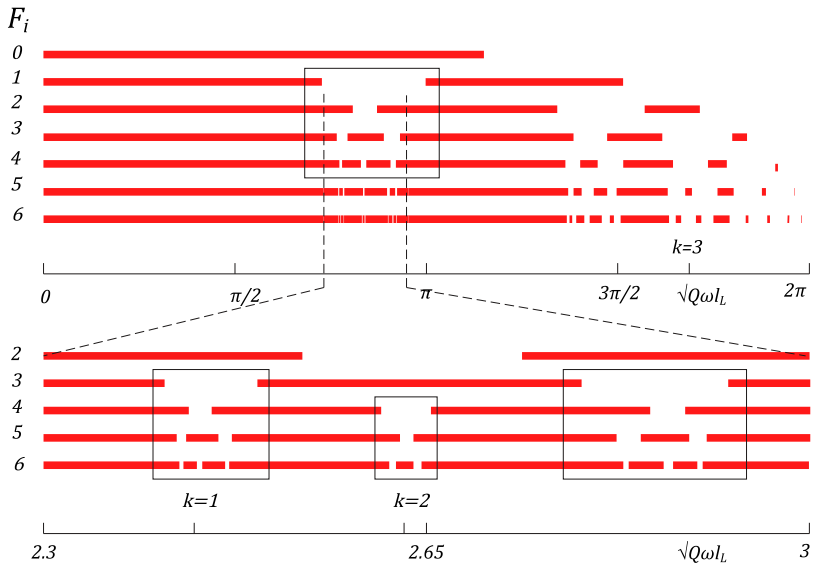

Figure 1.6. Typical scaling effect and self-similarity properties in dispersion layout for rods generated by sequence F_0 to F_6. The $\sqrt{Q}\omega l_L$ is dimensionless frequency. Red band represents passband and interval bandgap. Figure reproduced from Gei (2010)

is almost coincident with the eigenvector. The unique properties of quasicrystalline-based metamaterials can be obtained from investigating perturbations of periodic orbits. In addition, novel analytical tools can be further assessed for manipulating the bandgap properties of quasicrystalline structures.

Several investigators have studied the influence of periodic multilayer structures on the propagation of elastic waves during the past fifty years (Sun et al. 1968; Hegemier and Nayfeh 1973; Morvan et al. 1972; Nemat-Nasser et al. 1975; Rudykn and Boyce 2014). Advancements in focussing of elastic waves (Guenneau et al. 2007; Yang et al. 2004) and negative refraction have influenced the design of composites based on continuous and discrete periodic structures (Chen et al. 2017; Morvan et al. 2010; Morini and Gei 2018; Zhang and Liu 2004; Zhu et al. 2014). Several researchers have previously studied the unique problem for anti-plane shear waves, also known as shear horizontal (SH) waves, incident at the interface between a homogeneous substrate and a periodic bilayer laminate: Nemat-Nesser (2015a); Srivastava and Willis (2017); Morini and Gei (2018). Figure 1.7 demonstrates that, when the layering direction is perpendicular to the interface, it is possible to use a periodic laminate to achieve negative refraction, a phenomenon typically observed when elastic waves strike a custom-designed micro-architected interface (Brun et al. 2010; Jones et al. 2011; Sukhovich et al. 2008). However, only a positive refraction wave was detected when the stacking direction was perpendicular to the interface (Srivastava and Nemat-Nasser 2014). Negative refraction can occur in both instances, but with in-plane wave which coupled P and SV waves (Lustig et al. 2019; Mokhtari et al. 2020). Under specific hy-

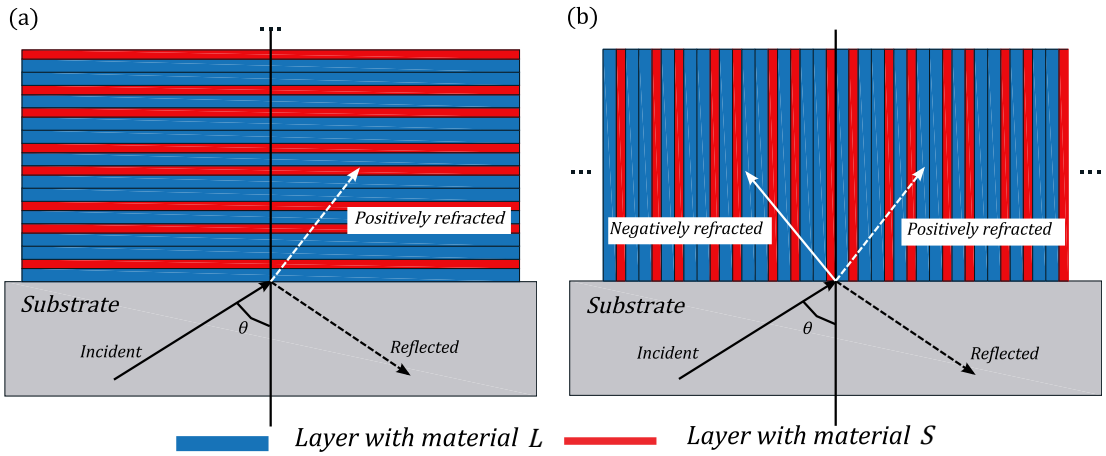

Figure 1.7. SH wave incident from an elastic homogenous substrate into Fibonacci laminate F_4, figure reproduced from Morini et al. (2019)

potheses, the results reported by Willis (2016) demonstrated the existence of both positive and negative refraction waves in a transmitted signal. According to Srivastava (2016), to create single negative refraction wave, it is essential to couple the incident wave number with the wave mode satisfied particular conditions. Thus, one component of the wave group velocity, which represents direction of energy propagation, becomes negative, which confirms the idea of Veselago (1964).

It is believed that some or all of these results may apply to electromagnetic (EM) waves in a layered periodic dielectric due to the similarities between SH and EM waves (Srivastava 2016). Figure 1.8 depicts the results of the FEM simulation by the commercial programme COMSOL Multiphysics of the negative SH wave refraction between the substrate and laminates. It is fascinating to explore negative refraction in quasicrystalline generated laminates, in which the two-phase material *A* or *B* are arranged using Fibonacci substitution rule, such that the effect or condition for negative refraction might be guided by Kohmoto's invariant. As they are essential for engineering applications, the negative transmission angle and energy associated with it require more research.

In wave physics, impedance is the characteristic that regulates scattered or reflected waves at material interfaces (waveguides). Bandgap in mechanical or acoustic phononic crystals is caused by an impedance mismatch in the phase material, which also defines how a material interacts with incoming waves. In addition, the bandgap structures result from the propagation of waves inside a periodic system. Therefore, there is a relationship between these quantities. Based on the analogy between these systems and quantum systems, the Zak phase may be described in photonic crystals (Xiao et al. 2014) or phononic crystals (Kane and Lubensky, 2013) for acoustic and mechanical waves (Haldane and Raghu 2008; Raghu and Haldane 2008; Raman and Fan 2010; Tan et al. 2014). Xiao and colleagues (2014) created periodic one-dimensional photonic crystals.

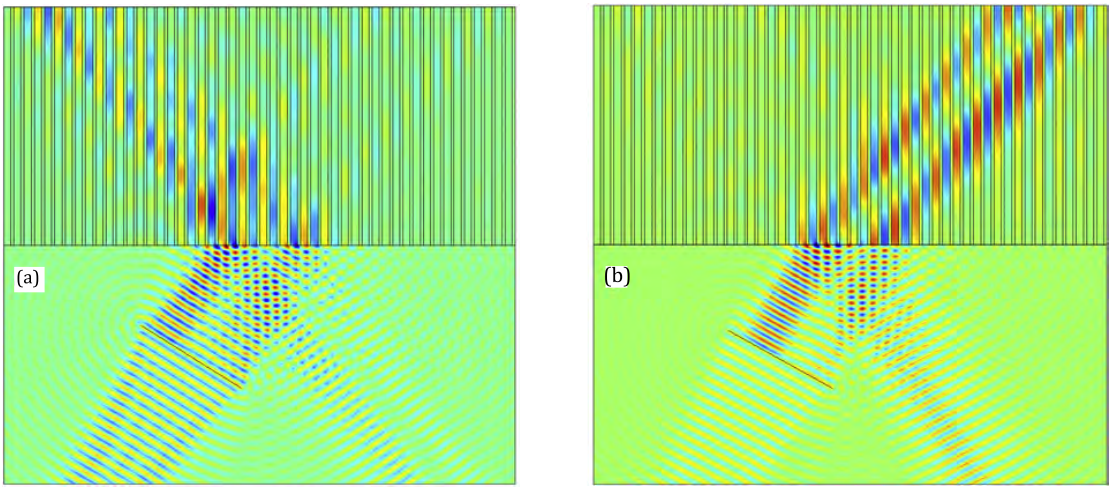

Figure 1.8. FEM simulation. Incident wave from below to enter laminates above with (a) negative refraction in laminates part, and (b) positive refraction laminates part, figure reproduced from Srivastava (2016)

Geometric topological phase of photonic crystals dictates the occurrence of interface states. As the topological phase of two semi-infinite systems on either side of an interface is distinct, interface states can arise in quantum systems (Hatsugai 1993; Hatsugai et al. 2006; Rudner et al. 2013; Regnault and Bernevig 2011).

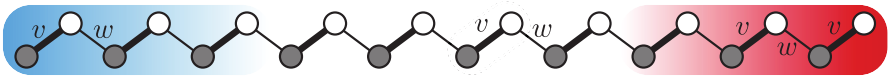

Figure 1.9. Geometry of the SSH model. Grey and white circles are sites on sublattice, each hosting a single state. The left and right edge regions shaded with blue and red. Figure reproduced from Asboth et al. (2015)

Figure 1.9 illustrates the Su-Schrieffer-Heeger (SSH) model for polyacetylene (Su et al. 1979; Su et al. 1980; Heeger et al. 1988). This model demonstrated the existence of an interface state when the Zak phase of the occupied passband on one side of the chain differs from that on the other side, which may be derived via gap inversion (Hasan and Kane 2010; Bernevig et al. 2006; Pankratov et al. 1987). Several articles on the topological interface state in phononic systems (Xiao et al. 2015; Yin et al. 2018; Meng et al. 2018; Li et al. 2018; Muhammad et al. 2019; Chen et al. 2021) are concerning the elementary cell holding inversion symmetry (Zak 1989). A common elastic interface condition exists when the sum of two surface impedances is zero at the interface of two finite (or infinite) periodic rods (Xiao et al. 2014). At the interface, the local wave field is amplified, resulting in improved sensitivity of the device at the desired frequency (Xiao et al. 2015). The wave field distribution is confined at the interface between two structures and phenomenon in spectra is similar to the occurrence of a small passband in bandgap, as seen in Figure 1.10. Applications such as sound detection (Buckingham et al. 1992) and biomedical

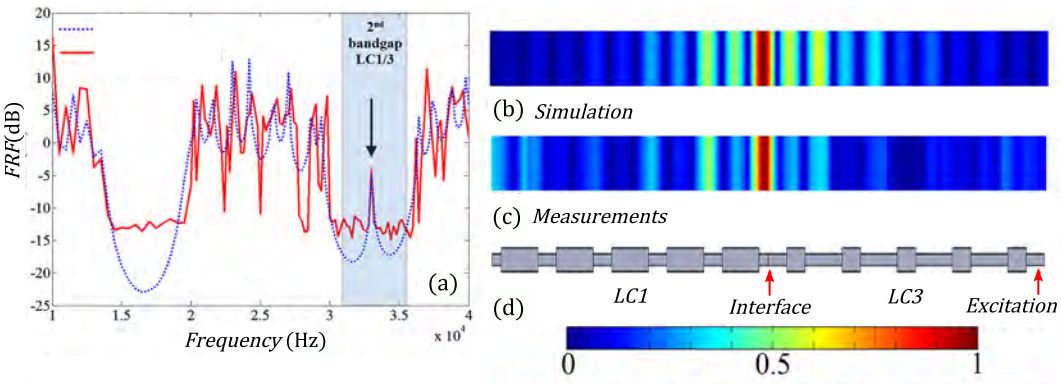

Figure 1.10. Forced response of the finite system comprised of two phononic crystals $LC1$ and $LC3$ with different topological properties obtained from measurements in comparison with numerical simulations using FEM. (a) Frequency response function of whole system where the structure is excited at the right end and velocity response picked up at the other end (the dashed blue lines represent simulated results using FEM and the solid red lines are measured results). A transmission peak at $33100Hz$ is observed within band gap region (colored area) indicating the existence of the interface mode. (b) the longitudinal normalised velocity field obtained from simulations and (c) the longitudinal normalised velocity field obtained from measurements at the peak frequency, respectively. Figure reproduced from Yin et al. (2018)

imaging (Fatemi 1998) demanded high wave intensities, and a system with an interface state can be in close proximity to a sensor/receiver. In this system, the canonical configuration can also be used to determine the effect, as the exact frequency for the interface state is not yet determined by the theoretical method.

Quasicrystalline structure to be investigated will reveal innovative features that are currently only partially known in mechanics and are useful specially for cutting frequencies in a vibrating system, for example, Micro-electromechanical system (MEMS) to devices able to suppress vibrations in mechanical engineering. The principles of quasicrystalline structures can be applied to beams, rods, plates and composite (layered) materials, depending on the type or scale of application. Pure negative refraction effect in the coupled substrate and quasicrystalline laminate can be used for energy focusing (Figure 1.2) or divergence as a perfect lens. The interface state effect in periodic rods can be used as an amplifier to place in close proximately to a sensor or receiver leading to an increasing of sensitivity at the target frequency.

1.2 Thesis Objectives

As mentioned above, there appears to be a lack of further understanding of the characteristics concerning dynamic spectra, self-similar patterns and scaling features in one-dimensional Fibonacci quasicrystalline generated structures (rods or laminates). The research presented in the thesis focuses on the Fibonacci sequences as the substitutional rule and the dispersion layout variations

with increasing of Fibonacci order. The dispersion spectra are obtained from the transfer matrix method using the Floquet-Bloch technique. A new geometric configuration (i.e., the canonical configuration) can let spectra be periodic in all Fibonacci sequence, which comes from investigation of saddle-points on Kohmoto's surface (Morini and Gei 2018). The role of the canonical configurations in the dispersion layouts of Fibonacci quasicrystalline generated rods is investigated thoroughly, especially with reference to the scaling properties. This thesis provides new design guidelines for their utilisation in 1D quasicrystalline rods whose passband topology can be adjusted and manipulated easily.

Moreover, even if many researchers have already investigated SH (anti-plane) wave propagating in periodic laminates, refraction angles and transmitted energy where pure negative refraction occurs have not been investigated thoroughly. The concept of canonical configuration is applied to quasicrystalline laminates generated by the Fibonacci sequence. The conditions for pure negative refraction are obtained. As such, the variation of pure negative refraction with different canonical ratio and two-phase material selected for maximising (or minimising) the possibility for pure negative refraction should be studied. In addition, it is possible to find a relationship among frequency, incident and transmission wave angles from eigenvector analyses with condition of zero Kohmoto's invariant. Also, the maximum transmission wave energy is studied.

Additionally, many researchers have already investigated the topological interface state by tuning material parameters to let the bandgap close and reopen (band inversion), which leads to changing the sign of surface impedance (topological phase) and Zak phase. However, the Zak phase is calculated by the complex Berry connection integral, and the frequency for the interface state is not determined. In this thesis, the concept of canonical configuration is applied on two periodic rods to create an interface state avoiding the Zak phase calculation. The symmetric properties of edge mode are used because they provide a clear connection when the structure holds an inversion symmetry. Furthermore, the surface impedance of finite and infinite periodic structures are analysed theoretically and combined to predict frequency for the interface state. Thus, it is possible to obtain the formula for frequency controlled by structure material and geometric parameters for real engineering applications.

Therefore, the main objectives are as follows:

1. Review the literature concerning quasicrystalline rods and laminates generated by Fibonacci sequence, especially with a focus on self-similar patterns and scaling factors. Kohmoto's invariant and universal torus are reviewed carefully which are the main tools for spectra analysis. Negative

refraction in the periodic laminates includes a method for calculating dispersion relation, transmission wave angle and energy, in particular, pure negative refraction. Moreover, the topological interface state in periodic structures covers the Zak phase integral, surface impedance, transmission and reflection coefficients and the bandgap inversion phenomenon.

2. Theoretical investigations regarding the application of the concept of canonical configuration to 1D quasicrystalline generated rods and laminates with regard to dispersion layouts, periodic orbits in the spectra, and Kohmoto's surface are included. Then, different scaling factors, explaining self-similarity properties of passband layout are investigated. The approaches for canonical structure are fully clarified in 1D quasicrystalline generated structure. Moreover, the differences between canonical structure and non-canonical are emphasised. Numerical codes are implemented to verify our theoretical analyses.

3. The condition for pure negative refraction when a SH wave approaches a quasicrytalline generated laminates from a homogeneous substrate is investigated. Then, the concept of canonical configuration is applied to laminates to optimise the possibility of pure negative refraction. Two components of the acoustic Poynting vector can be simplified in some conditions by employing eigenvector analyses and giving rise to 'inverse problems' possibly. The transmission wave energy is studied and the local maximum value is found under pure negative refraction conditions. Additionally, It is possible to use the linear approximation prediction technique in this problem.

4. Propose a novel analysis approach for topological interface state observed in two periodic finite or infinite elementary cells rods and determine the exact frequency for the interface state. The effect of canonical configuration on the sign of surface impedance and the Zak phase are analysed theoretically. The numerical results verify the frequency for the interface state and show the engineering application (the maximum displacement and force field are localised at the geometric interface of two structures). Indeed, this approach can be extended to other 1D periodic structures (laminates).

5. Identify any possible extension to multi-dimensional structures (beams, plates, etc.) where to apply the idea of new configuration in this thesis. The necessary numerical approaches are also explained.

1.3 Thesis Overview

This thesis is divided into seven chapters. The first three chapters cover introduction, literature review and methodology, respectively. The fourth, fifth and sixth chapters show novel research

works. The seventh chapter includes conclusions and possible future research.

Chapter 2 reviews the literature concerning elastic wave propagating in 1D quasiperiodic rods and laminates. First, the Fibonacci substitution rule is introduced, including precious mean structures and metal mean structures associated with the limit ratio. This thesis focuses on the golden ratio structure. The primary analysis tools in this thesis, the Floquet-Bloch and transfer matrix techniques, are introduced. The passband structures are introduced due to the impedance mismatch of the two phases. Nonlinear mapping and Kohmoto's invariant present the canonical ratio and frequencies (canonical configuration) associated with the periodic orbits. Secondly, the anti-plane (SH) wave propagating into laminates are introduced. This covers dispersion relations, acoustic Poynting vector, group velocity and transmission wave angle, all of which come from the conditions of continuity at the interface. Theoretical deduction concerning mode shape orthogonality and the relationship between Poynting vector and group velocity are demonstrated. Thirdly, the topological interface state is incorporated and the basic definition for surface impedance, the conditions for interface state and the process for Zak phase integration and band inversion are presented. Finally, some conclusions are shown. For instance, the Zak phase takes two particular values when the structure holds inversion symmetry, and the Zak phase is changed according to two symmetric of band-edge mode on isolated passband.

Chapter 3 presents the methodology which is implemented in this thesis. The important tool such as universal torus is shown due to its traces of the transfer matrix. The universal torus is convenient for analysing band inversion in interface state problems. The numerical method for calculating wave number K_y (or frequency when dimensionless wave number KL_i is known), the Newton method and matrix inverse iteration are shown. In addition, the approach for numerical calculations of integral of two components of the Poynting vector and the transmission angle are clarified, which originated from mode shape each phase can integrate w. The method to calculate scattering coefficients and energy: normal mode decomposition, is introduced. The numerical methods for calculating the Zak phase for each passband are presented. The transmission and reflection coefficients in finite periodic rods and wave field evaluation are shown. This chapter does not show the full code in software, but it is not difficult to program with this procedure.

Chapter 4 introduces the properties of the canonical rod. The conditions for canonical structure (it covers three different families) are easily obtained by resorting to the three initial traces. The full expressions for canonical frequencies are presented. As well as six saddle periodic orbits (canonical frequencies), other periodic orbits are analysed on Kohmoto's invariant. The scaling effects on passband, bandgap are investigated theoretically and numerically. Especially some

scaling factor is the square root of the maximum eigenvalue from linear approximation. Moreover, the conditions for Kohmoto's invariant being zero are analysed also which are helpful for the Chapter 5.

Chapter 5 shows the complete conditions for pure negative refraction when SH wave incident from the homogenous substrate to Fibonacci laminates. The concept of canonical configuration is applied to laminate to optimise the effect of pure negative refraction. Some local extremum values for three frequencies (condition) are obtained using the representation of the universal torus and flow line. These three edge frequencies are obtained using a linear approximation with derivatives of trace. One acoustic Poynting vector is simplified and explained in two extreme situations: incident angle equal to 0 and $\pi/2$. There exists a particular pair of frequencies and longitudinal wave numbers so that the Poynting vector is simplified and not associated with frequency. Then, a unique surface in space with coordinates covered frequencies, incident and transmission wave angles are presented. It corresponds to a straight line in the dispersion spectra associated with Kohmoto's invariant which is always zero. The energy in pure negative refraction is analysed. It is fascinating that there exist unusual maximum peaks when the wave number enters the second Brillouin zone, which means the negative refraction has enough energy. This phenomenon needs further investigation.

Chapter 6 presents the topological interface states in canonical rods. Using the symmetric condition in passband edge mode, the Zak phase for each band is obtained without evaluating complex numerical integrals and signs of surface impedance arisen. Two cases are analysed theoretically and numerically, which are: (i) one rod with canonical ratio and the other one with inverse canonical ratio under the condition two phase materials are same. The interface state is found when the value of traces is larger than 2, (ii) the other rod with swapping two phase materials while keeping canonical ratio the same, the interface state is found in each bandgap. In the first case, the frequency for interface state is obtained through explicit expression in both finite and infinite elementary cells. In the second case, an implicit expression of finite or infinite elementary cells is sought. This is beneficial as the conclusion can be extended to non-canonical rods. Moreover, it has more engineering applications because the target frequency is determined.

Chapter 7 is the concluding chapter, which describes the outcomes of this thesis in terms of analyses, modelling and coding. This investigation manifests the feasibility and potential for designing guidelines for quasicrystalline generated structures by applying the concept of canonical configurations. It can be generalised to waveguide consistent periodic beams, plates, and microarchitected materials. Finally, some suggestions and improvements for future works are presented.

1.4 Publication List

One journal paper has been already published based on the canonical configuration on quasicrystalline rods generated by Fibonacci sequence described in Chapter 4 of the thesis.

1. Gei, M. **Chen, Z**. Bosi, F. Morini, L. 2020. Phononic canonical quasicrystalline waveguides. *Applied Physics Letters* 116(24), p. 241903. doi: 10.1063/5.0013528

A further two journal papers have been accepted. The first one is based on the canonical configuration on laminates for optimising the condition of pure negative refraction and second is concerning theoretical solution of threshold frequency, simplifying Poynting vector and energy peak described in Chapter 5 of the thesis.

2. **Chen, Z**. Morini, L. Gei, M. 2022. Negative refraction for anti-plane elastic waves in canonical quasicrystalline laminates. *European Journal of Mechanics A-solids*. doi: 10.1016/j.euromechsol.2022.104577

3. **Chen, Z**. Morini, L. Gei, M. 2022. On the adoption of canonical quasicrystalline laminates to achieve pure negative refraction of elastic waves. *Philosophical Transactions A* 380(2237), p. 20210401. doi: 10.1098/rsta.2021.0401

Another paper is in preparation and is based on the topological interface state on two canonical rods described in Chapter 6 of the thesis.

4. **Chen, Z**. Morini, L. Gei, M. 2022. Topological interface state in canonical rods. In preparation.

Moreover, two conference papers have been presented, arising from Chapters 5 and 6.

1. Morini, L. **Chen, Z**. Gei, M. 2020. Canonical quasicrystalline multilayered metamaterials. Milano, 25th International congress of theoretical and applied mechanics.

2. **Chen, Z**. Morini, L. Gei, M. 2022. Design of topological interface states using canonical rod configurations. Galway, 11th European solid mechanics conference.

In addition, three conference papers have been presented in cooperation with colleagues.

3. Farhat, A.K.M. **Chen, Z**. Morini, L. and Gei, M. 2021. On generalised canonical axial waveguides. Modena, EM4SS21 - Engineering Materials for Sustainable Structures.

4. Farhat, A.K.M. **Chen, Z**. Morini, L. and Gei, M. 2021. Frequency spectra and stop-band optimisation of generalised canonical quasicrystalline phononic waveguides. Keele, Euromech Colloquium 626 Mechanics of High-Contrast Elastic Composites.

5. Farhat, A.K.M. **Chen, Z**. Morini, L. and Gei, M. 2021. Generalised canonical quasicrystalline phononic waveguides. London, Metamaterials2021.

Chapter 2 - Literature Review

2.1 Introduction

This chapter contains a literature review of earlier researchers' findings on Fibonacci sequences, one-dimensional quasicrystalline generated structures, negative refraction in laminates, and topological interface states in rods. In addition, some mathematical deductions are presented to complete the states for easy to explain previous research works. Thus, this chapter is a mixture of theory and traditional literature review. From the examination of the relevant literature, it is evident that there are several aspects to clarify, such as the scaling effects of dispersion diagram, the complete analysis of pure negative refraction, and the exact frequency for the interface state between two finite and semi-infinite periodic rods. Consequently, this thesis investigates and attempts to resolve these issues.

2.2 Fibonacci Sequence

A one dimensional infinite periodic binary quasicrystalline structure is presented with periodic element cells consisting of two individual elements called L and S in rod's problem. They could be springs, rods, supported beams, or multilayers permutated in series (Poddubny and Ivchenko 2010). Kolar and Ali (1989b) define a one-dimensional quasiperiodic chain generated according to the generic substitution rule:

$$L \to \mathcal{S}(L) = \overline{\mathcal{M}}_{\alpha\zeta}(L,S),\ S \to \mathcal{S}(S) = \overline{\mathcal{N}}_{o\iota}(L,S) \tag{2.1}$$

where $\overline{\mathcal{M}}_{\alpha\zeta}(L,S)$ and $\overline{\mathcal{N}}_{o\iota}(L,S)$ are two building blocks consisting of certain permutations of $\alpha+\zeta$ and $o+\iota$ elements, respectively. Parameters α and ζ denote the number of elements L and S in $\mathcal{S}(L)$, respectively, whilst o and ι are their counterparts in $\mathcal{S}(S)$. There is a structure parameter that controls conditions for existing quasicrystalline systems, which is $\varpi = \zeta o - \alpha\iota = \pm 1$. The generalised binary component Fibonacci sequence obeys the following deterministic rules, which is also a particular combination of equation (2.1):

$$L \to \mathcal{S}(L) = L^{\mathrm{m}}S^{\mathrm{l}},\ S \to \mathcal{S}(S) = L,\ \text{with}\ \mathrm{m},\mathrm{l} \geq 1 \tag{2.2}$$

where the exponents m and l point out the times the base is duplicated, for instance, $S^{\mathrm{l}} = SSS\ldots$ (l times). According to general definition (2.1), four parameters in the deterministic rules (2.2) can be chosen with $\alpha = \mathrm{m}$, $\zeta = \mathrm{l}$, $o = 1$, $\iota = 0$ so that $\varpi = \mathrm{l}$ which is satisfied quasicrystalline

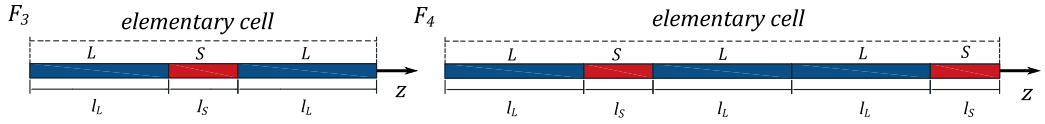

Figure 2.1. Quasicrystalline rod generated by Fibonacci golden mean chains F_3 (LSL) and F_4 (LSLLS), figure reproduced from Morini and Gei (2018)

condition ($\varpi = \zeta o - \alpha \iota = \pm 1$). The periodic elementary cell associated with finite generalised Fibonacci sequence of the ith order ($i = 0, 1, 2, ...$), here denoted by F_i, obeys the recursive rule:

$$F_i = F_{i-1}^{\mathrm{m}} F_{i-2}^{\mathrm{l}} \tag{2.3}$$

where the initial conditions are $F_0 = S$ and $F_1 = L$. The total number of elements of F_i corresponds to the generalised Fibonacci number $\tilde{n}_i$ given by the recursive rule:

$$\tilde{n}_i = \mathrm{m}\tilde{n}_{i-1} + \mathrm{l}\tilde{n}_{i-2}, \text{ with } i \geq 2 \tag{2.4}$$

with condition $\tilde{n}_0 = \tilde{n}_1 = 1$. The limit ϕ of the ratio $\tilde{n}_{i+1}/\tilde{n}_i$ for $i \to \infty$ is:

$$\phi = \lim_{i \to \infty} \frac{\tilde{n}_{i+1}}{\tilde{n}_i} = \frac{\mathrm{m} + \sqrt{\mathrm{m}^2 + 4\mathrm{l}}}{2} \tag{2.5}$$

The procedure for equation (2.5) is the following: divided $\tilde{n}_{i-1}$ in equation (2.4) and achieved:

$$\frac{\tilde{n}_i}{\tilde{n}_{i-1}} = \mathrm{m} + \mathrm{l}\frac{\tilde{n}_{i-2}}{\tilde{n}_{i-1}}$$

If the limit existed, the solution ϕ would be obtained:

$$\phi = \mathrm{m} + \frac{\mathrm{l}}{\phi}$$

One basic Fibonacci sequence is obtained from the deterministic rule (2.2) setting $\mathrm{m} = \mathrm{l} = 1$, for which ϕ equals to the golden mean (GM) $\phi = \phi_g = (1 + \sqrt{5})/2 \cong 1.618$, and total elements recursive rule (2.4) becomes the expression for the standard Fibonacci number $n_i = n_{i-1} + n_{i-2} (i \geq 2)$. Elementary cells for element F_3 and F_4 of the GM sequence are shown in Figure 2.1. The structures generated with parameters $\mathrm{m} = 2$ and $\mathrm{l} = 1$ are the silver mean (SM) sequence, whose limit equals to the silver mean $\phi = \phi_s = 1 + \sqrt{2} \cong 2.414$. The SM sequence F_3 is shown in Figure 2.2. Whereas for $\mathrm{m} = 3$ and $\mathrm{l} = 1$ the bronze mean (BM) deterministic rule is obtained with $\phi = \phi_b = (3 + \sqrt{13})/2 \cong 3.303$. Moreover, parameters with $\mathrm{m} = 1, \mathrm{l} = 2$ and $\mathrm{m} = 1, \mathrm{l} = 3$ are usually called copper ($\phi = \phi_c = 2$) and nickel mean sequence ($\phi = \phi_n = (1 + \sqrt{13})/2 \cong 2.302$), respectively, in generalised Fibonacci structure

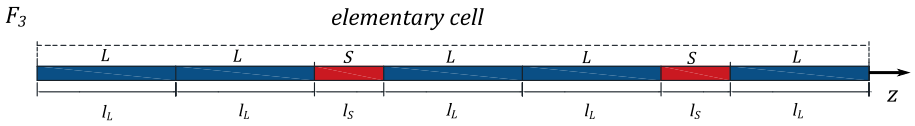

Figure 2.2. Quasicrystalline rod generated by Fibonacci silver mean chains F_3 (LLSLLSL)

configuration. Their applications are concerning the modelling of the quasiperiodic electronic and magnetic systems which has also been investigated (Gumbs and Ali 1988; Kolar and Ali 1989a).

Ratios ϕ_g, ϕ_s and ϕ_b are associated with GM, SM and BM whose parametric representation can be defined by setting $\mathrm{l} = 1$ in equation (2.5). According to the nomenclature proposed by Holzer (1988a) and Holzer (1988b), these values are called precious means and associated structures precious mean structures in the text. Conversely, ϕ_c, ϕ_n are ratios that correspond to $\mathrm{l} \geq 1$ referred to as metal means, and the associated structures are called metal mean structures. In conclusion, all precious mean structure have $\varpi = \mathrm{l} = 1$ and other $\varpi = \mathrm{l} > 1$ (Kolar 1993). Thus, the former is quasicrystalline, while the latter are deterministic non-quasicrystalline, quasiperiodic systems.

The Fibonacci sequence can also be equivalently defined by the cut-and-project method (Valsakumar and Kumar 1986). In this method, the Fibonacci chain is generated by projecting a stripe in the auxiliary 2D space under an irrational slope. For instance, the GM chains from 2D periodic lattice as shown in Figure 2.3, the angle tangent value of it is ϕ_g.

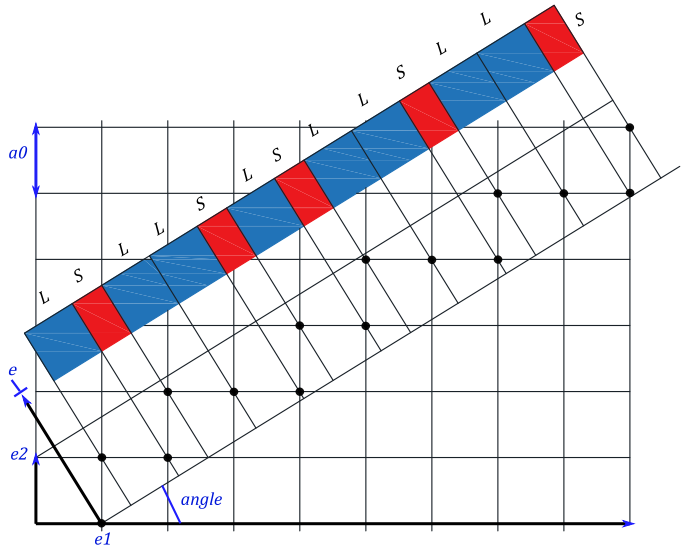

Figure 2.3. Illustration of the cut-and-project method, figure reproduced from Poddubny and Ivchenko (2010)

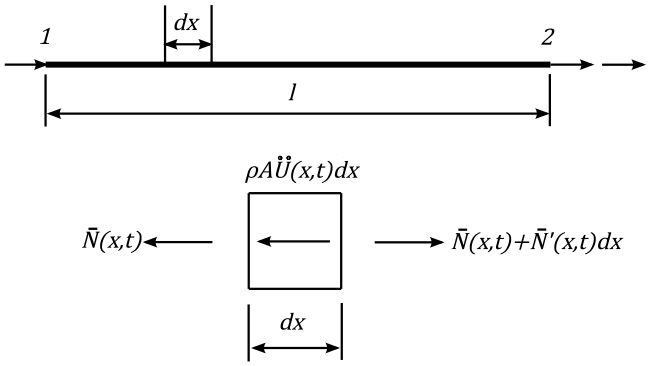

Figure 2.4. Force equilibrium in rod structure, figure reproduced from Timoshenko (1970)

2.3 One Dimensional Qusicrystalline Generated Structure

2.3.1 Axial wave problem in bars

In this research, the Fibonacci GM chain is investigated in rods or laminates, so that the substitution rule for the Fibonacci golden ratio is introduced. From now on we simply speak about Fibonacci sequence for the sake of simplicity. Equation (2.2) with $\mathrm{m} = 1$ and $\mathrm{l} = 1$ becomes:

$$L \to LS \text{ and } S \to L \tag{2.6}$$

The material and geometric parameters of elements with phases L and S are introduced. The lengths of the two phases are indicated with l_L and l_S, while A_X, E_X and ρ_X ($X \in L, S$) express cross-section area, Young's modulus and mass density per unit volume of the two elements, respectively. For each element, the governing equation for axial wave propagation is:

$$\frac{\partial \bar{N}(z,t)}{\partial z} = \rho A \frac{\partial^2 \bar{U}(z,t)}{\partial t^2} \tag{2.7}$$

This equation is derived from considering force equilibrium as shown in Figure 2.4. Following an established method in dynamics, dependency on space and time can be separated when investigating harmonic waves, so that $\bar{U}(z,t) = u(z)e^{\mathrm{i}\omega t}$($\omega$ is the circular frequency, the space variable is here z-x in the Figure plays the same role-) and axial force $\bar{N}(z,t) = N(z)e^{\mathrm{i}\omega t}$. By substituting this displacement function into equation (2.7) and considering each elements:

$$u_X''(z) + \frac{\rho_X}{E_X}\omega^2 u_X(z) = 0 \tag{2.8}$$

The equation (2.8) is the one dimensional Helmholtz equation that governs several dynamics problems in solid mechanics such as shear waves in anti-plane elasticity and plane dynamic compression and shear waves in two-dimensional elasticity (Ewing et al. 1956; Graff 1975). This equation

(2.8) can be solved by test function method $u(z) = e^{\bar{\lambda}z}$. The solution can be presented in two different forms:

$$u_X(z) = a\exp(\mathrm{i}\sqrt{\frac{\rho_X}{E_X}}\omega z) + b\exp(-\mathrm{i}\sqrt{\frac{\rho_X}{E_X}}\omega z) \tag{2.9}$$

$$u_X(z) = C_1\sin(\sqrt{\frac{\rho_X}{E_X}}\omega z) + C_2\cos(\sqrt{\frac{\rho_X}{E_X}}\omega z) \tag{2.10}$$

The solutions (2.9) and (2.10) can be replaced by each other through Euler's formula: $\cos(x) + \mathrm{i}\sin(x) = e^{\mathrm{i}x}$, in here, the constants C_1, C_2, a and b being complex number. However, the amplitude for left and right propagation waves can be found in equation (2.9) directly, equation (2.9) will be more useful in Chapter 6 for transmission and reflection coefficients calculation. Moreover, if the solution in equation (2.7) is assumed as $\bar{U} = \bar{u}e^{\mathrm{i}(\omega t - Kx)}$, the special solution $\bar{u} = ue^{\mathrm{i}Kx}$ would be obtained. It is called Bloch periodic part (Xiao et al. 2015) for calculation of the Zak phase. A counterpart problem involving laminates is introduced in next section.

To obtain the dispersion relation of periodic rods, the transfer matrix approach combined with the Floquet-Bloch technique is applied. Displacement and axial force at the right-hand boundary of the elementary cell, respectively u_r and N_r, have to be given in terms of those at the left-hand boundary, u_l and N_l, as:

$$\mathbf{U}_r = T_i\mathbf{U}_l \tag{2.11}$$

where $\mathbf{U}_j = [u_j\ N_j]^T\ (j = r, l)$ is called the state vector and T_i is a transfer (or transmission) matrix of the cell F_i. This matrix is the result of the product $T_i = \prod_{p=1}^{n_i}[T_X]_p,\ (X \in L, S)$, where T_X is the transfer matrix relating quantities across a single element. The transfer matrix method is usually performed to analyse the optical, acoustic and mechanical wave propagation through a 1D stratified or multilayer medium. As the fact that waves at different interfaces composed of multilayer material are partially transmitted and reflected in single layers, the reflection and transmission coefficients in the overall structure can be obtained from the transfer matrix combined with Chebyshev's identity, which will be introduced later. The principle for the transfer matrix is based on the continuity condition in different layer interfaces. The coefficients at the interface can represent the wave properties in one single layer, in our case, the displacement and axial force or amplitude for waves propagating right and left. Moreover, there exist other methods to obtain dispersion relation in different type of periodic structures, for instance, plane wave expansion (Kushwaha and Halevi 1996; Hsu and Wu 2006; Hou and Assouar 2008; Zhou et al. 2009; Zhao et al. 2008), multiple-scattering theory (Korringa 1947; Chen and Ye 2001; Mei et al. 2003), finite difference time domain (García-Pablos et al. 2000) and finite element method (Srivastava

2016; Meng et al. 2018; Muhammad et al. 2019). As the constraints in one-dimensional quasicrystalline rods or laminates, the transfer matrix is most straight and convenient method. Thus, the transfer matrix method is the main technique used in the thesis. As it is not hard to find that $C_1 = N_l/(EA\sqrt{\rho_X/E_X}\omega)$, $C_2 = u_l$ from Equation (2.10), the transfer matrix for single phase is given by:

$$T^X = \begin{bmatrix} \cos(\sqrt{\frac{\rho_X}{E_X}}\omega l_X) & \frac{\sin(\sqrt{\rho_X/E_X}\omega l)}{E_X A_X \sqrt{\rho_X/E_X}\omega} \\ -E_X A_X \sqrt{\frac{\rho_X}{E_X}}\omega \sin(\sqrt{\frac{\rho_X}{E_X}}\omega l_X) & \cos(\sqrt{\frac{\rho_X}{E_X}}\omega l_X) \end{bmatrix} \tag{2.12}$$

Matrices (2.12) have some important properties that can be exploited (1): they are unimodular, i.e. $\det T_i = 1$, (2): follow the recursion rule:

$$T_{i+1} = T_{i-1} T_i \tag{2.13}$$

with $T_0 = T_S$ and $T_1 = T_L$. Equation (2.13) be easily extended to other precious mean chains. Thus, the transfer matrix connect the initial and final state vector :

$$\begin{bmatrix} u(L_i) \\ N(L_i) \end{bmatrix} = T_i \begin{bmatrix} u(0) \\ N(0) \end{bmatrix} \tag{2.14}$$

As a final remark we recall that the total length of one rod generated by Fibonacci GM sequence F_i is:

$$L_i = n_i^{(L)} l_L + n_i^{(S)} l_S \tag{2.15}$$

where the $n_i^{(L)}$ and $n_i^{(S)}$ are the number of elements L and S included in the cell.

2.3.2 Floquet-Bloch technique

Floquet theory is a more than a century old has been adopted for the solution of linear differential equations with periodic coefficients (Floquet 1883). These types of equations are highly present in several fields of science and technology, and as a result, the application of Floquet theory range from quantum (Shirley 1965; Moskalets and Büttiker 2002) to classical physics (Gammaitoni et al. 1998; Schneider 1985), chemistry (Boland et al. 2009), electronics (Demir et al. 2000; Traversa and Bonani 2011), dynamic systems (Guckenheimer et al. 1984) and more. It is also a formidable tool to investigate nonlinear perturbations, noise, and stability of systems depending instantaneously on variables and admitting periodic steady states.

The 1D classical Bloch theorem (Bloch 1929) can be derived as a simple corollary of the Flo-

quet theorem applied to space-dependent periodic potentials, which has been initially presented to describe the motion of the electrons in crystals from quantum mechanics. Bloch states play a fundamental role in defining the concepts of allowed and forbidden energy bands in crystalline solids under the crystal dispersion relation.

The Floquet-Bloch technique relates the time-harmonic response at a given point in a unit cell to the corresponding point in an adjacent unit cell, namely:

$$\begin{bmatrix} u(z+L_i) \\ N(z+L_i) \end{bmatrix} = e^{\mathrm{i}KL_i} \begin{bmatrix} u(z) \\ N(z) \end{bmatrix} \tag{2.16}$$

where K is called the Bloch wave number which means the global effective wave field across the periodic medium. The term $e^{\mathrm{i}KL_i}$ is also called the Floquet multiplier (Traversa and Bonani 2011). Because the system is periodic, the variables z could be 0 and equation (2.16) and transfer matrix (2.14) can provide an eigenvalue problem which is:

$$\det(T_i - e^{\mathrm{i}KL_i}\mathbf{E}) = 0 \tag{2.17}$$

where $\mathbf{E}$ is the identity matrix. If we try to solve the equation (2.17):

$$\begin{vmatrix} T_{11} - e^{\mathrm{i}KL_i} & T_{12} \\ T_{21} & T_{22} - e^{\mathrm{i}KL_i} \end{vmatrix} = \left(T_{11} - e^{\mathrm{i}KL_i}\right)\left(T_{22} - e^{\mathrm{i}KL_i}\right) - T_{12}T_{21}$$

the transfer matrix is unimodular, which means $T_{11}T_{22} - T_{12}T_{21} = 1$ and $T_{11} + T_{22}$ is the trace of global transfer matrix trT_i. The final expression is, therefore:

$$e^{\mathrm{i}KL_i} - trT_i + e^{-\mathrm{i}KL_i} = 0 \rightarrow 2\cos(KL_i) = trT_i \tag{2.18}$$

Equation (2.18) provides dispersion relation (plots of f or ω versus Bloch wavenumber K), which is rewritten as below:

$$KL_i = \arccos\left(\frac{trT_i}{2}\right) \tag{2.19}$$

Actually, for a real number KL_i, the absolute value of trace $|trT_i|$ must be smaller than 2. The dispersion relation does not change whether the Floquet multiplier is $e^{\mathrm{i}KL_i}$ or $e^{-\mathrm{i}KL_i}$. In addition, the typical passband layouts have been shown in Figure 1.6 already:

$$|trT_i| \leq 2 \rightarrow \text{Pass band},\ |trT_i| > 2 \rightarrow \text{Band gap},\ |trT_i| = 2 \rightarrow \text{Standing wave} \tag{2.20}$$

Conditions (2.20) are very similar to Floquet discrimination for Floquet system stability analysis.

All information about wave propagation in a structure whose unit cell is an arrangement by Fibonacci sequence F_i is only contained in the trace trT_i in the irreducible first Brillouin zone $0 \leq KL_i \leq \pi$ (Farzbod and Leamy 2011). The trace trT_i becomes very complex with increasing of index i because the global transfer matrix is obtained from matrix multiplication. Therefore, the numerical computation is helpful for us to find some characteristics. The dispersion relation (2.19) can also be studied for laminate problems because they share the same mathematically meaning, which will be explained in the next section.

Bloch wave numbers calculated from equation (2.19) are real and positive or zero in certain frequencies (passband) and complex at other frequencies (bandgap). In general, the dimensionless Bloch wavenumber can be rewritten as:

$$KL_i = \mathrm{Re}(KL_i) \pm \mathrm{i}\ \mathrm{Im}(KL_i) \tag{2.21}$$

where $\mathrm{Im}(KL_i)$ in equation (2.21) is positive. It is not hard to find that when frequency is in a pass band, the imaginary part of wavenumber $\mathrm{Im}(KL_i) = 0$. According to equation (2.16):

$$\begin{bmatrix} u(z+L_i) \\ N(z+L_i) \end{bmatrix} = e^{\mathrm{i}\ \mathrm{Re}(KL_i)} \begin{bmatrix} u(z) \\ N(z) \end{bmatrix} \tag{2.22}$$

This means that displacement and axial force at positions z and $z + L_i$ differ only by a phase factor $e^{\mathrm{i}\ \mathrm{Re}(KL_i)}$, this indicates the Bloch wave is effectively a propagating one in this structure and forming the passband because it represents the rotation in complex plane. However, when frequency is in a bandgap, real part is $\mathrm{Re}(KL_i) = n\pi, n \in \mathbb{Z}$ (n depending on edge or centre of Brillouin zone). If the sign of imaginary part $\mathrm{Im}(KL_i)$ is positive, equation (2.16) would becomes:

$$\begin{bmatrix} u(z+L_i) \\ N(z+L_i) \end{bmatrix} = e^{-\mathrm{Im}(KL_i)} \begin{bmatrix} u(z) \\ N(z) \end{bmatrix} \tag{2.23}$$

which means that the displacement and axial force at positions z and $z + L_i$ do not have a phase difference, and this is a spatial exponent attenuation in the magnitude of strength proportional to $\mathrm{Im}(KL_i)$. This system represents an evanescent wave, which means waves in these frequency ranges are effectively forbidden, forming a bandgap. However, if the sign of imaginary part $\mathrm{Im}(KL_i)$ is negative, the equation (2.16) would become:

$$\begin{bmatrix} u(z+L_i) \\ N(z+L_i) \end{bmatrix} = e^{\mathrm{Im}(KL_i)} \begin{bmatrix} u(z) \\ N(z) \end{bmatrix} \tag{2.24}$$

Equation (2.24) means that the displacement and axial force at positions z and $z + L_i$ do not have a phase difference, and there is a spatial exponent amplification in the magnitude of strength proportional to $\mathrm{Im}(KL_i)$, which is not our research case since we consider wave propagation along positive direction. Thus, in this system, a wave is in the range frequency of bandgap, the imaginary part of the Bloch wave number is $+\mathrm{Im}(KL_i) > 0$. However, if the variables is increasing in minus sign, for instance, $z < 0$, the imaginary part of Bloch wave number should be $-\mathrm{Im}(KL_i) < 0$.

2.3.3 Kohmoto's Invariant and Manifold

Because the dispersion relation of the quasicrystalline rods (laminates) is governed by the trace of global transfer matrix T_i, the properties of trT_i associated with GM chain and characteristics that affect waves in structure are analysed and discussed. Nonlinear recursive rules with traces and succession sequences are deduced.

Kolar and Ali (1989) deduced recursive rule for the trace of unimodular 2×2 transfer matrix of generalised Fibonacci sequences according to Chebyshev's polynomials of the first and second kind. Setting these expressions to the case of GM sequence ($\mathrm{m} = \mathrm{l} = 1$ in equation (2.4)) we obtain:

$$x_{i+1} = x_{i-1}x_i - x_{i-2}, \text{ with } i \geq 2 \tag{2.25}$$

where the notation $x_i = trT_i$ is introduced and the initial three conditions are given by: [1]

$$\begin{aligned} x_0 &= 2\cos\left(\sqrt{\frac{\rho_S}{E_S}}\omega l_S\right) \\ x_1 &= 2\cos\left(\sqrt{\frac{\rho_L}{E_L}}\omega l_L\right) \\ x_2 &= 2\cos\left(\sqrt{\frac{\rho_S}{E_S}}\omega l_S\right)\cos\left(\sqrt{\frac{\rho_L}{E_L}}\omega l_L\right) - \beta\sin\left(\sqrt{\frac{\rho_S}{E_S}}\omega l_S\right)\sin\left(\sqrt{\frac{\rho_L}{E_L}}\omega l_L\right) \end{aligned} \tag{2.26}$$

β is:

$$\beta = \frac{A_L^2 E_L \rho_L + A_S^2 E_S \rho_S}{A_L\sqrt{E_L\rho_L}A_S\sqrt{E_S\rho_S}} \tag{2.27}$$

The significant term $A_X\sqrt{E_X\rho_X}$ is called mechanical impedance. When a wave is incident on

[1] There exists another way to prove equation (2.25), which will be shown in Appendix B.

a discontinuity, the impedance of the discontinuity compared to the impedance of the structure governs how the wave is reflected and transmitted (Junior and Savi 2016). The detailed method for determining the impedance of a rod is that considering the semi-infinite rod is excited by the dynamic force $N(z)e^{\mathrm{i}\omega t}$ at the end of the rod, which generates a one-way wave:

$$\bar{U}(z,t) = a\exp(\mathrm{i}\sqrt{\frac{\rho}{E}}\omega z)e^{\mathrm{i}\omega t}$$

taking derivatives with respect to space and time, we obtain, respectively:

$$\frac{\partial \bar{U}(z,t)}{\partial z} = \mathrm{i}\sqrt{\frac{\rho}{E}}\omega \bar{U}(z,t)$$

$$\frac{\partial \bar{U}(z,t)}{\partial t} = \mathrm{i}\omega \bar{U}(z,t)$$

The definition of mechanical impedance is the ratio of the applied force to the resulting velocity at the point leading to:

$$\frac{\bar{N}(0,t)}{V(0,t)} = \frac{EA\mathrm{i}\sqrt{\frac{\rho}{E}}\omega U(0,t)}{\mathrm{i}\omega U(0,t)} = A\sqrt{E\rho}$$

Therefore, β can be viewed as:

$$\beta = \frac{Z_L}{Z_S} + \frac{Z_S}{Z_L} \tag{2.28}$$

where $Z_L = A_L\sqrt{E_L\rho_L}$ and $Z_S = A_S\sqrt{E_S\rho_S}$ [2]. The impedance in the acoustic wave is similar one. Additionally, impedance is the ratio of permeability and permittivity in an electromagnetic wave.

With the goal of introducing Kohmoto's invariant and saddle points on Kohmoto's surface, a new set of variables are introduced for the current nonlinear map:

$$\tilde{x}_i = t_{i+2},\ \tilde{y}_i = x_{i+1},\ \tilde{z}_i = x_i \tag{2.29}$$

$$t_i = tr(T_{i-2}T_{i-1}) \tag{2.30}$$

It is important to recall that for GM sequence, $t_{i+2} = tr(T_iT_{i+1}) = trT_{i+2} = x_{i+2}$. By substituting coordinates (2.29) into expression (2.25), the nonlinear map determining the evolution of x_i for GM sequence is obtained:

$$\mathcal{T}_g(\tilde{x}_i, \tilde{y}_i, \tilde{z}_i) = (\tilde{x}_{i+1}, \tilde{y}_{i+1}, \tilde{z}_{i+1}) = (\tilde{x}_i\tilde{y}_i - \tilde{z}_i, \tilde{x}_i, \tilde{y}_i) \tag{2.31}$$

[2]The impedance for the laminate problem is $\sqrt{\rho\mu}$, which is proved in Appendix B.

Jacobian is:

$$J = \frac{\partial(\tilde{x}_{i+1}, \tilde{y}_{i+1}, \tilde{z}_{i+1})}{\partial(\tilde{x}_i, \tilde{y}_i, \tilde{z}_i)} = \begin{bmatrix} \frac{\partial \tilde{x}_{i+1}}{\partial \tilde{x}_i} & \frac{\partial \tilde{x}_{i+1}}{\partial \tilde{y}_i} & \frac{\partial \tilde{x}_{i+1}}{\partial \tilde{z}_i} \\ \frac{\partial \tilde{y}_{i+1}}{\partial \tilde{x}_i} & \frac{\partial \tilde{y}_{i+1}}{\partial \tilde{y}_i} & \frac{\partial \tilde{y}_{i+1}}{\partial \tilde{z}_i} \\ \frac{\partial \tilde{z}_{i+1}}{\partial \tilde{x}_i} & \frac{\partial \tilde{z}_{i+1}}{\partial \tilde{y}_i} & \frac{\partial \tilde{z}_{i+1}}{\partial \tilde{z}_i} \end{bmatrix} \tag{2.32}$$

and the Jacobian determinant is det$J = -1$ (conserved map). For instance, by substituting (2.31) into Jacobians (2.32):

$$J_g = \frac{\partial(\tilde{x}_{i+1}, \tilde{y}_{i+1}, \tilde{z}_{i+1})}{\partial(\tilde{x}_i, \tilde{y}_i, \tilde{z}_i)} = \begin{bmatrix} \tilde{y}_i & \tilde{x}_i & -1 \\ 1 & 0 & 0 \\ 0 & 1 & 0 \end{bmatrix} \tag{2.33}$$

It is not hard to find the det$J_g = -1$. An invariant quantity exists whose expression is:

$$I = \tilde{x}_i^2 + \tilde{y}_i^2 + \tilde{z}_i^2 - \tilde{x}_i \tilde{y}_i \tilde{z}_i - 4 \tag{2.34}$$

Substitute $(\tilde{x}_i, \tilde{y}_i, \tilde{z}_i)$ into $(\tilde{x}_{i+1}, \tilde{y}_{i+1}, \tilde{z}_{i+1})$ in invariant quantity (2.34) according to Fibonacci GM sequence recursive rule:

$$I = (\tilde{x}_i \tilde{y}_i - \tilde{z}_i)^2 + \tilde{x}_i^2 + \tilde{y}_i^2 - (\tilde{x}_i \tilde{y}_i - \tilde{z}_i)\, \tilde{x}_i \tilde{y}_i - 4 = \tilde{x}_i^2 + \tilde{y}_i^2 + \tilde{z}_i^2 - \tilde{x}_i \tilde{y}_i \tilde{z}_i - 4 \tag{2.35}$$

which expressed I as an invariant in the structure arrangement according to Fibonacci sequence F_i. Also, only initial three traces trT_0, trT_1, trT_2 determine the value of I in equation (2.35) which depends on geometry, material parameters and frequency. Invariant (2.35) can be mapped onto the three-dimensional space with the orthogonal system $O\tilde{x}\tilde{y}\tilde{z}$, as depicted in the Figure 2.5.

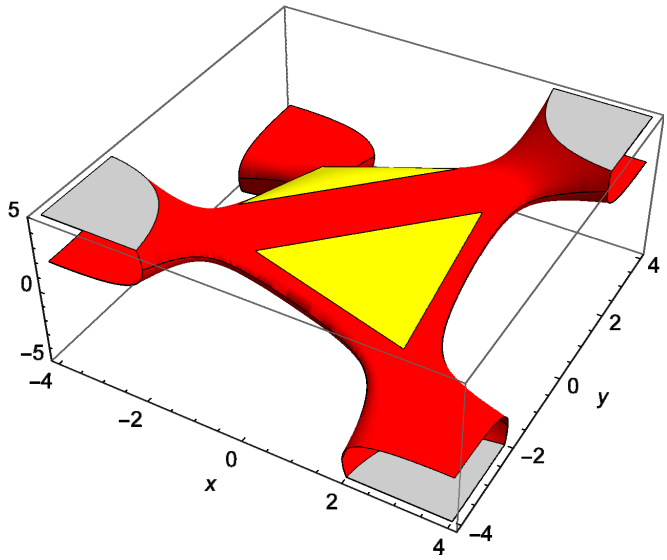

Figure 2.5. General Kohmoto's surface, which can be plot by invariant equation (2.34) *with given value Kohmoto's invariant I*

The sets of points generated by evaluation map (2.31) define different orbits which are fully constrained on the manifold Figure 2.5, which was first demonstrated by Kohmoto and Oono (1984) while investigating the spectrum of Schrödinger equations in quasiperiodic potential wells generated according to GM sequence. In recognition of the contribution to the areas by Kohmoto, $I(\omega)$ is called Kohmoto's invariant and the surface Kohmoto's surface (manifold). The map (2.31) can be viewed as 'scale transformations' by the terminology provided by renormalisation theory (Kohmoto and Oono 1984). Therefore, $I(\omega)$ is a 'scale invariant' of the structure.

There are six-saddle points P_j ($j = 1\ldots6$) on Kohmoto surface, which are in symmetric positions. A periodic closed orbit can start from any saddle points according to recursion rule (2.35). For all saddle points, one coordinate is different from zero whose value is $\sqrt{4 + I(\omega)}$ and the remaining two are zero. Through iteration map, the periodic transformation with six-cycle for the GM sequence is:

$$P_1\left(0, 0, \sqrt{4 + I(\omega)}\right) \to P_2\left(-\sqrt{4 + I(\omega)}, 0, 0\right) \to P_3\left(0, -\sqrt{4 + I(\omega)}, 0\right) \to$$

$$P_4(0, 0, -\sqrt{4 + I(\omega)}) \to P_5(\sqrt{4 + I(\omega)}, 0, 0) \to P_6(0, \sqrt{4 + I(\omega)}, 0) \to P_1 \tag{2.36}$$

Therefore, the starting point P_1 can be investigated and can predict coordinates for the other five saddle points. Because the initial point $P_1 = (x_2, x_1, x_0)$ in expressions (2.26) and combining saddle point condition (2.36):

$$trT_0 = trT_1 = 0;\ trT_0 = trT_2 = 0;\ trT_1 = trT_2 = 0 \tag{2.37}$$

For the initial three traces to satisfy these conditions, the material and geometric parameters of rods and frequency should be connected with some relations. For the Fibonacci sequence, the following relationships have been achieved (Morini and Gei 2018), which define here the class of canonical sequences shown and the corresponding canonical frequencies are given below:

$$\sqrt{\frac{\rho_S E_L}{\rho_L E_S}}\frac{l_S}{l_L} = \frac{1 + 2j}{1 + 2k},\ \sqrt{\frac{\rho_S E_L}{\rho_L E_S}}\frac{l_S}{l_L} = \frac{1 + 2j}{2q},\ \sqrt{\frac{\rho_S E_L}{\rho_L E_S}}\frac{l_S}{l_L} = \frac{2q}{1 + 2k},\ \text{with } j, k, q \in \mathbb{N} \tag{2.38}$$

$$\omega_{cj} = \pi\frac{\sqrt{E_S}}{2l_S\sqrt{\rho_S}}(1 + 2j_\omega);\ \omega_{ck} = \pi\frac{\sqrt{E_L}}{2l_L\sqrt{\rho_L}}(1 + 2k_\omega),\ \text{with } j_\omega, k_\omega \in \mathbb{N} \tag{2.39}$$

Theoretical analysis of canonical structure and canonical frequencies are shown in Chapter 4. The investigation of general properties of quasicrystalline rod constructed from canonical sequences (2.38) generated by Fibonacci GM sequence is the subject of this thesis. Furthermore, the deduced results can be used in dispersion relation for axial wave propagating in rods and determination of transition zones in laminates.

2.3.4 Papers by Gei, Morini and co-workers

Gei (2010) introduced in mechanics the concept of Fibonacci substitutional rule. The problems of harmonic axial wave and flexural wave propagating into a periodic rods and multi-supported beams were investigated. He introduced the relationship between the number of passbands and Fibonacci number n_{i+1}. The Kohmoto's invariant (Kohmoto et al. 1983; Kohmoto et al. 1987) was introduced and pointed out the crucial role in self-similarity and scaling properties in these quasicrystalline rods or beams. Due to the fact that the beam model had only two degrees of freedom when both ends are simply supported (only rotation angle at ends), the transfer matrix was still 2×2. In addition, the effects of the prestress on spectrum have been studied. If it was a tensile force, then a passband would shift to a higher frequency (highly impacted) and almost unchanged bandgaps (weakly influenced). In particular, if the prestress approached to the buckling load of beam, then the lower branch of dispersion layout would change extensively.

Then, Morini and Gei (2018) introduced the Fibonacci sequence substitution rule with precious mean sequence and metal mean sequence. A Kohmoto's invariant has been introduced for precious mean sequence. Four kinds of orbits existed on Kohmoto's manifold: (a) periodic orbits; (b) non-periodic bounded orbits; (c) escaping orbits with $\lim_{i\to\infty} |x_i| \leq 2$; (d) fully escaping orbits with $\lim_{i\to\infty} |x_i| > 2$, where x_i represents a generic coordinate $\tilde{x}_i$, $\tilde{y}_i$ or $\tilde{z}_i$. Bandgap area in the spectrum was increasing monotonically with increasing of order i. Thus, even points for a given frequency associated with wave propagation (passband) at low Fibonacci order, after several evaluations, the same frequency was in bandgap at high order, which presented an escaping or a fully escaping orbit. The escaping and non-periodic bounded trajectories of coordinates on Kohmoto's manifold could be investigated as perturbations of the periodic orbits (saddle points orbits is one of the periodic orbits) determined by scale transformations. With the investigation of saddle points on Kohmoto's manifold, the new quasicrystalline generated structure configuration, i.e. canonical structures, were proposed by to Morini and Gei (2018). The nonlinear map could be linearised analysing by employing the Jacobian of the transformation. They found the perturbation increases almost along the maximum eigenvalue direction. The scaling factor was calculated on

local (the point is the neighbourhood of periodic point) with enough numerical results, which shows a new analytical, topological tool for quasicrystalline generated structures. The details of the approach are shown in Chapter 3.

Morini et al. (2019) analysed the dynamic spectrum of the periodic quasicrystalline-generated rods through the recently introduced method of universal torus. The general characteristics of universal structure of the frequency spectrum were introduced and a parametric equation for the flow line in torus was derived. The bandgap density in a canonical structure depends on the slope of the flow line and impedance mismatch. Conversely, for non-canonical structures, the bandgap density only depends on impedance mismatch. Indeed, in terms of the boundary line in bandgap and passband for F_3, the widest bandgap for a given elementary cell with prescribed physical and geometrical properties could be identified and the optimisation of lowest band gap could be performed with the slope of flow line. In addition, the scaling effect of the spectrum was investigated by flow line intersection with subarea for bandgap on the representation of the universal torus.

Through the representation of the universal torus, bandgap optimization provides a clue for edge frequency for initial passband and bandgap when pure negative refraction in laminate is analysed, which is explained in Chapter 5. Moreover, the process for bandgap closure and reopening (band inversion) can be analysed easily and directly in square identification as shown in Chapter 6.

2.4 SH Waves and Negative Refraction in Laminates

2.4.1 Dispersion relation in Fibonacci laminates

A set of infinite two-component periodic laminates whose unit cells are generated by adopting the standard Fibonacci GM sequence F_i based on the recursion rule $F_i = F_{i-1}F_{i-2}$. The initial condition for the recursion rule is $F_0 = S$ and $F_1 = L$, where L and S are still the two homogeneous constituents. For each phase, shear modulus μ_X (also called second Lamé constant), mass density ρ_X and thickness h_X are defined (here and henceforth, $X \in \{L, S\}$). Total thickness (for the sake of same symbolic in rods problem, from now on we simply speak total length) of the laminate is $L_i = n_i^{(L)} h_L + n_i^{(S)} h_S$ as shown in Figure 2.6 where $n_i^{(L)}$ and $n_i^{(S)}$ are the number of laminae L and S included in the cell, the laminates are infinite occupying the half-space $y > 0$ (the $y < 0$ area for substrate). By assuming the coordinate system displayed in Figure 2.6, in which z is the out-of-plane axis, the non-zero displacement of the anti-plane shear wave is denoted by $u_z(x, y, t)$ and satisfies the following wave equation within any of the phases of the elementary cell (the index X is dropped to ease the notation):

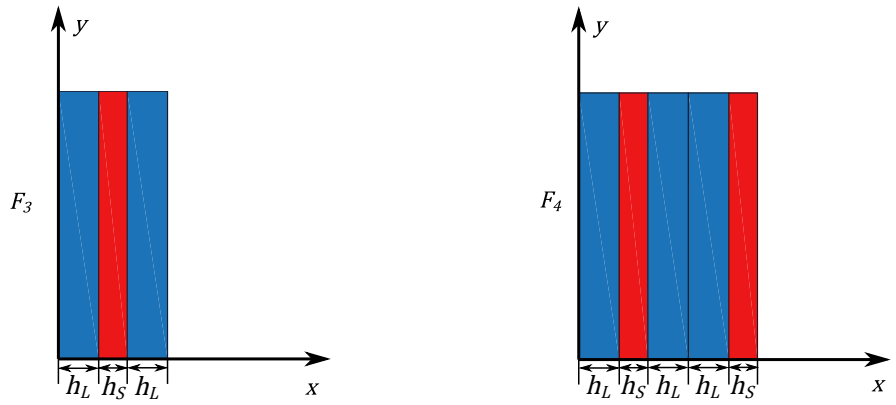

Figure 2.6. Elementary cells generated by Fibonacci sequence F_3 and F_4, figure reproduced from Morini et al. (2019)

$$\mu\left(\frac{\partial^2 u_z}{\partial x^2} + \frac{\partial^2 u_z}{\partial y^2}\right) = \rho\frac{\partial^2 u_z}{\partial t^2} \tag{2.40}$$

The harmonic solution to the equation (2.40) has the form:

$$u_z = w(x)e^{\mathrm{i}(\omega t - K_x x - K_y y)} \tag{2.41}$$

where ω is the circular frequency, K_x and K_y are the wave numbers and the amplitude function $w(x)$ is periodic, which is indeed the counterpart in last subsection $\bar{u}$. Displacement u_z and shear

stress σ_{xz} are continuous across all the interfaces. Substituting of equation (2.41) into (2.40) gives:

$$\frac{d^2w}{dx^2} - 2\mathrm{i}K_x\frac{dw}{dx} - K_x^2 w + \frac{\omega^2}{c^2}w - K_y^2 w = 0 \tag{2.42}$$

where c is shear wave phase velocity, which is $c = \sqrt{\mu/\rho}$. The auxiliary function is used to solve the equation ($w(x) = e^{\bar{\lambda}x}$) (2.40) and achieve:

$$\bar{\lambda}^2 - 2\mathrm{i}K_x\bar{\lambda} - K_x^2 = K_y^2 - \frac{\omega^2}{c_X^2}$$

The solution is $\bar{\lambda} = \mathrm{i}K_x \pm iq_X$, where $q_X = \sqrt{\omega^2/c_X^2 - K_y^2}$. Thus, the periodic part is:

$$w(x) = e^{\mathrm{i}K_x x}(C_1\cos(q_X x) + C_2\sin(q_X x))$$

Then the displacement and stress are obtained:

$$u_z = w(x)e^{i(\omega t - K_x x - K_y y)} = (C_1\cos(q_X x) + C_2\sin(q_X x))e^{\mathrm{i}(\omega t - K_y y)}$$

$$\sigma_{xz} = \mu_X q_X(-C_1\sin(q_X x) + C_2\cos(q_X x))e^{\mathrm{i}(\omega t - K_y y)} \tag{2.43}$$

Still, like in rod problem, the left boundary state vector is $u_z(x_l) = C_1 e^{\mathrm{i}(\omega t - K_y y)}$ and $\sigma_{xz}(x_l) = \mu_X q_X C_2 e^{\mathrm{i}(\omega t - K_y y)}$, where the term $e^{\mathrm{i}(\omega t - K_y y)}$ is dropped and the transfer matrix M_X has the form:

$$\begin{bmatrix}\sigma_{xz}(x)\\ u_z(x)\end{bmatrix} = \begin{bmatrix}\cos(q_X(x-x_l)) & -\mu_X q_X\sin(q_X(x-x_l))\\ \frac{\sin(q_X(x-x_l))}{\mu_X q_X} & \cos(q_X(x-x_l))\end{bmatrix}\begin{bmatrix}\sigma_{xz}(x_l)\\ u_z(x_l)\end{bmatrix} \tag{2.44}$$

The state vector on the right hand side is evaluated at the left-hand interface of the laminate concerned (x_l) while $x_l \le x \le h_X + x_l$. Therefore, the global transmission matrix M_i corresponding to the cell F_i is the result of the multiplication:

$$M_{i+1} = M_{i-1}M_i \tag{2.45}$$

with initial condition $M_0 = M_B$ and $M_1 = M_A$. Thus, similarly as before, the initial and final state vector are connected:

$$\begin{bmatrix}\sigma_{xz}(L_i)\\ u_z(L_i)\end{bmatrix} = M_i\begin{bmatrix}\sigma_{xz}(0)\\ u_z(0)\end{bmatrix} \tag{2.46}$$

We recall the dispersion relation (2.17), that is:

$$K_x L_i = \arccos\left(\frac{trM_i(f, K_y)}{2}\right) \tag{2.47}$$

The dynamic traces have two variables: frequency f and wavenumber K_y, which is different from the axial problem. The plot of the two-component wavenumber with fixed frequency is usually adopted for analysing the properties in dispersion relation of elastic problems of laminates (Willis 2016; Srivastava 2016; Nemat-Nasser 2015a; Srivastava and Willis 2017; Morini et al. 2019) with the pure real or imaginary number to observe the propagation wave or evanescent wave. It is possible to obtain more than one propagation (real) wavenumber K_y corresponding to one real solution K_x, which means waves are scattering, and an infinite quantity of evanescent waves. Then, with the mode shape decomposition and continuity condition at the interface, the acoustic Poynting vector and scattering coefficients are evaluated to be able to compute transmission angle and normalised energy.

2.4.2 Continuity at interface

The method for investigating SH waves refraction and reflection at the interface between a homogenous substrate and a quasicrystalline laminate of SH waves is shown below. The problems of an elastic substrate with shear modulus μ_0 and mass density ρ_0 occupying the half-space $y < 0$ and connected to a Fibonacci laminate with layering orthogonal to the axis y are considered as shown in Figure 2.6. An SH wave occurs at the interface from the homogenous substrate with the incident angle θ^{inc}, this wave generates finite number propagation waves and infinite number evanescent wave modes in transmitted and reflected waves (Srivastava and Willis 2017). However, if laminates with layering are parallel to the interface between substrate and laminate, there is only one real and positive refraction mode in transmitted and reflected wave (Srivastava and Willis 2017). The displacement field for the incident, transmitted and reflected waves, which are included as SH wave propagation into laminates (occupying $y > 0$) or substrate ($y < 0$), are presented that are satisfied governing equation (2.40) (Morini et al. 2019), respectively:

$$u_z^{\text{inc}} = Ae^{\mathrm{i}(\omega t - K_x^{\text{inc}} x - K_0 \cos(\theta^{\text{inc}}) y)} \tag{2.48}$$

$$u_z^{\text{trans}} = \sum_{l=0}^{\infty} T_l w_l(x) e^{\mathrm{i}(\omega t - K_x^{\text{trans}} x - K_y^{(l)} y)} \ (l \in \mathbb{N}) \tag{2.49}$$

$$u_z^{\text{ref}} = \sum_{m=-\infty}^{\infty} R_m U_m(x) e^{\mathrm{i}(\omega t - K_x^{\text{ref}} x + k_y^{(m)} y)} \ (m \in \mathbb{Z}) \tag{2.50}$$

where A, T_l and R_m are the scattering coefficients and $w_l(x)$ is periodic amplitude function in solution (2.41) for transmitted wave, $U_m(x) = \exp(-\mathrm{i}2m\pi x/L_i)$, which are also called mode shape for reflected wave, and:

$$k_y^{(m)} = \sqrt{K_0^2 - (K_0 \sin(\theta^{\mathrm{inc}}) + \frac{2m\pi}{L_i})^2} \tag{2.51}$$

Combining what deduced in Subsection 2.3.2. Thus, if $k_y^{(m)}$ is pure imaginary, it must be $k_y^{(m)} = -\mathrm{i}\bar{k}_y^{(m)}$ with $\bar{k}_y^{(m)} > 0$ because it represents evanescent reflected wave in substrate ($y < 0$). Then, the mode decomposition method is introduced for solving scattering coefficients. By applying the continuity condition of displacement u_z and shear stress σ_{yz} at the interface ($y = 0$), we yield:

$$\sum_{l=0}^{2N} T_l w_l e^{\mathrm{i}(\omega t - K_x^{\mathrm{trans}} x)} \approx A e^{\mathrm{i}(\omega t - K_x^{\mathrm{inc}} x)} + \sum_{m=-N}^{N} R_m U_m e^{\mathrm{i}(\omega t - K_x^{\mathrm{ref}} x)} \tag{2.52}$$

$$\sum_{l=0}^{2N} \mu K_y^{(l)} T_l w_l e^{\mathrm{i}(\omega t - K_x^{\mathrm{trans}} x)} \approx A\mu_0 K_{y0} e^{\mathrm{i}(\omega t - K_x^{\mathrm{inc}} x)} - \sum_{m=-N}^{N} \mu_0 k_y^{(m)} R_m U_m e^{\mathrm{i}(\omega t - K_x^{\mathrm{ref}} x)} \tag{2.53}$$

As these two equations must be satisfied at the interface along the x axis, the exponent terms must be equal. Then, $K_x^{\mathrm{inc}} = K_x^{\mathrm{trans}} = K_x^{\mathrm{ref}} = K_0 \sin(\theta^{\mathrm{inc}})$. Rigorous equality only exists in the limit of $N \to \infty$. In addition, these two boundary condition (2.52) and (2.53) can lead to mode decomposition method in Chapter 3 for solving scattering coefficients. Thus, the finite number N is used instead of infinite. Orthogonality conditions exist for different mode shape $w_l(x)$ introduced by Willis (2016), which means:

$$\int_0^{L_i} w \mu \tilde{w}^* dx = 0$$

$\tilde{w}^*$ is the complex conjugate of $\tilde{w}$. $\tilde{w}$ and w come from the same laminate system with same wave number K_x but two different K_y as in equation (2.47) ($K_x L_i = \arccos(trM_i(f, K_y)/2)$). The proof steps are the following: First, multiply $\tilde{w}^*$ to equation (2.42) and integrate over total cell length L_i:

$$\int_0^{L_i} \mu \left(\frac{d^2 w}{dx^2} \tilde{w}^* - 2\mathrm{i}K_x \frac{dw}{dx} \tilde{w}^* - K_x^2 w \tilde{w}^* \right) dx - \int_0^{L_i} \mu K_y^2 w \tilde{w}^* dx + \int_0^{L_i} \omega^2 \rho w \tilde{w}^* dx = 0 \tag{2.54}$$

The following equation can be obtained:

$$\int_0^{L_i} \mu \left(\frac{d^2 \tilde{w}}{dx^2} w^* - 2\mathrm{i}K_x \frac{d\tilde{w}}{dx} w^* - K_x^2 \tilde{w} w^* \right) dx - \int_0^{L_i} \mu \tilde{K}_y^2 \tilde{w} w^* dx + \int_0^{L_i} \omega^2 \rho \tilde{w} w^* dx = 0$$

Furthermore, get the conjugate from it:

$$\int_0^{L_i} \mu\left(\frac{d^2\widetilde{w}^*}{dx^2}w + 2\mathrm{i}K_x\frac{d\widetilde{w}^*}{dx}w - K_x^2 w\widetilde{w}^*\right)dx - \int_0^{L_i} \mu\widetilde{K}_y^2 w\widetilde{w}^* dx + \int_0^{L_i} \omega^2\rho w\widetilde{w}^* dx = 0 \quad (2.55)$$

Equation (2.54) minus (2.55) provides:

$$\int_0^{L_i} \mu\frac{d^2w}{dx^2}\widetilde{w}^* dx - \int_0^{L_i} \mu 2\mathrm{i}K_x\frac{dw}{dx}\widetilde{w}^* dx - \int_0^{L_i} \mu\frac{d^2\widetilde{w}^*}{dx^2}w dx$$

$$-\int_0^{L_i} \mu 2\mathrm{i}K_x\frac{d\widetilde{w}^*}{dx}w dx - \int_0^{L_i} \mu(K_y^2 - \widetilde{K}_y^2)w\widetilde{w}^* dx = 0 \quad (2.56)$$

that can be integrated by parts, i.e.:

$$\int_0^{L_i} \mu\frac{d^2w}{dx^2}\widetilde{w}^* dx = \int_0^{L_i} \mu\widetilde{w}^* d\frac{dw}{dx} = \mu\widetilde{w}^*\frac{dw}{dx}\bigg|_0^{L_i} - \int_0^{L_i} \mu\frac{dw}{dx}\frac{d\widetilde{w}^*}{dx}dx$$

$$\int_0^{L_i} \mu\frac{d^2\widetilde{w}^*}{dx^2}w dx = \int_0^{L_i} \mu w d\frac{d\widetilde{w}^*}{dx} = \mu w\frac{d\widetilde{w}^*}{dx}\bigg|_0^{L_i} - \int_0^{L_i} \mu\frac{dw}{dx}\frac{d\widetilde{w}^*}{dx}dx$$

$$\int_0^{L_i} \mu 2\mathrm{i}K_x\frac{dw}{dx}\widetilde{w}^* dx = \int_0^{L_i} \mu 2\mathrm{i}K_x\widetilde{w}^* dw = \mu 2\mathrm{i}K_x\widetilde{w}^* w|_0^{L_i} - \int_0^{L_i} \mu 2\mathrm{i}K_x\frac{d\widetilde{w}^*}{dx}w dx$$

μ, w and $\widetilde{w}^*$ are periodic in the interval $[0,\ L_i]$. The differentiation does not affect the periodicity, thus, $\frac{d\widetilde{w}^*}{dx}$ and $\frac{dw}{dx}$ are also periodic in range $[0,\ L_i]$. Thus, from equation $\int_0^{L_i} \mu(K_y^2 - \widetilde{K}_y^2)w\widetilde{w}^* dx = 0$, $(K_y^2 - \widetilde{K}_y^2 \neq 0)$, we reach:

$$\int_0^{L_i} w\mu\widetilde{w}^* dx = 0 \quad (2.57)$$

These orthogonality conditions do not exist when considering in-plane wave incidents into laminates (Lustig et al. 2019; Mokhtari et al. 2020). The method for decomposing mode shape to calculated scattering coefficients are presented in Chapter 3.

The wavenumber K_0L_i features the incident wave associated with the frequency and the wave phase velocity in the substrate, which is $c_0 = \sqrt{\mu_0/\rho_0}$. Therefore, the component K_xL_i is evaluated through:

$$K_xL_i = K_0\sin(\theta^{\text{inc}})L_i = 2\pi f\sqrt{\frac{\rho_0}{\mu_0}}\sin(\theta^{\text{inc}})L_i \quad (2.58)$$

Of course, the incident angle is in the range $0 \leq \theta^{\text{inc}} \leq \pi/2$. According to Morini et al. (2019), the normalised wavenumber K_xL_i belongs to the range $0 \leq K_xL_i \leq 2\pi f\sqrt{\rho_0/\mu_0}L_i$. This problem looks like the inverse problem of the axial wave because the dimensionless Bloch wavenumber K_xL_i has been determined to deduce the frequency and wavenumber K_y. Therefore, the Newton

method and matrix inverse iterations are utilized in the problem concerned shown in Chapter 3.

The real parts of the wavenumber $k_y^{(m)}$ for reflected mode wave are also investigated. Corresponding to equation (2.51), the real part is associated with propagation of the reflected wave. Pure imaginary corresponds to evanescent wave because it can not exist both a real and a imaginary part in equation (2.51) simultaneously. The number of propagating reflected modes increases with increasing order of the cell at fixed value of the frequency (Morini et al. 2019). Alternatively, at a given elementary cell F_i, a higher number of reflected modes with higher incident frequencies are found. Moreover, at least one propagation mode exists for any Fibonacci order, which is one with index $m = 0$. Thus, if we are interested to a reflectionless negative refraction, there must be only the wave with $m = 0$ and the scattering coefficients R_0 (or $\bar{R}_0$) is zero. Then, Morini et al. (2019) suggested a condition for reflected wave only with propagation mode $m = 0$:

$$0 < fL_i\sqrt{\frac{\rho_0}{\mu_0}}(1 - \sin(\theta^{\text{inc}})) < 1 \tag{2.59}$$

Actually, equation (2.59) is not entirely sufficient and the complete condition will be proposed on Chapter 5.

2.4.3 Acoustic Poynting vector and transmission angle

The acoustic Poynting vector in Willis (2016) is considering complex harmonic plane waves with a $e^{\mathrm{i}\omega t}$ dependence which gives an equation:

$$\mathcal{P} = -\frac{1}{2}\mathrm{Re}[\sigma\dot{U}^*] \tag{2.60}$$

This equation (2.60) means acoustic Poynting vector is in fact the time average energy flow (stress σ times speed $\dot{U}$). Again, the proof to reach equation (2.60) is described in Appendix B, which is very similar to the counterpart in electromagnetic fields (Yariv and Yeh 2003). Then, the stresses σ_{xz}, σ_{yz} and $\dot{u}_z^*$ are:

$$\sigma_{xz} = \mu(\frac{dw}{dx} - \mathrm{i}K_x w)e^{\mathrm{i}(\omega t - K_x x - K_y y)}$$

$$\sigma_{yz} = -\mu\mathrm{i}K_y w e^{\mathrm{i}(\omega t - K_x x - K_y y)}$$

$$\dot{u}_z^* = -\mathrm{i}\omega w^* e^{-\mathrm{i}(\omega t - K_x x - K_y y)}$$

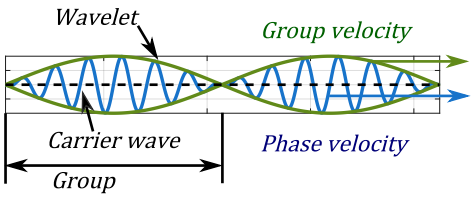

Figure 2.7. Propagation of a wave group, figure reproduced from Achenbach (2012).

Thus, the Poynting vector components can be calculated:

$$\mathcal{P}_x = \frac{1}{2}\mathrm{Re}(\omega\mu(\mathrm{i}\frac{dw}{dx}w^* + K_x w w^*)), \text{ and } \mathcal{P}_y = \frac{1}{2}\mathrm{Re}(\omega\mu K_y w w^*) \tag{2.61}$$

Then, the relationship between the Poynting vector and wave group velocity is investigated. The group velocity is initially introduced employing a kinematic argument. The first definition and derivation of the group velocity are apparently due to Stokes (Achenbach 2012). In his theory, the group velocity appears when two plane waves move forward in the positive x direction, with the same amplitude but slightly different wavenumber and hence slight different frequency. These two waves can be combined to obtain a new function, which looks like they become a new wave with an amplitude factor. It represents a modulation impressed on the carrier as shown in Figure 2.7. The group or wavelet with an amplitude propagation along with wave phase speed c_g in here is called group velocity in modulation. The original wave speed is called phase velocity c. The group velocity is:

$$c_g = \frac{d\omega}{dk} \tag{2.62}$$

This is just the same as the velocity of energy transport of a monochromatic wave (ibid), and the phase velocity depends on the material wave propagation. The wave group velocity is the frequency change rate corresponding to the wavenumber. Because the material is a composite with two different phases, the group velocity must be used to consider the energy propagation.

Willis (2016) deduced the relation with more general condition with mean energy flux over the time and space. The process for SH wave propagating into laminates is shown below, which is a case of that tackled by Willis (2016). However, the conclusion is as the same as that reached by Srivastava (2016):

$$\delta\left\{\int_0^{L_i}\sigma_{xz}\varepsilon_{xz}^* dx + \int_0^{L_i}\sigma_{yz}\varepsilon_{yz}^* dx - \omega^2\int_0^{L_i}\rho w w^* dx\right\} = 0 \tag{2.63}$$

where σ is stress and ε strain, ρ is density and ω circular frequency. Equation (2.63) is conservation of energy (Hamilton's principle) and with variation with respect to w (w is the term w_l in equation (2.49), in here, we can delete subscript l for the sake of simplicity) with K_x, K_y and ω fixed, and

the stationary value is zero. In terms of mode shape w, imposing stationarity gives:

$$\int_0^{L_i}\left(\frac{dw^*}{dx}+\mathrm{i}K_x w^*\right)\mu\left(\frac{dw}{dx}-\mathrm{i}K_x w\right)dx+\int_0^{L_i}\mu K_y^2 ww^* dx=\omega^2\int_0^{L_i}\rho ww^* dx \tag{2.64}$$

Now suppose that the set $\omega+\delta\omega$, $K+\delta K$, $w+\delta w$ satisfy the equation, too, i.e.:

$$\int_0^{L_i}\left(\frac{d(w^*+\delta w^*)}{dx}+\mathrm{i}(K_x+\delta K_x)(w^*+\delta w^*)\right)\mu\left(\frac{d(w+\delta w)}{dx}-\mathrm{i}(K_x+\delta K_x)(w+\delta w)\right)dx$$

$$+\int_0^{L_i}\mu(K_y+\delta K_y)^2(w+\delta w)(w^*+\delta w^*)dx=(\omega+\delta\omega)^2\int_0^{L_i}\rho(w+\delta w)(w^*+\delta w^*)dx \tag{2.65}$$

by neglecting the second-order terms we get:

$$\delta K_x\int_0^{L_i}\mu(\mathrm{i}w^*\frac{dw}{dx}+2K_x ww^*-\mathrm{i}w\frac{dw^*}{dx})dx+2\delta K_y\int_0^{L_i}\mu K_y ww^* dx=2\omega\delta\omega\int_0^{L_i}\rho ww^* dx \tag{2.66}$$

Now, by using the definition of group velocity (2.62), the wave group velocity is obtained:

$$v_x^g=\frac{\delta\omega}{\delta K_x}=\frac{\int_0^{L_i}\mu/4(\mathrm{i}w^*\frac{dw}{dx}+2K_x ww^*-\mathrm{i}w\frac{dw^*}{dx})dx}{\omega/2\int_0^{L_i}\rho ww^* dx};\ v_y^g=\frac{\delta\omega}{\delta K_y}=\frac{1/2\int_0^{L_i}\mu K_y ww^* dx}{\omega/2\int_0^{L_i}\rho ww^* dx} \tag{2.67}$$

The denominator $\omega/2\int_0^{L_i}\rho ww^* dx$ is associated with the total mean energy density:

$$E=\frac{1}{4L_i}\int_0^{L_i}\left(\frac{dw^*}{dx}+\mathrm{i}K_x w^*\right)\mu\left(\frac{dw}{dx}-\mathrm{i}K_x w\right)dx+\frac{1}{4L_i}\int_0^{L_i}\mu K_y^2 ww^* dx+\frac{1}{4L_i}\omega^2\int_0^{L_i}\rho ww^* dx$$

$$=\frac{1}{2L_i}\omega^2\int_0^{L_i}\rho ww^* dx \tag{2.68}$$

If group velocity (2.67) is multiplied by total mean energy (2.68), the results are the same as Willis (2016):

$$\langle\mathcal{P}_x\rangle=Ev_x^g=\frac{1}{4}\omega\frac{1}{L_i}\int_0^{L_i}\mu(\mathrm{i}w^*\frac{dw}{dx}+2K_x ww^*-\mathrm{i}w\frac{dw^*}{dx})dx$$

$$=\frac{1}{2}\mathrm{Re}(\omega\frac{1}{L_i}\int_0^{L_i}\mu(\mathrm{i}\frac{dw}{dx}w^*+K_x ww^*)dx) \tag{2.69}$$

$$\langle\mathcal{P}_y\rangle=Ev_y^g=\frac{1}{2}\omega^2\frac{1}{L_i}\int_0^{L_i}\rho ww^* dx\frac{2\int_0^{L_i}\mu K_y ww^* dx}{2\omega\int_0^{L_i}\rho ww^* dx}=\frac{1}{2}\mathrm{Re}(\omega\frac{1}{L_i}\int_0^{L_i}\mu K_y ww^* dx) \tag{2.70}$$

where $\langle\cdot\rangle$ represents the space mean utilizing the whole unit cell of laminate. Thus, angles for all transmitted propagation modes (even evanescent wave) can be estimated using the ratio of the two

components of the Poynting vector:

$$\tan(\theta^{\text{trans}}) = \frac{v_x^g}{v_y^g} = \frac{\langle \mathcal{P}_x \rangle}{\langle \mathcal{P}_y \rangle}. \tag{2.71}$$

The mode shape w_l can affect transmission wave angle θ^{trans} but the scattering coefficients $\bar{T}_l$ cannot. In addition, by observing the equation of the Poynting vector, it is significant to notice that (a): the component $\mathcal{P}_y$ is positive if wavenumber K_y is positive. Hence, only the component $\langle \mathcal{P}_x \rangle$ could be negative and then negative refraction. (b): the component $\mathcal{P}_y$ corresponding to a pure imaginary values of K_y is zero. As a result, the transmitted angle for evanescent wave could not be taken into consideration (It always 90 degree because the $\tan(\theta^{\text{trans}}) = \infty$). Of course, the transmission wave angle when SH wave is incident between two homogenous media is written here for comparison, which is Snell's Law (Achenbach 2012):

$$\frac{\sin(\theta^{\text{trans}})}{\sin(\theta^{\text{inc}})} = \frac{c_2}{c_1} \tag{2.72}$$

where c_2 and c_1 are the phase velocities for the media beyond and before the interface, respectively.

2.4.4 Papers by Willis, Srivastava and Nemat-Nasser

Nemat-Nasser (2015a) investigated the SH wave incident into a laminate with variation formulation instead of transfer matrix method in two- or three- phase laminates. In addition, combined with contour two-component wavenumber and different frequencies, the negative refraction was found when the layering was orthogonal to the interface but can not be found when the layering was parallel. He pointed out the occurrence of negative group velocity with positive phase velocity in each phase which also equals the negative energy refraction with positive phase refraction.

Willis (2016) found that when SH wave propagated into the periodic laminates, one of the group velocities was negative under some conditions. He represented the basic governing equation and transfer matrix approach combined with the Floquet-Bloch technique to analyse the dispersion relation. He found also the group velocity for the lower branch of $K_x L_i$ against $K_y L_i$ plot being negative. With variation principle, the exact relationship between acoustic Poynting vector and group velocity was clarified. The mode shape orthogonal condition was introduced through three displacements field for the incident, transmitted and reflected. A simple approach for calculating scattering coefficients was proposed in mode decomposition method. Reasonable experimental observation as evaluation energy metrics for each wave field was obtained. The research case of this thesis is one remarkable conclusion from his works.

Srivastava (2016) noticed the similarity between SH wave and EM wave so that he believed some or all of these results from analysing SH wave could be performed in the layered periodic dielectrics. Through the plot of the two-component wavenumber, the relationship between two wavenumbers was further investigated. Srivastava (2016) introduced methodology and shown the numerical results for normalised energy metrics and transmission angel through transfer matrix method and finite element software COMSOL. Two real propagation wave with 13 evanescent waves were used in the mode decomposition method. The total dimensionless energy was almost 1, which means that the accuracy for numerical calculation was reasonable. However, the energy in the transmission wave decreased monotonically when the transmission angle was negative with increasing of incident angle. The pure negative refraction could occur when wave number $K_x L_i$ enters the second Brillouin zone, but not the first. According to Srivastava (2016), periodic laminates could be used as a highpass frequency filter when the layer direction was parallel to the interface.

The method for solving scattering coefficients was the approximate approach. Srivastava and Willis (2017) proposed a novel approach for calculating scattering coefficients by imposing displacement and stress continuity at the geometric interface. As mentioned before, increasing the number of evanescent waves involved made the stress continuity more challenging to satisfy than the displacement one. Actually, if the difference between two shear modulus (μ_A and μ_B) for each phase were more significant, the stress continuity should be harder to satisfied. Thus, a new method only considering propagation wave with Lagrange multiplier was introduced and compared with decomposition through numerical results. Then, the method for calculating scattering coefficients and normalised energy concerning interface parallel to layers was also reported.

The theoretical and numerical approaches developed by the previous authors could be applied to laminate generated by Fibonacci GM sequences. From the results by Srivastava (2016), a question is naturally raised: can we obtain significant pure negative refraction with enough energy? which is solved partly in this thesis. In addition, it is hard to distinguish whether it is negative refraction or not on a plot of energy against incident angle. If wavenumber $K_x L_i$ is used as variables to replace the incident wave angle, the negative refraction could easily differ from the first Brillouin zone boundary π. Indeed, this configuration for plot energy and wavenumber method has already been performed in Mokhtari et al. (2020) for analysing in-plane wave propagation in laminates.

2.4.5 Papers by Morini, Gei and co-workers

Morini et al. (2019) summarised the previous publications concerning SH wave propagating into the periodic laminates to observe negative refraction. Quasicrystalline laminates generated by Fibonacci GM sequence with same material paraments (phase L-PMMA, phase S-steel) with previous publications (Nemat-Nasser 2015a; Nemat-Nasser 2015b; Srivastava 2016; Srivastava and Nemat-Nasser 2014; Willis 2016) has been investigated. The Kohmoto's invariant was introduced similar to the axial wave problem. With the same procedure proposed by Srivastava (2016), the dispersion relation between two components of the wavenumber K_xL_i and K_yL_i could be obtained. According to Morini et al. (2019), there existed a threshold for wavenumber K_y such that K_x was pure imaginary which means the wave propagated along y direction and was evanescent along x. In conclusion, with increasing of Fibonacci order, the limit value for K_yL_i and the number of the real solutions K_y at fixed frequency were increased. This is actually from the scaling and self-similarity effect of quasicrystalline structure (The passband layouts would be denser in the same range frequency with higher order F_i).

Moreover, Morini et al. (2019) proposed the concept of transition zone, that was associated with a particular range of frequencies. The frequency inside transition zone could lead to a determined number of real solutions K_y. The transition zone had a relationship with the initial value K_xL_i when $K_y = 0$, which was very similar to equation (2.12). Under some conditions, a transition zone was equivalent to a passband when considering SH wave perpendicular propagating into the Fibonacci laminates. Thus, the self-similarity and scaling effect could also be applied to the transition zone, as highlighted in Gei (2010) and Morini and Gei (2018) for quasicrystalline generated rods. Still, the self-similarity was governed by a local scaling whose factor could be obtained by analysing the specialised Kohmoto's invariant. Morini et al. (2019) used this principle to analyse the transition zone, and numerical results were in good agrement with the theory. However, there is a crucial thing that the two meaningful scalings may change significantly depending on the properties of the two components of the composite. Therefore, a question is naturally raised: Can we use the canonical configuration to laminates to obtain more precise results in scaling so that the transition zone can be controlled in a more reasonable way when this composite material is designed? This is novel work of Chapter 5.

For an aluminium substrate (Willis 2016; Srivastava 2016; Morini et al. 2019) and four Fibonacci elementary cells (F_2 to F_5), K_xL_i was plotted as functions of the incident angle for different values of f to enter different Brillouin zone boundary, each spanning a range of width π along the vertical axis. With increasing of generation index of the cell, the values of K_xL_i related to the same

frequency increased as well, which was due to the increasing of L_i. This means that for a given frequency, if two laminates were compared according to two different indices i, the higher-order one should access to the second (or third) Brillouin zone for a broader range of angles of incidences (Morini et al. 2019). This was an exciting phenomenon, the angle of transmission changed the sign when $K_x L_i$ enters the second Brillouin zone. The limit incident angle could be obtained from the dimensionless wavenumber $K_x L_i$ at the edge of the Brillouin zone. Also, higher-order Fibonacci laminates allowed negative refraction of a broader range of the incident angles.

In addition, 'pure' negative refraction, was investigated. Pure means that there is only one real solution in the laminates dispersion layouts, because in this configuration, the laminates could be used as a perfect acoustic lens for wave focusing. Combined with results by Willis (2016) and Srivastava (2016), Morini et al. (2019) proposed a minimum frequency to let the $K_x L_i$ entering the second Brillouin zone:

$$f_i^{\min} = \frac{\sqrt{\mu_0}}{2L_i\sqrt{\rho_0}} \tag{2.73}$$

If the frequency was lesser than $f_i^{\min}$, the dimensionless wavenumber $K_x L_i$ would be located in the first Brillouin zone, and the transmitted propagation pattern consisted of either a positively refracted mode or a pair of positively and negatively refracted waves. In order to have only one mode of propagation in laminates with negative refraction, the frequency could not be larger than the upper edge $\tilde{f}_i$ for the second transition zone due to the second transition zone meaning just one or two transmitted modes. As a consequence, if a single negatively refracted mode was transmitted, the frequency of the incident wave must belong to the interval $f_i^{\min} < f < \tilde{f}_i$. The scaling effect could analyse the value of $\tilde{f}_i$ in Fibonacci laminates. Morini et al. (2019) used the upper edge for the second Brillouin zone from laminates with phases PMMA and steel compared with $f_i^{\min}$ from the different substrate (iron, copper, nylon, polyethylene). They found that only nylon and polyethylene could produce pure negative refraction. The reason was that the wave phase velocity for these two materials was slower than other materials so that the $K_x L_i$ was large enough at relatively low frequency. However, it can lead to another problem in this research: transmitted energy is too small. In addition, if the $K_x L_i$ was entered the third Brillouin zone, the refracted angle should be positive again (change sign). There are still many aspects of pure negative refraction in Fibonacci laminates that are not clear and deserves to be deepened.

2.5 Topological Interface State in Periodic Rods

2.5.1 Surface impedance and condition for interface state

Xiao et al. (2014) proposed a topological interface state in periodic two-phase dielectric for EM wave with theory and numerical results. As there is a symmetry between 1D acoustic or mechanical waves and EM waves, that theory can be adopted here to both acoustic waves (Xiao et al. 2015; Meng et al. 2018; Li et al. 2018) and elastic waves (Yin et al. 2018; Muhammad et al. 2019; Chen et al. 2021).

According to Xiao et al. (2014), the surface impedance Z_s and the electric field reflection coefficient r is related by:

$$Z_s = \frac{1+r}{1-r} Z_0 \tag{2.74}$$

where Z_0 is the reference surface impedance. Equation (2.74) is coming from results from the problem where an EM wave incident from the material with surface impedance Z_0 to a structure with Z_s by the continuity condition at the reflection interface as shown in Figure 2.8 (Xiao et al. 2014). However, for an elastic wave, the axial force N equivalent to electric field and velocity V to the magnetic field. Thus, if equation (2.74) is used for elastic wave, the axial force reflection coefficient must be used instead of displacement. If displacement reflection coefficient is used, equation (2.74) would become:

$$Z_0 = \frac{1+r}{1-r} Z_s$$

Z_s is a pure imaginary number, that can be written $Z_s/Z_0 \equiv i\varsigma$, when frequency is in a bandgap, where ς is a purely real number. $\varphi = \pi - 2\arctan(\varsigma)$ is reflection phase in this problem which can be experimentally measured for predicting Zak phase (Xiao et al. 2015). Then, other periodic structures are connected, which can be both sides. The surface impedances, reflection coefficients and reflection phases are denoted as Z_{rhs}, Z_{lhs}, r_{rhs}, r_{lhs} and φ_{rhs}, φ_{lhs}, respectively, where rhs

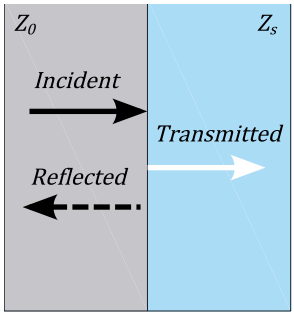

Figure 2.8. Wave incident from material with impedance Z_0 to periodic structure with surface impedance Z_s. The wave could be optical, acoustic or elastic. The structure could be a rod or laminate.

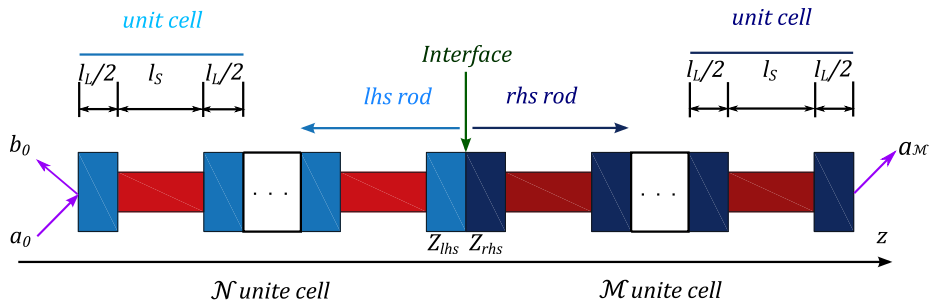

Figure 2.9. Two 1D quasiperiodic rods with $\mathcal{N}$ (and $\mathcal{M}$) unit cells in the right connections at the interface, a_0, b_0 and $a'_{\mathcal{M}}$ are incident, reflected and transmitted wave amplitude. lhs and rhs denote the left and right side quasiperiodic rod. Figure reproduced from Chen et al. (2021)

and lhs means the right hand side or left hand side as shown in Figure 2.9. The condition for the existence of an interface state is that the sum of two surface impedance is zero:

$$Z_{\text{rhs}} + Z_{\text{lhs}} = 0 \tag{2.75}$$

this condition implies that $(1 + r_{\text{rhs}})/(1 - r_{\text{rhs}}) + (1 + r_{\text{lhs}})/(1 - r_{\text{lhs}}) = 0$, which is equivalent to $r_{\text{rhs}} r_{\text{lhs}} = 1$ or $\varphi_{\text{rhs}} + \varphi_{\text{lhs}} = 2m\pi (m \in \mathbb{N})$. Since surface impedance is hard to measure, a concise way to achieve an interface state is to establish a system as frequency is inside a bandgap that has two periodic structures with the surface impedance opposite in sign. The sign of surface impedance for frequency inside bandgaps is decided by the geometrical phase of the bulk bands (passband), which is the sum of the Zak phases previous passbands. The dispersion relation can be obtained by the transfer matrix method (Xiao et al. 2014). Thus, the introduction of Berry connection in 1D systems, the Zak phase, is proposed.

2.5.2 Geometric topological phase-Zak phase

Moreover, there exists a relationship between the sign of surface impedance (also reflection phase and coefficients) and the Zak phase. A Zak phase only takes a value 0 or π if the origin of unit cell is chosen to be one of the inversion centres (Zak 1989), which is also proved by Xiao et al. (2015). The structures that hold inversion symmetry in rods generated by Fibonacci sequences only are F_2 and F_3 as shown in Figure 2.9. In fact, the F_3 is special case of F_2 (in Figure 2.9, obtained by changing $l_L/2$ into l_L). For each passband n, the Zak phase is calculated as (Xiao et al. 2015; Yin et al. 2018; Meng et al. 2018; Li et al. 2018; Muhammad et al. 2019; Chen et al. 2021) for acoustic and elastic waves:

$$\theta_n^{\text{Zak}} = \int_{-\pi/L_i}^{\pi/L_i} \left[\mathrm{i} \int_{\text{unit cell}} \frac{1}{2\rho c^2} d\mathbf{r} dz \mathcal{W}_{n,K}^*(z,\mathbf{r}) \partial_K \mathcal{W}_{n,K}(z,\mathbf{r}) \right] dK \tag{2.76}$$

where K is Bloch wavenumber, factor $1/(2\rho c^2)$ is the weight function for the acoustic or elastic structure. The term $\mathcal{W}_{n,K}$ represents the periodic part of the normalized force (elastic) or pressure (acoustic) in the nth passband with Bloch wavenumber K, which is $\mathcal{W}_{n,K} = N(n,K)e^{\mathrm{i}Kz}$. The term $\left[\mathrm{i}\int_{\text{unit cell}} \frac{1}{2\rho c^2} d\mathbf{r}dz\mathcal{W}^*_{n,K}(z,\mathbf{r})\partial_K\mathcal{W}_{n,K}(z,\mathbf{r})\right]$ is called Berry connection. In addition, the relationship between Zak phase (topological properties of bulk dispersion) and sign of surface impedance $\mathrm{sgn}(\varsigma^n)$ for nth bandgap (surface scattering properties) takes the following simple expression (Xiao et al. 2014; Xiao et al. 2015; Yin et al. 2018; Meng et al. 2018; Li et al. 2018; Muhammad et al. 2019; Chen et al. 2021):

$$\mathrm{sgn}[\varsigma^n] = (-1)^n(-1)^g e^{(\mathrm{i}\sum_{m=0}^{n-1}\theta_m^{\mathrm{Zak}})} \tag{2.77}$$

where integer g is the number of crossing points for passband under the nth gap, the Zak phase of the lowest 0th passband is determined by a formula, which is introduced in Chapter 6. Then, it is easy to determine whether there exists an interface state, for instance, two structures with opposite $\mathrm{sgn}[\varsigma]$ in a range of frequencies which are in a bandgap. Of course, if the exact frequency for the interface state is solved, the equation (2.75) should be used. The details for performance in the program for integral (2.76) are discussed in Chapter 3.

2.5.3 Papers by Xiao and co-workers

As mentioned before, there was a way to have an interface state, which was tuning the geometrical or material coefficients to let the bandgap across a topological transitional point (Xiao et al. 2014; Xiao et al. 2015). Xiao et al. (2014) slightly changed the parameter in one photonic laminate and calculated the Zak phase for each passband and the sign of surface impedance. Then, a bandgap changed the sign of surface impedance and the Zak phase near this bandgap, representing a topological phase transition. This happens when two passbands cross each other. They believed this topological phase transition was analogue to the SSH model in electronic systems (Su et al. 1979; Su et al. 1980), even the concept of impedance was not usually considered in electrons. This method could also be explained in another way: bandgap closure and reopening. Moreover, the condition for passband crossing was already explained by Xiao et al. (2014) with rigorous proof, which is the ratio of two wave paths, a rational number, namely:

$$\bar{\alpha} = \frac{\xi_L}{\xi_S} = \frac{\overline{m}_1}{\overline{m}_2} \ (\overline{m}_1, \overline{m}_2 \in \mathbb{N}^+) \tag{2.78}$$

then passbands $\overline{m}_1 + \overline{m}_2$ and $\overline{m}_1 + \overline{m}_2 - 1$ cross at the frequency:

$$\omega_{(\overline{m}_1+\overline{m}_2)} = \frac{(\overline{m}_1+\overline{m}_2)\pi c}{(\xi_L+\xi_S)} \tag{2.79}$$

This also means $(\overline{m}_1+\overline{m}_2)$th bandgap closes at this frequency at the centre or edge of the first Brillouin zone. If the $(\overline{m}_1+\overline{m}_2)$th bandgap was closed, all other closed bandgaps would be integer multiples of $\overline{m}_1+\overline{m}_2$. In this thesis, the representation based on the universal torus is used to investigate the condition of bandgap closure. Xiao et al. (2014) also deduced that the Zak phase of this band must be π (non-trivial topological phase) with $\sin(\xi_S) = 0$ existed in an isolated passband. Otherwise, it is zero (trivial topological phase) within a structure holding inversion symmetry. This rule applied to all passbands except the 0th passband, because this point could be a discontinuity point in the passband. Berry connection was an odd function corresponding to KL_i in full 1st Brillouin zone. Without this discontinuity point, equation (2.76) must be zero due to the symmetry of the periodic part. If this point exists in an isolated passband, the integration should be π.

The relationship between the Zak phase or surface impedance with symmetry properties of the edge mode is beneficial in the development of this thesis, because only the edge mode needs to be investigated without evaluating complex integral for the Zak phase. Of course, the term $\sin(\xi_S)$ also follows this rule. Edge mode means the displacement or force field at the frequency corresponding to dimensionless wavenumber KL_i is either equal to 0 or π ($-\pi$). Xiao et al. (2014) used the conclusion from Zak (1984) and Kohn (1959), which explained that Zak phase of the nth passband is 0 or π. Obviously, it had the relationship with terms $\sin(\xi_S) = 0$. The analogue phenomenon has been explained in the electronic system (Hasan and Kane 2010; Bernevig et al. 2006; Pankratov et al. 1987). Then, Xiao et al. (2014) called axial force with vanish amplitude at the origin as A (antisymmetric) state and the other as S (symmetric) state (in fact, it should be maximise (Liboff 1992)). It was exciting to see that the electric field was zero at the edge for the A state, which was analogue to a perfect electric conductor edge condition, whereas the electric field was maximum at the edge for the S state, which leads a perfect magnetic conductor.

In this thesis, axial force and displacement are subject to a similar phenomenon, since the edge mode across the bandgap is orthogonal (different symmetric). For A state, the reflection coefficients must be $r = -1$, associated with a reflection phase $\varphi = \pi$. If the S state is surveyed, $r = 1$ and $\varphi = 0$ or 2π should be obtained. In terms of relation $\varphi = \pi - 2\arctan(\varsigma)$, for a bandgap with A state at the lower edge, the function ς takes a value 0 at the lower edge and decrease monotonically to $-\infty$ as the upper edge is approached. For a bandgap with state S at the lower edge, the function ς decreases monotonically from ∞ to 0 as the upper edge is entered. It can be proved by

the edge mode with the term $\sin(\xi_S) = 0$ connected to Zak phase via the equation (2.76). Thus, the sign of ς can be determined by the type of state at the lower edge (or upper edge because they are different). In our cases, the axial force N is used to replace electric field. Combined with symmetric properties of edge mode and topological transition point, the Dirac cone was plotted in many research publications (Xiao et al. 2015; Li et al. 2018; Yin et al. 2018; Muhammad et al. 2019).

Xiao et al. (2014) also explained that this process could be performed on other 1D structures in an acoustic or elastic wave. They also performed acoustic systems by considering the reflection phase for the Zak phase (Xiao et al. 2015). The determined geometrical phase has already been deduced theoretical and experimental in the cold atom (Atala et al. 2013). By measuring the reflection phase of two bandgap, which were sandwiching of choose passband, the results were agreed with the theoretical prediction. In addition, the results from the pressure field as the frequency for the topological interface state were investigated with point by point measurement and the conclusion was wave field localised at the geometric interface of two different structures.

2.5.4 Papers by Meng, Li and co-workers

Meng et al. (2018) used the periodic acoustic system for analysing the interface state. They used different two material parameters which were δr and δd controlling the radius of two element (area) and length differences of unit cells, respectively (in Figure 2.9, $(l_L - L_S)/2 = \delta d$). They derived a full phase diagram for the initial four bandgaps based on the transfer matrix method. Thus, this material could be designed following the diagram, which could supply complete geometric and material information with single or multiple arbitrary bandgaps for having an interface state. In addition, the numerical results from COMSOL and experiments were performed to verify theoretical analysis (Meng et al. 2018). In this thesis, the extended torus can be performed and easier for observing interface state than the full phase diagram because it needs n number of figures if an interface state at nth bandgap is designed. In addition, the pressure fields were surveyed and results like before. The reason for the difference in results between transfer matrix and COMSOL also were clarified due to the impact from cross-section area in periodic tubes. The impact from the number of unit cells on interface state also was studied with results whose number of unit cell was larger than 3, the frequency error was smaller than 5%.

Li et al. (2018) performed experiments on periodic acoustic structures with a different radius on tube junctions similar to intercell hopping and intracell in the SSH model. The Zak phase and edge mode relationship were analysed again, same with Xiao et al. (2015). However, in this

case, the difference between radius injunction could be tuned to lead to the topological phase inversion (bandgap inversion). The topological interface state was measured by setting periodic holes in the structure. In addition, topological edge states were numerical simulation and verified by theoretical solution, which existed when structure held non-trivial topological phase π but not contrary. The robustness of the interface state against local perturbations (defects) also was verified. The wave field and transmission spectrum at interface state were impacted by thermal and acoustic leakage heavily. Moreover, the edge state in this acoustic system was topological protected, proved by numerical simulation.

2.5.5 Papers by Yin, Muhammad, Chen and co-workers

Because of investigation in this area being extremely new, there are only several publications about elastic wave systems. Some general results, for instance, the Zak phase and the sign of surface impedance or symmetric properties of edge mode, are identical in previous papers. Only differences are introduced in here. Yin et al. (2018) introduced axial wave and flexural wave with Timoshenko beam theory to investigate the effect on Zak phase and topological interface state through finite element methods and experiments. With the variation of parameters, the Dirac cone plot was symmetric in the axial wave but not symmetric in the flexural wave problem, resulting from the non-linear dispersion relation in the elastic beam model. Thus, this investigation extended the concept in topological interface state from optical and acoustic waves to elastic waves. However, they noticed the interface state only happens in a range of frequency as bandgap inversion.

Muhammad et al. (2019) also introduced interface states for axial and flexural wave problems but with Euler beam theory. The relationship between slenderness ratio and shear effect were analysed so that the error could be allowed Euler beam theory utilised (because only bending effect in Euler theory). The dispersion relation was obtained from the transfer matrix method and the modified matrix method. The Von-Mises equivalent stress was used to substitute pressure or force for checking the wave field effect at the interface state. The wave energy with Q-factor was demonstrated to further show their localisation at the geometrical interface between two different structures and the robustness effect to defend material damping and material loss. It was presented that the large damping ratio decreases extremely the effect of energy localisation at the geometric interface.

The complete process for evaluating reflection coefficient, transmission spectrum and wave field on the finite periodic rods were introduced by Chen et al. (2021), especially on the junction of two structures with different topological phases. Moreover, the numerical Zak phase process was

proved comparing with the general form in the elastic wave system. They investigated the non-linear material with incremental theory. The soft material with the large-deformation ability and strain stiffening effect were studied to change the topological interface state. They summarised the effect of prestressing and non-linear material on the frequency for interface state with theoretical and numerical analysis. The bandgap inversion process was changed by prestressing and initial geometric coefficients. The prestress could decrease the frequency for interface state monotonically under the neo-Hookean theory but the variation with prestressing in a non-monotones way under Gent theory.

2.6 Conclusion and Remarks

The literature review concerning 1D structure generated by Fibonacci GM sequences is established. Fibonacci GM sequence generated by substitution rule is derived and compared other precious mean sequence, which is the topic of this thesis. Moreover, governing differential equation for axial wave propagation into rod and shear horizontal (called SH or anti-plane shear wave) wave propagating in laminate are explained in detail. The transfer matrix is introduced for dispersion spectrum analyses. Then the Floquet-Bloch technique is introduced that is combined with the transfer matrix to derive the dispersion relation of quasicrystalline generated structure from a standard eigenvalue problem. Then, Kohmoto's invariant and multi-variables Jacobian are introduced, which govern the scaling and self-similar properties of the frequency spectra. With the investigation in the saddle point on Kohmoto's surface, a novel configuration for the quasicrystalline structure is proposed, called canonical structure. These configurations let two of the initial three traces to become zero. The works by Gei and Morini is completed by pointing out that they analyse quasicrystalline rods generated by Fibonacci GM sequence with Kohmoto's invariant and universal torus. According to Kohmoto's manifold and principle for the universal torus, the details for local scaling are introduced in Chapter 3. The configuration for canonical structure has already been derived, but the exact relationship with canonical frequencies and canonical ratio still need to be clarified, for example, the relationship between parameters j, k, q in equation (2.38) and ω_{cj}, ω_{ck}. Moreover, the scaling effect with canonical configuration should be verified theoretically and numerically.

In addition, negative refraction when a SH wave incident from a homogenous substrate to quasicrystalline laminates is explained with three wave fields and mode decomposition using the condition of mode shape orthogonality and continuity at the interface. Furthermore, the acoustic two-component Poynting vector is evaluated to compute the transmission angle in laminates.

Willis, Srivastava and Nemat-Nasser show the basic theory about dispersion relationship, evanescent wave and negative refraction under some conditions. The methodology concerning scattering coefficients and normalised energy are shown in Chapter 3. However, Willis, Srivastava and Nemat-Nasser investigate the phenomenon of periodic laminates, which is especially the case in quasicrystalline GM sequences (F_2 or F_3). Thus, the findings of Morini and Gei are also introduced as our one of our topic is quasicrystalline generated laminates. They find that the negative refraction governing by two frequencies. One is the minimum frequency (threshold) to render wave number $K_x L_i$ entering second Brillouin zone ($K_x L_i > \pi$). The other one is the upper edge for the second transition zone, which is equivalent to the passband layouts in the 1D rod problem. Thus, Kohmoto's invariant can be utilised for scaling the transition zone. In their papers, there are also listed some interesting phenomena but without full explanation. For instance, the transmission angle that is equal to zero when wavenumber is at the edge of Brillouin zone, the reflectless, total reflection phenomena and relationship between the number of propagation wave with higher Fibonacci order. Furthermore, a way to control the transmission angle and enough energy for pure negative refraction should be studied. It is possible to obtain the closed-form expression for transmission angle instead of Poynting vector formulation, and energy extreme value as pure negative transmission happened can be observed.

Finally, the topological interface state is introduced, which exists in two periodic structures with different topological phases evaluated by the Zak phase. The exact condition for interface state is the vanishing sum of surface impedances from two structures. Then, the approach for calculating reflection and transmission coefficients and wave field (force) of finite rods are demonstrated in Chapter 3. According to Xiao's work, several significant theoretical derivation were introduced, including the fundamental principle for Zak phase calculating, relationship with symmetric edge mode, topological phase inversion. The sign of surface impedance is changed with bandgap close and reopen (band inversion) and numerical results verify the existence of the interface state. The works by Meng and Li demonstrated the same principle but in the acoustic system with further numerical results and experiments. Finally, the works by Yin, Muhammad and Chen showed the interface state in the elastic system, which is similar to our problem in both axial and flexural waves. The investigation in this part is still growing. A very significant inference is that the symmetric edge mode at the lower or upper of a bandgap determine the sign of impedance with a structure that holds inversion symmetry. The frequency for the interface state should be checked whether it can be determined with phases that have the unique combination of material and geometric parameters because the engineer can design this material better when they know how to control the frequency for the interface state.

Chapter 3 - Methodology

Methods and processes to lead to the codes implemented are described in this chapter, including the dispersion spectrum tool for quasicrystalline generated structures (Kohmoto's invariant and universal torus), shear horizontal wave reflection and refraction in laminates (numerical integration and Newton iteration), and the topological interface state problem (transmission, reflection coefficients and wave field). Thus, the theoretical analysis concerning problems above can be verified by numerical results in this chapter. Complete codes are shown in Appendix A.

3.1 Dispersion Relation in Quasicrystalline-Generated Structures

The trace of global transfer matrix for one element unit cell can be obtained by utilizing the vector which manages the different elementary cells in any order of sequence. For the problem of axial rod, only manipulating circular frequency ω and obtaining the trace of global transfer matrix is enough. It means the eigenvalue problem does not need to be solved. Thus, two vectors for frequency and trace trT_i are created. The passband layouts are plotted with the definition from Equation (2.20). Moreover, the universal torus with two dimensionless frequencies are also plotted using this method. However, for SH wave propagating into the laminate problem is slightly different, because this problem has two wavenumbers K_y (or dimensionless K_yL_i) and $K_xL_i = K_0\sin(\theta^{\text{inc}})L_i$. As the trace of transfer matrix M_i is associated with K_xL_i, the wavenumber K_y can be obtained with fixed frequency from dispersion relation (2.47). The frequency can also be solved as the same process with fixed K_y. If the complete passband layout for SH wave propagation into laminate is needed, the principle must be identical to plotting universal torus because this problem also takes two variables (f and K_y) but with passband being a real number, the bandgap being a complex number. The computational process is shown in Figure 3.1.

3.2 Tools for Analysing Spectrum-Universal Torus

The dispersion relation analysed through the representation of the universal torus takes advantage of the introduction of the following dimensionless frequencies (Morini et al. 2019; Shmuel and Band 2016; Lustig and Shmuel 2018; Barra and Gaspard 2000; Berkolaiko and Winn 2010; Band and Berkolaiko 2013):

$$\xi_X = \sqrt{\frac{\rho_X}{E_X}}\omega l_X \ (X \in (L,S)) \tag{3.1}$$

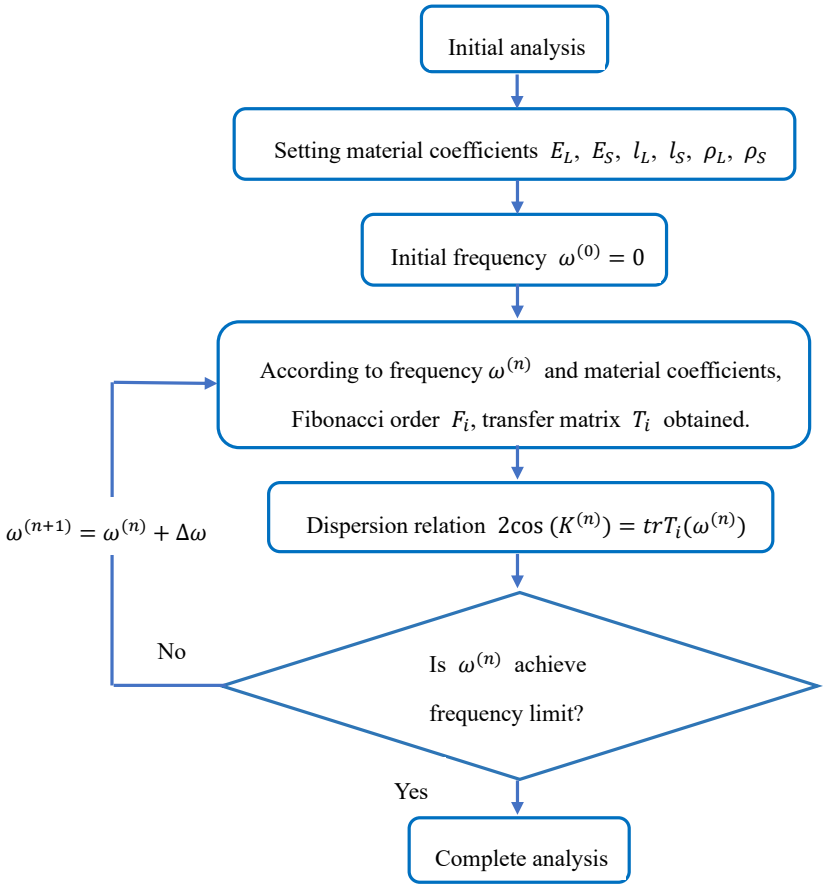

Figure 3.1. Computational process for dispersion layout.

For GM sequence, the recursive rule for trace whose governing the dynamic spectrum properties has already deduced from equation (2.25), which indicates the following recursive relation (2.25) for the half trace:

$$\frac{x_{i+1}}{2} = 2\frac{x_{i-1}}{2}\frac{x_i}{2} - \frac{x_{i-2}}{2} \tag{3.2}$$

where the initial conditions are:

$$\frac{x_0}{2} = \cos(\xi_S),\ \frac{x_1}{2} = \cos(\xi_L),\ \frac{x_2}{2} = \cos(\xi_L)\cos(\xi_S) - \frac{\beta}{2}\sin(\xi_L)\sin(\xi_S) \tag{3.3}$$

where β is impedance mismatch $\beta = \frac{Z_L}{Z_S} + \frac{Z_S}{Z_L}$. When the impedance mismatch is $\beta = 2$, there is no difference between phases, and the structure resembles a homogeneous one in wave problem, since the impedance for $Z_L = Z_S$ (The material in L may different with material in S with the same impedance value). Equation (3.3) demonstrates that for every given amount of mismatch impedance β, the half trace is determined by sums and multiplications of periodic functions with the same period. This demonstrates that the half trace $x_i/2$ is a function of the 2D torus with edge length 2π and toroidal and poloidal coordinates ξ_S and ξ_L. According to inequality (2.20), the area of the toroidal is consistent with two components corresponding to passband and bandgap.

This approach involving standing waves split these two locations. Impedance mismatch uniquely determines the section of the bandgap. Therefore, a topological torus may regulate these structures, as the dynamic characteristics are identical if the mismatch impedance is identical, regardless of the two-phase material or geometric factors (Shmuel and Band 2016).

According to Morini et al. (2019), a sketch of the toroidal domains for the Fibonacci order F_2 is displayed in Figure 3.2, where the half of impedance mismatch is almost $\beta/2 \approx 2.125$. The pink zone is associated with the passband area in plots, while the bandgap one is plotted in grey. Equation (2.19) is invariant under the transformation:

$$\xi_S \to \xi_S + \bar{S}\pi \text{ and } \xi_L \to \xi_L + \bar{L}\pi \ (\bar{S}, \bar{L} \in \mathbb{N}) \tag{3.4}$$

Shmuel and Band (2016) mentioned that the map on the torus could be equivalently demonstrated on a reduced π edge length torus, which can be effectively represented by the so-called square identification (Arnold et al. 2013). It means that the curved area is flatted and transformed to a square whose edges coordinates are still ξ_S and ξ_L, both ranging from 0 to π. In the new square representation, the bandgap subarea is represented by $\mathbb{D}_i(\beta)$, which are implied with torus $\mathbb{T}_i$. At the same time, this reduced torus for the Fibonacci order F_i can be extended into $\bar{S}\pi$ and $\bar{L}\pi$ range (extended torus), which is helpful in particular problems (how the sign of surface impedance is changed with variables ξ_S and ξ_L changing).

In Figure 3.2, the reduced torus $\mathbb{T}_2$ is reported. The plot's light blue, red and brown areas present the subareas determined for different $\beta/2$. Therefore, the dispersion spectrum of any Fibonacci order can be investigated by analysing the dynamic flow line on the toroidal areas, where the frequency ω plays a role of a time-like parameter. This flow line is the image on $\mathbb{T}_i$ whose trajectories on the original torus are angles between ξ_S and ξ_L. One example of the flow line is the blue line sketched in Figure 3.2. In order to represent these lines on $\mathbb{T}_i$, equation (3.1) can be translated into a rectilinear trajectory on the square. For any Fibonacci unit cell F_i for which a specific indication for the length l_L and l_S is given, equation (3.1) can be plotted on $\mathbb{T}_i$. If we consider values of the frequency such that $\xi_X > \pi$, by recalling the invariance of $\mathbb{T}_i$ and of its subarea $\mathbb{D}_i(\beta)$ with respect to transformations (3.4), expression (3.1) can be written in the transformed form as:

$$\xi_S = \sqrt{\frac{\rho_S}{E_S}}\omega l_S - \bar{S}\pi \text{ and } \xi_L = \sqrt{\frac{\rho_L}{E_L}}\omega l_L - \bar{L}\pi \ (\bar{S}, \bar{L} \in \mathbb{N}) \tag{3.5}$$

Therefore, the flow line plotted on $\mathbb{T}_i$ looks like a set of the parallel lines which is reported in blue in Figure 3.2. The flow line with rational number as tangent angle must be closed in torus.

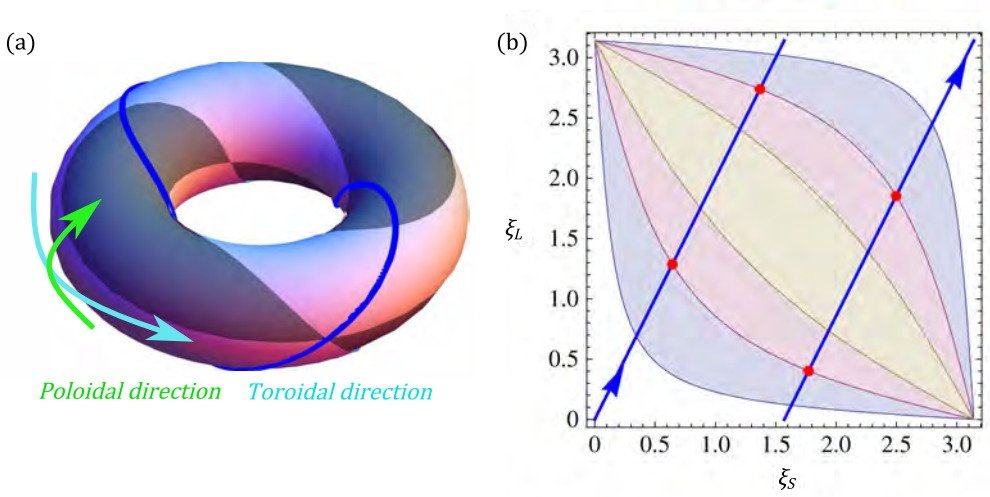

Figure 3.2. (a). Toroidal domains of edge length 2π for Fibonacci cells F_2. The passbands regions are depicted in pink. The bandgap are highlighted in grey. An example of a periodic, close flow line is reported in blue. (b). Square identification of the π period torus for cell F_2; light blue, red and brown regions associated with the subarea for bandgap with decreasing mismatch impedance β, figure reproduced from Morini et al. (2019).

Thus, it is not surprising the frequency at the flow line intersecting the boundary with subarea $\mathbb{D}_i(\beta)$ coincides with the edge of the bandgaps. A parametric equation for the flow lines on the representation of the universal torus or square torus is deduced in equation (3.6):

$$\xi_L = \pi(\frac{\bar{S}}{C} - \bar{L}) + \frac{\xi_S}{C} \tag{3.6}$$

which defines the direction (angle) of the flow. The flow line, in particular, is emerging from the $\omega = 0^+$ ($\bar{S} = \bar{L} = 0$) with the equation $\xi_L = \xi_S/C$ also the flow line in the extended torus. This analysis method of analysis dispersion relation benefits from a technique developed for the investigation of Schrödinger operators on metric graphs (Barra and Gaspard 2000; Berkolaiko and Winn 2010; Band and Berkolaiko 2013) and can be extended to laminate structure (Shmuel and Band 2016).

3.3 Numerical Approach in Wave Propagation in Laminate

3.3.1 Newton method and inverse iterations

As the acoustic Poynting vector is calculated from mode shape w and the trace M_i becomes too complicated with increasing of Fibonacci order i to solve eigenvalues, so that the eigenvector in equation (2.46) should be obtained numerically. The Newton method can be used here. First, a vector for $K_y L_i$ with fixed frequency f is substituted into the transfer matrix (2.47) to evaluate $K_x L_i$, then compared with $K_0 \sin(\theta^{\text{inc}}) L_i$ to determine a small interval of K_y. Thus, the mission is

to solve the eigenvalue problem:

$$(M_i(K_y) - e^{\mathrm{i}K_x L_i}\mathbf{E})\begin{bmatrix}\sigma_{xz}(0)\\ u_z(0)\end{bmatrix} = \begin{bmatrix}0\\0\end{bmatrix} \tag{3.7}$$

where $\mathbf{E}$ is the identity matrix. It must have a non-trivial solution, so that the wavenumber K_y can be seen as a non-linear general eigenvalue of matrix $M_i - e^{\mathrm{i}K_x L_i}\mathbf{E}$. K_y^* is the approximation solution of exact $\hat{K}_y$ and using Taylor expansion for matrix $\bar{M}_i$ (for simplicity $\bar{M}_i = M_i - e^{\mathrm{i}K_x L_i}\mathbf{E}$):

$$\bar{M}_i(\hat{K}_y) = \bar{M}_i(K_y^*) + (\hat{K}_y - K_y^*)\frac{d\bar{M}_i(K_y^*)}{dK_y} + \frac{(\hat{K}_y - K_y^*)^2}{2}\frac{d^2\bar{M}_i(K_y^*)}{dK_y^2} + o((K_y^* - \hat{K}_y)^3) \tag{3.8}$$

Multiplying the exact eigenvector $[\sigma_{xz}(0), u_z(0)]^T$ in equation (3.8) and ignore the second and higher order:

$$\bar{M}_i(\hat{K}_y)[\sigma_{xz}(0), u_z(0)]^T \approx \bar{M}_i(K_y^*)[\sigma_{xz}(0), u_z(0)]^T + (\hat{K}_y - K_y^*)\frac{d\bar{M}_i(K_y^*)}{dK_y}[\sigma_{xz}(0), u_z(0)]^T \tag{3.9}$$

because $\bar{M}_i(\hat{K}_y)[\sigma_{xz}(0), u_z(0)]^T \equiv 0$. Thus:

$$\bar{M}_i(K_y^*)[\sigma_{xz}(0), u_z(0)]^T \approx -(\hat{K}_y - K_y^*)\frac{d\bar{M}_i(K_y^*)}{dK_y}[\sigma_{xz}(0), u_z(0)]^T \tag{3.10}$$

Equation (3.10) expresses that for a approximation eigenvalue, if $\bar{M}_i(K_y^*)$ and $d\bar{M}_i(K_y^*)/dK_y$ are already known, the more exact eigenvalue and eigenvector could be solved from general linear eigenvalue problem:

$$\bar{M}_i(K_y^*)[\sigma_{xz}(0), u_z(0)]^T \approx \eta(K_{yu} - K_{yl})\frac{d\bar{M}_i(K_y^*)}{dK_y}[\sigma_{xz}(0), u_z(0)]^T \tag{3.11}$$

where K_{yu} and K_{yl} are associated with upper and lower eigenvalue when corresponding $K_x L_i$ across target wavenumber $K_0 \sin(\theta^{\mathrm{inc}}) L_i$ (details shown in Figure 3.3). Because the dispersion relation $K_x L_i$ and $K_y L_i$ creates two vectors for two components wavenumber within a determined small interval, the exact $\hat{K}_y$ must belong to the range (K_{yl}, K_{yu}) and also let the Newton method must be convergence. Then:

$$\eta = \frac{K_y^* - \hat{K}_y}{K_{yu} - K_{yl}} \tag{3.12}$$

There are many methods for solving general linear eigenvalues, such as inverse matrix iteration, subspace iterations and Lanczos method. In this thesis, the derivative of a matrix is obtained using

the central difference method:

$$\frac{d\bar{M}_i(K_y^*)}{dK_y} = \frac{\bar{M}_i(K_{yu}) - \bar{M}_i(K_{yl})}{(K_{yu} - K_{yl})} \tag{3.13}$$

Thus, the problem converts into a linear eigenvalue problem:

$$\bar{M}_i(K_y^*)[\sigma_{xz}(0), u_z(0)]^T = \eta(\bar{M}_i(K_{yu}) - \bar{M}_i(K_{yl}))[\sigma_{xz}(0), u_z(0)]^T \tag{3.14}$$

Because of equation (3.12), the $|\eta| < 1/2$ is a convergence standard for numerical results. Also, an approximate value $K_{y\eta}$ can be obtained with second-order exact (Yuan et al. 2004):

$$K_{y\eta} = \frac{(K_{yl} + K_{yu})}{2} - \eta((K_{yu} - K_{yl})) \tag{3.15}$$

This method can be used to solve some other non-linear general eigenvalues, such as the natural frequency of structure using the Wittrick-Williams algorithm (Yuan et al. 2004). The steps for inverse matrix iteration are following:

$$\bar{D}^{(n+1)} = \bar{M}_i^{-1}((K_{yl} + K_{yu})/2)(\bar{M}_i(K_{yu}) - \bar{M}_i(K_{yl}))D^{(n)} \text{ with } D^{(0)} = \text{ random vector}$$

$$D^{(n+1)} = \frac{\bar{D}^{(n+1)}}{\max|\bar{D}^{(n+1)}|}$$

$$\eta^{(n+1)} = \text{Re}(\frac{1}{\max|\bar{D}^{(n+1)}|})$$

which is terminated when:

$$\max(|D^{(n+1)} - D^{(n)}|) < \text{Tol or } n = n_{\max}$$

where $D^{(n)}$ is the nth iteration results, which is also the numerical eigenvector results, Tol is error tolerance defined by users, and $n_{\max}$ is the maximum iteration amount allowed. Notice that $D^{(0)}$ is a vector composed of random complex numbers in the range of $(0, 1)$. This method can also solve the frequency at the passband edge in the first Brillouin zone $KL_t = 0$ or π. The computational process for obtaining K_y^* and associated eigenvector $[\sigma_{xz}(0), u_z(0)]^T$ is shown in Figure 3.3.

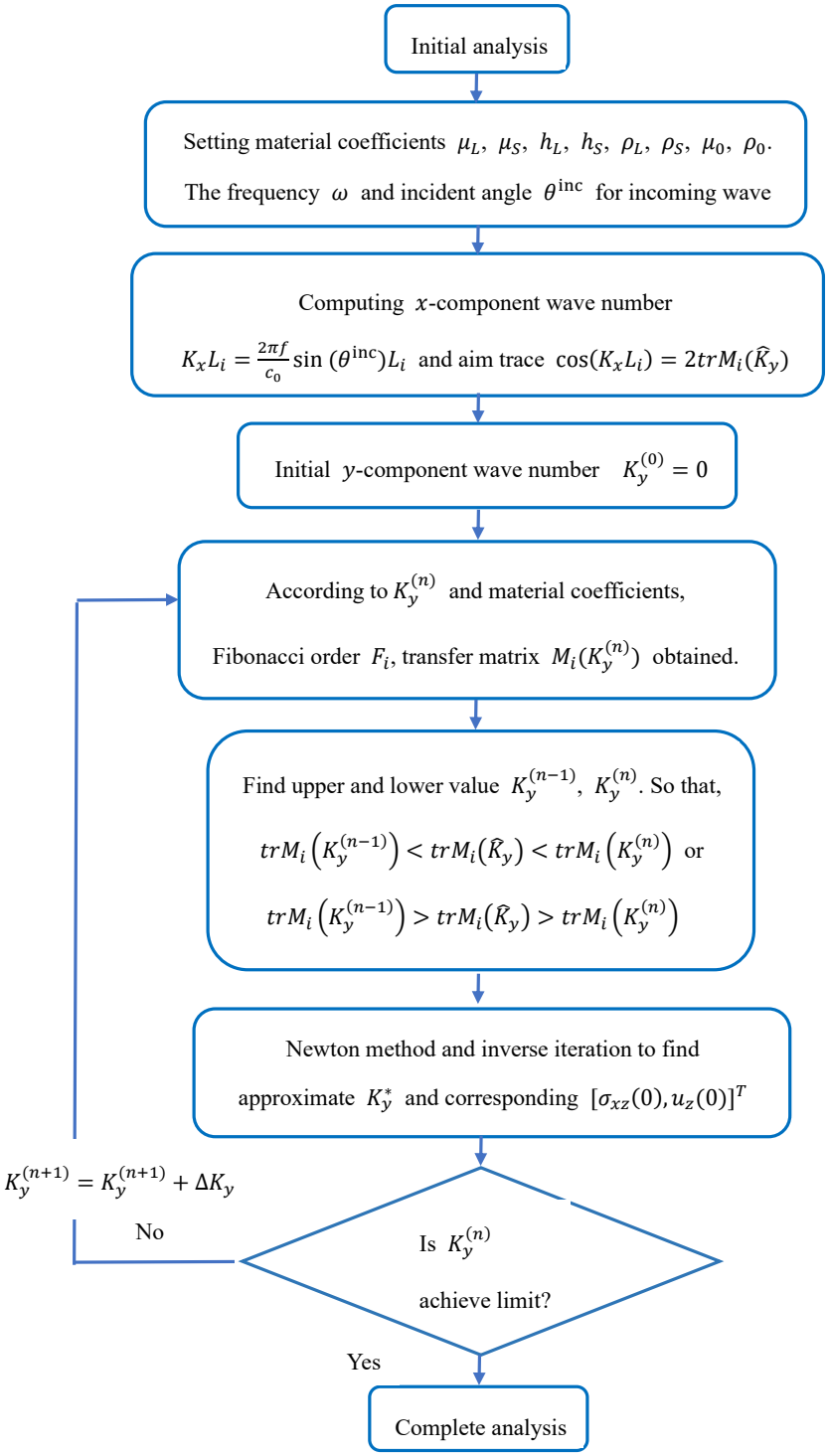

Figure 3.3. Computational process for K_y^* and associated eigenvector $[\sigma_{xz}(0), u_z(0)]^T$.

3.3.2 Integrate mode shape *w* by each phase

The transmission wave angle and energy as SH wave incidents into laminates formulated from the mode shape w, which is obtained from displacement u_z (neglect the time and K_y from the equation (2.41)):

$$w = u_z e^{\mathrm{i}K_x x} \tag{3.16}$$

From the results deduced before, the initial value for $[\sigma_{xz}(0), u_z(0)]^T$ is obtained by the Newton method and inverse matrix iterations. Therefore, the mode shape should be normalised (Willis 2016; Willis and Srivastava 2017):

$$\int_0^{L_i} w\mu w^* dx = \overline{\mu} L_i \tag{3.17}$$

where $\overline{\mu}$ is the mean shear modulus across the elementary unit cells $\overline{\mu} = (n_i^{(L)}\mu_L h_L + n_i^{(S)}\mu_S h_S)/L_i$ which is determined by Fibonacci order and two-phase material. The formulation of Poynting vector and mode decomposition comes from integral terms with μ varying within the integral interval. Thus, these integrals must be evaluated by parts, for ease of illustration of the computing principle, the part in integrand setting as $f(x)$ except μ:

$$\int_0^{L_i} \mu f(x) dx = \sum_{m=1}^{m=n_i} \int_{x_l}^{x_l+h_X} \mu_X f(x) dx$$

where n_i is still the total number of two phases in an elementary unit cells, i.e. x_l means the interface between this phase and the last left phase, varying with different phases. Still $X \in \{L, S\}$. Assuming $x = \bar{x} + x_l$, the following equation is obtained:

$$\int_0^{L_i} \mu f(x) dx = \sum_{m=1}^{m=n_i} \int_0^{h_X} \mu_X f(\bar{x} + x_l) d\bar{x} \tag{3.18}$$

As transfer matrix (2.44), the variable is $(x - x_l) = \bar{x}$. Thus, the transfer matrix can be changed into another expression:

$$\begin{bmatrix} \sigma_{xz}(\bar{x} + x_l) \\ u_z(\bar{x} + x_l) \end{bmatrix} = \begin{bmatrix} \cos(q_X(\bar{x})) & -\mu_X q_X \sin(q_X(\bar{x})) \\ \frac{\sin(q_X(\bar{x}))}{\mu_X q_X} & \cos(q_X(\bar{x})) \end{bmatrix} \begin{bmatrix} \sigma_{xz}(x_l) \\ u_z(x_l) \end{bmatrix} \tag{3.19}$$

Then, as $w = u_z(\bar{x} + x_l)e^{\mathrm{i}K_x(\bar{x}+x_l)}$, it can be rewritten as:

$$w(\bar{x} + x_l) = \left(\frac{\sin(q_X(\bar{x}))}{\mu_X q_X} \sigma_{xz}(x_l) + \cos(q_X(\bar{x})) u_z(x_l) \right) e^{\mathrm{i}K_x(\bar{x}+x_l)} \tag{3.20}$$

Therefore, equation (3.20) can be used for calculating integral with a variable of integration $\bar{x}$, which is performed for each phase with fixed μ_X. The displacement u_z and stress σ_{xz} are computed for each phase. This method can be performed to all integrals in Poynting vector, scattering coefficients calculation and next numerical Zak phase. Equation (3.20) will be simplified more in Chapter 5. The computational process for obtaining mode shape w by each phase and then transmission angle θ^{trans} is shown in Figure 3.4.

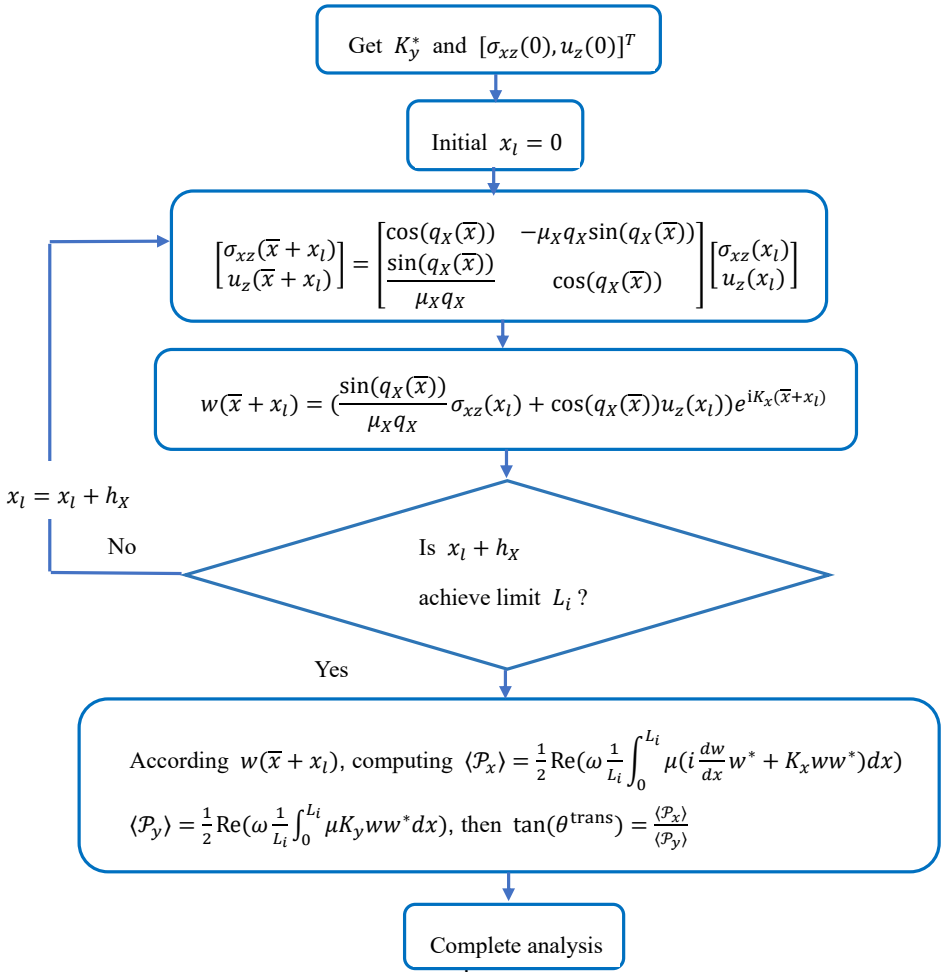

Figure 3.4. Computational process for mode shape w and then transmission angle θ^{trans}.

3.3.3 Scattering coefficients from mode shape decomposition

As mentioned before, the scattering coefficients are based on the continuity of displacements and stress (2.52) and (2.53) as below.

$$\sum_{l=0}^{2N} T_l w_l e^{i(\omega t - K_x^{\text{trans}} x)} \approx A e^{i(\omega t - K_x^{\text{inc}} x)} + \sum_{m=-N}^{N} R_m U_m e^{i(\omega t - K_x^{\text{ref}} x)} \tag{3.21}$$

$$\sum_{l=0}^{2N} \mu K_y^{(l)} T_l w_l e^{i(\omega t - K_x^{\text{trans}} x)} \approx A\mu_0 K_{y0} e^{i(\omega t - K_x^{\text{inc}} x)} - \sum_{m=-N}^{N} \mu_0 k_y^{(m)} R_m U_m e^{i(\omega t - K_x^{\text{ref}} x)} \tag{3.22}$$

This are continuity conditions can be transformed into a system of $2(2N+1)$ equations by imposing the orthogonality of mode shape w. As a consequence, this yields:

$$\begin{bmatrix} [M_1] & [M_2] \\ [M_3] & [M_4] \end{bmatrix} [\mathbf{c}] = [\mathbf{d}] \tag{3.23}$$

where $\mathbf{c}$ is a column vector of size $2(2N+1)$ with elements $\bar{T}_0 ... \bar{T}_{2N}$ and $\bar{R}_{-N} ... \bar{R}_N$ which are normalised scattering coefficients with $\bar{T}_l = T_l/A$ and $\bar{R}_m = R_m/A$, where T_l, A and R_m are scattering coefficients in continuity conditions (3.21) and (3.22). Submatrices $[M_i]$ are square matrices of size $(2N+1) \times (2N+1)$ with the following values:

$$[M_1]_{ii} = \int_0^{L_i} w_i \mu w_i^* dx, [M_2]_{ij} = -\int_0^{L_i} U_{j-N} \mu w_i^* dx.$$

$$[M_3]_{ii} = K_y^{(i)} \int_0^{L_i} w_i \mu w_i^* dx, [M_4]_{ij} = \mu_0 k_y^{(j-N)} \int_0^{L_i} U_{j-N} w_i^* dx \tag{3.24}$$

where $i, j = 0..., 2N$ and $\mathbf{d}$ is a column vector of size $2(2N+1)$ with values:

$$\mathbf{d}_i = \int_0^{L_i} \mu w_i^* dx,\ 0 \le i \le 2N; \mathbf{d}_i = \mu_0 K_0 \cos(\theta^{\text{inc}}) \int_0^{L_i} w_{i-2N-1}^* dx,\ i \ge 2N \tag{3.25}$$

The scattering coefficients are achieved with the matrix calculation:

$$[\mathbf{c}] = \begin{bmatrix} [M_1] & [M_2] \\ [M_3] & [M_4] \end{bmatrix}^{-1} [\mathbf{d}]$$

However, according to Srivastava and Willis (2017), because there is no strict equality in equations (3.21) and (3.22) even though this method already included all propagation waves, the evanescent waves still affect the scattering coefficients solution. They noticed that the displacement continuity condition can be satisfied more easily than the stress continuity condition with enough evanescent number waves. Thus, they used the propagation wave with Lagrange multiplier whose objective function is the displacement continuity, and the constraint is the conservation of energy. This system is solved through a gradient descent algorithm which is usually used in optimisation for minimising objective function (loss function). However, since it is tough to control the step size (learning rate) in the gradient descent algorithm, we do not use it in this thesis.

3.3.4 Wave normalised energy metrics

The normalised energy metrics can be obtained with scattering coefficients and one component of Poynting vector $\langle \mathcal{P}_y \rangle$. Neglecting any dissipating mechanisms from total energy incident into the laminates should be balanced the energy transmitted and reflected. The mean energy entering is the mean energy flux over time and space:

$$E = \langle \mathcal{P}_y \rangle = \frac{1}{2}|A|^2 \omega \mu_0 K_0 \cos(\theta^{\text{inc}}) \tag{3.26}$$

Therefore, the entering energy is consists of two parts: refracted or transmitted energy and reflected one, which are:

$$\text{trans energy: } \sum \frac{1}{2}|T_l|^2 \left(\omega \frac{1}{L_i} \int_0^{L_i} \mu K_y^l w w^* dx\right), \text{ ref energy: } \sum \frac{1}{2}|R_m|^2 \omega \mu_0 k_y^{(m)} \tag{3.27}$$

where $\sum$ means summation over all propagation energy from transmitted, plus energy from reflected should equal to energy that is entering, which is energy conserving:

$$E = \langle \mathcal{P}_y \rangle = \frac{1}{2}|A|^2 \omega \mu_0 K_0 \cos(\theta^{\text{inc}}) = \sum \frac{1}{2}|T_l|^2 \left(\omega \frac{1}{L_i} \int_0^{L_i} \mu K_y^l w w^* dx\right) + \sum \frac{1}{2}|R_m|^2 \omega \mu_0 k_y^{(m)}$$

The energy metrics can also be normalised, which means the total dimensionless energy equal to 1 (Srivastava 2016; Srivastava and Willis 2017):

$$\bar{E} = \sum \left|\bar{T}_l\right|^2 \frac{(1/L_i \int_0^{L_i} \mu K_y^l w w^* dx)}{K_0 \cos(\theta^{\text{inc}})\, \mu_0} + \sum \left|\bar{R}_m\right|^2 \frac{k_y^{(m)}}{K_0 \cos(\theta^{\text{inc}})} = 1 \tag{3.28}$$

The evanescent waves in y direction are still with energy in x direction because $K_x L_i$ cannot be pure imaginary. Equation (3.28) can be used to check scattering coefficients calculations because they come from an approximate method (mode decomposition). Also, it is the constraint when using the Lagrange multiplier method.

3.4 Numerical Techniques for The Analysis of Interface States

3.4.1 Numerical method for the Zak phase

The Zak phase is very significant in the topological interface state topic, which determines the topological phase in a 1D periodic structure (surface impedance). The theoretically equation (2.76)

will be shown here again

$$\theta_n^{\text{Zak}} = \int_{-\pi/L_i}^{\pi/L_i} \left[\mathrm{i} \int_{\text{unit cell}} \frac{1}{2\rho c^2} d\mathbf{r}dz \mathcal{W}_{n,K}^*(z,\mathbf{r}) \partial_K \mathcal{W}_{n,K}(z,\mathbf{r}) \right] dK \tag{3.29}$$

Equation (3.29) can be transformed into discretized (numerical) type:

$$\theta_n^{\text{Zak}} = -\text{Im} \sum_{i=1}^{N} \ln \left[\int_{\text{unitcell}} \frac{1}{2\rho c^2} d\mathbf{r}dz \mathcal{W}_{n,K_i}^* \mathcal{W}_{n,K_{i+1}} \right] \tag{3.30}$$

where n, ρ, c are the same with equation (3.29) which is proved by Xiao et al. (2015) and Chen et al. (2021). Still, the force periodic field $\mathcal{W}_{n,K} = N(n,K)e^{\mathrm{i}Kz}$ needs to be normalised with the relationship:

$$\int_{\text{unitcell}} \frac{1}{2\rho c^2} d\mathbf{r}dz |\mathcal{W}_{n,K}|^2 = 1 \tag{3.31}$$

p points are used to equally divide the complete first Brillouin zone from $K = -\pi/L_i$ to $K = \pi/L_i$. In the limit of $p \to \infty$, $\Delta K = K_{i+1} - K_i \to 0$, which leads to $\partial_K \mathcal{W}_{n,K} = (\mathcal{W}_{n,K+\Delta K} - \mathcal{W}_{n,K})/\Delta K$. Thus, equation (3.29) for the Zak phase can be equivalently expressed as (notice equation (3.31)):

$$\theta_n^{\text{Zak}} = \int_{-\pi/L_i}^{\pi/L_i} \left[\frac{\mathrm{i}}{\Delta K} \left(\int_{\text{unitcell}} \frac{1}{2\rho c^2} d\mathbf{r}dz \mathcal{W}_{n,K}^* \mathcal{W}_{n,K+\Delta K} - 1 \right) \right] dK \tag{3.32}$$

Because $\mathcal{W}_{n,K+\Delta K} \approx \mathcal{W}_{n,K}$ and equation (3.31), we can obtain:

$$\int_{\text{unitcell}} \frac{1}{2\rho c^2} d\mathbf{r}dz \mathcal{W}_{n,K}^* \mathcal{W}_{n,K+\Delta K} \to 1$$

By discretizing K and noting the relation $\ln(x) \approx x - 1$ in the limit of $x \to 1$, equation (3.32) with $\Delta K \to 0$ can be rewritten in a discretized form as:

$$\theta_n^{\text{Zak}} = \mathrm{i} \sum_{i=1}^{p} \left[\ln \left(\int_{\text{unitcell}} \frac{1}{2\rho c^2} d\mathbf{r}dz \mathcal{W}_{n,K_i}^* \mathcal{W}_{n,K_i+\Delta K} \right) \right] \tag{3.33}$$

It is obvious that term $\int_{\text{unitcell}} \frac{1}{2\rho c^2} d\mathbf{r}dz \mathcal{W}_{n,K}^* \mathcal{W}_{n,K+\Delta K}$ is a complex number, so that complex logarithm returns logarithm of absolute value of this complex (real part) plus complex angle of it (imaginary part) which is also shown in equation (3.34):

$$\ln(x + iy) = \ln(\sqrt{x^2 + y^2}) + \mathrm{i}\arctan(y/x),\ (x,y) \in \mathbb{R} \tag{3.34}$$

Then, the term $\int_{\text{unitcell}} \frac{1}{2\rho c^2} d\mathbf{r}dz\mathcal{W}^*_{n,K}\mathcal{W}_{n,K+\Delta K} \to 1$ lead absolute value in equation (3.33) approximate to 1 and $\ln(1) = 0$. Hence, only negative imaginary part should be counted.

The numerical integral (3.30) can be integrated by each phase similar to the method in the Subsection 3.3.2, because the radius, density and wave phase speed are changed within different phase materials. The frequency at first Brillouin zone edge 0 and π can be solved from the Newton method and inverse iterations. The complete steps for the Zak phase are evaluated as follows:

(1). As the dispersion relation, the frequency vector, trace for different Fibonacci order and passband layouts have been obtained, a vector for wavenumber in the first Brillouin zone $KL_i \in(0, \pi)$ can be obtained according to dispersion relation.

(2). The Zak phase should be integrated along the complete first Brillouin zone $KL_i \in(-\pi, \pi)$. Thus, obtaining eigenvector for each KL_i and f in $(0, \pi)$, taking conjugate of each eigenvector, which are the eigenvector from wavenumber KL_i in $(-\pi, 0)$. This is because a real matrix with complex eigenvalue and eigenvector must be conjugated with each other (Strang 2021). Therefore, the eigenvector at Brillouin edge (0 or π) is a real number.

(3). Using equation (3.31) to normalise eigenvector.

(4). Using equation (3.30) to calculate the numerical Zak phase, because it is sum of negative complex angle of term $\int_{\text{unitcell}} \frac{1}{2\rho c^2} d\mathbf{r}dz\mathcal{W}^*_{n,K_i}\mathcal{W}_{n,K_{i+1}}$.

The computational process for obtaining numerical Zak phase is shown in Figure 3.5.

However, this method cannot calculate the Zak phase for passbands crossing each other (bandgap closed). Thus, the approaches for checking whether passbands cross each other can be coded. The topological phase and sign of surface impedance or reflection phase can be calculated. The numerical Zak phase can verify the correctness for the results from symmetric of band edge mode.

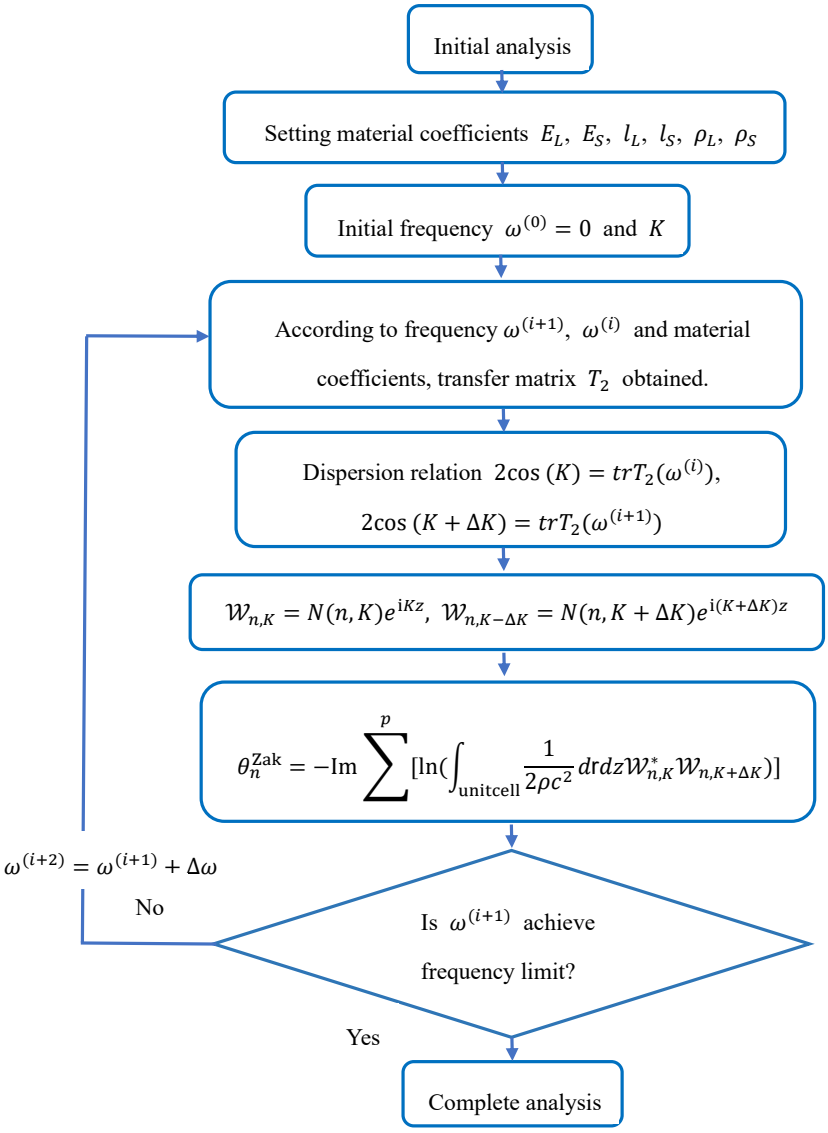

Figure 3.5. Computational process for numerical Zak phase.

3.4.2 Transmission and reflection coefficients

Equation (2.74) has reflection coefficient r and surface impedance Z_0. For homogenous material, surface impedance Z_0 is impedance for this material. Thus, the reflection coefficient r will be evaluated numerically to verify the theoretical solution in Chapter 6. In this thesis, the problem is constrained in a one-dimensional rod, and it has two different type displacement solutions (2.9) and (2.10). However, usually first type (2.9) is used for computing reflection and transmission coefficients because this equation naturally decomposes the wave forward and backwards. According to Chen et al. (2021), the axial displacement in subelement p of $\mathcal{N}$th unit cell F_2 (see Figure 2.9) can be written as:

$$u_{\mathcal{N}}^{p}(z) = a_{\mathcal{N}}^{p}\exp(\mathrm{i}\sqrt{\frac{\rho_X}{E_X}}\omega(z-\mathcal{N}L_2)) + b_{\mathcal{N}}^{p}\exp(-\mathrm{i}\sqrt{\frac{\rho_X}{E_X}}\omega(z-\mathcal{N}L_2)) \tag{3.35}$$

It is another present type for equation (2.9), where $a_{\mathcal{N}}^{p}$ and $b_{\mathcal{N}}^{p}$ are the undetermined complex coefficients denoting the amplitude of incident and reflected waves, respectively. Then axial force in subelement p presents as:

$$N_{\mathcal{N}}^{p}(z) = \mathrm{i}\omega Z_p(a_{\mathcal{N}}^{p}\exp(\mathrm{i}\sqrt{\frac{\rho_X}{E_X}}\omega(z-\mathcal{N}L_2)) - b_{\mathcal{N}}^{p}\exp(-\mathrm{i}\sqrt{\frac{\rho_X}{E_X}}\omega(z-\mathcal{N}L_2))) \tag{3.36}$$

where Z_p is the impedance for phase p, for simplicity, the state vector in phase p of the $\mathcal{N}$th unit cell as shown in Figure 3.7 is defined as:

$$S_{\mathcal{N}}^{(p)} = [a_{\mathcal{N}}^{p}, b_{\mathcal{N}}^{p}]^T \tag{3.37}$$

This state vector is different from before $\mathbf{U}_j = [u_j, N_j]^T$ but they have the same mathematical meanings due to the axial wave field solution only have two unknown variables. The state vectors (3.37) in unit cell are not independent of each other and can be connected through the continuity condition by displacement u and axial force N. We recalling Figure 2.9 in here as 3.7 and plus a Figure 3.6.

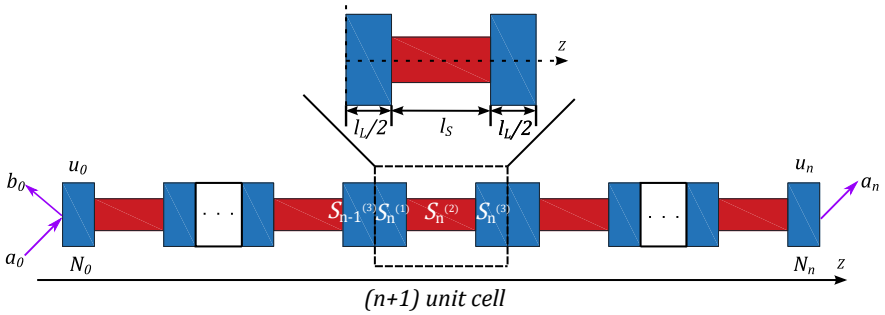

Figure 3.6. One dimension quasiperiodic rod with $(n+1)$ unit cell, a_0, b_0 and a_n are incident, reflected and transmitted wave amplitude. $u_{0,n}$ and $N_{0,n}$ are displacements and the axial force on the boundary of the elementary cell. Figure reproduced from Chen et al. (2021)

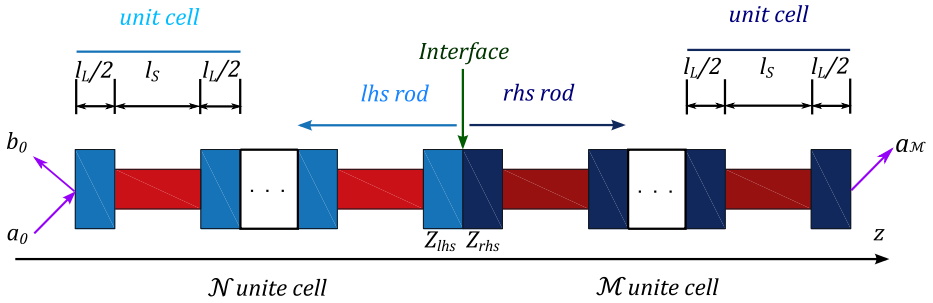

Figure 3.7. Two 1D quasiperiodic rods with $\mathcal{N}$ (and $\mathcal{M}$) unit cells in the right connections at the interface, a_0, b_0 and $a'_{\mathcal{M}}$ are incident, reflected and transmitted wave amplitude. lhs and rhs denote the left and right side quasiperiodic rod. Figure reproduced from Chen et al. (2021)

The continuity condition between $S_{n-1}^{(3)}$ and $S_n^{(1)}$ is expressed as if we take Figure 3.6 as a reference:

$$u_{n-1}^3 = u_n^1,\ N_{n-1}^3 = N_n^1,\ \text{at } z = (n-1)L_2; \tag{3.38}$$

By substituting equation (3.35) and (3.36) into (3.38), we obtain:

$$\begin{bmatrix} 1 & 1 \\ 1 & -1 \end{bmatrix} S_{n-1}^{(3)} = \begin{bmatrix} e^{-\mathrm{i}\sqrt{\rho_L/E_L}\omega L_2} & e^{\mathrm{i}\sqrt{\rho_L/E_L}\omega L_2} \\ e^{-\mathrm{i}\sqrt{\rho_L/E_L}\omega L_2} & -e^{\mathrm{i}\sqrt{\rho_L/E_L}\omega L_2} \end{bmatrix} S_n^{(1)} \tag{3.39}$$

The continuity condition between $S_n^{(1)}$ and $S_n^{(2)}$ is expressed:

$$u_n^1 = u_n^2,\ N_n^1 = N_n^2,\ \text{at } z = (n-1)L_2 + l_L/2; \tag{3.40}$$

By substituting equation (3.35) and (3.36) into (3.40), we obtain:

$$\begin{bmatrix} e^{-\mathrm{i}\sqrt{\rho_L/E_L}\omega(l_L/2+l_S)} & e^{\mathrm{i}\sqrt{\rho_L/E_L}\omega(l_L/2+l_S)} \\ e^{-\mathrm{i}\sqrt{\rho_L/E_L}\omega(l_L/2+l_S)} & -e^{\mathrm{i}\sqrt{\rho_L/E_L}\omega(l_L/2+l_S)} \end{bmatrix} S_n^{(1)} =$$

$$\begin{bmatrix} e^{-\mathrm{i}\sqrt{\rho_S/E_S}\omega(l_L/2+l_S)} & e^{\mathrm{i}\sqrt{\rho_S/E_S}\omega(l_L/2+l_S)} \\ \frac{Z_S}{Z_L}e^{-\mathrm{i}\sqrt{\rho_S/E_S}\omega(l_L/2+l_S)} & -\frac{Z_S}{Z_L}e^{\mathrm{i}\sqrt{\rho_S/E_S}\omega(l_L/2+l_S)} \end{bmatrix} S_n^{(2)} \tag{3.41}$$

Then, the continuity condition between $S_n^{(2)}$ and $S_n^{(3)}$ is expressed:

$$u_n^2 = u_n^3,\ N_n^2 = N_n^3,\ \text{at } z = nL_2 - l_L/2 = (n-1)L_2 + l_L/2 + L_S \tag{3.42}$$

By substituting equation (3.35) and (3.36) into (3.42), we obtain:

$$\begin{bmatrix} e^{-\mathrm{i}\sqrt{\rho_S/E_S}\omega l_L/2} & e^{\mathrm{i}\sqrt{\rho_S/E_S}\omega l_L/2} \\ e^{-\mathrm{i}\sqrt{\rho_S/E_S}\omega l_L/2} & -e^{\mathrm{i}\sqrt{\rho_S/E_S}\omega l_L/2} \end{bmatrix} S_n^{(2)} = \begin{bmatrix} e^{-\mathrm{i}\sqrt{\rho_L/E_L}\omega l_L/2} & e^{\mathrm{i}\sqrt{\rho_L/E_L}\omega l_L/2} \\ \frac{Z_L}{Z_S}e^{-\mathrm{i}\sqrt{\rho_L/E_L}\omega l_L/2} & -\frac{Z_L}{Z_S}e^{\mathrm{i}\sqrt{\rho_L/E_L}\omega L_2} \end{bmatrix} S_n^{(3)} \tag{3.43}$$

Through some mathematical manipulations, the transfer matrix can be expressed as:

$$S_{\mathcal{N}}^{(3)} = \begin{bmatrix} \mathbf{f}_{11} & \mathbf{f}_{12} \\ \mathbf{f}_{21} & \mathbf{f}_{22} \end{bmatrix} S_{\mathcal{N}-1}^{(3)} \tag{3.44}$$

Formulating this transfer matrix is more challenging than before due to the continuity conditions in different phases are displacement and force. It is easy to show the components, the variables in the universal torus ($\xi_X = \sqrt{\rho_X/E_X}\omega l_X$) are used:

$$\begin{aligned} \mathbf{f}_{11} &= e^{(\mathrm{i}\xi_L)}[\cos(\xi_S) + \frac{\mathrm{i}}{2}(\frac{Z_S}{Z_L} + \frac{Z_L}{Z_S})\sin(\xi_S)] \\ \mathbf{f}_{12} &= -\mathbf{f}_{21} = \frac{\mathrm{i}}{2}(\frac{Z_S}{Z_L} - \frac{Z_L}{Z_S})\sin(\xi_S) \\ \mathbf{f}_{22} &= e^{(-\mathrm{i}\xi_L)}[\cos(\xi_S) - \frac{\mathrm{i}}{2}(\frac{Z_S}{Z_L} + \frac{Z_L}{Z_S})\sin(\xi_S)] \end{aligned} \tag{3.45}$$

This transfer matrix is unimodular, and the Floquet-Bloch technique can be performed on it. The dispersion relation is the same with equation obtained from transfer matrix considering displacement and axial force, because the same physical problem is considered. Now consider a finite periodic rods with $\mathcal{N}$ identical unit cells arranged in the axial direction as shown in Figure 3.7, a expression can be obtained:

$$\begin{bmatrix} a_{\mathcal{N}}^{(3)} \\ b_{\mathcal{N}}^{(3)} \end{bmatrix} = \begin{bmatrix} \mathbf{f}_{11} & \mathbf{f}_{12} \\ \mathbf{f}_{21} & \mathbf{f}_{22} \end{bmatrix}^{\mathcal{N}} \begin{bmatrix} a_0^{(3)} \\ b_0^{(3)} \end{bmatrix} \equiv \mathbf{F}_t \begin{bmatrix} a_0^{(3)} \\ b_0^{(3)} \end{bmatrix},\ \begin{bmatrix} \mathbf{f}_{11} & \mathbf{f}_{12} \\ \mathbf{f}_{21} & \mathbf{f}_{22} \end{bmatrix}^{\mathcal{N}} = \mathbf{F}_t \tag{3.46}$$

where $a_0^{(3)}$ and $b_0^{(3)}$ are the amplitude coefficients of the incident and reflected waves at the incident side, respectively. To calculate transmission and reflection coefficients, usually setting the reflection coefficient at the output side is zero ($b_{\mathcal{N}}^{(3)} = 0$). As a result:

$$r_{\mathcal{N}} = \frac{b_0^{(3)}}{a_0^{(3)}} = -\frac{\mathbf{F}_t(2,1)}{\mathbf{F}_t(2,2)}; \tag{3.47}$$

$$t_{\mathcal{N}} = \left|\frac{a_n^{(3)}}{a_0^{(3)}}\right|^2 = \left|\mathbf{F}_t(1,1) - \frac{\mathbf{F}_t(1,2)\mathbf{F}_t(2,1)}{\mathbf{F}_t(2,2)}\right|^2 \tag{3.48}$$

where $\mathbf{F}_t(i,j)$ is corresponding term with ith row and jth column in matrix $\mathbf{F}_t$. Then, if another periodic rods are added with $\mathcal{M}$ unit cells (in Figure 3.7) to the right hand side of the previous rod, the transmission and reflection coefficients would be still evaluated with small changes.

Notice that for the right hand side structure, wave field (3.35) and (3.36) still can be used. To easily distinguish the state vector, transfer matrix and material parameters, the upper bar is used when these coefficients are for the right hand side rods. Then, the state vector is:

$$\bar{S}_{\mathcal{M}}^{(p)} = [\bar{a}_{\mathcal{M}}^p, \bar{b}_{\mathcal{M}}^p]^T \tag{3.49}$$

$$\begin{bmatrix} \bar{a}_{\mathcal{M}}^{(3)} \\ \bar{b}_{\mathcal{M}}^{(3)} \end{bmatrix} = \begin{bmatrix} \bar{\mathbf{f}}_{11} & \bar{\mathbf{f}}_{12} \\ \bar{\mathbf{f}}_{21} & \bar{\mathbf{f}}_{22} \end{bmatrix}^{\mathcal{M}} \begin{bmatrix} \bar{a}_0^{(3)} \\ \bar{b}_0^{(3)} \end{bmatrix} \equiv \bar{\mathbf{F}}_t \begin{bmatrix} \bar{a}_0^{(3)} \\ \bar{b}_0^{(3)} \end{bmatrix} \quad \begin{bmatrix} \bar{\mathbf{f}}_{11} & \bar{\mathbf{f}}_{12} \\ \bar{\mathbf{f}}_{21} & \bar{\mathbf{f}}_{22} \end{bmatrix}^{\mathcal{M}} = \bar{\mathbf{F}}_t \tag{3.50}$$

Furthermore, the continuity at the interface of two different periodic rods is written as:

$$u_{\mathcal{N}}^3 = \bar{u}_0^1,\ N_{\mathcal{N}}^3 = \bar{N}_0^1,\ \text{at } z = (\mathcal{N}+1)L_2;$$

Thus, a matrix expression is obtained:

$$\begin{bmatrix} 1 & 1 \\ 1 & -1 \end{bmatrix} S_{\mathcal{N}}^{(3)} = \begin{bmatrix} e^{-\mathrm{i}\sqrt{\bar{\rho}_L/\bar{E}_L}\omega L_2} & e^{\mathrm{i}\sqrt{\bar{\rho}_L/\bar{E}_L}\omega L_2} \\ \frac{\bar{Z}_L}{Z_L} e^{-\mathrm{i}\sqrt{\bar{\rho}_L/\bar{E}_L}\omega L_2} & -\frac{\bar{Z}_L}{Z_L} e^{\mathrm{i}\sqrt{\bar{\rho}_L/\bar{E}_L}\omega L_2} \end{bmatrix} \bar{S}_0^{(1)}$$

Through some mathematical manipulations, a matrix to transfer two state vectors $\mathbf{F}_{\text{int}}$ can be arrived:

$$\mathbf{F}_{\text{int}} = \begin{bmatrix} \frac{\bar{Z}_L+Z_L}{2\bar{Z}_L} e^{\mathrm{i}\sqrt{\bar{\rho}_L/\bar{E}_L}\omega L_2} & \frac{\bar{Z}_L-Z_L}{2\bar{Z}_L} e^{\mathrm{i}\sqrt{\bar{\rho}_L/\bar{E}_L}\omega L_2} \\ \frac{\bar{Z}_L-Z_L}{2\bar{Z}_L} e^{-\mathrm{i}\sqrt{\bar{\rho}_L/\bar{E}_L}\omega L_2} & \frac{\bar{Z}_L+Z_L}{2\bar{Z}_L} e^{-\mathrm{i}\sqrt{\bar{\rho}_L/\bar{E}_L}\omega L_2} \end{bmatrix} \tag{3.51}$$

Thus, the final matrix connect initial and final state vector is:

$$\mathbf{F}_g = \bar{\mathbf{F}}_t \mathbf{F}_{\text{int}} \mathbf{F}_t \tag{3.52}$$

Thus, the transmission coefficients for these systems are: (stili assume $\bar{b}_{\mathcal{M}}^{(3)} = 0$)

$$t_{\mathcal{N}+\mathcal{M}} = \left|\frac{\bar{a}_{\mathcal{M}}^{(3)}}{a_0^{(3)}}\right|^2 = \left|\mathbf{F}_g(1,1) - \frac{\mathbf{F}_g(1,2)\mathbf{F}_g(2,1)}{\mathbf{F}_g(2,2)}\right|^2 \tag{3.53}$$

where $\mathbf{F}_g(i,j)$ is the corresponding term with ith row and jth column in matrix $\mathbf{F}_g$.

3.4.3 Wave field for a finite waveguide

Displacement and force, which are included in the wave field for a finite deformed rod consisting of $\mathcal{N}$ unit cells type in the left hand side and $\mathcal{M}$ unit cells in the right-hand side are derived according to Chen et al. (2021). Furthermore, unit cells with only single type rod can be derived with the same technique. In view of the equation (3.52) which connect the initial state vector $S_0^{(3)}$ and $\bar{S}_{\mathcal{M}}^{(3)}$, still assuming $\bar{b}_{\mathcal{M}}^{(3)} = 0$ (reflection wave at the output side is zero), the relation is $b_0^{(3)}/a_0^{(3)} = -\mathbf{F}_g(2,1)/\mathbf{F}_g(2,2)$. Without loss of generality, input amplitude is $a_0^{(3)} = 1$ and the state vector composed of the complex amplitude coefficients at the input side:

$$S_0^{(3)} = [1, -\mathbf{F}_g(2,1)/\mathbf{F}_g(2,2)]^T \tag{3.54}$$

which combined with transfer relation (3.41) with elementary transfer matrix (3.44). The coefficients for amplitude $a_{\mathcal{N}}^p$ and $b_{\mathcal{N}}^{(p)}$ in each phase of each rods can be determined. Then, according to wave field (3.35) and (3.36), displacement and force in a finite rods are fully determined. Similarly, the state vector of finite rods in right hand side is determined by considering the matrix $\mathbf{F}_{\text{int}}$ (3.51). Then, the wave field of finite rods with one or two types unit cell is calculated through this method (theoretically, the wave field is obtained no matter how many types of rods are connected). If displacement function (2.10) is used, the wave field would be obtained with the analogy process, which does not show here. If the frequency is at interface state, the wave field should be localised on the geometric interface between two structures as shown in Figure 1.10.

3.5 Conclusion and Remarks

In this Chapter methodology, several methods which includes dispersion relation both in quasicrystalline generated rods (f, KL_i) or laminates (K_xL_i, K_yL_i) are shown. The tool for analysing spectrum: universal torus is represented with enough mathematical support. In the next three Chapters, several new conclusions concerning universal torus are investigated. Scattering coefficients are calculated from the continuity condition of stress and displacement in mode shape

orthogonality. However, it is an approximate calculation because the evanescent wave can influence the strict continuity condition.

Moreover, scattering coefficients and y component Poynting vector can give the normalised energy. Thus, two crucial aspects, transmitted angle and energy, are evaluated in laminate problem with detail numerical calculation steps. Newton method and inverse iteration as approaches to calculate eigenvalue problems for terms K_y or f in transfer matrix with wavenumber $K_x L_i$ or KL_i are clarified. The full process for numerical evaluated Zak phase is shown. The reflection, transmission coefficients, and wave field in finite rods are obtained no matter one or more type rods, which is very useful for calculating of surface impedance and verifying interface state existing.

These methods have been performed in software with the steps introduced here. The complete MATLAB codes are shown in Appendix A, divided into three parts for axial wave propagation in Fibonacci rods, anti-plane shear wave (SH) in Fibonacci laminates and the interface state of periodic rods. Because there must be some numerical error in these techniques, the results are checked by duplicating works in some previous publications with enough minor errors (for example, papers in Chapter 2). Codes for plotting Kohmoto's manifold are presented in Appendix C.

Chapter 4 - Wave Propagation in Canonical Rods

Quasicrystalline generated rods are useful specially for cutting frequencies in a vibrating system, for example, Micro-electromechanical system (MEMS) to devices able to suppress vibrations in mechanical engineering. Therefore, the bandgap in dispersion spectra for these structure should be investigated. A strong relationship exists between the dispersion spectra during wave propagation in quasicrystalline generated rods and the trace of the global dynamic transfer matrix. In addition, there are three different canonical ratios $C^{(1,2,3)}$ (2.38) which are also connected to different initial saddle points on Kohmoto's manifold with Fibonacci GM sequence. Thus, in this chapter, three traces under different canonical configurations are investigated. Furthermore, the relationship between two canonical frequencies ω_{cj} and ω_{ck} and three canonical ratios is established in Section 4.1. The period of canonical frequency, dynamic traces and Kohmoto's invariant are obtained. The principle for scaling is demonstrated with the required theoretical support in Section 4.2. The scaling factor is associated with the maximum eigenvalue of the linearized map corresponding to periodic orbits on Kohmoto's manifold. The numerical results with three families and scaling on periodic orbits with passband (or bandgap) length and traces verify the theoretical analysis in Section 4.3. Furthermore, the reason for the scaling factor is the square root of the general scaling factor is analysed in Section 4.5. It shows the canonical configuration and scaling effect can be used as a new tool to design quasiperiodic generated rods more rationally.

4.1 Theoretical Analysis for Three Canonical Families

We have investigated a set of infinite two-phase structured rod (Figure 4.1 only shows F_3 and F_4) whose elementary cells are generated by Fibonacci GM sequence, which is a particular case of the class of generalised Fibonacci sequences that follow the recursion rule $F_i = F_{i-1}F_{i-2}$ with $F_0 = S$; $F_1 = L$ setting the initial conditions in terms of the two basic constituents L and S. The lengths of the two segments L and S are indicated with l_L and l_S, while E_X and ρ_X ($X \in (L,S)$ denote Young's modulus and mass density per unit length of each element, respectively. The Floquet-Bloch dispersion diagram for axial waves is governed uniquely by the trace of the transmission matrix trT_i, which is explained in Chapter 2. We recall equation for canonical ratios (2.38), canonical frequencies (2.39) and initial three traces (2.26) in here:

$$\sqrt{\frac{\rho_S E_L}{\rho_L E_S}}\frac{l_S}{l_L} = \frac{1+2j}{1+2k}, \sqrt{\frac{\rho_S E_L}{\rho_L E_S}}\frac{l_S}{l_L} = \frac{1+2j}{2q}, \sqrt{\frac{\rho_S E_L}{\rho_L E_S}}\frac{l_S}{l_L} = \frac{2q}{1+2k}, \text{ with } j,k,q \in \mathbb{N} \tag{4.1}$$

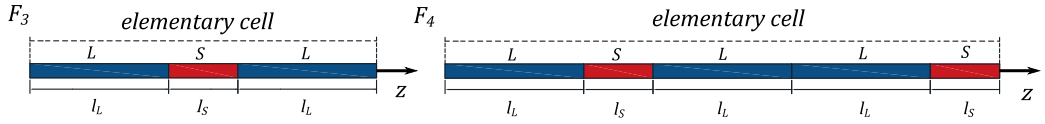

Figure 4.1. Quasicrystalline rod generated by Fibonacci golden mean chains F_3 and F_4, figure reproduced from Morini and Gei (2018)

$$\omega_{cj} = \pi\frac{\sqrt{E_S}}{2l_S\sqrt{\rho_S}}(1+2j_\omega);\ \omega_{ck} = \pi\frac{\sqrt{E_L}}{2l_L\sqrt{\rho_L}}(1+2k_\omega),\ \text{with } j_\omega, k_\omega \in \mathbb{N} \tag{4.2}$$

$$x_0 = 2\cos\left(\sqrt{\frac{\rho_S}{E_S}}\omega l_S\right)$$

$$x_1 = 2\cos\left(\sqrt{\frac{\rho_L}{E_L}}\omega l_L\right) \tag{4.3}$$

$$x_2 = 2\cos\left(\sqrt{\frac{\rho_S}{E_S}}\omega l_S\right)\cos\left(\sqrt{\frac{\rho_L}{E_L}}\omega l_L\right) - \beta\sin\left(\sqrt{\frac{\rho_S}{E_S}}\omega l_S\right)\sin\left(\sqrt{\frac{\rho_L}{E_L}}\omega l_L\right)$$

Thus, we have enough material to analyse the properties of canonical configuration on dispersion spectrum and trace for transfer matrix leading an adjustable and predictable bandgap and passband dispersion layouts.

4.1.1 Canonical family no. one

Canonical family no. one is associated with the canonical ratio is:

$$C^{(1)} = \sqrt{\frac{\rho_S E_L}{\rho_L E_S}}\frac{l_S}{l_L} = \frac{1+2j}{1+2k},\ j,k \in \mathbb{N} \tag{4.4}$$

Because the coordinates for saddle points is (x_2, x_1, x_0), the initial saddle points are $(\pm\sqrt{4+I}, 0, 0)$, which means x_0 and x_1 are equal to zero at canonical frequency. By substituting canonical frequency ω_{cj} into the initial three traces (4.3) we obtain:

$$x_0 = 2\cos\left(\frac{\pi}{2}(1+2j_\omega)\right) = 0;\ x_1 = 2\cos\left(\frac{\pi}{2}(1+2j_\omega)\frac{1+2k}{1+2j}\right) = 0 \tag{4.5}$$

Because the relationship between parameters j_ω (k_ω) in canonical frequency and j (k) in canonical ratio is not clear (they are equal or not), it is hard to determine if trace $x_1 = 0$ in equation (4.5). Therefore, considering that canonical ratio is an irreducible fraction and the lowest terms in denominator and numerator and terms of the definition of (4.4) $C^{(1)}$ must be odd/odd, the odd term $(1+2m)$ can be multiplied into canonical ratio to keep ratio and family (because odd×odd=odd):

$$C^{(1)} = \sqrt{\frac{\rho_S E_L}{\rho_L E_S}}\frac{l_S}{l_L} = \frac{1+2j}{1+2k} = \frac{(1+2j)(1+2m)}{(1+2k)(1+2m)},\ m \in \mathbb{N} \tag{4.6}$$

Next, assuming the relationship between canonical ratio and frequency (j_ω and j or k_ω and k) is:

$$1+2j_\omega = (1+2j)(1+2m);\ 1+2k_\omega = (1+2k)(1+2m) \tag{4.7}$$

Now, by substituting canonical frequencies (4.7) into (4.2) with canonical family no. one, we obtain:

$$\omega_{cj} = \frac{\pi\sqrt{E_S}}{2l_S\sqrt{\rho_S}}(1+2j)(1+2m) = \frac{\pi\sqrt{E_L}}{2l_L\sqrt{\rho_L}}(1+2k)(1+2m) = \omega_{ck} \tag{4.8}$$

Then, the traces $x_0 = x_1 = 0$ and $x_2 = -\beta = -\sqrt{4+I}$. Hence, initial assumption (4.6) satisfies properties of canonical frequency and saddle point on Kohmoto's manifold. A numerical example is shown here and verifies our theoretical analysis with simplified material and geometric parameters $l_L = 2l_S = 1$, $E_L = E_S = 1$ and $\rho_L = 1$ and $\rho_S = 4C^2$ which lead to a canonical ratio of $C^{(1)} = 5/9$, meaning $j = 2$ and $k = 4$. The initial three dynamic traces are shown in Figure 4.2 with ω_{cj} and $j_\omega = 0, 1, 2, 3$. Dimensionless frequency $\sqrt{\rho_L/E_L}\omega l_L$ can be used similar to work from Morini and Gei (2018) and the variable in universal torus (3.1) ($\sqrt{\rho_L/E_L}\omega l_L = \xi_L$). The red

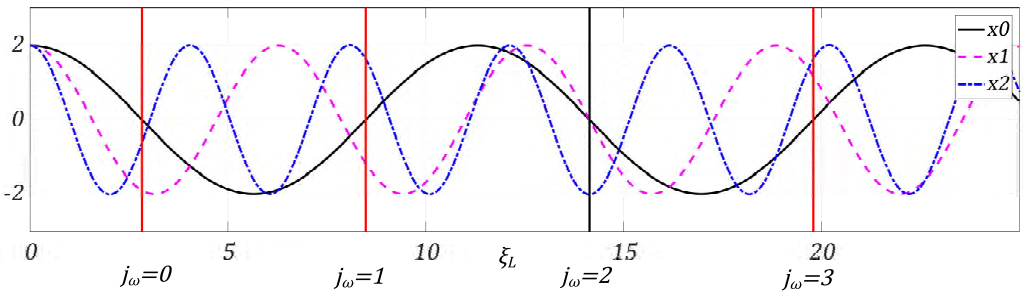

Figure 4.2. The plot for initial dynamic trace x_0 (black solid line), x_1 (magenta dotted line) and x_2 (blue dashed line) for cantorial ratio $5/9$. Canonical frequency ω_{cj} with different j_ω (vertical black line satisfied canonical condition, vertical red lines not).

lines are associated with frequencies ω_{cj} with $j_\omega = 0, 1, 3$ and black vertical line represents $j_\omega = 2$. Through the definition of canonical frequency and saddle points $(\pm\sqrt{4+I}, 0, 0)$, only $j_\omega = 2$ satisfies the condition for canonical frequency because x_0 and x_1 should vanish at this frequency but not x_2. It also means that the parameter j_ω cannot be an arbitrary value. To further understand the principle behind the relationship between j, k and j_ω, k_ω, the dimensionless frequency limit is increased to 45 in Figure 4.3 (a) and with other figure (b) but count with k_ω. In terms of numerical results, the frequency at $j_\omega = 2$ is the same with $k_\omega = 4$ simultaneously satisfied definition of canonical frequency. It is, in particular, the parameters j and k in canonical ratio (4.4). In addition, the frequency at $j_\omega = 7$ is same with $k_\omega = 13$ and also being canonical frequency, because the

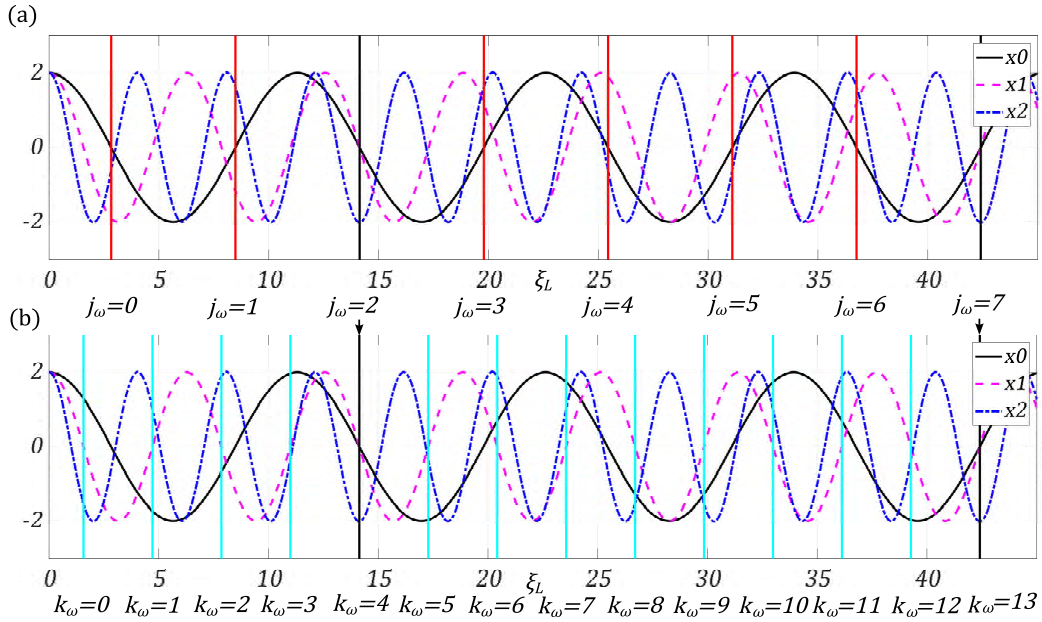

Figure 4.3. The plot for initial dynamic trace x_0 (black solid line), x_1 (magenta dotted line) and x_2 (blue dashed line) for cantorial ratio $5/9$. (a) canonical frequency ω_{cj} with different j_ω (vertical black lines satisfied canonical condition, vertical red lines not). (b) canonical frequency ω_{ck} with different k_ω (vertical black lines satisfied canonical condition, vertical cyan lines not).

canonical ratio $(1+2*7)/(1+2*13) = 5/9 = (1+2*2)(1+2*1)/(1+2*4)(1+2*1)$ do not change. According our assumption (4.7), the $m = 1$ is this case so that equation (4.7) in fact explains the relationship between parameters j_ω, k_ω and j, k. Thus, the relationship between the two parameters in canonical frequency and canonical ratio is exactly equation (4.8) for family no. one.

Because m can be an arbitrary natural number, the example in Figure 4.3 and equation (4.8) for canonical family no. one demonstrates an infinite number of canonical frequencies in the dispersion spectra. The periodic canonical structure can be found. Therefore, the canonical frequency associated with canonical family no. one have been derived from the initial dynamic trace and saddle point successfully.

4.1.2 Canonical family no. two

Canonical family no. two is associated with the canonical ratio is:

$$C^{(2)} = \sqrt{\frac{\rho_S E_L}{\rho_L E_S}} \frac{l_S}{l_L} = \frac{1+2j}{2q},\ j,q \in \mathbb{N} \tag{4.9}$$

Because the coordinates for saddle points is (x_2, x_1, x_0), the initial saddle point is $(0, \pm\sqrt{4+I}, 0)$, which means x_0 and x_2 equal to zero, x_1 is not at canonical frequency. Similar to family no.

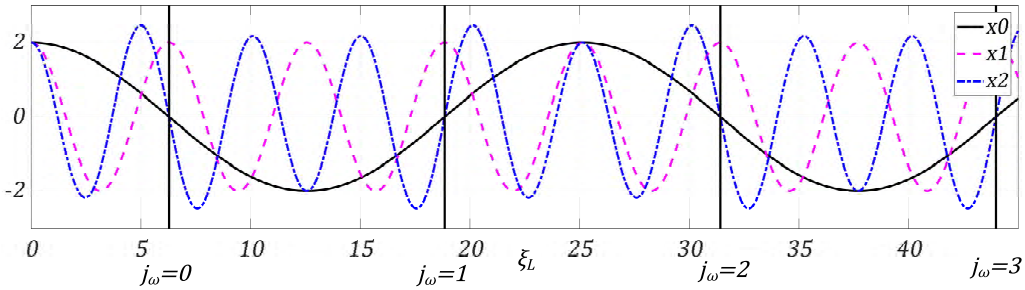

Figure 4.4. The plot for initial dynamic trace x_0 (black solid line), x_1 (magenta dotted line) and x_2 (blue dashed line) for cantorial ratio $1/4$. Canonical frequency ω_{cj} with different j_ω (vertical black lines all satisfied canonical condition).

one, considering $1 + 2j$ and $2q$ do not have common factors and equation (4.9) is already in the lowest terms. Furthermore, as definition for a family no. two, $C^{(2)}$ must be odd/even, the odd term $(1 + 2m)$ still can be used to multiply into numerator and denominator simultaneously (because odd×even=even):

$$C^{(2)} = \sqrt{\frac{\rho_S E_L}{\rho_L E_S}}\frac{l_S}{l_L} = \frac{1+2j}{2q} = \frac{(1+2j)(1+2m)}{2q(1+2m)},\ m \in \mathbb{N} \tag{4.10}$$

In family no. two, the canonical frequency ω_{ck} is not the canonical frequency now because $x_1 = 2\cos(\frac{\pi}{2}(1 + 2k_\omega)) = 0$, which is contrary to the definition of initial saddle point. In addition, taking same assumption similar to equation (4.7) by substituting ω_{cj} into dynamic traces (4.3), we obtain:

$$x_0 = 2\cos(\frac{\pi}{2}(1+2j)(1+2m)) = 0;\ x_1 = 2\cos(\frac{\pi}{2}2q(1+2m)) = \pm 2$$
$$x_2 = 2\sin(\frac{\pi}{2}2q(1+2m)) = 0 \tag{4.11}$$

which is fully satisfied the definition of family no. two. Still, a numerical example is given to verify our theoretical analysis with $C^{(2)} = 1/4$, which means $j = 0$ and $q = 2$ with dimensionless frequency limit 45 as depicted in Figure 4.4.

Through the assumption (4.7), $1 + 2j_\omega = (1 + 2j)(1 + 2m)$ and in this case $j = 0 \Rightarrow j_\omega = m$. Therefore, the parameters j_ω can be any natural number and, as expected, four j_ω in Figure 4.4 are the canonical frequencies with checked the definition of an initial saddle point. Moreover, as the canonical ratio (4.9), there is another canonical frequency that can be deduced, which is called ω_{cq}:

$$\omega_{cq} = \frac{\pi\sqrt{E_L}}{2l_L\sqrt{\rho_L}}(2q)(1+2m) = \omega_{cj} \tag{4.12}$$

Therefore, the canonical frequency associated with canonical family no. two has been derived

from the initial dynamic trace and saddle point successfully.

4.1.3 Canonical family no. three

In terms of canonical family no. three, the steps for canonical frequency derivation are similar to family no. two and start from the associated canonical ratio:

$$C^{(3)} = \sqrt{\frac{\rho_S E_L}{\rho_L E_S}}\frac{l_S}{l_L} = \frac{2q}{1+2k},\ k,q \in \mathbb{N} \tag{4.13}$$

Because the coordinates for saddle points is (x_2, x_1, x_0), the initial saddle point on Kohmoto's manifold is $(0, 0, \pm\sqrt{4+I})$, which represented dynamic traces x_1 and x_2 are zero but $x_0 = \pm\sqrt{4+I}$ at canonical frequency. Still, two terms $1+2k$ and $2q$ are in lowest terms and times $(1+2m)$ simultaneously on numerator and denominator to keep the form $C^{(3)}$ =even/odd:

$$C^{(3)} = \sqrt{\frac{\rho_S E_L}{\rho_L E_S}}\frac{l_S}{l_L} = \frac{2q}{1+2k} = \frac{2q(1+2m)}{(1+2k)(1+2m)},\ m \in \mathbb{N} \tag{4.14}$$

As for family no. three, the canonical frequency ω_{cj} is definitely not the solution here because of $x_0 = 2\cos(\frac{\pi}{2}(1+2j_\omega)) = 0$ which in contrast of family no. three definition. Moreover, taking same assumption similar to equation (4.7) and substitution ω_{ck} into dynamic traces (4.3), we obtain:

$$x_1 = 2\cos(\frac{\pi}{2}(1+2k)(1+2m)) = 0,\ x_2 = 2\sin(\frac{\pi}{2}2q(1+2m)) = 0 \tag{4.15}$$

Through the canonical ratio (4.14), there is another canonical frequency ω_{cq} that can be deduced like family no. two:

$$\omega_{cq} = \frac{\pi\sqrt{E_S}}{2l_S\sqrt{\rho_S}}(2q)(1+2m) = \omega_{ck} \tag{4.16}$$

There is a numerical example for family no. three with $C^{(3)} = 4/3$ corresponding to $q = 2$ and $k = 1$ with dimensionless frequency limit 16 as shown in Figure 4.5. As expected, frequencies with $k_\omega = 1, 4$ are canonical frequency and satisfied definition of initial saddle points (because $1 + 2 \times 4 = (1 + 2 \times 1)(1 + 2 \times 1)$). Thus, the assumption meets theory again. The canonical frequency associated with canonical family no. three have been derived from the initial dynamic trace and saddle point successfully.

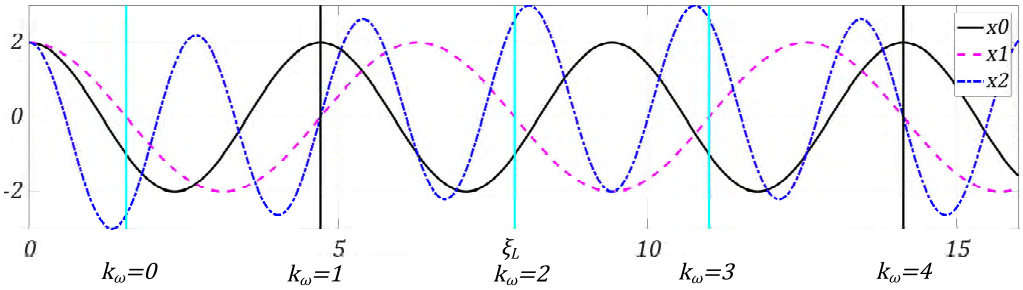

Figure 4.5. The plot for initial dynamic trace x_0 (black solid line), x_1 (magenta dotted line) and x_2 (blue dashed line) for cantorial ratio $4/3$. Canonical frequency ω_{ck} with different k_ω (vertical black lines satisfied canonical condition, vertical cyan lines not).

4.1.4 The period for canonical frequency and dynamic trace

Indeed, there are infinite number of canonical frequencies in dispersion relation. It is not hard to find the period of canonical frequency. First, by substituting $m+1$ into equation (4.8), subscript $m+1$ means $(1+2(m+1))$:

$$\omega_{cj,m+1} = \frac{\pi\sqrt{E_S}}{2l_S\sqrt{\rho_S}}(1+2j)(3+2m) = \frac{\pi\sqrt{E_L}}{2l_L\sqrt{\rho_L}}(1+2k)(3+2m) = \omega_{ck,m+1} \tag{4.17}$$

Using equation (4.17) minus (4.8) to obtain the canonical frequency period:

$$\omega_{cj,m+1} - \omega_{cj,m} = \omega_{ck,m+1} - \omega_{ck,m} = \frac{\pi\sqrt{E_S}}{l_S\sqrt{\rho_S}}(1+2j) = \frac{\pi\sqrt{E_L}}{l_L\sqrt{\rho_L}}(1+2k) \tag{4.18}$$

Equation (4.18) is period for canonical family no. one, which is determined material and geometrical parameters and j and k in canonical ratio. The period for canonical family no. two and three can be obtained with the same process as the following equations:

$$\omega_{cj,m+1} - \omega_{cj,m} = \omega_{cq,m+1} - \omega_{cq,m} = \frac{\pi\sqrt{E_S}}{l_S\sqrt{\rho_S}}(1+2j) = \frac{\pi\sqrt{E_L}}{l_L\sqrt{\rho_L}}(2q) \tag{4.19}$$

$$\omega_{ck,m+1} - \omega_{ck,m} = \omega_{cq,m+1} - \omega_{cq,m} = \frac{\pi\sqrt{E_S}}{l_S\sqrt{\rho_S}}(2q) = \frac{\pi\sqrt{E_L}}{l_L\sqrt{\rho_L}}(1+2k) \tag{4.20}$$

Equations (4.18), (4.19) and (4.20) are period for canonical frequency. The period for the initial three dynamic traces is significant. As the fact that Fibonacci sequence is composed of elementary phase L and S, the period for the initial three traces is just the lowest common period for x_0 and x_1. Then:

$$\sqrt{\frac{\rho_S}{E_S}}\omega l_S = \bar{S}2\pi = \bar{L}2\pi = \sqrt{\frac{\rho_L}{E_L}}\omega l_L,\ (\bar{S},\bar{L} \in \mathbb{N}) \tag{4.21}$$

where parameters $\overline{S}$ and $\overline{L}$ do not have common factors and by substituting canonical ratio (4.4) into (4.21):

$$\frac{1+2j}{1+2k} = \frac{\overline{S}}{\overline{L}} \tag{4.22}$$

Both sides of equation (4.22) are in lowest terms so that $\overline{S} = 1 + 2j$ and $\overline{L} = 1 + 2k$ and period for trace in the canonical family no. one is:

$$\text{period}_1 = 2\frac{\pi\sqrt{E_S}}{l_S\sqrt{\rho_S}}(1+2j) = 2\frac{\pi\sqrt{E_L}}{l_L\sqrt{\rho_L}}(1+2k) \tag{4.23}$$

The period for the other two families can also be derived with the same process:

$$\text{period}_2 = 2\frac{\pi\sqrt{E_S}}{l_S\sqrt{\rho_S}}(1+2j) = 2\frac{\pi\sqrt{E_L}}{l_L\sqrt{\rho_L}}(2q) \tag{4.24}$$

$$\text{period}_3 = 2\frac{\pi\sqrt{E_S}}{l_S\sqrt{\rho_S}}(2q) = 2\frac{\pi\sqrt{E_L}}{l_L\sqrt{\rho_L}}(1+2k) \tag{4.25}$$

It is interesting to find the relationship between canonical frequency and period of dynamic trace. The period of canonical frequency is half of period of the trace. Thus, there must be two canonical frequencies in one period. From canonical frequency (4.8), by substituting $m = 0, 1$ into it and deviated by period of traces (4.23):

$$\frac{\omega_{ck,0}}{\text{period}_1} = \frac{1}{4}, \frac{\omega_{ck,1}}{\text{period}_1} = \frac{3}{4} \tag{4.26}$$

There are precisely two canonical frequencies at the quarter and three-quarters of one trace period. Hence, the investigation method is usually in one period of trace and obtaining canonical frequencies to improve the computation speed in software. With the same process, the relationship between canonical frequencies and period of the trace for other families are the same as family no. one.

4.1.5 Period of Kohmoto's invariant

Next, according to simplified Kohmoto's invariant (4.27):

$$I = (\beta^2 - 4)\sin^2\left(\sqrt{\frac{\rho_L}{E_L}}\omega l_L\right)\sin^2\left(\sqrt{\frac{\rho_S}{E_S}}\omega l_S\right) \tag{4.27}$$

Half of period in equations (4.23), (4.24) and (4.25) when the concept of canonical is applied to

structure is the period or Kohmoto's invariant, because of period of trigonometric function $\sin(\omega)$ is 2π and $\sin^2(\omega)$ is π. It also means canonical frequency and Kohmoto's invariant share same period. By substituting canonical frequency (4.8) into (4.27), the Kohmoto's invariant becomes:

$$\sin\left(\sqrt{\frac{\rho_S}{E_S}}\frac{\pi\sqrt{E_S}}{2l_S\sqrt{\rho_S}}(1+2j)(1+2m)l_S\right)=1;\ \sin\left(\sqrt{\frac{\rho_L}{E_L}}\frac{\pi\sqrt{E_L}}{2l_L\sqrt{\rho_L}}(1+2k)(1+2m)l_L\right)=1$$

$$I=\beta^2-4 \tag{4.28}$$

Therefore, Kohmoto's invariant reaches the maximum value as the canonical frequency for family no. one because of the properties of sine function. When canonical configuration belongs family no. two or three, as expressions (4.12) and (4.16), one of two $\sin(\sqrt{\rho_X/E_X}\omega l_X)$ terms must be zero and then invariant is zero. This also helps us to distinguish whether family no. two or three.

Kohmoto's invariant is a crucial invariant governing the scaling factor at canonical frequency during eigenvalue of Jacobian analysis and self-similarity of passband layouts. In addition, this is also a key clue when investigating negative refraction in Fibonacci laminates, significantly as $I=0$, which is also implied other periodic orbits existed in Kohmoto's manifold except for saddle points. More results concerning Kohmoto's invariant are shown in the following few sections.

4.1.6 Table for three canonical families

The characteristics from three canonical family structures (canonical frequency, ratio and period of trace) are shown in Table 4.1.

Table 4.1. The characteristics of three canonical families

Family no. 1	Ratio	$C^{(1)} = \sqrt{\frac{\rho_S E_L}{\rho_L E_S}} \frac{l_S}{l_L} = \frac{1+2j}{1+2k}$
	ω_c	$\omega_{cj} = \frac{\pi\sqrt{E_S}}{2l_S\sqrt{\rho_S}}(1+2j)(1+2m) = \frac{\pi\sqrt{E_L}}{2l_L\sqrt{\rho_L}}(1+2k)(1+2m) = \omega_{ck}$
	Period	$\omega_t = 2\frac{\pi\sqrt{E_S}}{l_S\sqrt{\rho_S}}(1+2j) = 2\frac{\pi\sqrt{E_L}}{l_L\sqrt{\rho_L}}(1+2k)$
Family no. 2	Ratio	$C^{(2)} = \sqrt{\frac{\rho_S E_L}{\rho_L E_S}} \frac{l_S}{l_L} = \frac{1+2j}{2q}$
	ω_c	$\omega_{cj} = \frac{\pi\sqrt{E_S}}{2l_S\sqrt{\rho_S}}(1+2j)(1+2m) = \frac{\pi\sqrt{E_L}}{2l_L\sqrt{\rho_L}}(2q)(1+2m) = \omega_{cq}$
	Period	$\omega_t = 2\frac{\pi\sqrt{E_S}}{l_S\sqrt{\rho_S}}(1+2j) = 2\frac{\pi\sqrt{E_L}}{l_L\sqrt{\rho_L}}(2q)$
Family no. 3	Ratio	$C^{(3)} = \sqrt{\frac{\rho_S E_L}{\rho_L E_S}} \frac{l_S}{l_L} = \frac{2q}{1+2k}$
	ω_c	$\omega_{cq} = \frac{\pi\sqrt{E_S}}{2l_S\sqrt{\rho_S}}(2q)(1+2m) = \frac{\pi\sqrt{E_L}}{2l_L\sqrt{\rho_L}}(1+2k)(1+2m) = \omega_{ck}$
	Period	$\omega_t = 2\frac{\pi\sqrt{E_S}}{l_S\sqrt{\rho_S}}(2q) = 2\frac{\pi\sqrt{E_L}}{l_L\sqrt{\rho_L}}(1+2k)$

4.2 Theory of Scaling of the Spectrum

The passbands layout in the neighbourhood of a frequency at which a p-point periodic orbit takes place displays a self-similar pattern controlled by a scaling factor which is revealed by perturbing the corresponding periodic orbit and linearising map (4.29) (Kohmoto and Oono 1984):

$$\mathcal{T}_g(\tilde{x}_i, \tilde{y}_i, \tilde{z}_i) = (\tilde{x}_{i+1}, \tilde{y}_{i+1}, \tilde{z}_{i+1}) = (\tilde{x}_i\tilde{y}_i - \tilde{z}_i, \tilde{x}_i, \tilde{y}_i) \tag{4.29}$$

In particular, by denoting $R_i = P_i(\omega + \delta\omega)$, where $\delta\omega$ is the perturbation in frequency and:

$$\delta\mathbf{r}_i = R_i - P_i \tag{4.30}$$

where $\delta\mathbf{r}_i$ is perturbation in points on Kohmoto's manifold, it turns out that after p applications of map (4.29) the position of R_{i+p} can be approximated by the linear relationship:

$$R_{i+p} = \mathcal{T}_g{}^p\,(R_i) \rightarrow \delta\mathbf{r}_i = \mathbf{A}\delta\mathbf{r}_i \tag{4.31}$$

where 3×3 matrix $\mathbf{A}$ is given by $\mathbf{A} = J_g(P_{i+p})...J_g(P_i)$, and J_g is a Jacobian (2.33) calculated in the periodic point concerned. As $\det J = -1$, $\det\mathbf{A}$ can be either 1 or -1 depending on whether p is even or odd, respectively. One eigenvalue for matrix $\mathbf{A}$ is $\vartheta^0 = 1$ corresponding the eigenvector ψ^0 with the additional two eigenvalues, ϑ^+ and ϑ^- ($\vartheta^+ = 1/\vartheta^-$), and the corresponding eigenvectors are $\psi^\pm$. For GM sequence, if P_1 is assumed as first saddle point, the $\mathbf{A}$ would be:

$$\mathbf{A} = \begin{bmatrix} I(\omega)^2 + 7I(\omega) + 13 & (I(\omega)+4)^{3/2} & 0 \\ (I(\omega)+4)^{3/2} & I(\omega)+5 & 0 \\ 0 & 0 & 1 \end{bmatrix}$$

and then, the eigenvalues except ϑ^0 are:

$$\vartheta^\pm(\omega) = \frac{1}{4}(\sqrt{4 + (4 + I\,(\omega))^2} \pm (4 + I\,(\omega)))^2$$

Thus, $\delta\mathbf{r}_i$ can be expressed as linear combination of three eigenvectors $\psi^0,\ \psi^+,\ \psi^-$; $C^{(+,-,0)}$ are the general coefficients in linear space associated with eigenvectors:

$$\delta\mathbf{r}_i = C^+\psi^+ + C^-\psi^- + C^0\psi^0 \tag{4.32}$$

and, we obtain:

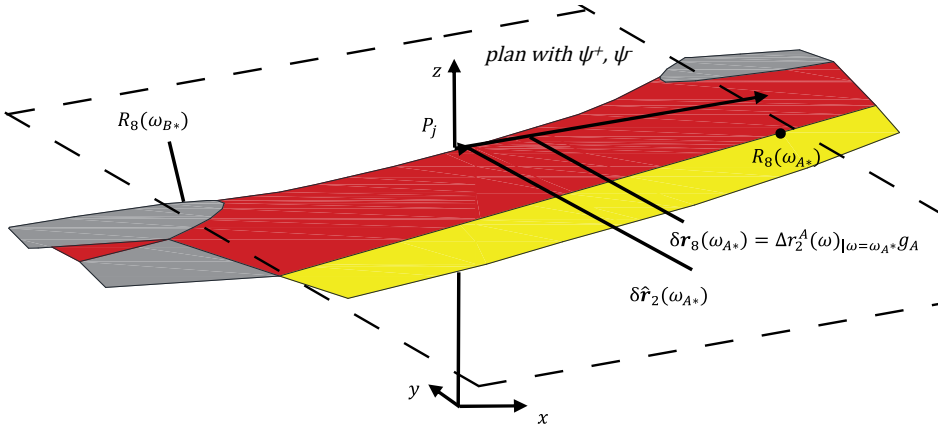

Figure 4.6. Part of Kohmotos surface, figure reproduced from Morini and Gei (2018).

$$\delta\mathbf{r}_{i+p} = \mathbf{A}\delta\mathbf{r}_i = C^+\vartheta^+\psi^+ + C^-\vartheta^-\psi^- + C^0\vartheta^0\psi^0 \tag{4.33}$$

The $\mathbf{A}$ with the eigenvector ψ^0 for $\vartheta^0 = 1$ must be orthogonal to another two eigenvectors $\psi^{\pm}$ (Strang 2021). As $\vartheta^+(\omega) \gg \vartheta^0 = 1 \gg \vartheta^-(\omega)$, if the $\bar{k}$ times are applied to maps, the result would be:

$$\delta\mathbf{r}_{i+p\bar{k}} = C^+(\vartheta^+)^{\bar{k}}\psi^+ + C^-(\vartheta^-)^{\bar{k}}\psi^- + C^0\vartheta^0 \approx C^+(\vartheta^+)^{\bar{k}}\psi^+ \tag{4.34}$$

It can be derived that from every complete iteration for the Fibonacci sequence, the evolution of $\delta\mathbf{r}_i$ can be approximated expressed only by the term along eigenvectors ψ^+ respectively. It is called unstable eigendirections (Arnold et al. 2013). As a consequence, equation (4.34) is approximately by:

$$\delta\mathbf{r}_{i+p\bar{k}} \approx (\vartheta^+)^{\bar{k}}\delta\hat{\mathbf{r}}_i \tag{4.35}$$

where $\delta\hat{\mathbf{r}}_i = C^+\psi^+$. Based on the principles of renormalisation theory, equation (4.35) provides the approximate prediction of the position of R_i from the periodic point P_i. Thus, the scaling properties of non-periodic bounded orbits about periodic points of the linear transformations are determined by the maximum eigenvalues ϑ^+ and the associated eigenvector.

Scaling is illustrated by a case having a narrow stop band for which it is shown the role of the eigenvalue ϑ^+. For instance, considering the stop band $(\omega_{A*} - \omega_{B*})$ centred at frequency for sequence F_8 which is saddle point P_1 as shown in Figure 4.6. Points $R_8(\omega_{A*})$ and $R_8(\omega_{B*})$ are therefore on the boundary of the all passband region on Kohmoto's manifold. In the neighbourhood of point P_1, the positions of the two points with respect to P_1 can be approximated by two vectors, respectively $\delta\mathbf{r}_8(\omega_{A*})$ and $\delta\mathbf{r}_8(\omega_{B*})$ on the tangent plane of P_1 whose equation is $\tilde{z} = \sqrt{4 + I(\omega)}$, then, two equations yield:

$$\delta\hat{\mathbf{r}}_2(\omega_{A*}) = \frac{\delta\mathbf{r}_8(\omega_{A*})}{\vartheta^+} \text{ and } \delta\hat{\mathbf{r}}_2(\omega_{B*}) = \frac{\delta\mathbf{r}_8(\omega_{B*})}{\vartheta^+} \tag{4.36}$$

Eigenvector ψ^0 must be orthogonal to the tangent plane of this saddle point and another two eigenvectors $\psi^{\pm}$, these two new eigenvectors are much shorter than the parent vectors $\delta\mathbf{r}_8(\omega_{A*})$ and $\delta\mathbf{r}_8(\omega_{B*})$. Moreover, $\delta\hat{\mathbf{r}}_2(\omega_{A*})$ and $\delta\hat{\mathbf{r}}_2(\omega_{B*})$ projections to the Kohmoto's surface identify are approximated with points $R_2(\omega_{A*})$ and $R_2(\omega_{B*})$, respectively, whose coordinates $\tilde{z}_2(\omega_{A*})$ and $\tilde{z}_2(\omega_{B*})$ are greater than 2, therefore the two frequencies are within a band gap for F_2. Now, rewrite $\delta\hat{\mathbf{r}}_2(\omega_{A*})$ as:

$$C^{+}_{\omega_{A*}}\psi^{+} = \delta\hat{\mathbf{r}}_2(\omega_{A*}) = \Delta r_2^A(\omega)_{|\omega=\omega_{A*}\mathbf{g}_A} \tag{4.37}$$

$\mathbf{g}_A$ is a elementary vector with same direction of ψ^{+}, then $\Delta r_2^A(\omega)_{|\omega=\omega_{A*}\mathbf{g}_A} = C^{+}_{\omega_{A*}}$, which can be expanded in Taylor series and $\delta\hat{\mathbf{r}}_2\left(\omega_{P_i}\right) = 0$ about ω_{P_i}, retaining only the first order:

$$\Delta r_2^A(\omega_{A*}) = C^{+}_{\omega_{A*}} \approx D(\omega_{A*} - \omega_{P_i}) \tag{4.38}$$

Then, the approximate frequency $\tilde{\omega}_A$ at the edge of a passband for the sequence F_2 is such that $\Delta r_2^A(\tilde{\omega}_A)$ matches the norm of vector $\delta\mathbf{r}_8(\omega_{A*})$:

$$\Delta r_2^A(\tilde{\omega}_A) = \|\delta\mathbf{r}_8(\omega_{A*})\| \tag{4.39}$$

With the same process, the $\Delta r_2^A(\tilde{\omega}_A) = C^{+}_{\tilde{\omega}_A} \approx D(\tilde{\omega}_A - \omega_{P_i})$. Using equations (4.38) and (4.39) yields:

$$D(\tilde{\omega}_A - \omega_{P_i}) = \vartheta^{+} D(\omega_{A*} - \omega_{P_i}) \tag{4.40}$$

Therefore, the following final results can be recorded:

$$(\tilde{\omega}_A - \omega_{P_i}) = \vartheta^{+}(\omega_{A*} - \omega_{P_i}) \tag{4.41}$$

For $\delta\mathbf{r}_8(\omega_{B*})$ and $\delta\hat{\mathbf{r}}_2(\omega_{B*})$ with same procedure, obtaining $(\tilde{\omega}_B - \omega_{P_i}) = \vartheta^{+}(\omega_{B*} - \omega_{P_i})$. Consequences, the analytical scaling process is deduced:

$$\omega_{A*} - \omega_{B*} = \frac{\widetilde{\omega}_A - \widetilde{\omega}_B}{\vartheta^{+}} \tag{4.42}$$

With the proposed case, the scaling occurring between parts of the diagrams of order F_i and F_{i+p} is governed by equation (4.42), coherently with the linearisation of the complete-cycle transformation $\mathcal{T}_g$. In addition, if we only considering half period of complete-cycle transformation $\mathcal{T}_g$ (F_i and $F_{i+p/2}$, if p can be divisible by 2), which means $(\omega_{A*} - \omega_{B*})$ and the bandgap $(\omega_{A'} - \omega_{B'})$ can be scaled without fully theory support but numerical proved by Morini and Gei (2018), which are:

$$\omega_{A*} - \omega_{B*} = \frac{\widetilde{\omega}_{A'} - \widetilde{\omega}_{B'}}{\lambda^{+}} \tag{4.43}$$

where $\widetilde{\omega}_{A'}$ and $\widetilde{\omega}_{B'}$ are the two approximate frequencies at the edge of the bandgap. According to Morini and Gei (2018), the scaling factor is $\lambda^{+} \approx \sqrt{\vartheta^{+}}$. Indeed, this is not surprising because λ^{+} dominates the scaling of the initial bandgap of the case after the application of the half of complete iterations.

4.3 Numerical Results for Dispersion Relation and Local Scaling About Periodic Point

4.3.1 Results for canonical family no. one

By substituting $j = 0$ and $k = 0$ into canonical ratio (4.4) yields the value $C = 1$, which belongs to family no. one. The passband layouts, initial three traces and Kohmoto's invariant are plotted to facilitate the analysis of their relationship. The Fibonacci sequence reachs F_{11} for a better analysis of the scaling effect. In Figure 4.7 (a), the blue segments are the passband of dynamic traces associated with a dimensionless frequency corresponding to the Fibonacci sequence order F_i. Being $F_{0,1}$ waveguides composed of a single material, the wave with any frequency can propagate without bandgap. In addition, the passband, dynamic trace and Kohmoto invariant are periodic and symmetric with respect to the canonical frequencies. The canonical frequencies are also located at a quarter and three quarters in one period of traces, which verified our theoretical findings. Initial three traces satisfy condition $x_0 = x_1 = 0$, $x_2 = \pm\beta$ at canonical frequency for family no. one.

Then, the effects for scaling are checked with compared the bandgap frequency length and associated dynamic traces centred at the first canonical frequency for F_2, F_5, F_8 and F_{11}. The Kohmoto's invariant at canonical frequency is equation (4.28) $I = 2.25$ with the maximum eigenvalue of Jacobian (4.33) $\vartheta_6^{+} \approx 41.038$. the subscript 6 means the number of complete periodic points. It is more larger than other two eigenvalues $\vartheta_6^{0} = 1$ and $\vartheta_6^{-} \approx 0.0243$. The numerical results are shown in Table 4.2.

Table 4.2. Numerical results for bandgap length at first canonical frequency for Fiboancci sequence F_2, F_5, F_8 and F_{11} with ratio $C = 1$, scaled factors are $\vartheta_6^{+} = 41.038$, $\lambda_6^{+} = \sqrt{\vartheta_6^{+}} \approx 6.406$

F_2 bandgap	F_5 bandgap	F_8 bandgap	F_{11} bandgap
0.679	0.135	0.0210	0.00327
F_2/F_8	F_5/F_{11}	F_5/F_8	F_8/F_{11}
32.436	41.183	6.429	6.423

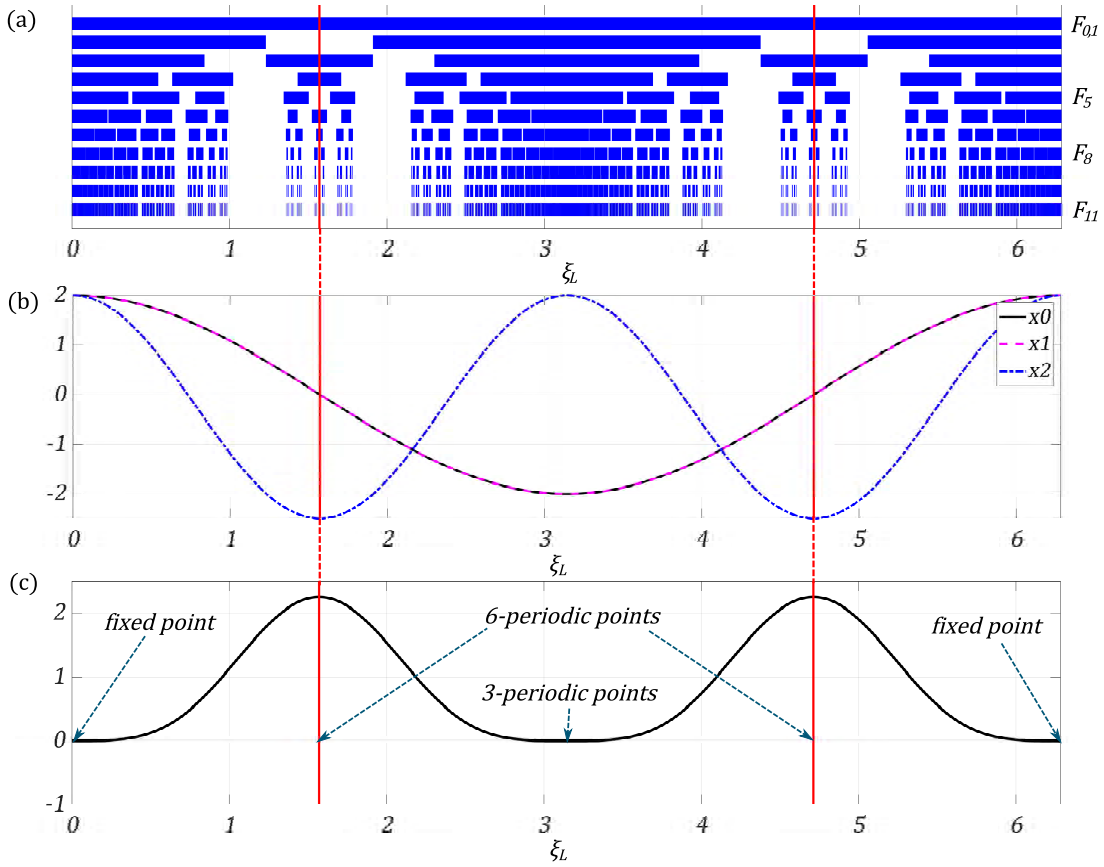

Figure 4.7. Three plots of canonical ratio 1 *with dimensionless frequency* ξ_L *in one dynamic trace period, (a) the passband layout for a Fibonacci sequence* F_0 *to* F_{11}*. (b) initial three dynamic traces* x_0*,* x_1 *and* x_2*. (c) Kohmoto's invariant with periodic points. Red vertical lines are canonical frequencies.*

Even numerical result $F_2/F_8 \approx 32.436$ is not perfectly equal to the maximum eigenvalue $\vartheta_6^+ = 41.038$. However, after three iterations, the result $F_5/F_{11} \approx 41.183$ almost matchs eigenvalue due to the equation (4.34) with $\bar{k}$ increasing. Moreover, the links between F_i and F_{i+3} are verified with results $F_5/F_8 \approx 6.429$ and $F_8/F_{11} \approx 6.423$, which almost approximate square root of eigenvalue $\lambda_6^+ = \sqrt{\vartheta_6^+} \approx 6.406$.

From Figure 4.8 (a), the effects for local scaling passband layouts and traces are described in detail. The length of bandgap of scaled $x_5(\omega)$, $x_8(\omega\lambda_6^+)$ and $x_{11}(\omega\vartheta_6^+)$ are almost the same with little different scaled $x_2(\omega/\lambda_6^+)$. These results agree with theoretical analysis (4.34), which implies the increasing direction of perturbation approximating to eigenvector ψ^+ with $6\bar{k}$ times iterations. The sign of trace with 6 iterations is same but opposite with 3 iterations, for instance, scaled x_2 and x_8 or x_5 and x_{11}. This is because the saddle point with complete 6 iterations goes back to initial point but opposite saddle point with half 3 iterations on Kohmoto's manifold as shown in Figure 4.8 (b). The Kohmoto's manifold with red area demonstrated at least one of three traces are in bandgap $|\tilde{x}| > 2$, $|\tilde{y}| > 2$ or $|\tilde{z}| > 2$ and yellow represented all three traces in passband

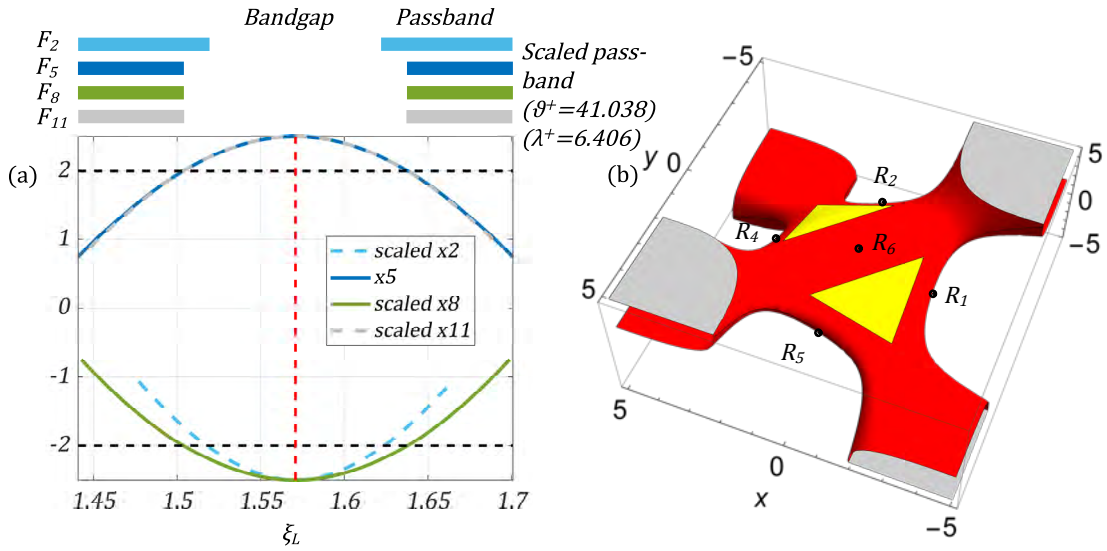

Figure 4.8. Canonical GM rod with $C = 1$ (a) Plot of traces $x_2(\omega/\lambda_6^+)$, $x_5(\omega)$, $x_8(\omega\lambda_6^+)$ and $x_{11}(\omega\vartheta_6^+)$ in the neighbourhood of canonical frequency (red dash vertical line). (b) Plot of Kohmoto's manifold at canonical frequency with periodic saddle point.

$(|\tilde{x}|, |\tilde{y}|, |\tilde{z}|) \leq 2$, which is used to illustrate local scaling principle by Morini and Gei (2018).

There are other periodic orbits associated with $I = 0$ in Figure 4.7 (c). They are frequency at complete period ω_t ($\omega = 0$ is also period point) and half period $\omega_t/2$ which are associated with fixed points $(2, 2, 2)^T$ ($R_{i+1} = R_i$) and 3-periodic points with initial traces $(2, -2, -2)^T$ ($R_{i+3} = R_i$). According to principle for local scaling, the Jacobian is analysed similar to saddle points but only with 1 iteration or 3 iterations. The maximum eigenvalue ϑ_i^+ can be obtained (i is the number of iteration) which are $\vartheta_1^+ = (\sqrt{5} + 3)/2 = \phi^2$ and $\vartheta_3^+ = \phi^6$. Then, the scaling can be performed on passband length with same procedures similar to before but changed frequency ω_c into ω_t and $\omega_t/2$.

Table 4.3. Numerical results for passband length for Fiboancci sequence F_2 to F_{11} with ratio $C = 1$ at $\omega = 0$, scaled factor is $\phi_g \approx 1.618$

F_2	F_3	F_4	F_5	F_6	F_7	F_8	F_9	F_{10}	F_{11}
1.231	0.841	0.547	0.358	0.225	0.141	0.0872	0.0539	0.0334	0.0206

	F_2/F_3	F_3/F_4	F_4/F_5	F_5/F_6	F_6/F_7	F_7/F_8	F_8/F_9	F_9/F_{10}	F_{10}/F_{11}
	1.464	1.536	1.531	1.589	1.600	1.613	1.615	1.617	1.618

From Table 4.3, it is very strange that the scaling factor does not approximate the maximum eigenvalue $\vartheta_1^+ = \phi^2 \approx 2.618$ but the square root of it $\phi \approx 1.618$. The reason will be explained in the next subsection.

From Table 4.4, the scaling factor is still the square root of the maximum eigenvalues $\sqrt{\vartheta_3^+} = \phi^3 \approx 4.236$. In addition, the passband length at frequency $\omega_t/2$ is double times compared with at

frequency ω_t. This is due to the symmetric properties of passband layouts in canonical structures and can be applied to other canonical ratios, which can be seen from Figure 4.7 (a). In addition, the scaled traces and Kohmoto's invariant are plotted for the explanation as depicted in Figure 4.9. The scaling factor is the square root of the maximum eigenvalue according to the results.

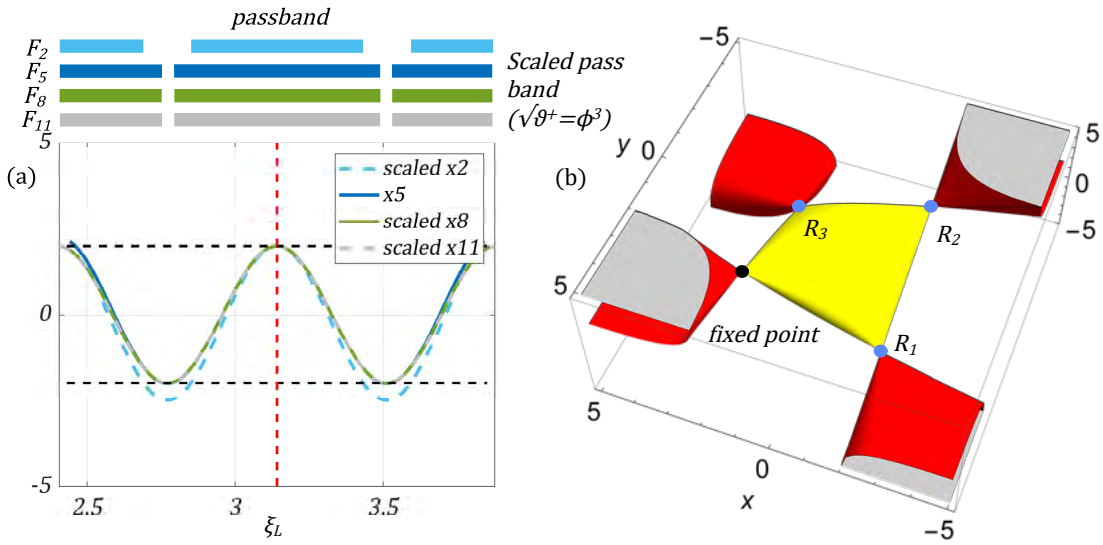

Figure 4.9. Canonical GM rod with $C = 1$ (a) Plot of traces $x_2(\omega/\phi^3)$, $x_5(\omega)$, $x_8(\omega\phi^3)$ and $x_{11}(\omega\phi^6)$ in the neighbourhood of half period frequency (red dash vertical line). (b) Plot of Kohmoto's manifold with fixed point (black) and 3-periodic points (cyan).

The effect becomes more precise with the increasing of Fibonacci order i similar to canonical frequencies.

Let us introduce another case in family no. one obtained from substitution $j = 1$, $k = 0$ and ratio $C = 3$, with the same process in case $C = 1$, the passband layouts, traces, and Kohmoto invariant are plotted. From Figure 4.10, the passband area associated with F_2 to F_{11} with a large portion that looks corresponding to Kohmoto's invariant is zero. Still, the effects of local scaling are checked with bandgap length similar to case ratio $C = 1$ at the first canonical frequency for $F_{2,5,8,11}$. The Kohmoto's invariant is $I \approx 34.028$ and the maximum eigenvalue is $\vartheta_6^+ \approx 1448.111$ which is much larger than other two eigenvalues $\vartheta_6^0 = 1$ and $\vartheta_6^- \approx 0.000691$. Thus, the same procedure can be duplicated to check local scaling. Moreover, the traces $x_{0,1,2}$ still satisfy the

Table 4.4. Numerical results for bandgap length for Fiboancci sequence F_2, F_5, F_8 and F_{11} with ratio $C = 1$ at $\omega = \omega_t/2$, scaled factor is $\sqrt{\vartheta_3^+} = \phi^3 \approx 4.236$

F_2 passband	F_5 passband	F_8 passband	F_{11} passband
2.462	0.715	0.174	0.0413
F_2/F_5	F_5/F_8	F_8/F_{11}	
3.442	4.102	4.226	

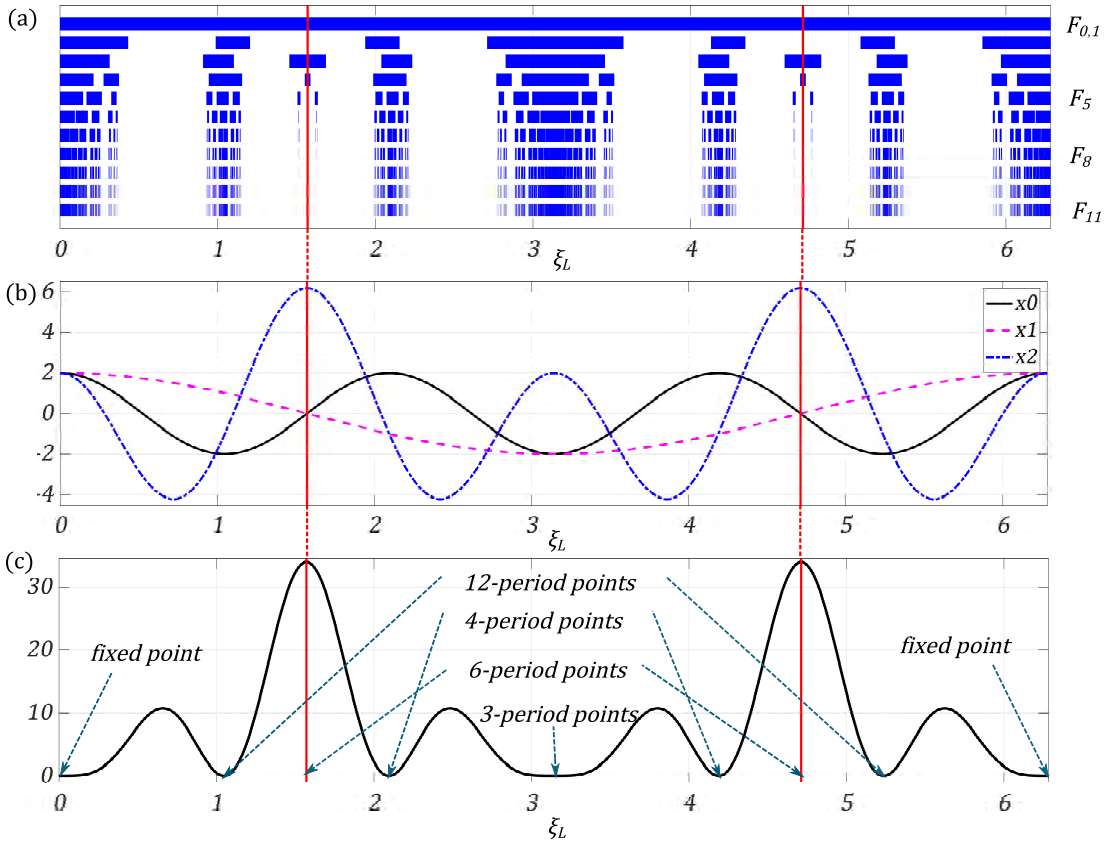

Figure 4.10. Three plots of canonical ratio 3 *with dimensionless frequency* ξ_L *in one dynamic trace period, (a) the passband layout for a Fibonacci sequence* F_0 *to* F_{11}*. (b) initial three dynamic traces* x_0*,* x_1 *and* x_2*. (c) Kohmoto's invariant. Red vertical lines are canonical frequencies.*

condition $R_1 = (\pm\beta, 0, 0)$ at canonical frequency for family no. one.

From Table 4.5, the initial numerical result $F_2/F_8 \approx 305.921$ is far away from the maximum eigenvalue $\vartheta_6^+ \approx 1448.111$. Converse, after three iterations the results $F_5/F_{11} \approx 1450.000$ almost matching the value ϑ_6^+. The reason is same with case ratio $C = 1$. In addition, the ratio between F_i and F_{i+3} also verified with results $F_5/F_8 \approx 38.443$ and $F_8/F_{11} \approx 37.807$, which almost approximate square root of eigenvalue $\lambda_6^+ = \sqrt{\vartheta_6^+} \approx 38.054$.

Table 4.5. Numerical results for bandgap length at first canonical frequency for Fiboancci sequence F_2*,* F_5*,* F_8 *and* F_{11} *with ratio* $C = 3$*, scaled factors are* $\vartheta_6^+ \approx 1448.111$*,* $\lambda_6^+ = \sqrt{\vartheta_6^+} \approx 38.054$

F_2 bandgap	F_5 bandgap	F_8 bandgap	F_{11} bandgap
0.730	0.0911	0.00239	6.283e-5
F_2/F_8	F_5/F_{11}	F_5/F_8	F_8/F_{11}
305.921	1450.000	38.443	37.807

From Figure 4.11, the effect of local scaling is perfect performed with $F_{5,8,11}$ except F_2. The

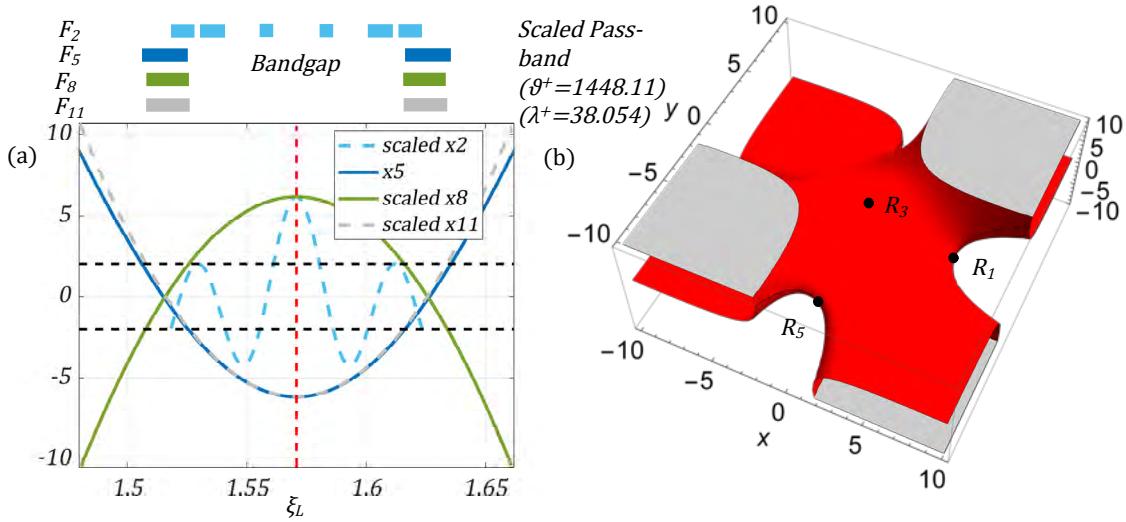

Figure 4.11. Canonical GM rod with $C = 3$ (a) Plot of traces $x_2(\omega/\lambda_6^+)$, $x_5(\omega)$, $x_8(\omega\lambda_6^+)$ and $x_{11}(\omega\vartheta_6^+)$ in the neighbourhood of canonical frequency (red dash vertical line). (b) Plot of Kohmoto's manifold at canonical frequency with periodic saddle point.

reason for the big gap between scaled trace x_2 and the other three scaled traces may be because of the Kohmoto's invariant being too large. Moreover, the scaling effects of other periodic points are analysed. Since the fixed point and 3-periodic points are explained in detail before, the 12- ($R_{12+i} = R_i$) and 4- ($R_{4+i} = R_i$) periodic points are analysed. The maximum eigenvalues are $\vartheta_{12}^+ \approx -321.997$ and $\vartheta_4^+ \approx -6.854$. It is fascinating that the length of the passband of 12-periodic points is the same as 4-periodic points. This phenomenon will be explained later as the periodic properties of the trigonometric function. Thus, only 4-periodic points orbit should be investigated.

Table 4.6. Numerical results for passband length for Fiboancci sequence $F_{2,6,10,14}$ with ratio $C = 3$ at dimensionless frequency $\xi_L = 2\pi/3$, scaled factor is $\vartheta_4^+ = -\phi^4 \approx -6.854$

F_2 passband	F_6 passband	F_{10} passband	F_{14} passband
0.218	0.0477	0.00813	0.00123
F_2/F_6	F_6/F_{10}	F_{10}/F_{14}	
4.566	5.875	6.582	

From the results of scaling passbands (Table 4.6) and scaled dynamic traces (Figure 4.12), the numerical results F_2/F_6, F_6/f_{10} and F_{10}/F_{14} confirm theoretical analysis (with increasing of Fibonacci order, results would be closer to ϑ_4^+). Interestingly, the scaled passbands (inside magenta area) are not symmetric, comparing to the frequency associated with canonical frequency. The maximum eigenvalue $\vartheta_4^+ = -\phi^4 \approx -6.854$ being negative one, so that increasing direction of perturbation follows the opposite of eigenvector ψ^+. Nevertheless, the length of passband scaled follow the same method as before.

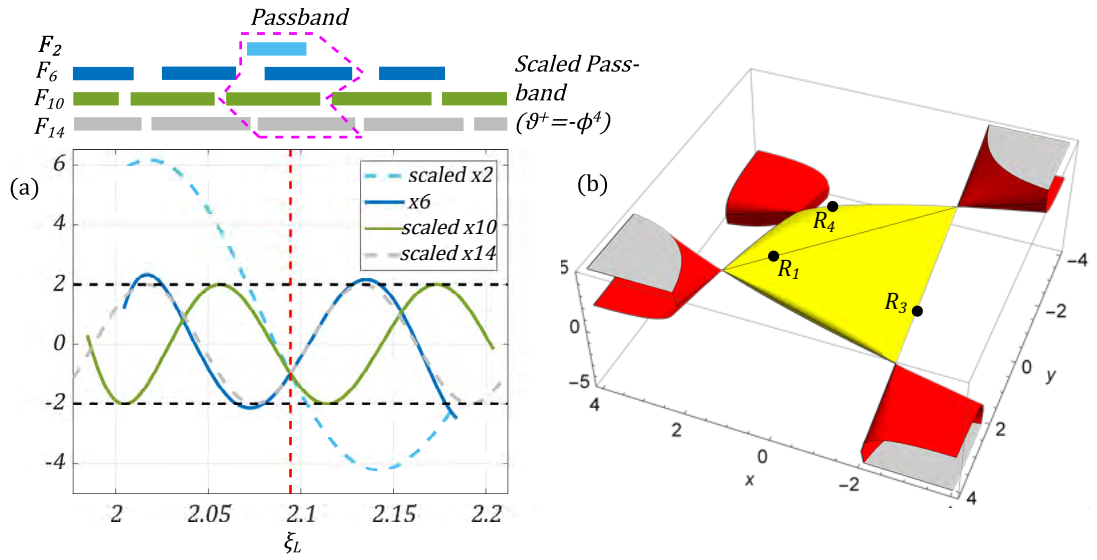

Figure 4.12. Canonical GM rod with $C = 3$ (a) Plot of traces $x_2(\omega/\vartheta_4^+)$, $x_6(\omega)$, $x_{10}(\omega\vartheta_4^+)$ and $x_{14}(\omega(\vartheta_4^+)^2)$ in the neighbourhood of dimensionless frequency $\xi_L = 2\pi/3$ (red dash vertical line). (b) Plot of Kohmoto's manifold with 4-periodic points orbits.

4.3.2 Results for canonical family no. two

By substituting $j = 1$ and $q = 1$ into canonical ratio (4.9) $C = \frac{1+2\times1}{2\times1} = \frac{3}{2}$ belongs family no. two. The passband layouts, initial dynamic traces and Kohmoto's invariant are plotted in one period. Unlike canonical family no. one, there are always passbands at the canonical frequency with any Fibonacci order in family no. two because of $x_2 = 0$, $R_1 = (0, \pm2, 0)$ and Kohmoto's invariant is $I = 0$ at ω_c, which is verified in numerical results Figure 4.13.

The local scaling can be performed on passband length, not just bandgap. Since $I = 0$, the scaling factor also the maximum eigenvalue is $\vartheta_6^+ = 9 + 4\sqrt{5} = \phi^6 \approx 17.944$. Thus, the scaling effect can be checked with the same procedures as before. The passband length of $F_{2,5,8,11}$ can be chosen. Actually, the passband in any Fibonacci order can also be selected in canonical family one. Nevertheless, the bandgap in family no. one should be checked so that $F_{2,5,8,11}$ are picked.

Table 4.7. Numerical results for passband length at first canonical frequency for Fiboancci sequence F_2, F_5, F_8 and F_{11} with ratio $C = 3/2$, scaled factors are $\vartheta_6^+ = \phi^6 \approx 17.944$, $\lambda_6^+ = \phi^3 \approx 4.236$

F_2 passband	F_5 passband	F_8 passband	F_{11} passband
0.736	0.216	0.0559	0.0135
F_2/F_8	F_5/F_{11}	F_5/F_8	F_8/F_{11}
13.177	15.958	3.414	4.1348

Comparing with results F_2/F_8 and F_5/F_{11}, the latter is closer to the maximum eigenvalue, and the reason is similar to two cases in family no. one. The results for half periodic transformation is

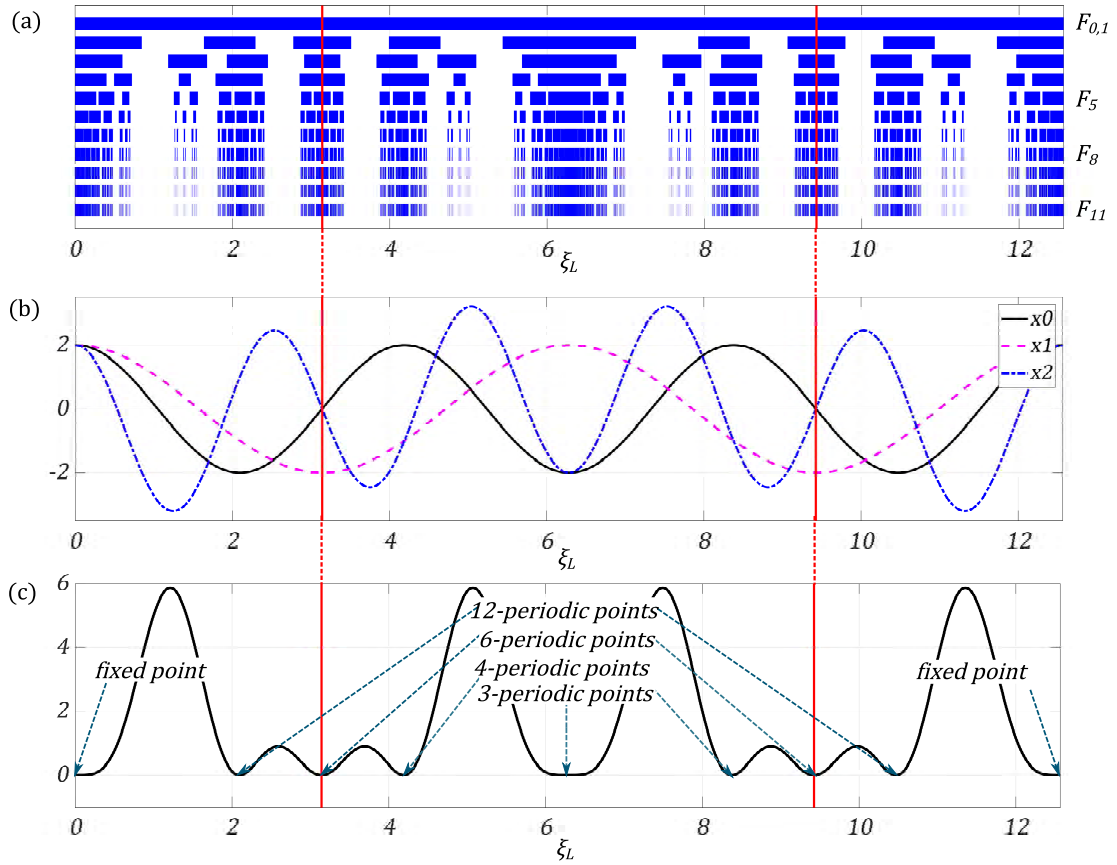

Figure 4.13. Three plots of canonical ratio $3/2$ *with dimensionless frequency* ξ_L *in one dynamic trace period, (a) the passband layout for a Fibonacci sequence* F_0 *to* F_{11}*. (b) initial three dynamic traces* x_0*,* x_1 *and* x_2*. (c) Kohmoto's invariant. Red vertical lines are canonical frequencies.*

good enough comparing with theoretical value $\lambda_6^+ = \phi^3 \approx 4.236$. It is believed that the local scaling for complete or half periodic transformation is more precise with increasing of Fibonacci order (also $\bar{k}$). Still, the scaled dynamic trace and corresponding Kohmoto's manifold are plotted in detail for the scaled effects to see the periodic orbits as shown in Figure 4.14. With Figure 4.14, the local scaling effect is verified once again but with passband length and traces. The local scaling effect is strongest concerning the canonical frequency and slacked with frequency away because the middle scaled passband in $F_{5,8,11}$ is almost identical. Moreover, the other passbands are also, which similarity with the increasing of Fibonacci order.

There exist 12- and 4-periodic points orbits that are similar to cases in $C = 3$ so that we do not study them again. They follow the same periodic orbits on Kohmoto's manifold with different initial points R_0 compared with cases in $C = 3$.

4.3.3 Results for canonical family no. three

In last case, family no. three, the ratio $C = 2/5$ is used to $k = 2$ and $q = 1$. Still, like previous cases, the passband layouts, initial three traces and Kohmoto's invariant in one trace period are

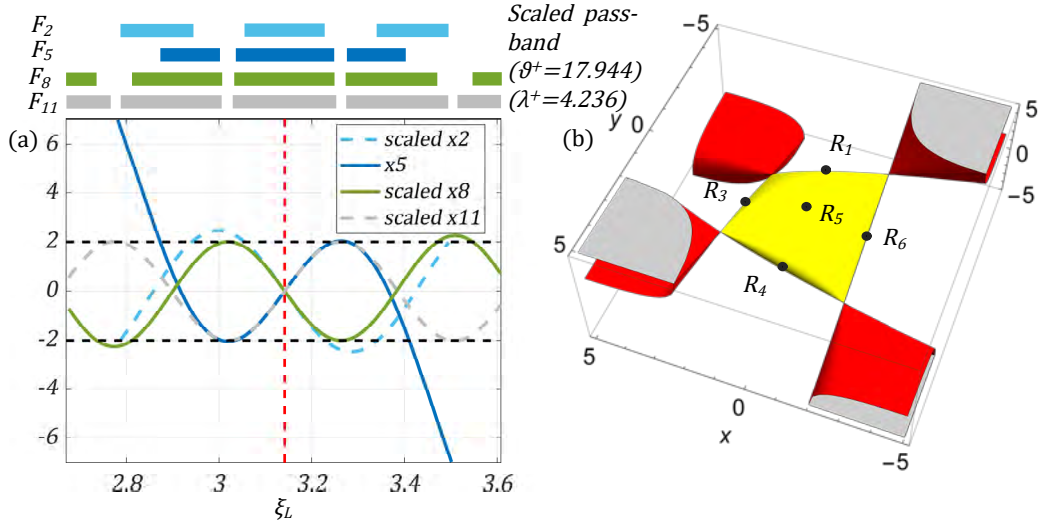

Figure 4.14. Canonical GM rod with $C = 3/2$ (a) Plot of traces $x_2(\omega/\lambda_6^+)$, $x_5(\omega)$, $x_8(\omega\lambda_6^+)$ and $x_{11}(\omega\vartheta_6^+)$ in the neighbourhood of canonical frequency (red dash vertical line). (b) Plot of Kohmoto's manifold at canonical frequency with periodic saddle point.

obtained with traces $x_0 = \pm 2$, $x_1 = 0$ and $x_2 = 0$ at canonical frequency as shown in Figure 4.15. As canonical family no. two or three actually means one of two sine terms $\sin(\xi_S)$ or $\sin(\xi_L)$ equal to zero, that is reason for $I = 0$ at canonical frequency, the maximum eigenvalue is still $\vartheta_6^+ = 9 + 4\sqrt{5} \approx 17.944$ and square root $\lambda_6^+ = \sqrt{\vartheta_6^+} \approx 4.236$, which are same with the case in family no. two. The table for passband scaling is given below in Table 4.8 with results from $F_{2,5,8,11}$.

Table 4.8. Numerical results for passband length at first canonical frequency for Fiboancci sequence F_2, F_5, F_8 and F_{11} with ratio $C = 2/5$, scaled factors are $\vartheta_6^+ = \phi^6 \approx 17.944$, $\lambda_6^+ = \phi^3 \approx 4.236$

F_2 passband	F_5 passband	F_8 passband	F_{11} passband
2.101	0.492	0.119	0.0281
F_2/F_8	F_5/F_{11}	F_5/F_8	F_8/F_{11}
17.7070	17.502	4.2662	4.2169

The results perfectly match the theoretical analysis. Then, the scaled dynamic traces around the canonical frequency and periodic orbits on Kohmoto's manifold are plotted for scaled effect in detail. From Figure 4.16, the local scaling effects are verified with length of passband and traces. In this case, the scaling effect is dramatic, the scaled passband x_2 is also coincide with scaled $x_{5,8,11}$. The Figure 4.16 (b) is not same with Figure 4.14 (b) due to the initial saddle point R_1 is different, which locates the opposite surface of R_4.

In addition, 30- ($R_{30+i} = R_i$) and 10- ($R_{10+i} = R_i$) periodic points orbits are existed on the Kohmoto's manifold. The maximum eigenvalues are $\vartheta_{30}^+ = -\phi^{30}$ and $\vartheta_{10}^+ = -\phi^{10}$, respectively.

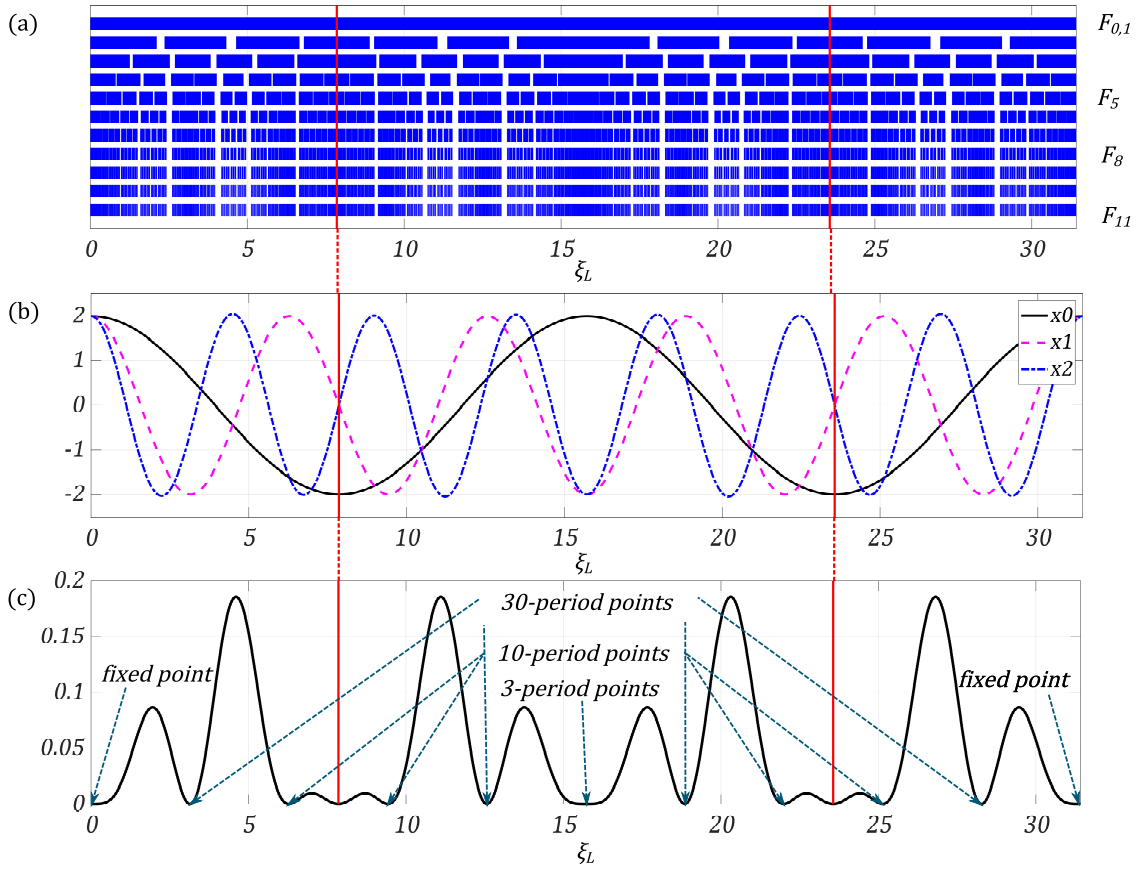

Figure 4.15. Three plots of canonical ratio $2/5$ *with dimensionless frequency* ξ_L *in one dynamic trace period, (a) the passband layout for a Fibonacci sequence* F_0 *to* F_{11}*. (b) initial three dynamic traces* x_0*,* x_1 *and* x_2*. (c) Kohmoto's invariant. Red vertical lines are canonical frequencies.*

For the same reason in 12- and 4-periodic points, only 10-periodic points orbit is investigated with initial points $(-\phi, 2, -\phi)^T$, because 30-periodic points share the same passband length and shape with 10-periodic points orbits.

Table 4.9. Numerical results for passband length for Fiboancci sequence F_2*,* F_7 *and* F_{12} *with ratio* $C = 2/5$ *at dimensionless frequency* $\xi_L = 2\pi$*, scaled factors are* $\vartheta_{10}^{+} = -\phi^{10} \approx -122.992$*,* $\lambda_{10}^{+} = \phi^5 \approx 11.090$

F_2 passband	F_7 passband	F_{12} passband
2.021	0.188	0.0171
F_2/F_7	F_7/F_{12}	F_2/F_{12}
10.774	10.956	118.042

From Table 4.9, the scaling results are perfectly matching absolute value of the maximum eigenvalue $\vartheta_{10}^{+} \approx -122.992$ and square root of it $\lambda_{10}^{+} \approx 11.090$ (just simply $\lambda_{10}^{+} = \sqrt{|\vartheta_{10}^{+}|}$). The scaled dynamic traces are plotted to show results. From Figure 4.17, the length of scaled passbands inside magenta area are almost same in $F_{2,7,12}$ but with opposite direction between $x_{2,12}$.

The reason is that the maximum eigenvalue ϑ_{10}^{+} being a negative number.

The results from three canonical families show that the bandgap and passband or dynamic traces can be scaled with the maximum eigenvalue ϑ^{+} or square root $\lambda^{+} = \sqrt{\vartheta^{+}}$ with good matching around frequency with other periodic orbits on Kohmoto's manifold. The frequency with other periodic orbits correspond to $I = 0$ are noticed except canonical frequency. Thus, the complete investigation about periodic orbits on Kohmoto's manifold and the reason for scaled factor is not the maximum eigenvalue should be made, which is shown in next section.

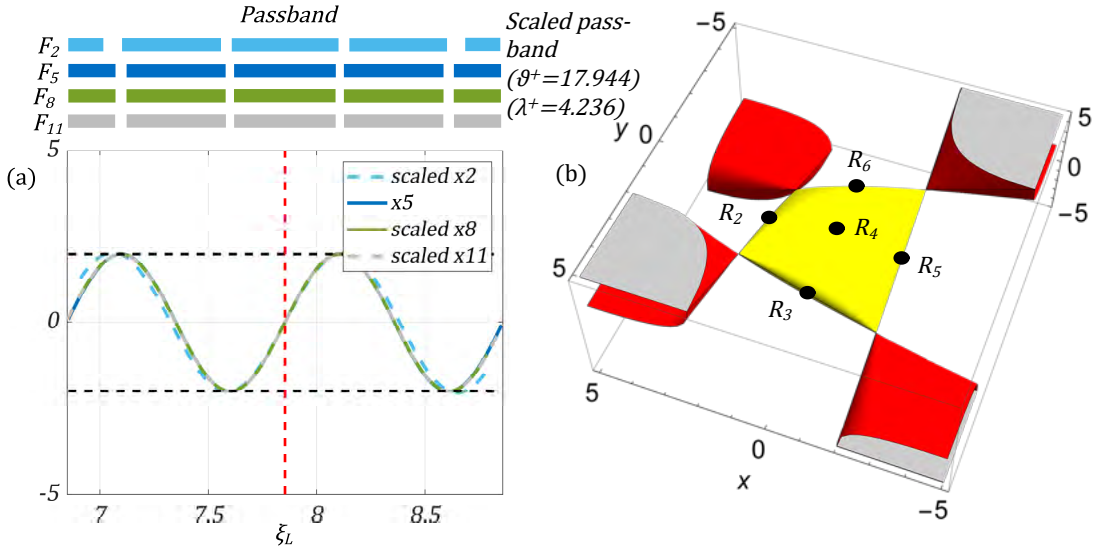

Figure 4.16. Canonical GM rod with $C = 2/5$ (a) Plot of traces $x_2(\omega/\lambda_6^{+})$, $x_5(\omega)$, $x_8(\omega\lambda_6^{+})$ and $x_{11}(\omega\vartheta_6^{+})$ in the neighbourhood of canonical frequency (red dash vertical line). (b) Plot of Kohmoto's manifold at canonical frequency with periodic saddle point.

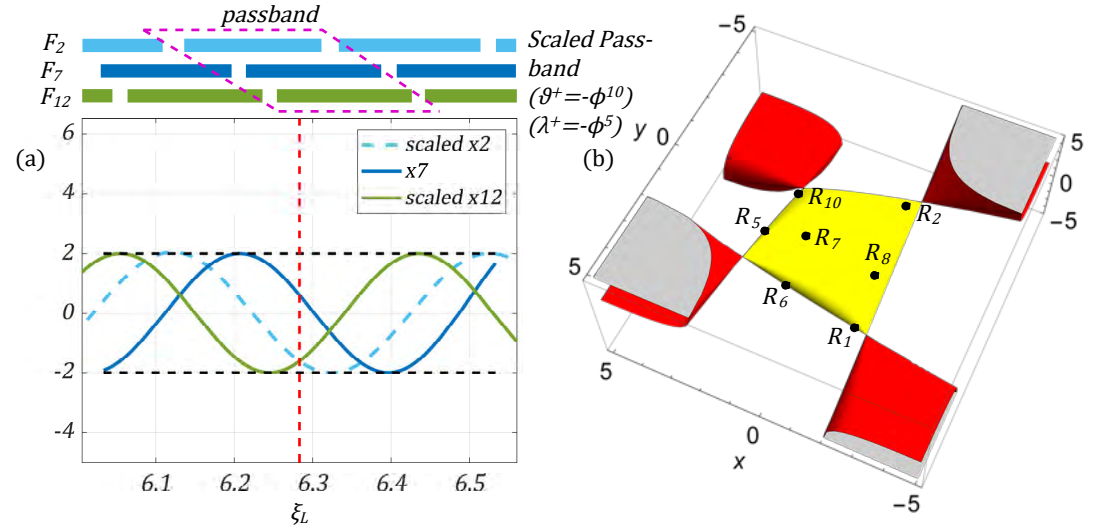

Figure 4.17. Canonical GM rod with $C = 2/5$ (a) Plot of traces $x_2(\omega/\phi^5)$, $x_7(\omega)$ and $x_{12}(\omega\phi^5)$ in the neighbourhood of dimensionless frequency $\xi_L = 2\pi$ (red dash vertical line). (b) Plot of Kohmoto's manifold with 10-periodic saddle point.

4.4 Experimental Results on Wave Transmission

The finite canonical rods were CNC machined from Nylon cylinders to produce phases L and S with a cross-section of diameter 40mm and 20mm, respectively. Four canonical configurations, namely three-cell F_2, three-cell F_3 and two-cell F_5, were fabricated with a phase length of 70mm to characterize the response up to the first period $2\omega_c$, while a two-cell F_2^l structure was manufactured with a phase length of 140mm to investigate the wave propagation in the first two periods, in the frequency range $\omega = [0, 4\omega_c^l]$. The specimens are shown in Figure 4.18 (a).

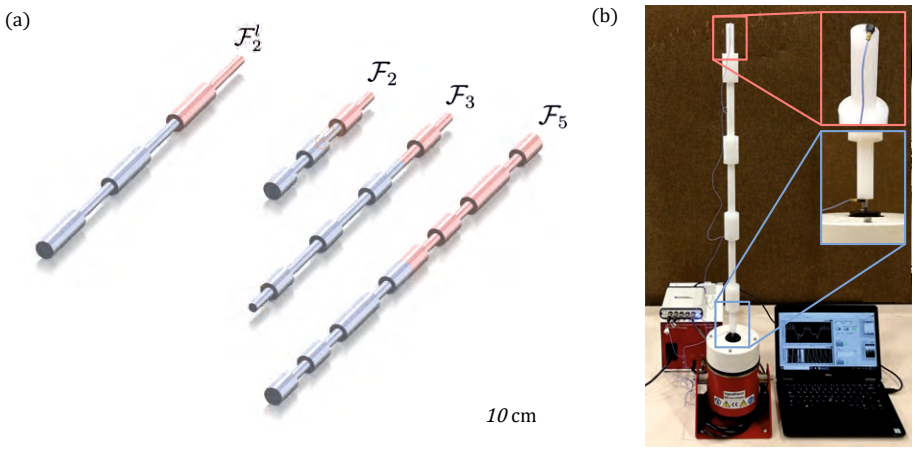

Figure 4.18. (a) *Finite canonical rods employed in the experiments and constituted of phases L and S arranged in configurations* F_2^l, F_2, F_3 *and* F_5, *where the repeated unit cell is highlighted in red. (b) Experimental setup for the propagation of axial waves in finite canonical waveguides: a three-cell* F_3 *rod is longitudinally excited through a shaker while the accelerations of the end surfaces are recorded via the miniaturized accelerometers shown in the insets.*

The fabricated structures were mounted on a V20 SignalForce shaker (Data Physics), connected with a PA100E power amplifier (Data Physics) and a USB 4431 DAQ (National Instruments). A DC uniform white noise signal was generated through a LabVIEW script to excite the canonical waveguide. Two 352C22 miniaturised uniaxial accelerometers (PCB Piezotronics) were installed at the sample edges and interfaced with the DAQ to measure the acceleration. From the recorded accelerometer signals, the magnitude, phase and coherence were calculated. The transmissibility was obtained as:

$$T_r = 20\log_{10}(\frac{a_r}{a_l}) \tag{4.44}$$

where a_r and a_l represent the magnitude of the acceleration of the excited and free ends of the specimen, respectively. The experimental setup is reported in Figure 4.18 (b).

Figure 4.19 shows the measured transmissibility T_r of four finite canonical waveguides in excellent agreement with analytical predictions for both the natural frequencies and the regions where wave propagation is significantly attenuated. Three configurations, namely, three-cell F_2 (a), three-cell

F_3 (c), and two-cell F_5 (d), present a phase length of 70mm and their dynamic spectra, plotted over the first period, result symmetric with respect to the canonical frequency ω_c. The three-cell F_2^l canonical rod (b), designed with a 140mm phase length, shows the periodic response of the frequency spectrum with a period $2\omega_c^l$ and the symmetry of the graph of T_r with respect to the first two canonical frequencies ω_c^l and $3\omega_c^l$. It should be noted that $\omega_c = 2\omega_c^l$ as the length of each phase for F_2; F_3, and F_5 is half of that of F_2^l. On each plot, the stop bands characterizing the infinite periodic waveguides are shown as shaded areas, thus well approximating the regions of negligible wave propagation even for a small number of cells $\mathcal{N}$. Exceptions are represented by limited extension stop bands, Figure 4.19 (d), which can be detected only with a greater number of unit cells. Finally, the mismatch between the measured and predicted response at high frequencies for F_5 is attributed to the large number of interfaces and the viscoelastic behavior of the constituent material, also testified by the decrease in the height of the spikes as the frequency increases.

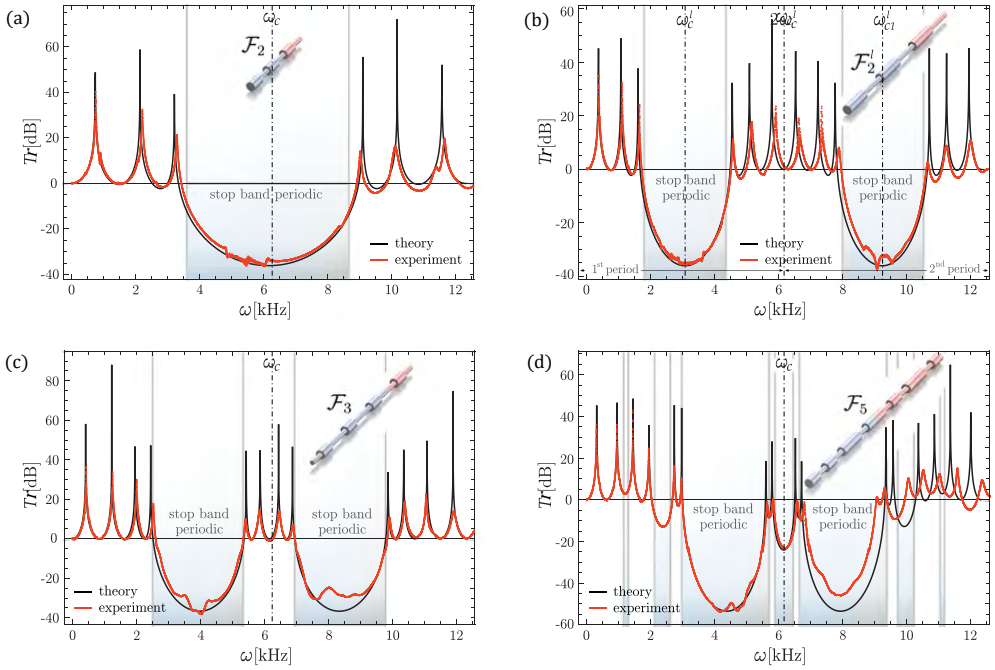

Figure 4.19. Comparison between experimental measurements (red line) and analytical predictions (black line) for the transmissibility Tr of finite canonical waveguides. The response of (a) three-cell F_2, (b) three-cell F_2^l, (c) three-cell F_3 and (d) two-cell F_5 configurations for $C = 1$ is reported as a function of the frequency ω_c. The stop bands characterizing the infinite periodic waveguides are represented by the underlaid shaded areas. The insets show the geometry of the finite rods, where the red assemblies represent the elementary cells F_i.

4.5 Periodic Orbits on Kohmoto's Manifold

Other periodic orbits exist on Kohmoto's manifold is addition to those involving saddle points, which are already shown in the Section 4.2 associated with Kohmoto's invariant $I = 0$. Thus, the

expression for Kohmoto's invariant (4.27) should be investigated. It could be rewritten in here for introducing the variables $\xi_X = \sqrt{\rho_X/E_X}\omega l_X$, $X \in (L, S)$:

$$I(\omega) = (\beta^2 - 4)\sin^2(\xi_L)\sin^2(\xi_S) \tag{4.45}$$

If impedance mismatch is $\beta = 2$, the quasicrystalline rods must be similar to homogenous waveguide because x_2 is:

$$x_2 = 2\cos(\xi_L)\cos(\xi_S) - 2\sin(\xi_L)\sin(\xi_S) = 2\cos(\xi_L + \xi_S)$$

Thus, the absolute value of x_2 cannot be larger than 2 and wave can propagate with any frequency. In addition, with trace iterations expression (4.29), the trace $|x_i| \leq 2$ with any Fibonacci order i can be obtained under condition $\beta = 2$. Therefore, in bandgap structure with $\beta > 2$, only one or all of two terms $\sin(\xi_L)$ or $\sin(\xi_S)$ are zero to let $I = 0$.

4.5.1 Initial three dynamic traces of periodic orbits

According to the properties of the trigonometric function, the solution of equation (4.45) can be written:

$$\xi_S = \bar{S}\pi \text{ or } \xi_L = \bar{L}\pi \ (\bar{S}, \bar{L}) \in \mathbb{N} \tag{4.46}$$

According to the definition of canonical ratio, C and variable ξ_S and ξ_L:

$$C = \frac{\xi_S}{\xi_L}$$

From canonical family no. one ratio (4.4) $C^{(1)} = (1 + 2j)/(1 + 2k)$ and trace period in Table 4.1, variable ξ_L and ξ_S are increased from 0 to $2(1 + 2k)\pi$ and $2(1 + 2j)\pi$, respectively. Thus, two conclusions are achieved. (1): If $\xi_S = \bar{S}\pi$, the initial three traces would become:

$$x_0 = (-1)^{\bar{S}}2,\ x_1 = 2\cos\left(\frac{\bar{S}\pi}{C^{(1)}}\right),\ x_2 = (-1)^{\bar{S}}2\cos\left(\frac{\bar{S}\pi}{C^{(1)}}\right);\ \bar{S} = 0, 1 \ldots 2(1 + 2j) \tag{4.47}$$

(2): If $\xi_L = \bar{L}\pi$, the initial three traces would become:

$$x_0 = 2\cos(\bar{L}\pi C^{(1)}),\ x_1 = (-1)^{\bar{L}}2,\ x_2 = (-1)^{\bar{L}}2\cos(\bar{L}\pi C^{(1)});\ \bar{L} = 0, 1 \ldots 2(1 + 2k) \tag{4.48}$$

Expressions (4.47) and (4.48) demonstrate that the solution for Kohmoto's invariant $I = 0$ is also periodic orbits except for saddle points in family no. one. If equations (4.46) are substituted into

canonical ratio for family no. two and three, the initial three traces would keep the same, but except $\bar{L} = q\pi$ and $\bar{S} = q\pi$ for family no. two and three, the values also changed $\bar{L} = 0, 1...4q$ and $\bar{S} = 0, 1...4q$, respectively. Moreover, the relative locations between frequency associated with $I = 0$ and trace period w_t are:

$$\frac{\bar{S}}{2(1+2j)};\ \frac{\bar{S}}{4q} \text{ and } \frac{\bar{L}}{2(1+2k)};\ \frac{\bar{L}}{4q} \tag{4.49}$$

For instance, the canonical structure associated with ratio $C^{(3)} = 2/5$ ($q = 1$, $k = 2$), in terms of theory (4.49), the periodic points are $\bar{S} = 0, 2, 4 \Rightarrow 0/4, 2/4, 4/4$ associated with fixed points, 3-periodic points, fixed points ($\bar{S} = 1, 3$ corresponding to canonical frequencies). In addition, $\bar{L} = 0, 1, 2, 3, 4, 5, 6, 7, 8, 9, 10$ and $0/10$, $5/10$ and $10/10$ are associated with fixed, 3-periodic and fixed point. $1/10$, $4/10$, $6/10$ and $9/10$ are associated with 30-periodic points. $2/10$, $3/10$, $7/10$ and $8/10$ are associated with 10-periodic points. Thus, any periodic orbits concerning Kohmoto's invariant $I = 0$ locate in one canonical period determined by equation (4.49).

In terms of powerful symbolic calculation tool, the general term formula for any Fibonacci order i with periodic orbits on Kohmoto's manifold can be obtained, which are (mod is modulo operation function):

$$x_i = 2(-1)^{(\mathrm{mod}(i,3)+1)\bar{S}}\cos\left(\frac{\tilde{n}_i\bar{S}\pi}{C}\right);\ \bar{S} = 0, 1...2(1+2j) \text{ or } 0, 1...4q \tag{4.50}$$

$$x_i = 2(-1)^{(\mathrm{mod}(i+1,3)+1)\bar{L}}\cos\left(\tilde{n}_{i-1}\bar{L}C\pi\right);\ \bar{L} = 0, 1...2(1+2k) \text{ or } 0, 1...4q \tag{4.51}$$

However, only using equations (4.50) and (4.51) cannot predict the number of iterations (or number of periodic points), which should be a topic of future investigations.

4.5.2 The reason why the scaling factor is the square root of the maximum eigenvalue

According to numerical results in Section 4.2, only fixed and 3-periodic points are associated with scaled factor which is approximating to square root of the maximum eigenvalue $\sqrt{\vartheta_1^+} = \phi$ and $\sqrt{\vartheta_3^+} = \phi^3$. This subsection will explain why.

Reconsider equation (4.30), we decompose it by Taylor series and retained first linear order term at frequency ω_{Ri}. As a result, the following expression can be obtained:

$$\delta\mathbf{r}_i = R_{iA*}(\omega_{A*}) - R_i(\omega_{Ri}) \approx \mathbf{D}_i(\omega_{Ri})d(\omega_{Ri})(\omega_{A*} - \omega_{Ri}) \tag{4.52}$$

where $R_{iA*}(\omega_{A*})$ is perturbation point on Kohmoto's manifold with frequency ω_{A*} and $R_i(\omega_{Ri})$ is one of periodic points with frequency at ω_{Ri}. According to multivariables first order derivatives, the $\mathbf{D}_i$ matrix is composed of Jacobian (2.32) and d vector are initial three variables taking differential to frequency ω as follows:

$$\mathbf{D}_i(\omega_{Ri}) = \begin{bmatrix} \frac{\partial \tilde{x}_i}{\partial \tilde{x}_{i-1}} & \frac{\partial \tilde{x}_i}{\partial \tilde{y}_{i-1}} & \frac{\partial \tilde{x}_i}{\partial \tilde{z}_{i-1}} \\ \frac{\partial \tilde{y}_i}{\partial \tilde{x}_{i-1}} & \frac{\partial \tilde{y}_i}{\partial \tilde{y}_{i-1}} & \frac{\partial \tilde{y}_i}{\partial \tilde{z}_{i-1}} \\ \frac{\partial \tilde{z}_i}{\partial \tilde{x}_{i-1}} & \frac{\partial \tilde{z}_i}{\partial \tilde{y}_{i-1}} & \frac{\partial \tilde{z}_i}{\partial \tilde{z}_{i-1}} \end{bmatrix} \cdots \begin{bmatrix} \frac{\partial \tilde{x}_1}{\partial \tilde{x}_0} & \frac{\partial \tilde{x}_1}{\partial \tilde{y}_0} & \frac{\partial \tilde{x}_1}{\partial \tilde{z}_0} \\ \frac{\partial \tilde{y}_1}{\partial \tilde{x}_0} & \frac{\partial \tilde{y}_1}{\partial \tilde{y}_0} & \frac{\partial \tilde{y}_1}{\partial \tilde{z}_0} \\ \frac{\partial \tilde{z}_1}{\partial \tilde{x}_0} & \frac{\partial \tilde{z}_1}{\partial \tilde{y}_0} & \frac{\partial \tilde{z}_1}{\partial \tilde{z}_0} \end{bmatrix} \Bigg|_{\omega=\omega_{Ri}} ; \; d(\omega_{Ri}) = \begin{bmatrix} \frac{\partial \tilde{x}_0}{\partial \omega} \\ \frac{\partial \tilde{y}_0}{\partial \omega} \\ \frac{\partial \tilde{z}_0}{\partial \omega} \end{bmatrix} \Bigg|_{\omega=\omega_{Ri}} \tag{4.53}$$

In fact, vector $\mathbf{D}_i d$ is the explicit expression for function D in equation (4.38). The determinant of matrix $\mathbf{D}_i$ cannot be zero, which has already been proved before (conserved map), where three terms in $d(\omega_{Ri})$ are:

$$\frac{\partial \tilde{x}_0}{\partial \omega} = -(2l_L\sqrt{\frac{\rho_L}{E_L}} + \beta l_S\sqrt{\frac{\rho_S}{E_S}})\cos(\xi_S)\sin(\xi_L) - (2l_S\sqrt{\frac{\rho_S}{E_S}} + \beta l_L\sqrt{\frac{\rho_L}{E_L}})\cos(\xi_L)\sin(\xi_S)$$

$$\frac{\partial \tilde{y}_0}{\partial \omega} = -2l_L\sqrt{\frac{\rho_L}{E_L}}\sin(\xi_L); \; \frac{\partial \tilde{z}_0}{\partial \omega} = -2l_S\sqrt{\frac{\rho_S}{E_S}}\sin(\xi_S) \tag{4.54}$$

By substituting $\omega = \omega_t$ or $\omega = \omega_t/2$ ($\omega_t = 2\frac{\pi\sqrt{E_S}}{l_S\sqrt{\rho_S}}(1+2j) = 2\frac{\pi\sqrt{E_L}}{l_L\sqrt{\rho_L}}(1+2k)$ (family no. one, we can also use ω_t in family no. two or three)) into ξ_L and ξ_S then all three terms in $d(\omega)$ are vanish. It is indicated that the first-order Taylor series are zero. Thus, the Taylor series must be expanded in the second order for this approximation analysis. The expression (4.52) becomes:

$$\delta\mathbf{r}_i = R_{iA*}(\omega_{A*}) - R_i(\omega_{Ri}) \approx \mathbf{G}_i(\omega_{Ri})\frac{(\omega_{A*} - \omega_{Ri})^2}{2} \tag{4.55}$$

where vector $\mathbf{G}_i$ is the counterpart of $\mathbf{D}_i d$ but with second-order derivatives corresponding to the frequency. Combined with expression (4.40):

$$\mathbf{G}_i(\tilde{\omega}_A - \omega_{R_i})^2 = \vartheta^+\mathbf{G}_i(\omega_{A*} - \omega_{R_i})^2 \tag{4.56}$$

That is the reason for scaling factor at $\omega = \omega_t$ or $\omega = \omega_t/2$ which is square root of the maximum eigenvalue $\sqrt{\vartheta^+}$. Other periodic points cannot lead all terms in vector d to null, because in fact the ξ_L and ξ_S cannot be an integer multiple for π simultaneously except at frequency ω_t or $\omega_t/2$.

4.6 Conclusion and Remarks

The effects of axial wave propagation into quasicrystalline generated canonical rods have been investigated in detail. With the definition of canonical ratio and value of initial three dynamic traces $x_{0,1,2}$, the relationships between coefficients in canonical ratio C, which must be rational number, and canonical frequencies ω_c established for all three families. The numerical results for traces $x_{0,1,2}$ with dimensionless frequency $\sqrt{\rho_L/E_L}\omega l_L = \xi_L$ proved the theoretical analysis. Several examples show that two canonical frequency $\omega_{cj} = \omega_{cj}$ in family no. one, $\omega_{cj} = \omega_{cq}$ in family no. two and $\omega_{ck} = \omega_{cq}$ in family no. three. The periodicity for canonical frequency and Kohmoto's invariant are analysed, which is half of the period for traces. Finally, a compact Table for the formula of three canonical families is given.

The passband layouts, dynamic traces and Kohmoto's manifold have been analysed theoretically in one canonical period ω_t. The three plots are symmetric and periodic according to the canonical configuration in all three families. In addition, the different periodic orbits with the associated number of the cycles are shown in the associated Figures. The scaling effects in the length of bandgap (family no. one) and passbands (family no. two and three or other periodic orbits) have been studied in detail with good agreements of approach supplied by Morini and Gei (2018) in several numerical results. Even there are significant mismatches between the ratio of length and scaling factor, the result is good enough with increasing of Fibonacci order i. These effects exist in canonical frequencies (saddle points) and frequency for other periodic points. The scaled passband and trace are symmetric about the frequency with the positive maximum eigenvalue ϑ^+ and are not symmetric as the maximum eigenvalue ϑ^+ is negative one which means the increasing perturbation direction is the opposite comparing with initial direction.

The most special cases are frequency at period ω_t and half $\omega_t/2$. The scaling factor is not the maximum eigenvalue but the square root of it. According to the principle of linear approximation, the coefficient of the Taylor series first-order term becoming null is found. Thus, if this approximation approach is used, the Taylor series must be expanded into second order and then theory meet numerical results. In addition, the initial three traces for periodic orbits are also investigated in detail except for saddle points. The frequency at periodic orbits and location in one period ω_t have been obtained. Moreover, the general formula for traces x_i are solved associated with periodic orbits in any Fibonacci order i.

In principle, the canonical configuration takes advantage of the periodic properties of the trigonometric function, cosine and sine, leading to periodic trace and dispersion layouts, which is the

particular solution of these systems. This is first time to show how the canonical configuration on rods to influence the effects for dispersion layout. In addition, the scaling effects concern periodic points are investigated in both positive, negative or square roots of eigenvalue comparing with previous research works.

A new mechanics methodology concerning one-dimensional quasicrystalline rods generated by Fibonacci GM sequence can be obtained from the results and investigations from this chapter. In addition, a necessary guideline for their possible exploitation in the design of novel construction metamaterials whose bandgap and passband topology can be easily modulated and controlled according to canonical ratio and scaling factor can be provided.

For design dispersion spectrum in quasicrystalline-generated rods is following steps:
(1): The frequency at bandgap can be computed by canonical frequency $\omega_{cj} = \frac{\pi\sqrt{E_S}}{2l_S\sqrt{\rho_S}}(1+2j)(1+2m) = \frac{\pi\sqrt{E_L}}{2l_L\sqrt{\rho_L}}(1+2k)(1+2m) = \omega_{ck}$ as structure belongs familiy no .1 at Fibonacci order F_2, F_5, F_8 (F_{2+3n}, $n \in \mathbb{N}$). Thus, engineer can design this system to forbidden desire frequency wave $\omega = \omega_c$.
(2): The bandgap length at Fibonacci order F_2, F_5, F_8 (F_{2+3n}, $n \in \mathbb{N}$) can be predicted by scaling technique with scaling factor ϑ^+ by using $\omega_{A*} - \omega_{B*} = \frac{\widetilde{\omega}_A - \widetilde{\omega}_B}{\vartheta^+}$ ($\omega_{A*} - \omega_{B*}$ assuming as bandgap length for F_i, $\omega_{A*} - \omega_{B*}$ is bandgap length for F_{i+6}) or with scaling factor λ^+ by using $\omega_{A*} - \omega_{B*} = \frac{\widetilde{\omega}_{A'} - \widetilde{\omega}_{B'}}{\lambda^+}$ ($\widetilde{\omega}_{A'} - \widetilde{\omega}_{B'}$ assuming as bandgap length for F_i, $\omega_{A*} - \omega_{B*}$ is bandgap length for F_{i+3}). Therefore, engineer can design a structure with very narrow bandgap at desire frequency.

Chapter 5 - Wave Propagation in Quasicrystalline and Canonical Laminates

The fundamental principles of pure negative refraction when SH waves propagate into a quasicrystalline generated laminate are presented in this Chapter. It means that only one real solution K_y of the $K_x L_i = \arccos(trM_i(f, K_y)/2)$ exists in this system and demonstrates the incoming wave frequency should satisfy some conditions in Section 5.1. According to Morini et al. (2019), the transition zones govern the number of several real solutions. Then, the concept of canonical configuration in Chapter 4 can be also applied to laminates to obtain periodic passband layouts in Section 5.2. The effects of impedance mismatch and canonical ratio to negative refraction are investigated. Moreover, in terms of the linear approximation approach, the edge frequency of the transition zone is predicted to a certain extent in Section 5.3. Through boundary line on the representation of the universal torus, several extreme values for edge frequency of transition zones are obtained with the closed-form expression in Section 5.4. In addition, when Kohmoto's invariant vanishes, a particular pair of longitudinal wavenumber and frequency can be taken into consideration, so that the components of the acoustic Poynting vector and the transmission angle can be simplified. It is fascinating that the transmission wave angle does not depend on frequency under this condition, which rises to an 'inverse problem' in Section 5.5. Finally, the number of reflected modes can be deeply understood with the more precise equation. The pure negative refraction with enough transmission energy is investigated for engineering application in Section 5.6.

5.1 The Condition of Pure Negative Refraction

SH wave transmission across the interface between a homogenous elastic substrate and a periodic laminate as shown in Figure 5.1 is a coupled problem. On the one hand, the possible number of real transmitted modes depends on the frequency of the incoming wave and the dynamic properties of laminates $trM_i(f, K_y = 0)$. On the other hand, the function $\cos(K_x L_i)$ depends on the substrate, frequency and angle of incidence θ^{inc} in terms of expression (2.57) with some changes:

$$K_x L_i = K_0 \sin(\theta^{\text{inc}}) L_i = 2\pi f / c_0 \sin(\theta^{\text{inc}}) L_i \tag{5.1}$$

where c_0 is wave phase speed of substrate $\sqrt{\mu_0/\rho_0}$. It demonstrates that as the trace of transfer matrix M_i has been already known, the quantity K_y should be solved from expression (3.7) ($2\cos(K_x L_i) = trM_i(K_y, f)$) using Newton method as introduced in Chapter 3. Numerous academics in the past have examined this issue by plotting the real solutions of the dispersion relation

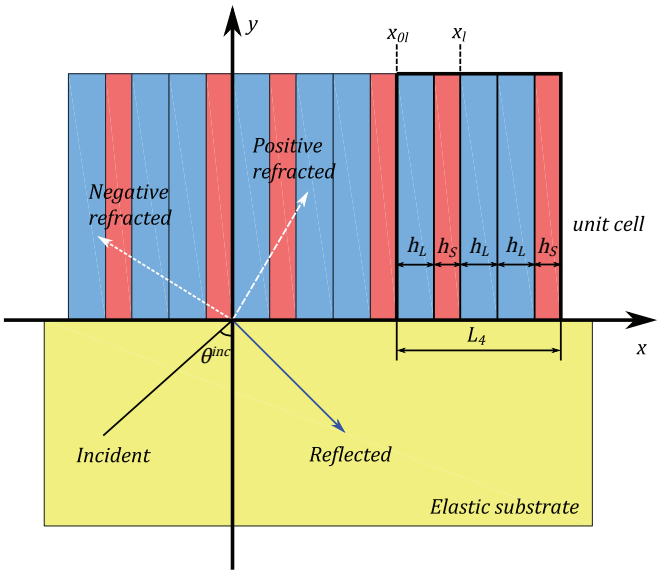

Figure 5.1. Substrate-periodic laminate system where the represented unit cell of the laminate is F_4. Coordinate x_{0l} is the left-hand boundary of the generic cell whereas x_l is the left-hand boundary of a generic layer.

with $K_x L_i$ versus $K_y L_i$, as seen in Figure 5.2 (Nemat-Nasser 2015; Srivastava 2016; Willis 2016; Srivastava and Willis 2017; Morini et al. 2019a).

The plots in Figure 5.2 are for the laminate which combines PMMA (polymethyl methacrylate) which is material L with shear modulus $\mu_L = 3$GPa, density per volume $\rho_L = 1180$kg/m^3 and thickness $h_L = 3$mm and steel which is material S with $\mu_S = 80$GPa, $\rho_S = 8000$kg/m^3 and $h_S = 1.3$mm. This analysis allows us to understand how to achieve pure negative refraction in quasicrystalline-generated GM periodic laminates in F_2. In addition, the trace of transfer matrix x_2 is sketched to show the limit frequency (edge frequency) for the number of transmission wave modes (transition zone).

Particularly, the frequency range corresponding to the second Brillouin zone, such as $\pi < \mathrm{Re}(K_x L_i) < 2\pi$, is examined. As the incoming wave frequency is less than 93.24 kHz (grey line in Figure 5.2(a)), there may be either no or one solution in terms of $K_x L_i$. One solution is confirmed for frequencies between $f = 93.24$ and 261.34 kHz and there may be one or two actual solutions for frequencies between $f = 261.34$ and 296.63 kHz; if frequency is $f > 296.63$ kHz, there must be two real solutions. In Figure 5.2 (c), the trace is shown and color-coded to correspond to frequencies of 93.24 kHz, 261.34 kHz, and 296.63 kHz.

The transmission angle in laminates is determined by the two components of the Poynting vector $\mathcal{P}_x$ and $\mathcal{P}_y$, which have the same direction of the group velocity v_x^g and v_y^g, respectively. In Figure 5.2 (a), it is straightforward to determine that the true solution lies in the first Brillouin zone, the

group velocity v_x^g and v_y^g, are both positive. On the other hand, the true solution in the second Brillouin zone and v_x^g is negative, but v_y^g is positive, then the transmission wave angle is negative, which is the desired result. In Figure 5.2 (b), it is evident that both positive and negative refraction waves coexist (beam splitting). Therefore, pure negative refraction is only conceivable up to a well-defined frequency ($f = 296.63$ kHz in this example) for the task at hand; otherwise, many waves are transmitted and the uniqueness is lost.

According to the definition introduced by Morini et al. (2019a), the two intervals $[0, 93.24]$kHz and $[261.34, 296.63]$kHz are transition zones for the laminates F_2, where the number of real solutions of the dispersion equation depends on the frequency with increasing of unity as frequency reaching the upper limit of the zone (from 0 to 1 in the former interval, from 1 to 2 in the latter). If a frequency is not located in a transition zone, the number of solutions must be fixed at $K_x L_i$ or $K_y L_i$. It goes without saying that a threshold $\bar{K}_x L_i$ does exist for each frequency belonging to a transition zone and the number of possible transmission modes depends on the comparison between $K_x L_i = K_0 \sin(\theta^{\text{inc}}) L_i$ and $\bar{K}_x L_i$ (in dimensionless form, of course L_i is irrelevant).

As $\bar{K}_x L_i$ values are read from the abscissa of the graph, where $K_y = 0$, the limits of the transition zone can be derived from the analysis of the uniaxial problem in which the SH wave propagates orthogonally to the laminates, a condition mathematically governed by function $x_i(f, 0)$ in equation $2\cos(\bar{K}_x L_i)) = x_i(f, 0)$. In the particular case of the laminate F_2, the function $x_2(f, 0)$ is depicted in Figure 5.2 (c), from which it is easy to draw the following conclusion: since the transition zone coincides with the passband, its boundaries may be computed with relative ease. These three locations restrict the first two passbands and correspond to 93.24kHz, 261.34kHz, and 296.63kHz, respectively. From Morini et al (2019a), these three frequencies are $f_i^{1\text{st}}$ (upper boundary of the first transition zone), $f_i^{1\text{bg}}$ (upper boundary of the first bandgap), and $\tilde{f}_i$ (upper boundary of the second passband).

Thus, pure negative refraction can be obtained if the normalised wavenumber of the incident wave $K_x L_i$ enters the second Brillouin zone. The minimum frequency for wavenumber $K_x L_i \geq \pi$ (if $f = f_i^{\min}$, $K_x L_i = \pi$):

$$f_i^{\min} = c_0/(2L_i) \tag{5.2}$$

Therefore, the conditions that must be simultaneously fulfilled to achieve pure negative refraction are:

(1): the frequency f of incoming wave should satisfy $f_i^{\min} < f < \tilde{f}_i$;

(2): if $f < f_i^{1\text{st}}$, $K_0 \sin(\theta^{\text{inc}}) L_i > 2\pi - \bar{K}_x L_i$; if $f_i^{1\text{st}} \leq f \leq f_i^{1\text{bg}}$, $K_x L_i > \pi$ should be satisfied; if

$f_i^{1bg} < f < \tilde{f}_i$, it still should be $K_x L_i > 2\pi - \bar{K}_x L_i$.

From Figure 5.2, it can be deduced that entire reflection also occurs only in $f < f_i^{1st}$ and if $2\pi - \bar{K}_x L_i > K_x L_i > \bar{K}_x L_i$. It indicates that there is no real solution K_y, simply an evanescent wave. Due to the absence of energy in evanescent waves (which is discussed later), all incident energy is now converted into reflected energy.

As the number of transmitted modes across the interface depends on the comparison between $K_x L_i$ and $\bar{K}_x L_i$, the former is determined by the frequency, wave speed in the substrate, angle of incident and total length of the cell. The latter is determined by function $x_i(f, 0)$; Thus, the propagation of waves orthogonally to the laminates should be investigated further.

5.2 Canonical Laminate: Configurations and Properties

5.2.1 Transfer matrix corresponding to $K_y = 0$ and canonical configuration

In this subsection, the transfer matrix for SH wave propagating orthogonal to the expected direction of interfaces ($K_y = 0$) along with the quasicrystalline generated laminates is investigated to extend the concept of canonical configuration and associated canonical frequency proposed in Chapter 4 in axial wave propagation in periodic standard Fibonacci GM rods to the current type of microstructure.

We recalling wave governing equation (2.40) and transfer matrix (2.44) below:

$$\mu\left(\frac{\partial^2 u_z}{\partial x^2} + \frac{\partial^2 u_z}{\partial y^2}\right) = \rho\frac{\partial^2 u_z}{\partial t^2} \tag{5.3}$$

$$\begin{bmatrix}\sigma_{xz}(x)\\ u_z(x)\end{bmatrix} = \begin{bmatrix}\cos(q_X(x-x_l)) & -\mu_X q_X \sin(q_X(x-x_l))\\ \frac{\sin(q_X(x-x_l))}{\mu_X q_X} & \cos(q_X(x-x_l))\end{bmatrix}\begin{bmatrix}\sigma_{xz}(x_l)\\ u_z(x_l)\end{bmatrix} \tag{5.4}$$

If $K_y = 0$, it means wave field should eliminate $y-$component in equation (5.3) and becomes:

$$\mu\frac{\partial^2 u_z}{\partial x^2} = \rho\frac{\partial^2 u_z}{\partial t^2} \tag{5.5}$$

The elementary transfer matrix is obtained by just substituting $K_y = 0$ into matrix (5.4). The properties of traces from the global transfer matrix x_i are satisfied the recursive rule in rod problem:

$$x_{i+1} = x_{i-1}x_i - x_{i-2},\ (i \geq 2) \tag{5.6}$$

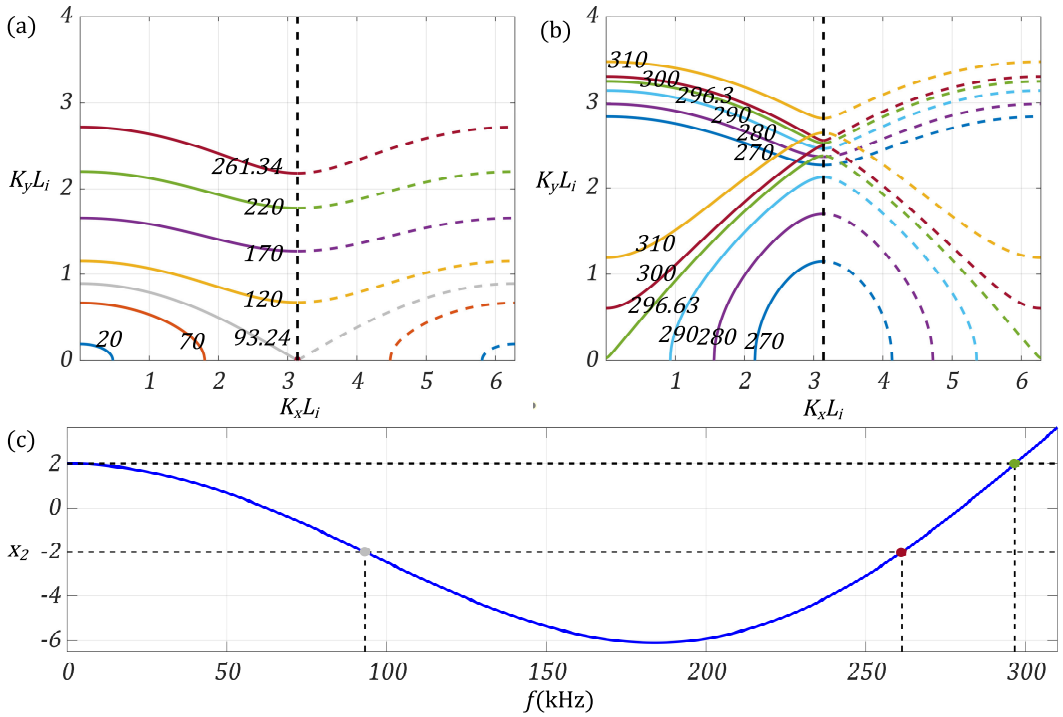

Figure 5.2. Plots of K_xL_2 versus K_yL_2 at several fixed frequencies with the trace of the transfer matrix. (a) For the number of transmission modes 0 or 1. Frequency range ($f = 20-261.34kHz$); (b) For the number of transmission mode 1 or 2, frequency range $f = 270 - 296.63kHz$. (c) The situation for the trace of transfer matrix with $K_y = 0$. The grey point corresponds to the upper edge of the first passband, red to the first bandgap and green to the second passband.

where the initial three traces are:

$$t_0 = 2\cos(2\pi f h_S/c_S), \quad t_1 = 2\cos(2\pi f h_L/c_L),$$

$$t_2 = 2\cos(2\pi f h_S/c_S)\cos(2\pi f h_L/c_L) - \beta\sin(2\pi f h_S/c_S)\sin(2\pi f h_L/c_L) \tag{5.7}$$

where β in here is still the impedance mismatch ($\beta = (\mu_S c_L)/(\mu_L c_S) + (\mu_L c_S)/(\mu_S c_L)$). The Kohmoto's invariant is a function of frequency:

$$I(f) = \tilde{x}_i^2 + \tilde{y}_i^2 + \tilde{z}_i^2 - \tilde{x}_i\tilde{y}_i\tilde{z}_i - 4 = (\beta^2 - 4)\sin^2(2\pi f h_L/c_L)\sin^2(2\pi f h_S/c_S) \tag{5.8}$$

which is independent of Fibonacci order i. According to what we derived in Chapter 4, in the 3D space described by the orthogonal cartesian system $O\tilde{x}\tilde{y}\tilde{z}$. $I(f)$ is the surface or manifold. Points $R_i = (\tilde{x}_i, \tilde{y}_i, \tilde{z}_i)$ is a triplet whose entries are traces of three consecutive GM orders like before and $p-$point periodic orbits or non-periodic orbits on Kohmoto's manifold. Thus, the concept of canonical configuration in a laminate is similar to the situation in a rod with the initial three traces condition:

$$x_0 = x_1 = 0;\ x_0 = x_2 = 0;\ x_1 = x_2 = 0 \tag{5.9}$$

The material and geometric characteristics of quasicrystalline and frequency should be based on the same criterion as before for the initial three traces, with three established family ratios:

$$C^{(1)} = \frac{1+2j}{1+2k};\ C^{(2)} = \frac{1+2j}{2q};\ C^{(3)} = \frac{2q}{1+2k}\ (j,k,q \in \mathbb{N}) \tag{5.10}$$

where $C = (c_L h_S)/(c_L h_S)$ is the canonical ratio. The frequency f in this problem is engineering frequency $f = \omega/2\pi$. The canonical frequencies for each family can be written as $f_{cn}^{(r)} = f_c^{(r)}(1+2n)$, $(n \in \mathbb{N})$ (r represents which family is associated), where:

$$f_c^{(1)} = \frac{c_L}{4h_L}(1+2k) = \frac{c_S}{4h_S}(1+2j), \quad f_c^{(2)} = \frac{c_L}{4h_L}2q = \frac{c_S}{4h_S}(1+2j),$$

$$f_c^{(3)} = \frac{c_L}{4h_L}(1+2k) = \frac{c_S}{4h_S}2q. \tag{5.11}$$

The requirements (5.9) and (5.10) compel the traces x_i of canonical laminates to be periodic and symmetric with respect to their canonical frequency, resulting in periodic bandgap and passband layouts. As the features of traces, the period of both the frequency spectra and the invariant $I(f)$ is $2f_c$, whereas the period of periodic traces is $4f_c$. Figure 5.3 depicts examples of the different sequences of passbands (transition zone) and bandgaps for F_0 to F_8 assuming different materials

L and S (mentioned in the caption). For simplicity, $C^{(1)} = 1$ (Family No. 1) in all graphs with total thickness for $L_2 = 0.0043$m; Consequently, h_L and h_S rely on the canonical ratio and phase speed in the two materials. For example, $h_L \approx 0.0014$ m and $h_S \approx 0.0029$ m from Table 5.1 for the combination of PMMA (L) and steel (S).

Table 5.1. Properties of the materials adopted in the case studies.

	Steel	Iron	Copper	Aluminium	Nylon	PMMA	Polyethylene
μ (GPa)	80	52.5	44.7	26	4	3	0.117
ρ (kg/m^3)	8000	7860	8940	2700	1150	1180	930

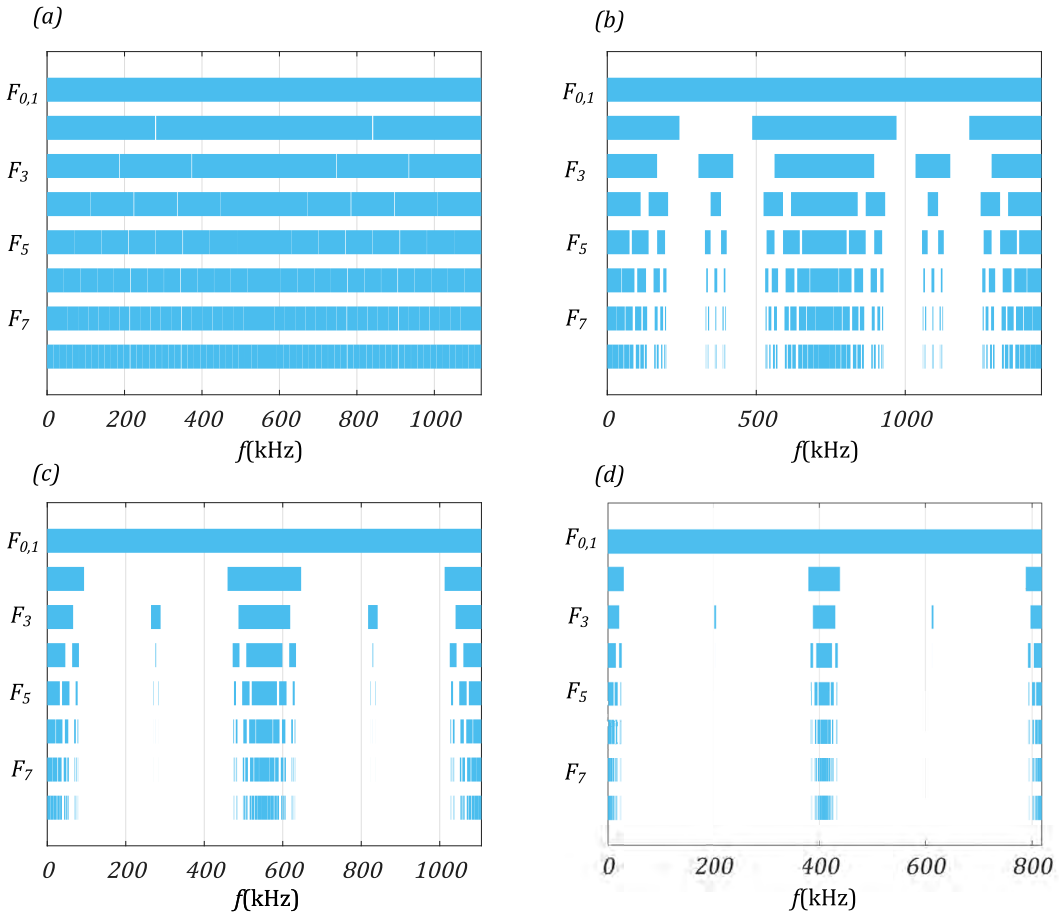

Figure 5.3. Bandgap and Passband (transition zone) layout for canonical Fibonacci laminates F_0 to F_8 with four different impedance mismatches and same ratio $C^{(1)} = 1$ in one canonical traces period $4f_c$. (a) Material L: iron, material S: copper, $\beta = 2.0002$; (b) L: steel, S: aluminium, $\beta = 3.351$; (c) L: PMMA, S: steel, $\beta = 13.520$; (d) L: steel, S: polyethylene, $\beta = 76.706$.

The domain illustrated is $f \in [0, 4f_c]$ for all possible combinations. There are two axes of symmetry corresponding to canonical frequencies at $1/4$ and $3/4$ in the domain, which have been explained in Chapter 4. Clearly, the impedance mismatch β affects the density of bandgaps: if $\beta = 2$, the laminate behaves as a homogeneous waveguide and the whole frequency range is in a passband, as shown in Figure 5.3 (a), since β is extremely near to 2. These outcomes are compara-

ble to those obtained by analysing bandgap density using the representation of the universal torus (Morini et al. 2019b). The bandgap density is directly proportional to the mismatch impedance value. Other traits can also be discovered, as discussed in the next section. Finally, it is important to note that comparable considerations will be offered for other families' canonical ratios.

The Figure 5.3 have same implication with dispersion layout in Chapter 4 for rods problem. We put it here again for easy to check the effect from mismatch impedance to effect of pure negative refraction. Therefore, aims should be to focus on the first two passbands at relatively low frequencies, as these correspond with the first two transition zones for the periodic laminates.

5.2.2 Scaling of traces (transition zone) at low frequencies

Similar to the quasicrystalline generated rods problem, the transition zone, bandgap, and traces for the global transfer matrix of Fibonacci quasicrystalline laminates have scaling effects. The effects of negative refraction are governed by the second transition zone's upper edge frequency (also passband). The fixed point whose Kohmoto's invariant with frequency $f = 0$kHz, scaling factor is the golden ratio $\phi_g = (\sqrt{5}+1)/2$, corresponds to the closest periodic orbit with the second and first upper edge of the transition zone. Figure 5.4 depicts the scenario for a canonical structure $C = 1/5$ with the materials L: PMMA and S: steel, since it is close to the ratio derived from the thicknesses $h_L = 3$mm and $h_S = 1.3$mm. The traces $x_6(f)$ with scaled traces $x_5(f/\phi_g)$, $x_7(\phi_g f)$, and $x_8(\phi_g^2 f)$ are compared and the scaled trace and transition zone layouts are nearly identical. When $x_i \approx -2$, the theory captures the upper limit of the first passband (i.e., frequency $f_i^{1\text{st}}$) and the lower limit of the second passband (i.e., frequency $f_i^{1\text{bg}}$) quite well. A little poorer match is produced for the top limit of the second passband (i.e., frequency $\tilde{f}_i$), but this can be well explained by the fact that the relevant frequencies are very away from the origin and the scaling is significantly more effective at relatively high index i. In portions (b) and (d) of the same figure, the first two passbands for each traces shown beside are depicted together with red marks showing a forecast of their limits produced by scaling up or down the precise values for F_6. (black markers). Again, the two graphs illustrate that scaling is an excellent method for controlling the width of the first two passbands. From the perspective of the laminate as an elastic device, a quantitative calculation of the scaling of the self-similar pattern of transition zone at low frequencies may aid in selecting the index of the elementary cell most suited to produce pure negative refraction when connected to an isotropic substrate.

Furthermore, due to the existence of periodic orbits in transition zone layouts that are previously inferred in Chapter 4, the number of transmission modes can be accurately predicted in compari-

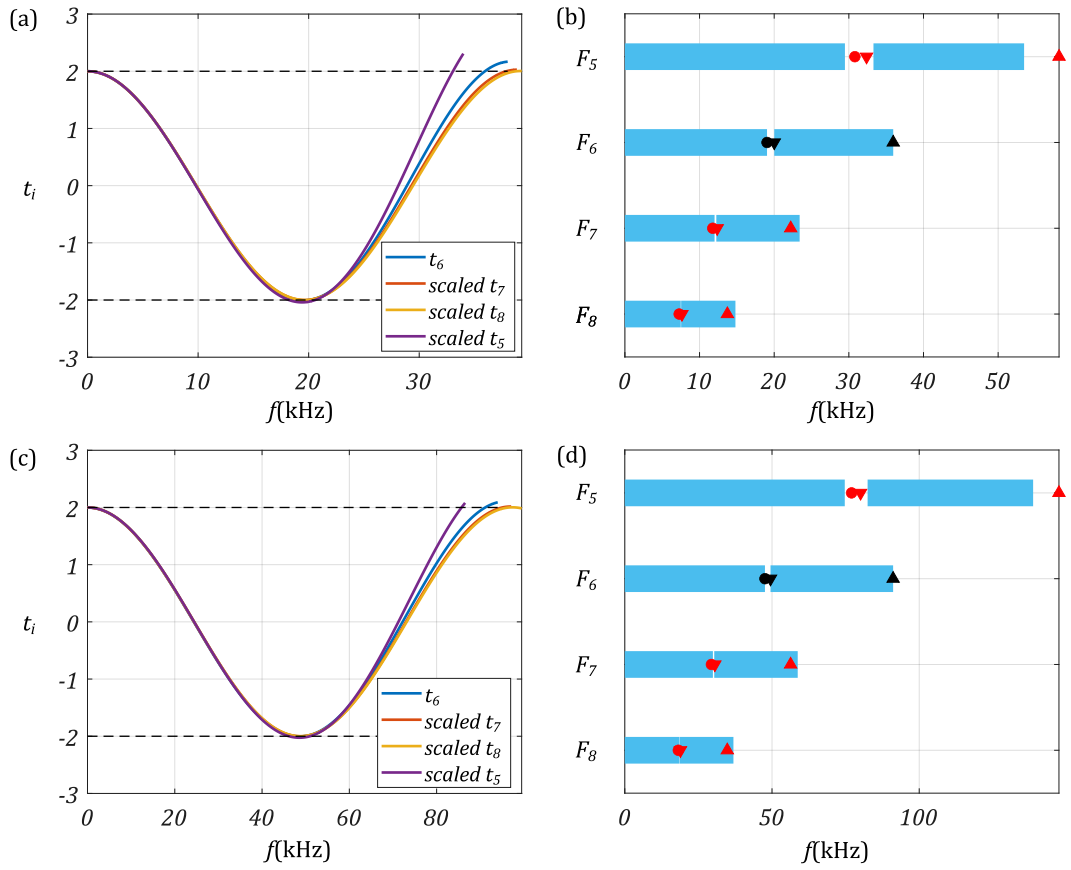

Figure 5.4. Scaling of trace at low frequencies in the vicinity of $f = 0$. Plot of traces for (a) $C = 1/5$, $\beta = 13.520$ and (c) $C = 1$, $\beta = 3.351$; in both plots, the adopted scaling factor is ϕ_g. (b) and (d) Plot of the first two passbands with prediction of their limits by red markers obtained using the scaling factor ϕ_g starting from the exact limits of the passbands for x_6 (black markers)

son to non-canonical ones. Therefore, if the number of transition zones at one canonical frequency is identified, the number of transmission modes at any frequency must be determined. In addition, $\bar{K}_x L_i$'s value can be anticipated. For instance, the periodic orbits at canonical frequency are denoted as six-periodic points with two of three traces are zero and other is $\pm\beta$ or ± 2. $\bar{K}_x L_i = \pi/2$ as trace equals to 0, and $\bar{K}_x L_i = 0$ and π if the absolute value of traces $|(trM_i)| \geq 2$, respectively. Therefore, if the frequency at periodic orbits (including orbits except saddle points) and the position for $\bar{K}_x L_i$ is determined, the incidence angle and substrate can be modified for wave transmission in laminates with a known number of transmission modes.

5.2.3 The effects from swapping material for phases L and S

The concept of canonical configuration influences the whole spectra, but only the initial two pass-bands are useful for pure negative refraction. Canonical frequency might be utilised as a tool to determine the possibility of having pure negative refraction. Using different materials L and S with the same canonical ratio to increase the $\tilde{f}_i$ with a fixed L_2, the canonical frequency may be utilised as a criteria to evaluate the frequency changes with varying impedance mismatch.

From the initial three traces (5.7) and Figure 5.3, an increase in the impedance mismatch β favours the occurrence of bandgaps over passbands. As the periodic and symmetric features of traces, the number of transition zones inside the interval $[0, f_c]$ for the same canonical ratio and is independent of β, or the two materials that make up the elementary cell, which is related to the dispersion relation mathematical principle. Consequently, the ratios between each of the three frequencies and the canonical frequency ($f_i^{1\text{st}}/f_c$, $f_i^{1\text{bg}}/f_c$ and $\tilde{f}_i/f_c$) may be used to evaluate the effects of β on the edge of the first two transition zones. In this regard, Figure 5.5 depicts the pertinent plots for $C^{(1)} = 1$, which can be shown that as the β increases, $f_i^{1\text{st}}$ and $\tilde{f}_i$ drop monotonically in relation to f_c; In contrast, $f^{1\text{bg}}/f_c$ grows for F_2 and F_3, reaching $2f_c$ and f_c in the limit of infinite impedance, but the ratio decreases for higher sequence indices, respectively. Similar phenomena occur when $\tilde{f}_3/f_c$ reaches the value 1 for $\beta \to \infty$ for F_3. In addition, due to the existence of the transition point frequency $f = 2f_c$ in F_2, $\tilde{f}_2/f_c$ is always 2 under $C = 1$. In addition, what if phases L and S are

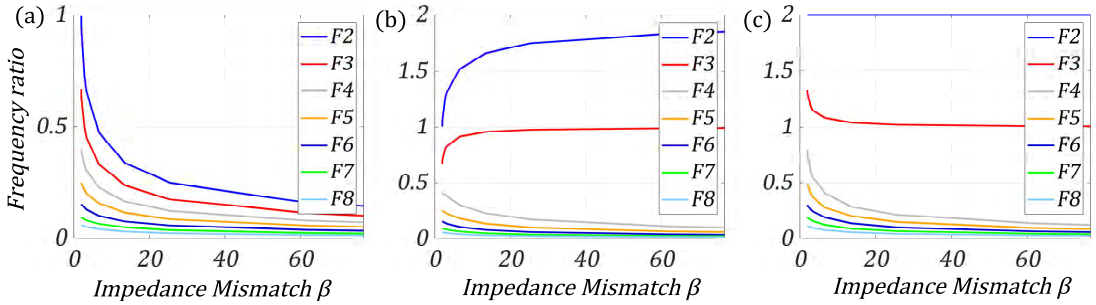

Figure 5.5. Plot of frequency ratio (a) f_i^{1st}/f_c; (b) f_i^{1bg}/f_c; (c) $\tilde{f}_i/f_c$ as a function of impedance mismatch β with canonical ratio $C^{(1)} = 1$

swapped? Since the immutability of β, the dispersion spectra take the same form with different frequency range. In canonical structure, all three edge frequencies occupy the same percentage in the canonical frequency with the same C and β (h_L and h_S are connected with C). Therefore, the different canonical frequencies are compared for this problem. For $f_i^{\min} = c_0/(2L_i)$ (Morini et al. 2019a), where c_0 is the wave speed in the substrate, which cannot vary, while L_i is the entire length of the cell, can change as a result of material variation (only L_2 is fixed). Thus, $L_i f_c$ should be explored to determine the maximum value for $L_i\tilde{f}_i$ that governs the possibility of pure negative

refraction.

The total length of cell is $L_i = n_i^{(L)} h_L + n_i^{(S)} h_S$ and the h_S can be solved from canonical ratio (5.10), yielding $h_S = C(c_S)/(c_L)h_L$. Thus, the $L_i f_c$ should be obtained within three families of canonical laminates as follows:

$$L_i f_c^{(1)} = (c_L(1+2k)n_i^{(L)} + c_S(1+2j)n_i^{(S)})/4,$$

$$L_i f_c^{(2)} = (c_L 2q n_i^{(L)} + c_S(1+2j)n_i^{(S)})/4,$$

$$L_i f_c^{(3)} = (c_L(1+2k)n_i^{(L)} + c_S 2q n_i^{(S)})/4 \tag{5.12}$$

Thus, the two materials should be chosen to maximise the value derived from expression (5.12), for example, $L_3 f_3^{1\text{st}}$, $L_3 f_3^{1\text{bg}}$ and $L_3 \tilde{f_3}$ are greater for the combination (L: steel, S: PMMA) than the opposite combination (L: PMMA, S: steel) with the same canonical ratio. Consequently, the canonical frequency can be used as a criteria to determine the effect of impedance mismatch and swapping of the two-phase material on possibility for pure negative refraction. It is more practical than non-canonical laminates, which lacks a periodic spectrum.

5.3 Prediction of All Three Edge Frequencies by Linear Approximation

From the findings above, the three edge frequencies $f_i^{1\text{st}}$, $f_i^{1\text{bg}}$ and $\tilde{f_i}$ are significant as $\tilde{f_i}$ governs the possibility of pure negative refraction and the first two frequencies modify the condition for the phenomenon to occur. All three frequencies can be easily predicted using a linear approximation for sequences F_2 and F_3 (note that F_3 can be seen as a special case of F_2 with $h_{3L} = 2h_{2L}$, therefore $C_{F_3} = C_{F_2}/2$).

This method comes from the initial three dynamic traces (5.7) and trace x_2 can be differentiated with respect to the frequency f:

$$\frac{dt_2}{df} = -2\pi((2\frac{h_L}{c_L} + \beta\frac{h_S}{c_S})\sin(\frac{h_L}{c_L}2\pi f)\cos(\frac{h_S}{c_S}2\pi f) + (2\frac{h_S}{c_S} + \beta\frac{h_L}{c_L})\sin(\frac{h_S}{c_S}2\pi f)\cos(\frac{h_L}{c_L}2\pi f)). \tag{5.13}$$

Equation (5.13) is relatively complex, but it is composed of trigonometric functions. If those functions can be evaluated at certain frequencies for which they are assumed values either of 0 or ± 1, the equation must be simplified, and then this slope can be used to predict all three

frequencies. Because the canonical frequency is usually larger than the upper edge for the second transition zone ($f_c > \tilde{f}_i$), other frequencies at periodic orbits are used for linear approximation.

Chapter 4 has shown that other frequencies exist rather than canonical ones at which periodic orbits are taken place, for instance when $h_L/c_L 2\pi f = \bar{L}\pi$ or $h_S/c_S 2\pi f = \bar{S}\pi$, ($\bar{L}, \bar{S} \in \mathbb{R}^+$). Only $\bar{L} = 1$ or $\bar{S} = 1$ can be selected, $f_L = c_L/(2h_L)$ or $f_S = c_S/(2h_S)$, respectively. In this configuration, the lowest frequency between f_L and f_S is lower than $\tilde{f}_i$. It is easy to distinguish among them: if $C > 1$ ($C < 1$), f_S (f_L) is the lowest. Because of this condition, the initial three traces and $\frac{dx_2}{df}$ can be simplified. For $f_L = c_L/(2h_L)$ ($C < 1$):

$$x_0 = 2\cos(C\pi), \quad x_1 = -2, \quad x_2 = -2\cos(C\pi), \quad \frac{dx_2}{df}(f_L) = 2\pi(2\frac{h_S}{c_S} + \beta\frac{h_L}{c_L})\sin(C\pi). \quad (5.14)$$

Alternatively, $f_S = c_S/(2h_S)$ ($C > 1$):

$$x_0 = -2, \quad x_1 = 2\cos(\pi/C), \quad x_2 = -2\cos(\pi/C), \quad \frac{dx_2}{df}(f_S) = 2\pi(2\frac{h_L}{c_L} + \beta\frac{h_S}{c_S})\sin(\pi/C). \quad (5.15)$$

In both cases, trace x_2 is inside a passband ($-2 < x_2 < 2$). The slope at this frequency is obtained by $\frac{dx_2}{df}$. Then two edge frequencies f_2^{1bg} and $\tilde{f}_2$ can be estimated via the linear approximations:

$$f_2^{1bg} \approx f - \frac{2 + x_2}{\frac{dx_2}{df}}, \quad \tilde{f}_2 \approx f + \frac{2 - x_2}{\frac{dx_2}{df}}. \quad (5.16)$$

According to equation (5.16), the $x_2 \approx 2$ as $C\pi \approx \pi$ for f_L or $\frac{\pi}{C} \approx \pi$ for f_S are depending which frequency is chosen. In this condition, the $\tilde{f}_2$ is approximated better than f_2^{1bg} due to $x_2 = 2$ associates with $\tilde{f}_2$. On the contrary f_2^{1bg} is better. Here are 6 examples with different canonical ratio to show approximation results with material L PMMA and S steel, fixed the total length $L_2 = 4.3$mm as depicted in Figure 5.6. For easy to show the results, the half canonical periodic which means $f_t/2 = 2f_c$, are plotted.

The results perfectly satisfy the condition above. Only one of f_2^{1bg} or $\tilde{f}_2$ can be approximated better. However, if the canonical ratio is $C = 2$ ($C = 1/2$ also), the linear approximation should be perfect fitted with both f_2^{1bg} and $\tilde{f}_2$, due to the f_L (f_S) is canonical frequency currently and the trace for $x_2 = 0$.

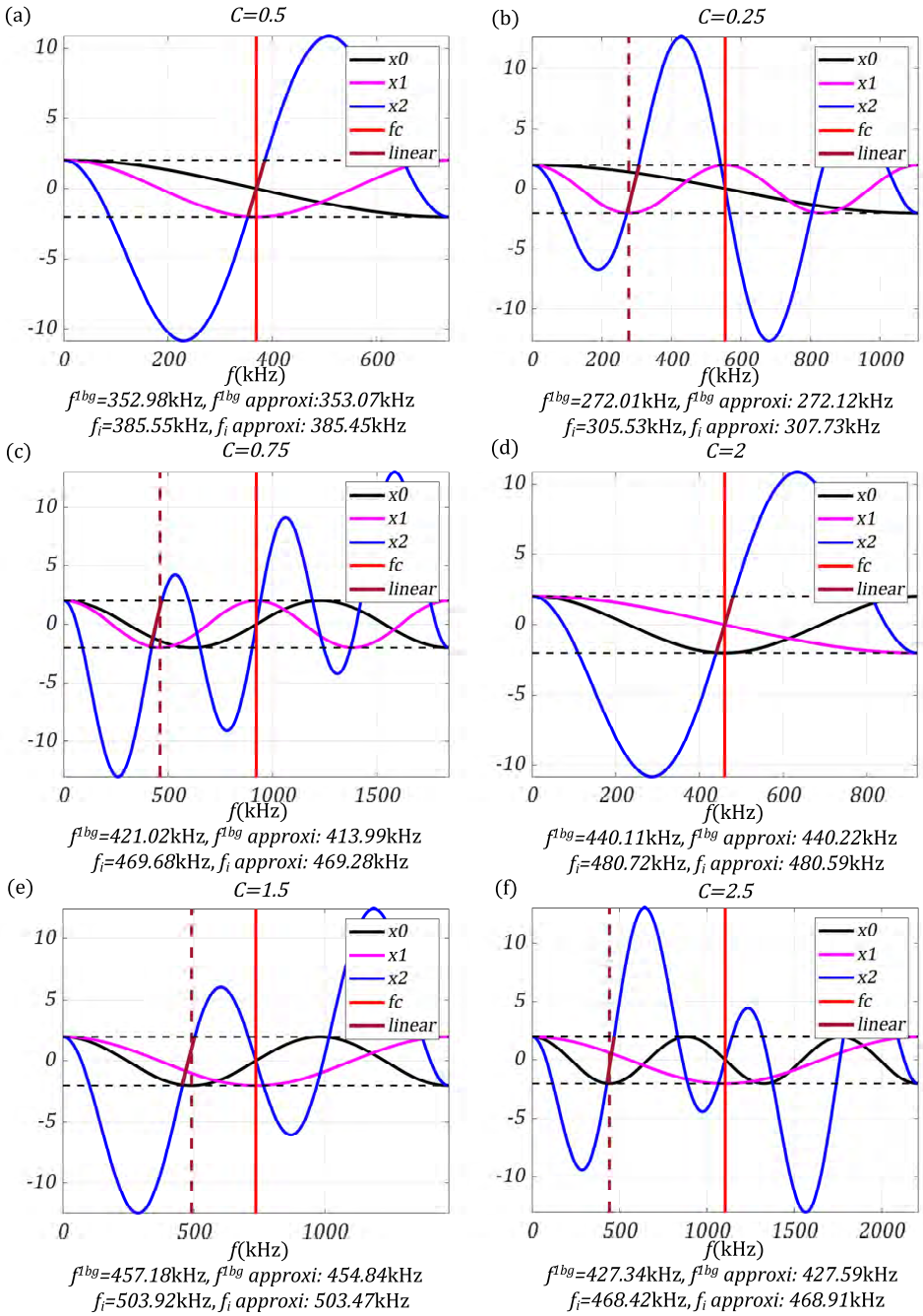

Figure 5.6. Half canonical periodic with linear approximation in different canonical ratio. (a). $C = 0.5$. (b). $C = 0.25$. (c). $C = 0.75$. (d). $C = 2$. (e). $C = 1.5$. (f). $C = 2.5$.

Moreover, the f_2^{1st} can also be predicted using linear approximation. In this condition, the $h_L/c_L 2\pi f$ or $h_S/c_S 2\pi f = \pi/2$ should be used with the smallest one chosen the same with before between $f_L = c_L/(4h_L)$ and $f_S = c_S/(4h_S)$. In this configuration, the approach to distinguish the smallest one is still by canonical ratio C. Then, the initial three traces are simplified and then derivative trace x_2. For $f_L = c_L/(4h_L)$ ($C < 1$):

$$x_0 = 2\cos(\frac{\pi}{2}C); x_1 = 0; x_2 = -\beta\sin(\frac{\pi}{2}C);$$

$$\frac{dx_2}{df}(f_L) = -2\pi(2\frac{h_L}{c_L} + \beta\frac{h_S}{c_S})\cos(\frac{\pi}{2}C); \tag{5.17}$$

or $f_S = c_S/(4h_S)$ ($C > 1$):

$$x_0 = 0; x_1 = 2\cos(\frac{\pi}{2C}); x_2 = -\beta\sin(\frac{\pi}{2C});$$

$$\frac{dt_2}{df}(f_S) = -2\pi(2\frac{h_S}{c_S} + \beta\frac{h_L}{c_L})\cos(\frac{\pi}{2C}); \tag{5.18}$$

With the same procedure, the linear approximation can be made to predict the f_2^{1st}:

$$f_2^{1st} \approx f + \frac{-2 - x_2}{\frac{dx_2}{df}} \tag{5.19}$$

If the x_2 is approached -2, the linear approximation would work better. Comparing with equations (5.17) and (5.18). the value for x_2 depends on β and the canonical ratio C. If impedance mismatch is low (β close to 2), C should be close to 1 for a better prediction. On the contrary, if β is large, C should be remarkably different than unity (in other words: $C >> 1$ or $C << 1$) for a reliable prediction.

In Figure 5.7, six examples are displayed. The three different two-phase materials are chosen, (1). material L PMMA, S steel ($\beta \approx 13.5202$); (2) material L Iron, S copper ($\beta \approx 2.0002$); (3) material L steel, S polyethylene ($\beta \approx 76.7060$) with total length of cell $L_2 = 4.3$ mm. For ease of representation, the frequency range are $2f_L$ or $2f_S$. For the same two phases material combination, the canonical ratios in two plots are inverse of each other, for instance, $1/8.5 \approx 0.118$ as shown in Figure 5.7 (a) and (b). It is also very interesting that for inverse canonical ratio, the dynamic trace F_2 does not change and x_0 and x_1 are substituting into each other ($x_0 \rightarrow x_1$ and $x_1 \rightarrow x_0$) in different frequency range. This conclusion is beneficial for the topological interface state in the next chapter.

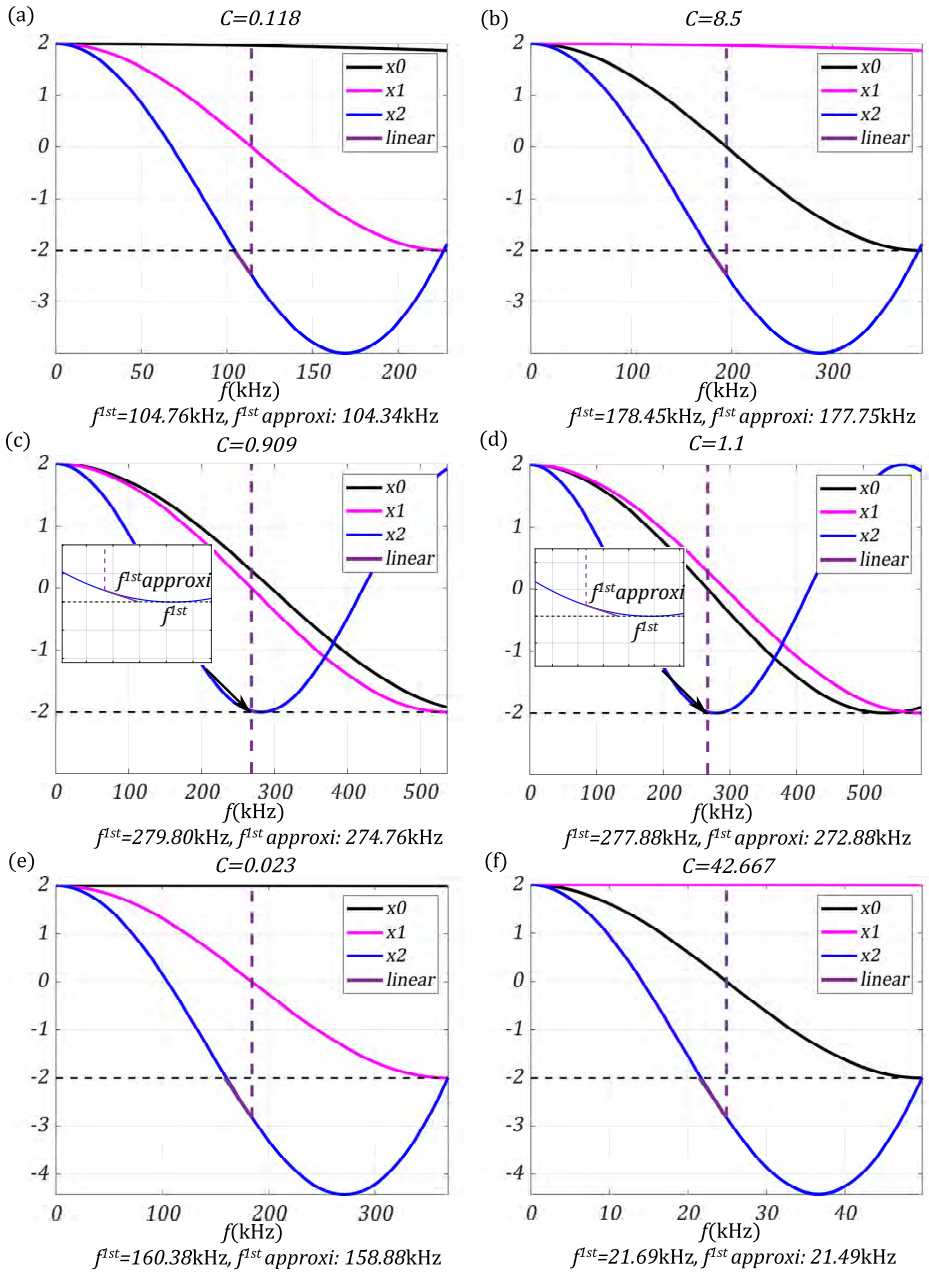

Figure 5.7. Linear approximation for f_2^{1st} in different canonical ratio with different material combination. (a). L PMMA and S steel ($\beta \approx 13.5202$) with $C = 0.118$. (b). L PMMA and S steel ($\beta \approx 13.5202$) with $C = 8.5$. (c). L Iron and S copper ($\beta \approx 2.0002$) with $C = 0.909$. (d). L Iron and S copper ($\beta \approx 2.0002$) with $C = 1.1$. (e). L steel and S polyethylene ($\beta \approx 76.7060$) $C = 0.023$. (f). L steel and S polyethylene ($\beta \approx 76.7060$) $C = 42.667$.

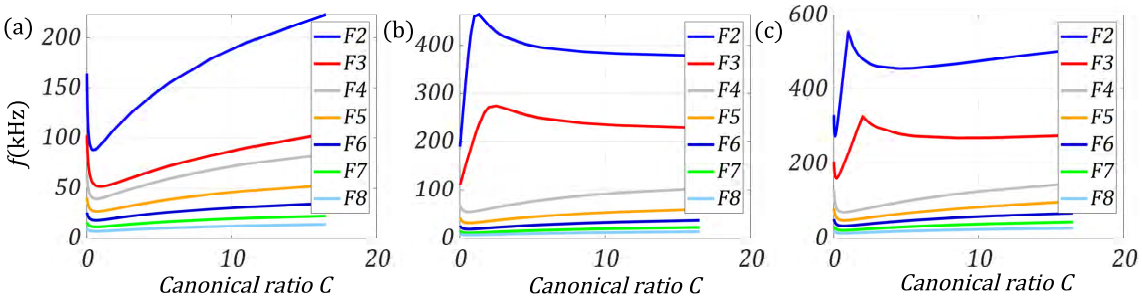

Figure 5.8. Variation of upper edge within fixed total length of cell L_i with L PMMA S Steel. (a) first transition zone. (b) first bandgap. (c). second transition zone.

Therefore, the linear approximation method and results for f_2^{1st}, f_2^{1bg} and $\tilde{f}_2$ are obtained. If the canonical ratio are $C = 2$ or $C = 1/2$, then both f_2^{1bg} and $\tilde{f}_2$ can be predicted with good accuracy. Otherwise, only one of them can be predicted well with different C range. Moreover, the better approximation for f_2^{1st} depends on impedance mismatch β and canonical ratio C. If $\beta >> 2$, better prediction with the $C \approx 1$ can be obtained. If $\beta \approx 2$, better prediction with the $C << 1$ or $C >> 1$ can be obtained.

5.4 Optimisation of the Three Frequencies Using Universal Torus

The theory reported in Section 5.1 recognizes that the three frequencies f^{1st}, f^{1bg} and $\tilde{f}$ play an important role in defining the possibility of pure negative refraction in the substrate-laminate problem. Based on the notion of canonical laminate, our goal is now to investigate how we can exploit the ratio C in order to maximize (or minimize), with the same phases L and S, the values of f^{1st}, f^{1bg} and $\tilde{f}$.

It is not hard to find that the following limits exist:

$$\lim_{C\to\infty} f_i^{1st} = \lim_{C\to\infty} f_i^{1bg} = c_S/(2L_i),\ \lim_{C\to\infty} \tilde{f}_i = c_S/L_i$$

$$\lim_{C\to 0} f_i^{1st} = \lim_{C\to 0} f_i^{1bg} = c_L/(2L_i),\ \lim_{C\to 0} \tilde{f}_i = c_L/L_i$$

To this end, we propose an analysis to reveal what is the influence of C for cells with the same two phases and maintaining the length L_i fixed when analysing the same cell. We study the combination L: PMMA, S: steel, and vary the thickness ratio h_L/h_S (recall canonical ratio). In particular, we assume preliminarily $h_L = 3$mm and $h_S = 1.3$mm, and calculate the length $L_i = n_i^L h_L + n_i^S h_S$; then the thicknesses of the two phases are varied to scan all possible values of C as shown in Figure 5.8. In the plots of Figure 5.8, the three quantities f^{1st}, f^{1bg} and $\tilde{f}$ are reported for cells F_2 to F_8 as a function of canonical ratio C. It is evident that, for the adopted phases, in all functions, there

exists at least one stationary point; in addition, cusps exist for frequency $\tilde{f}$ in the graphs for both F_2 and F_3. The knowledge of the values of C at which maxima/minima occur would be very helpful for design purposes. To accomplish the goal, we take advantage of the universal representation of the frequency spectrum proposed for elastic waveguides in Chapter 3, and effective to represent in a compact fashion pass and stop bands.

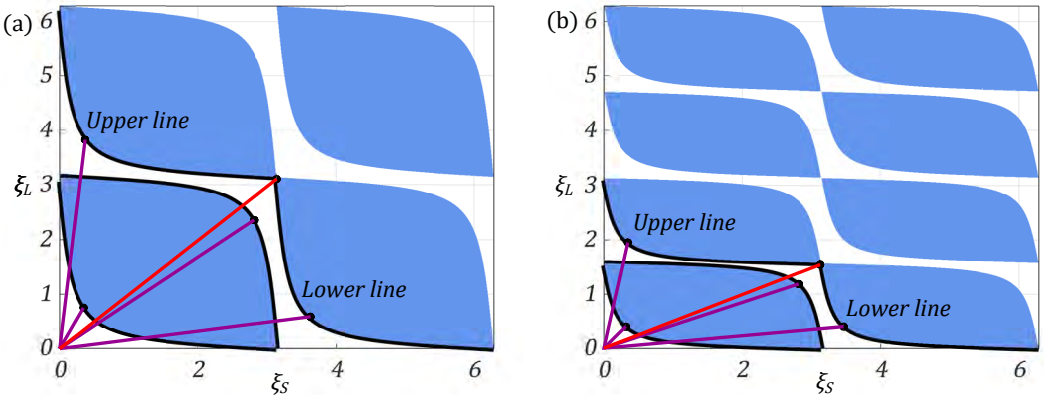

Figure 5.9. Torus for (a) F_2 and (b) F_3. The black lines are boundary lines. The red line is the corresponding flow line pass through the transitional point. The purple lines correspond to local extreme points except for transitional points

In Figure 5.9, the cases F_2 and F_3 are reported. It is interesting to note that along the two cartesian axes, a pass band is always met except in a set of isolated points placed at regular intervals where either $|t_i(\xi_S, 0)| = 2$ or $|t_i(0, \xi_L)| = 2$ $(i \geq 2)$. At the upper limit of the first pass band, the boundary lines for F_2 and F_3 that is the one which corresponds to $f_i^{1\text{st}}$ have equations:

$$F_2 : \xi_L = 2\arctan\left(\frac{\Gamma^-}{\tan(\xi_S/2)}\right);\ F_3 : \xi_L = \arctan\left(\frac{\Gamma^-}{\tan(\xi_S/2)}\right)$$

where $\Gamma^{\pm}$:

$$\Gamma^{\pm} = \beta/2 \pm \sqrt{(\beta/2)^2 - 1}$$

The boundary lines for F_2 and F_3 associated with $f^{1\text{bg}}$ are represented by the same equations, but with Γ^+ in place of Γ^-:

$$F_2 : \xi_L = 2\arctan\left(\frac{\Gamma^+}{\tan(\xi_S/2)}\right);\ F_3 : \xi_L = \arctan\left(\frac{\Gamma^+}{\tan(\xi_S/2)}\right)$$

The union of the two lines is the boundary of the first pass-band (blue) region encountered by a flow line at low frequencies. The boundary line which sets the upper limit of the second transition zone is composed of two branches whose parametric equations are:

$$F_2 : \xi_L = 2\arctan\left(\frac{\Gamma^-}{\tan\left(\frac{\xi_S}{2}\right)}\right) + \pi,\ \xi_L = 2\arctan\left(\frac{\Gamma^+}{\tan\left(\frac{\xi_S}{2}\right)}\right) + \pi$$

$$F_3 : \xi_L = \arctan\left(\frac{\Gamma^-}{\tan\left(\frac{\xi_S}{2}\right)}\right) + \frac{\pi}{2},\ \xi_L = \arctan\left(\frac{\Gamma^+}{\tan\left(\frac{\xi_S}{2}\right)}\right) + \frac{\pi}{2}$$

They are represented in Figure 5.9 (a) and (b) by the black curves bounding from below the two blue domains encountered by a flow line satisfying $2\pi > \max\{\xi_L, \xi_S\} > \pi$ for F_2, $2\pi > \max\{\xi_S\} > \pi$ and $\pi > \max\{\xi_L\}$ for F_3. As length of laminate cell L_i is fixed, then the frequency expression could be obtained in terms of ξ_L and ξ_S, respectively:

$$f = \xi_L \frac{(n_i^{(L)} c_L + n_i^{(S)} c_S C)}{2\pi L_i};\ f = \xi_S \frac{(n_i^{(L)} c_L / C + n_i^{(S)} c_S)}{2\pi L_i} \tag{5.20}$$

First, the extreme value for $f_i^{1\text{st}}$ is studied. The rest $f_i^{1\text{bg}}$ and $\tilde{f}_i$ are analysed in same way. Because of the right hand side term in equation (5.20), the point (ξ_L, ξ_S) must be on the boundary line for the reason $f_i^{1\text{st}}$ is the boundary point. Thus, the $C = \xi_S/\xi_L$:

$$1/C = \frac{2}{\xi_S}\arctan\left(\frac{\Gamma^-}{\tan\left(\frac{\xi_S}{2}\right)}\right) \tag{5.21}$$

By substituting equation (5.21) into (5.20) and $n_2^{(L)} = 1,\ n_2^{(S)} = 1$. The following expression is obtained:

$$f_2^{1\text{st}} = \xi_S \frac{(c_L \frac{2}{\xi_S}\arctan\left(\frac{\Gamma^-}{\tan\left(\frac{\xi_S}{2}\right)}\right) + c_S)}{2\pi L_2} \tag{5.22}$$

Then, the equation (5.22) can be differentiated with respect to C using the chain rule, namely:

$$\frac{df_2^{1\text{st}}}{dC} = \frac{df_2^{1\text{st}}}{d\xi_S}\frac{d\xi_S}{dC} = 0$$

The term $d\xi_S/dC$ is hard to solve from equation (5.21), but it is easy to observe from Figure 5.9 that its value is negative as $C \in \mathbb{R}^+$. Thus, equation $df_2^{1\text{st}}/dC = 0$ can be replaced by $df_2^{1\text{st}}/d\xi_S = 0$ whose solution is:

$$\xi_S = 2\text{arccot}(\epsilon_1) \tag{5.23}$$

$$\epsilon_1 = \sqrt{\frac{\rho_L \rho_S (c_L - c_S \Gamma^+)^2}{(\mu_L - \mu_S)(\rho_L - \rho_S)}} \tag{5.24}$$

Then, the local minimum value for the upper edge first transition zone is:

$$f_2^{1st} = \frac{1}{2\pi L_2}(2c_S \text{arccot}(\epsilon_1) + 2c_L \arctan(\epsilon_1 \Gamma^-)) \tag{5.25}$$

Thus, the frequency at extreme value for f_2^{1st} is found. The same procedure can be performed with the Fibonacci sequence F_3:

$$f_3^{1st} = \frac{1}{2\pi L_3}(2c_S \text{arccot}(\epsilon_1) + 2c_L \arctan(\epsilon_1 \Gamma^-)) \tag{5.26}$$

Expressions (5.25) and (5.26) are very similar except total length of cell L_i, this is because the F_3 structure can be seen as special F_2 ones with double h_L so that only the general form is written in the latter. The Fibonacci order i can be 2 and 3. With the same procedure, the answer for f_i^{1bg} can be obtained:

$$f_i^{1bg} = \frac{1}{2\pi L_i}(2c_S \text{arccot}(\epsilon_2) + 2c_L \arctan(\epsilon_2 \Gamma^+)) \tag{5.27}$$

where:

$$\epsilon_2 = \sqrt{\frac{\rho_L \rho_S (c_L - c_S \Gamma^-)^2}{(\mu_L - \mu_S)(\rho_L - \rho_S)}} \tag{5.28}$$

The local maximum and minimum values for upper edge of second transition zone $\tilde{f}_i$ for F_2 and F_3 are:

$$\tilde{f}_{iu} = \frac{1}{2\pi L_i}(2c_S \text{arccot}(\epsilon_1) + c_L\,(\pi + 2\arctan(\epsilon_1 \Gamma^-))) \tag{5.29}$$

$$\tilde{f}_{il} = \frac{1}{2\pi L_i}((c_L + 2c_S)\,\pi - 2c_S \text{arccot}(\epsilon_2) - 2c_L \arctan(\epsilon_2 \Gamma^+)) \tag{5.30}$$

where u and l associate with upper boundary line and lower one, respectively, and i can be 2 and 3. These four extreme values (upper edge first transition zone and first bandgap, second transition zone) are shown in the Figure 5.9 with purple lines. The associated material ratio is obtained due to the ξ_S/ξ_L and Equation (5.21). Moreover, the intersection for two boundary lines when $C = 1$, $\tilde{f}_2 = (c_L + c_S)/(2L_2)$ and $C = 2$, $\tilde{f}_3 = (c_L + c_S)/(2L_3)$ are not shown in these explicit expressions (5.25), (5.26), (5.27), (5.29) and (5.30) (red line shown in Figure. 5.9), this is perfectly consistent as case F_3 can be traced back to that for F_2 by rearranging the unit cell between the periodic layout of layers. From the point of view of one willing to maximize the range of frequencies for which pure negative refraction may occur, the performed analysis shows that, for cell F_2, the canonical ratio C to be selected should be equal to 1, as this value maximizes f_2^{min}.

It is worth noting that a close inspection of functions ϵ_1 and ϵ_2 reveals that these expressions are only valid if either $\rho_L > \rho_S, \mu_L > \mu_S$ or $\rho_L < \rho_S, \mu_L < \mu_S$, as those are the only requirements

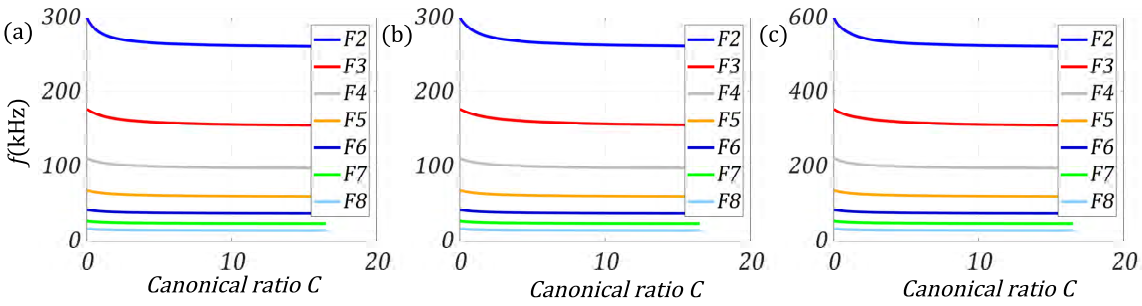

Figure 5.10. Variation of upper edge within fixed total length of cell L_i with L Iron and S Copper. (a) first transition zone. (b) first bandgap. (c). second transition zone.

which ensure that functions ϵ_1 and ϵ_2 are real. If densities and shear modules do not satisfy the given inequalities, local stationary values for the investigated frequencies do not exist as shown in Figure 5.10 (material L is Iron ($\mu_L = 52.5$GPa, $\rho_L = 7860$kg/m^3) and S Copper ($\mu_S = 44.7$GPa, $\rho_S = 8940$kg/m^3).

In addition, the smallest frequency $f_i^{\min}$ leads to dimensionless transverse wave number $K_x L_i$ entering the second Brillouin zone. It can be plotted by different Fibonacci order i with selected substrate materials comparing the Figure 5.8 and 5.11 to check whether pure negative refraction happened. The substrate material can be chosen as steel, Aluminium, copper, Iron, PMMA, Nylon, polyethylene as shown in Table 5.1

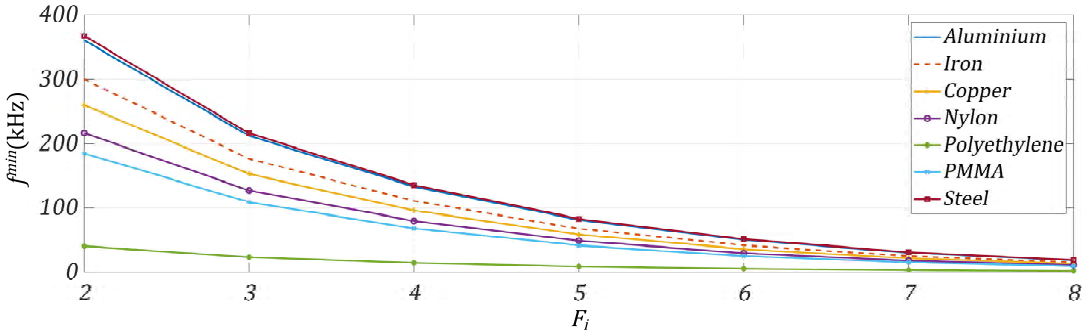

Figure 5.11. Plot of the minimum frequency f_i^{min} to enter the second Brillouin zone for different substrate-laminate systems.

5.5 Poynting Vector Simplification and Investigation on 'Inverse Problem'

5.5.1 Further simple format for two components of Poynting vector

The angle of refraction of a transmitted wave across the interface between a substrate and a transverse quasicrystalline generated laminate can be determined through the relationship (2.70) and rewritten here:

$$\tan(\theta^{\text{trans}}) = \frac{v_x^g}{v_y^g} = \frac{\langle \mathcal{P}_x \rangle}{\langle \mathcal{P}_y \rangle}. \tag{5.31}$$

where $v_x^g = (\partial\omega)/(\partial K_x)$ and $v_y^g = (\partial\omega)/(\partial K_y)$ are the components of the group velocity parallel and perpendicular to the interface, respectively, $\mathcal{P}_x$ and $\mathcal{P}_y$ are analogous to the time-averaged real part components of the Poynting vector, the brackets $\langle\rangle$ denote the space average over the unit cell F_i. According to Willis (2016), the real part of the time-averaged acoustic Poynting vector is given by the components $\mathcal{P}_j$ averaged over the unit cell given in Chapter 2 (equations (2.68) and (2.69)) and rewritten here:

$$\langle \mathcal{P}_x \rangle = \frac{1}{2}\text{Re}[\frac{1}{L_i}\int_0^{L_i} \text{i}\omega\sigma_{xz}u_z^* dx] = \frac{1}{2}\text{Re}\left[\frac{1}{L_i}\omega\int_0^{L_i}\mu(\text{i}\frac{dw}{dx}w^* + K_x w w^*)dx\right]; \tag{5.32}$$

$$\langle \mathcal{P}_y \rangle = \frac{1}{2}\text{Re}[\frac{1}{L_i}\int_0^{L_i} \text{i}\omega\sigma_{yz}u_z^* dx] = \frac{1}{2}\text{Re}\left[\frac{1}{L_i}\omega\int_0^{L_i}\mu K_y w w^* dx\right]$$

The function $w(x)$ in equations (5.32) is the mode shape defined in equation displacement field for incident wave (5.34) (for a generic mode), and corresponding to the real solution K_y of the dispersion relation of the laminate at a given K_x as introduced in Chapter 2. The displacement fields for incident, transmitted and reflected will be rewritten here for easy to recalling:

$$u_z^{\text{inc}} = Ae^{\text{i}(\omega t - K_x^{\text{inc}}x - K_0\cos(\theta^{\text{inc}})y)} \tag{5.33}$$

$$u_z^{\text{trans}} = \sum_{l=0}^{\infty} T_l w_l(x) e^{\text{i}(\omega t - K_x^{\text{trans}}x - K_y^{(l)}y)} \ (l \in \mathbb{N}) \tag{5.34}$$

$$u_z^{\text{ref}} = \sum_{m=-\infty}^{\infty} R_m U_m(x) e^{\text{i}(\omega t - K_x^{\text{ref}}x + k_y^{(m)}y)} \ (m \in \mathbb{Z}) \tag{5.35}$$

We now focus on the derivation of simplified expressions for $\langle \mathcal{P}_x \rangle$ and $\langle \mathcal{P}_y \rangle$ in order to obtain an explicit formula for $\tan(\theta^{\text{trans}})$. By using the definition of transmission matrix (5.4), in one phase, the stress σ_{xz} and displacement u_z^* can be written as:

$$\sigma_{xz}(x + x_l) = \cos(q_X x)\sigma_{xz}(x_l) - \mu_X q_X \sin(q_X x) u_z(x_l), \tag{5.36}$$

$$u_z^*(x+x_l) = \frac{\sin(q_X x)}{\mu_X q_X}\sigma_{xz}^*(x_l) + \cos(q_X x)u_z^*(x_l), \tag{5.37}$$

where x is the relative coordinate, and x_l is the coordinate of the left boundary for this phase (layers). Thus we can do an integral in one phase material (The principle for whole elementary cell integral is the sum of each phase introduced in Chapter 3):

$$\frac{1}{2}\mathrm{Re}\left[\frac{1}{L_i}\int_0^{h_X} \mathrm{i}\omega\,(\sigma_{xz}u_z^*)\,dx\right] = \frac{\omega}{2L_i}\left(\mathrm{Re}\left[\int_0^{h_X}\mathrm{i}\left(\frac{\cos(q_X x)\sin(q_X x)}{\mu_X q_X}|\sigma_{xz}^*(x_l)|^2\right)dx\right]\right.$$

$$-\mathrm{Re}\left[\int_0^{h_X}\mathrm{i}\left(\cos(q_X x)\sin(q_X x)\mu_X q_X|u_z^*(x_l)|^2\right)dx\right]+$$

$$\left.\mathrm{Re}\left[\int_0^{h_X}\mathrm{i}\left(\cos^2(q_X x)\sigma_{xz}(x_l)u_z^*(x_l)\right)dx\right] + \mathrm{Re}\left[\int_0^{h_X}\mathrm{i}\left(\sin^2(q_X x)\sigma_{xz}^*(x_l)u_z(x_l)\right)dx\right]\right) \tag{5.38}$$

If q_X is pure real, the three terms must be pure real, and if $q_X = \mathrm{i}\bar{q}_X$ is pure imaginary ($\bar{q}_X$ is pure real), three terms $\cos(q_X x)$, $q_X\sin(q_X x)$ and $\sin(q_X x)/q_X$ must be pure real also. This can be proved by Euler Formula:

$$\cos(\mathrm{i}\bar{q}_X x) = \frac{e^{-\bar{q}_X x}+e^{\bar{q}_X x}}{2};\ \mathrm{i}\bar{q}_X\sin(\mathrm{i}\bar{q}_X x) = \bar{q}_X\frac{e^{-\bar{q}_X x}-e^{\bar{q}_X x}}{2};\ \frac{\sin(\mathrm{i}\bar{q}_X x)}{\mathrm{i}\bar{q}_X} = \frac{e^{-\bar{q}_X x}-e^{\bar{q}_X x}}{-2\bar{q}_X};$$

Thus, the initial two terms in equation (5.38) are purely real, and times imaginary unit i is pure imaginary number so that real part of integral is zero. Finally, equation (5.38) becomes:

$$\frac{1}{2}\mathrm{Re}\left[\frac{1}{L_i}\int_0^{h_X}\mathrm{i}\omega\,(\sigma_{xz}u_z^*)\,dx\right] = \frac{h_X\omega}{2L_i}\mathrm{Im}[\sigma_{xz}^*(x_l)\,u_z(x_l)] \tag{5.39}$$

By observing the properties of the eigenvalue problem, it is clear that the stress displacement vector at the left-hand boundary of the cell is an eigenvector of the same problem that can be written as:

$$M_i - e^{-\mathrm{i}K_x L_i}\mathbf{E} = \begin{bmatrix} M_{11}-e^{-\mathrm{i}K_x L_i} & M_{12} \\ M_{21} & M_{22}-e^{-\mathrm{i}K_x L_i}\end{bmatrix} \Rightarrow \begin{bmatrix} \varrho \\ -\varrho\frac{M_{11}-e^{-\mathrm{i}K_x L_i}}{M_{12}}\end{bmatrix} \tag{5.40}$$

The rightmost one is the eigenvector associated with eigenvalue $e^{-\mathrm{i}K_x L_i}$ which is also initial boundary $[\sigma_{xz}(0), u_z(0)]$. The ϱ is constant value in eigenvector solution. As M_{11} and M_{12} are real numbers, this leads to $\mathrm{Im}[\sigma_{xz}^*(x_{0l})u_z(x_{0l})] = -|\varrho|2\sin(K_x L_i)/M_{12}$. Note that equation (5.4) is valid within each layer and that the four elements of each local matrix M_X are real numbers, therefore it can be shown that $\mathrm{Im}[\sigma_{xz}^*(x_{0l})u_z(x_{0l})] = \mathrm{Im}[\sigma_{xz}^*(x_l)u_z(x_l)]$ for each layer. Actually, from the expressions (5.36), (5.37) and (5.39), the material parameters do not have influence on integral

in each phase. Thus, the Poynting vector becomes:

$$\langle \mathcal{P}_x \rangle = -|\varrho|^2 \frac{\omega \sin(K_x L_i)}{2M_{12}} \tag{5.41}$$

Equation (5.41) shows that the transmission angle is null when the value of $K_x L_i$ is at the boundary of a Brillouin zone (i.e. . . . 0, π, 2π, . . .). In order to obtain an explicit expression of $\mathcal{P}_y$, the integral $\int_0^{L_i} w\mu w^* dx$ must be calculated, namely:

$$\int_0^{h_X} w\mu w^* dx = \frac{|\sigma_{xz}(x_l)|^2}{\mu_X q_X^2}\left(\frac{h_X}{2} - \frac{\sin(2q_X h_X)}{4q_X}\right) +$$

$$\sigma_{xz}^*(x_l)\, u_z(x_l) \frac{\sin^2(q_X h_X)}{2q_X^2} + \sigma_{xz}(x_l)\, u_z^*(x_l) \frac{\sin^2(q_X h_X)}{2q_X^2} + \mu_X |u_z(x_l)|^2 \left(\frac{h_X}{2} + \frac{\sin(2q_X h_X)}{4q_X}\right) \tag{5.42}$$

Equation (5.42) can be simplified under some assumptions concerning Kohmotos invariant. For $K_y \neq 0$, the invariant, that is a generalization of $I(f)$. The initial three traces with $K_y \neq 0$ are:

$$x_0 = 2\cos(q_S h_S); \quad x_1 = 2\cos(q_L h_L)$$

$$x_2 = 2\cos(q_S h_S)\cos(q_L h_L) - \left(\frac{\mu_S q_S}{\mu_L q_L} + \frac{\mu_L q_L}{\mu_S q_S}\right)\sin(q_S h_S)\sin(q_L h_L) \tag{5.43}$$

Thus, Kohmoto's invariant $I(f, K_y)$ is obtained (K_y inside I means it does not vanish):

$$I = \left(\frac{\mu_S^2 q_S^2 - \mu_L^2 q_L^2}{\mu_L q_L \mu_S q_S}\right)^2 \sin^2(q_S h_S) \sin^2(q_L h_L) \tag{5.44}$$

The case where expression (5.44) is null independently of the values of sinusoidal functions provides a special configuration of laminates for which the sought-after simplification can be achieved. In particular, this leads to $q_L \mu_L = q_S \mu_S = Z$, a real quantity, which results in the following relationship between f and K_y:

$$K_y = \kappa\omega. \tag{5.45}$$

where κ is $\sqrt{(\mu_L \rho_L - \mu_S \rho_S)/(\mu_L^2 - \mu_S^2)}$. The κ can be real positive or pure imaginary which is associated with propagation and evanescent wave. In this thesis, the propagation wave should be considered so that $\kappa > 0$. Hence, the two elementary transfer matrices are:

$$M_L = \begin{bmatrix} \cos(q_L h_L) & -Z\sin(q_L h_L) \\ \frac{\sin(q_L h_L)}{Z} & \cos(q_L h_L) \end{bmatrix}, \quad M_S = \begin{bmatrix} \cos(q_S h_S) & -Z\sin(q_S h_S) \\ \frac{\sin(q_S h_S)}{Z} & \cos(q_S h_S) \end{bmatrix}, \tag{5.46}$$

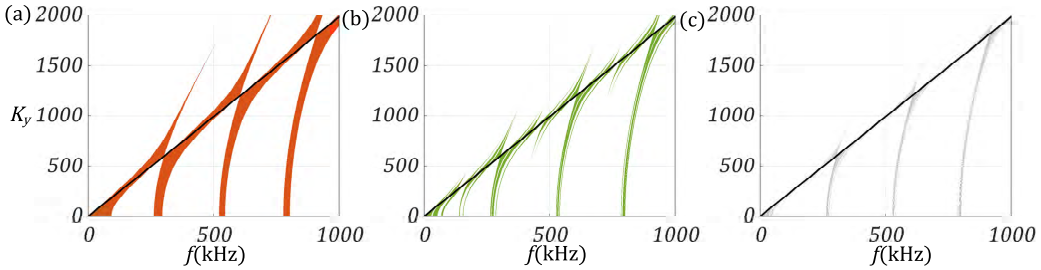

Figure 5.12. Plot of the laminate passbands with frequency f and wavenumber K_y. (a) F_2. (b) F_5. (c) F_8. The black straight line is the function of (5.45)*. The dispersion relation will be all passbands along with this line.*

Actually, equation (5.45) represents a straight line in passband layouts for laminates when considering frequency f and wavenumber K_y as shown in Figure 5.12 with Fibonacci order F_2, F_5 and F_8. Whereas the global transfer matrix M_i assumes the form:

$$M_i = \begin{bmatrix} \cos(\nu\omega L_i) & -Z\sin(\nu\omega L_i) \\ \frac{\sin(\nu\omega L_i)}{Z} & \cos(\nu\omega L_i) \end{bmatrix}. \tag{5.47}$$

$$\nu\omega L_i = n_i^{(L)} q_L h_L + n_i^{(S)} q_S h_S \tag{5.48}$$

where:

$$\nu = \frac{n_i^L c_L Q_L + C n_i^S c_S Q_S}{c_L n_i^L + C c_S n_i^S};\ \ Q_L = \sqrt{1/c_L^2 - \kappa^2};\ \ Q_S = \sqrt{1/c_S^2 - \kappa^2}. \tag{5.49}$$

The term κ is a purely real number and conditions are derived: terms $\mu_L\rho_L - \mu_S\rho_S$ and $\mu_L^2 - \mu_S^2$ must share the same sign. Two terms Q_L and Q_S actually demonstrate the q_L and q_S respectively (if times circular frequency ω). The terms $1/c_L^2$ can be slightly decreased:

$$\frac{1}{c_L^2} = \frac{\rho_L}{\mu_L} > \frac{\rho_L\mu_L - \rho_S\mu_S}{\mu_L^2} > \frac{\mu_L\rho_L - \mu_S\rho_S}{\mu_L^2 - \mu_S^2}$$

so that $Q_L > 0$ and with the same reason term $Q_S > 0$. The dispersion equation (5.50) provides the relationships:

$$K_x L_i = \arccos\left(\frac{trM_i(f, K_y)}{2}\right). \tag{5.50}$$

$$\cos(K_x L_i) = \cos(\nu\omega L_i), \quad \sin(K_x L_i) = \pm\sin(\nu\omega L_i). \tag{5.51}$$

and the eigenvector (5.40) becomes, in this case, $[\varrho, \pm\varrho i/Z]^T$. The criterion for the selection of the sign in equation (5.51) will be clarified later, however we anticipate that $+(-)$ is for a positive (negative) refracted wave. Then, for an arbitrary layer, the left-hand boundary conditions at $x = x_l$ of each layer can be calculated by repeated applications of matrices equation (5.46) to the eigenvector, namely:

$$\begin{bmatrix}\sigma_{xz}(x_l)\\ u_z(x_l)\end{bmatrix}=\begin{bmatrix}\varrho\cos(\hat{n})\mp\varrho\mathrm{i}\sin(\hat{n})\\ \frac{\varrho\sin(\hat{n})}{Z}\pm\mathrm{i}\frac{\varrho\cos(\hat{n})}{Z}\end{bmatrix} \tag{5.52}$$

where $\hat{n}=n^{(L)}q_Lh_L+n^{(S)}q_Sh_S$, In this expression, the $n^{(L)}$ and $n^{(S)}$ are the number of layers L and S before the left boundary condition $x=x_l$ and $x=x_0$, respectively (the two integer values run from 0 to $n_i^{(L)}$ or $n_i^{(S)}$, respectively). By substituting state vector (5.52) into equation (5.42), note that $\sigma_{xz}^*(x_l)\,u_z(x_l)+\sigma_{xz}(x_l)\,u_z^*(x_l)=0$, $|\sigma_{xz}(x_l)|^2=|\varrho|^2$ and $|u_z(x_l)|^2=|\varrho|^2/Z^2$. Thus, integral (5.42) becomes:

$$\frac{1}{|\varrho|^2}\int_{x_l}^{x_l+h_X}w\mu w^*dx=\frac{1}{Zq_X}\left(\frac{h_X}{2}-\frac{\sin(2q_Xh_X)}{4q_X}\right)+\frac{(\cos(\hat{n})\pm\mathrm{i}\sin(\hat{n}))(\sin(\hat{n})\pm\mathrm{i}\cos(\hat{n}))}{Z}$$

$$\frac{\sin^2(q_Xh_X)}{2q_X^2}+\frac{(\cos(\hat{n})\mp\mathrm{i}\sin(\hat{n}))(\sin(\hat{n})\mp\mathrm{i}\cos(\hat{n}))}{Z}\frac{\sin^2(q_Xh_X)}{2q_X^2}+\frac{1}{Zq_X}\left(\frac{h_X}{2}+\frac{\sin(2q_Xh_X)}{4q_X}\right),$$

And then simplified to yield significant part in y-component Poynting vector:

$$\int_{x_l}^{x_l+h_X}w\mu w^*dx=\frac{|\varrho|^2}{Z}\left(\frac{h_X}{q_X}\right) \tag{5.53}$$

Through equation (5.47) and (5.51), equation (5.41) can be simplified so that the components of the averaged Poynting vector for the assumption (5.45) finally become:

$$\langle\mathcal{P}_x\rangle=\pm\frac{|\varrho|^2\omega}{2Z},\quad\langle\mathcal{P}_y\rangle=\frac{|\varrho|^2\omega K_y}{2L_iZ}\left(n_i^{(L)}\frac{h_L}{q_L}+n_i^{(S)}\frac{h_S}{q_S}\right) \tag{5.54}$$

Using these expressions in (5.54), from Equation (5.31), we finally obtain:

$$\tan(\theta^{\text{trans}})=\pm\frac{L_i}{K_y\left(n_i^{(L)}\frac{h_L}{q_L}+n_i^{(S)}\frac{h_S}{q_S}\right)}. \tag{5.55}$$

Note that equation (5.54) and (5.55) hold true for a Fibonacci laminate of any index i. Equation (5.55) can be further manipulated by taking advantage of the definition of q_X, of equation (5.45) and the fact that $h_L=L_i/\left(n_i^{(L)}+n_i^{(S)}\frac{Cc_S}{c_L}\right)$ and $h_S=L_i/\left(n_i^{(L)}\frac{c_L}{Cc_S}+n_i^{(S)}\right)$, to yield:

$$\tan(\theta^{\text{trans}})=\pm\frac{Q_LQ_S\left(n_i^L+n_i^S\frac{Cc_S}{c_L}\right)\left(n_i^L\frac{c_L}{Cc_S}+n_i^S\right)}{\kappa\left[n_i^L\left(n_i^L\frac{c_L}{Cc_S}+n_i^S\right)Q_S+n_i^S\left(n_i^L+n_i^S\frac{Cc_S}{c_L}\right)Q_L\right]}, \tag{5.56}$$

In both (5.55) and (5.56), the fraction in the right hand side is a positive real number, therefore it becomes clear now that the sign $+$ and $-$ also determine the sign of the angle θ^{trans}. Equation (5.56) shows that θ^{trans} does not depend explicitly on f, nor the angle θ^{inc}, nor the properties of

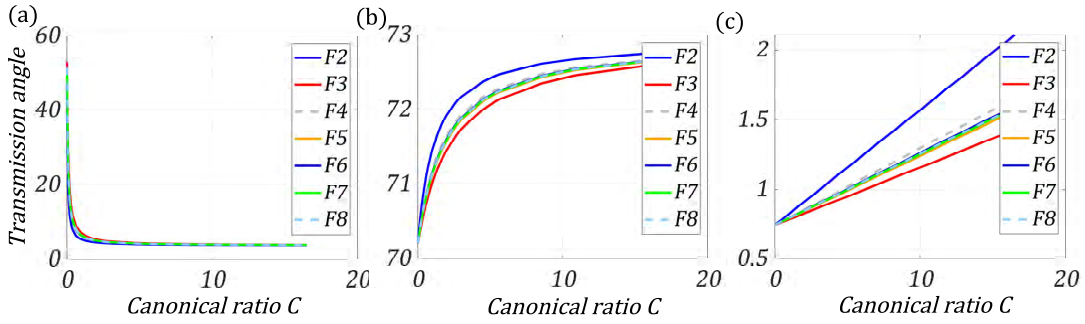

Figure 5.13. The transmission wave angle with the canonical ratio for different Fibonacci laminates. (a). L PMMA and S steel ($\kappa \approx 0.316 \times 10^{-4}$s/m). (b). L Iron and S Copper ($\kappa \approx 1.311 \times 10^{-4}$s/m). (c). L Steel and S Polyethylene ($\kappa \approx 3.162 \times 10^{-4}$s/m).

the substrate. Thus, it is interesting to investigate its relationship with the materials of the two phases and the canonical ratio C.

5.5.2 'Inverse problem' investigation

This subsection is devoted to the presentation of the 'inverse problem' consisting of the determination of the properties of laminate and substrate to obtain a particular value of the transmission angle θ^{trans}. As suggested in closing the previous part, the first aspect to consider is how θ^{trans} depends on C in Equation (5.56). To illustrate this, three different laminates are considered in Figure 5.13 for unit cells F_2 to F_8, where the sign + in the equation is assumed: (a) L: PMMA, S: steel, (b) L: iron, S: copper and (c) L: steel, S: polyethylene. The derivative of tan θ^{trans} with respect to C may help in the discussion; this yields:

$$\frac{\partial \tan(\theta^{\text{trans}})}{\partial C} = \pm(Q_S - Q_L)\frac{c_L c_S n_i^L n_i^S Q_L Q_S}{\kappa(c_L n_i^L Q_S + C c_S n_i^S Q_L)^2}. \tag{5.57}$$

The term $\pm(Q_S - Q_L)$ governs the sign of the derivative. If $(Q_S - Q_L) > 0$, with the positive (negative) sign, tangent and angle increase (decrease) with C increasing.

As $(Q_S - Q_L) = -5.2166 \times 10^{-4}$s/m in Figure 5.13 (a), the curves are monotonic decreasing, whereas functions in Figure 5.13 (b), (c) display an opposite behaviour as $(Q_S - Q_L) = 6.3524 \times 10^{-5}$s/m and $(Q_S - Q_L) = 2.7975 \times 10^{-3}$s/m, respectively. Through a representation akin to Figure 5.13, the canonical ratio corresponding to a required transmission angle could be selected. Figure 5.13 also demonstrates that the range of possible angle θ^{trans} for a given laminate is, in general, limited, an issue that should be taken into account.

The procedure for the 'inverse problem' is the following: first, from the target value of θ^{trans} the associated canonical ratio can be determined from Equation (5.56) with selected materials for

phases L and S. Second, the corresponding value of ν can be obtained from Equation (5.49). Then, Equation (5.51) can be used to determine the connection between $K_x L_i$ and $\nu\omega L_i$ which provides, through Equation (5.1), the relationship between frequency f of the incoming wave, wave speed of the substrate c_0 and angle of incidence θ^{inc}.

First, the situation for $\nu\omega L_i > 2\pi$ is proved with the frequency is $f = 1/(\nu L_i)$ as $\nu\omega L_i = 2\pi$ and the two extremes of function $1/(\nu L_i)(C)$ and $\tilde{f}_i(C)$ are:

$$\lim_{C\to 0} \frac{1}{\nu L_i} = \lim_{C\to 0} \frac{c_L n_i^{(L)} + C c_S n_i^{(S)}}{(n_i^{(L)} c_L Q_L + C n_i^{(S)} c_S Q_S) L_i} = \frac{1}{L_i Q_L} > \frac{c_L}{L_i} \tag{5.58}$$

$$\lim_{C\to \infty} \frac{1}{\nu L_i} = \lim_{C\to \infty} \frac{c_L n_i^{(L)} + C c_S n_i^{(S)}}{(n_i^{(L)} c_L Q_L + C n_i^{(S)} c_S Q_S) L_i} = \frac{1}{L_i Q_S} > \frac{c_S}{L_i}$$

The results from Section 5.4 tell that the $\tilde{f}_i$ is convex function except F_2 and F_3. In addition, the monotonic properties of frequency $1/(\nu L_i)(C)$ is:

$$\frac{\partial 1/(\nu L_i)}{\partial C} = \frac{c_L c_S n_i^L n_i^S (Q_L - Q_S)}{L_i (c_L n_i^L Q_L + C c_S n_i^S Q_S)^2}$$

Which means frequency $f = 1/(\nu L_i)$ keep same monotonic properties in all canonical ratio range. In addition, the local maximum value for $\tilde{f}_i$ can also be verified smaller than $1/(\nu L_i)$. For example, $C = 1$ for Fibonacci order 2:

$$\frac{1}{\nu L_2}(C = 1) = \frac{c_L + c_S}{(c_L Q_L + c_S Q_S) L_2} > \frac{c_L + c_S}{2 L_2} \tag{5.59}$$

With the same procedure, the Fibonacci order 3 with $C = 2$ can also be verified. Thus, frequency always $1/(\nu L_i) > \tilde{f}_i$ also means the term $\nu\omega L_i < 2\pi$ must satisfied under pure negative refraction condition. Recalling Equation (5.51), now with sign $-$, negative refraction occurs provided the following conditions are satisfied:

$$\cos(K_x L_i) = \cos(\nu\omega L_i), \quad \sin(K_x L_i) = -\sin(\nu\omega L_i). \tag{5.60}$$

These condition is very interesting and the complete solution steps in Chapter 6, whose solution is:

$$K_x L_i = \frac{\omega}{c_0} \sin(\theta^{\text{inc}}) L_i = 2g\pi - \nu\omega L_i. \ (g \in \mathbb{N}^*).$$

We restrict the analysis to the case $g = 1$, which means that $K_x L_i$ should lie in the second Brillouin zone. For this to occur, it is necessary that $\nu\omega L_i < \pi$ or, alternatively, $f < 1/(2\nu L_i)$. Equation

(5.1) provides the required connection between θ^{inc}, c_0 and frequency as:

$$(\frac{1}{fL_i} - \nu)c_0 = \sin(\theta^{\text{inc}}) \tag{5.61}$$

in which the term in brackets is positive as a consequence of the inequality $f < 1/(2\nu L_i)$, whereas the whole left hand should be less than one for a real angle of incidence ($\theta^{\text{inc}} = \pi/2$). As a conclusion, under the condition set by Equation (5.45), pure negative refraction must satisfy the conditions listed at the end of Section 5.1, with:

$$f \in [f_i^{\min}, \min(1/(2\nu L_i), \tilde{f}_i))] \tag{5.62}$$

and $\nu\omega L_i < \overline{K}_x L_i$. The substrate must be chosen so that the speed c_0 is such that the left hand side of Equation (5.61) is less than one; the same equation determines the angle of incidence θ^{inc}.

To illustrate the proposed analytical procedure, an application based on a prototype example is proposed for a laminate with the usual combination (L: PMMA, S: steel). We start by choosing the transmission angle in Figure 5.13 (a) (pertinent to our case). For simplicity, assume $\theta^{\text{trans}} = -5.431$ that corresponds to $C = 1$. Then, the frequency f of the incoming wave can be decided and the value of $K_x L_2$ selected from Figure 5.14 that is for this canonical ratio. In this figure, triangles mark the pairs $(f, K_y L_2)$ which satisfy Equation (5.45) for negative refraction. For instance, for $f = 460$kHz, the data deduced from the figure used in Equation (5.61) provide an angle of incidence of $\theta^{\text{inc}} = 74.4$ for a substrate made of aluminium and $\theta^{\text{inc}} = 35.4$ for a substrate made of nylon.

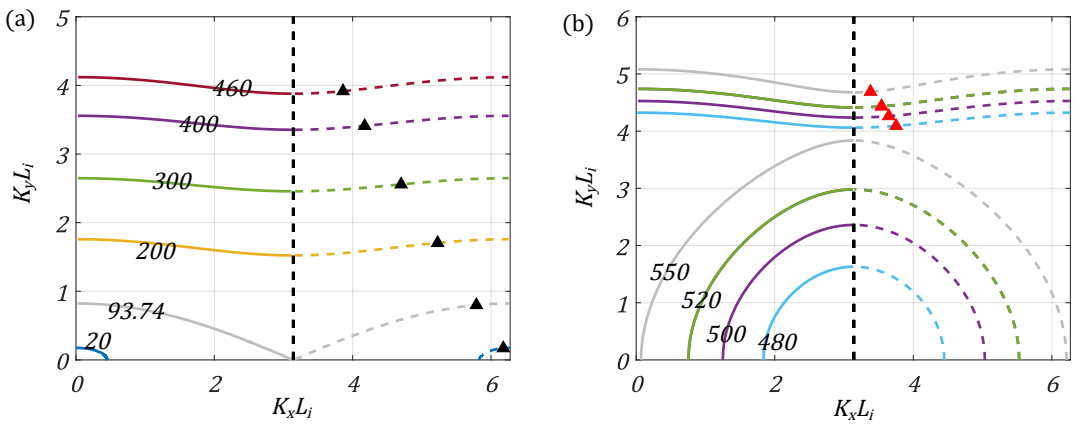

Figure 5.14. Laminate F_2 with material combination (L: PMMA, S: steel) with $C = 1$. Plots of real solutions of the dispersion equation in graph K_yL_2 versus K_xL_2 for several given frequencies; in particular, (a) selected frequencies in the range $f \in [20, 460]kHz$, (b) selected frequencies in the range $f \in [480, 550]kHz$. The black and red triangles mark points that satisfy Equation (5.45) *and are relevant for negative refraction.*

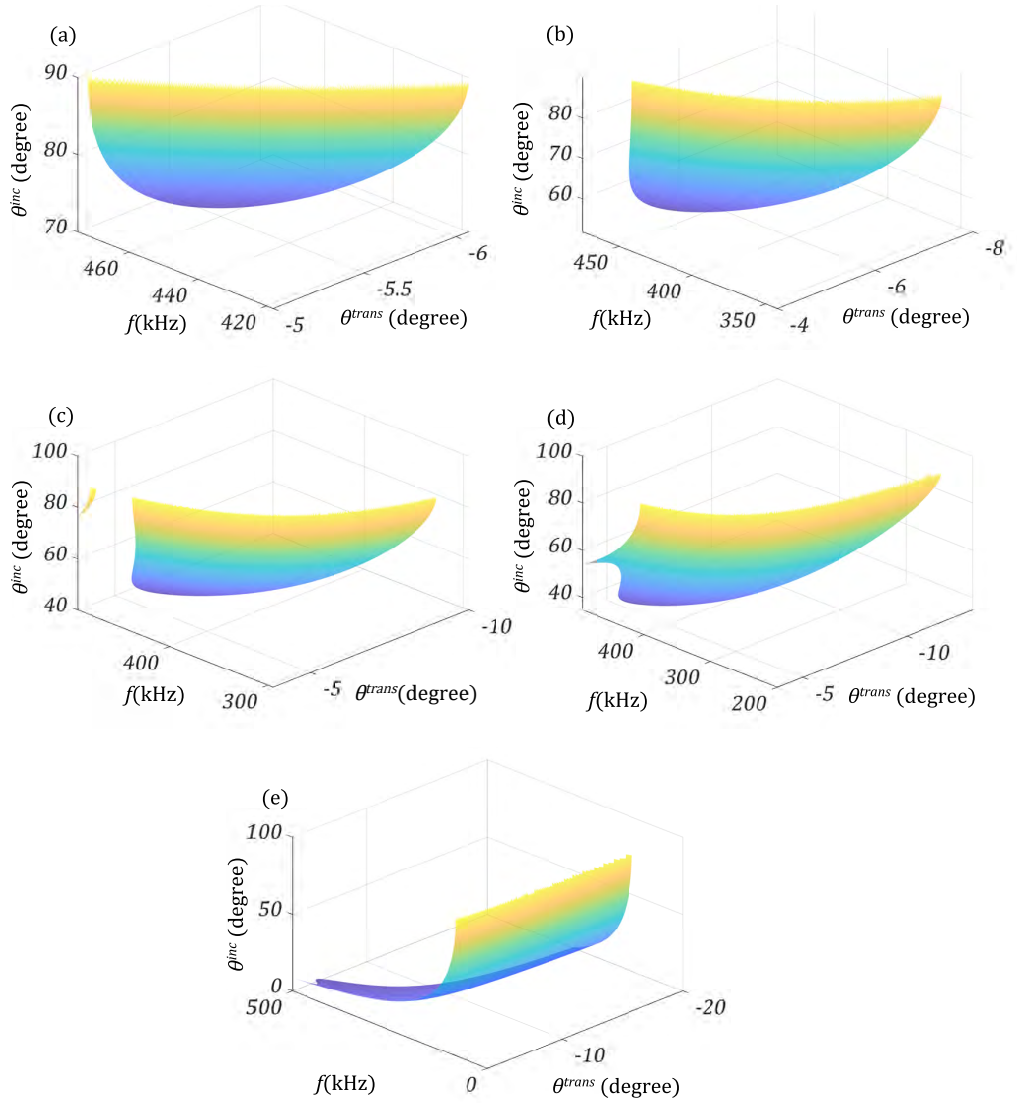

Figure 5.15. The incident wave angle (degree) corresponding to transmission angle (degree) and frequency (kHz) with the different substrates under F_2. (a). The substrate is Aluminium. (b). Iron. (c). Copper. (d). Nylon. (e). Polyethylene.

To complete the investigation, Figure 5.15 reports five plots for the adopted laminate coupled with the different substrates, where all possible admissible combinations between angle of incidence θ^{inc}, frequency f and angle of refraction θ^{trans} are displayed which satisfy Equation (5.61). As the value of $f_i^{\min}$ in (5.62) depends linearly on c_0 (see Equation (5.2)), the softer material, for instance, nylon, which has a value of c_0 that is approximately 60 percent that of aluminium, ensures a wider range of the involved parameters (f, θ^{inc}, θ^{trans}) for negative refraction as becomes evident by comparing part (d) to part (a) of Figure 5.15. Therefore, a substrate with a relatively low shear wave speed should be preferred to maximize the combinations between the involved parameters.

5.6 Pure Negative Refraction Energy

Up to this point, it has been shown how to control negative refraction through an accurate selection of mechanical and geometrical properties of both substrate and layers of the laminate. However, the transmission problem has an additional aspect that is related to the fraction of the energy of the incoming wave that is transmitted across the laminate. In order to effectively exploit a negative refracted wave, a sufficient amount of energy should be conveyed across the laminate. We address this point in this section by highlighting the fact that some substrate laminate combinations show a peak in the transmitted energy carried by the negative refracted wave.

5.6.1 Reflected mode

To calculate energy fluxes, the method traditionally adopted restricts the number of both reflected and transmitted modes to arrange a finite-size linear system where the unknowns are the scattering coefficients (see Equations (5.34) and (5.35)). For the former, the selected range of modes is $0 \leq l \leq 2N$, for the latter the involved indices are $-N \leq m \leq N$; in both cases, real solutions and evanescent waves are included.

The mode shape for reflected wave is $U_m = \exp(-\frac{\mathrm{i}2m\pi x}{L_i}) = \cos(\frac{2m\pi x}{L_i}) - \mathrm{isin}(\frac{2m\pi x}{L_i})$. The boundary continuity conditions (3.21) and (3.22), are actually Fourier series expansions and $\bar{R}_m$ are Fourier coefficients. Hence, if the number of Fourier series is big enough, the continuity condition must be satisfied. However, due to the difficult expression for mode shape w_l for transmission wave which is changed at the boundary of two phase, it is hard to obtain the expression for w_l.

Then, the real reflected mode problem can be investigated. It should be started with the equation (2.51) ($k_y^{(m)} = \sqrt{K_0^2 - (K_0 \sin(\theta^{\mathrm{inc}}) + 2m\pi/L_i)^2}$). $K_0^2 - \left(K_0 \sin\left(\theta^{\mathrm{inc}}\right) + 2m\pi/L_i\right)^2 \geq 0$ is associated with real propagation wave. On the contrary, $K_0^2 - \left(K_0 \sin\left(\theta^{\mathrm{inc}}\right) + 2m\pi/L_i\right)^2 < 0$, corresponds to evanescent wave. Then:

$$K_0^2 - \left(K_0 \sin\left(\theta^{\mathrm{inc}}\right) + \frac{2m\pi}{L_i}\right)^2 = (K_0 + K_0 \sin\left(\theta^{\mathrm{inc}}\right) + \frac{2m\pi}{L_i})(K_0 - K_0 \sin\left(\theta^{\mathrm{inc}}\right) - \frac{2m\pi}{L_i}) \quad (5.63)$$

For now the problem becomes simple. First, the situation for $\left(K_0 + K_0 \sin\left(\theta^{\mathrm{inc}}\right) + 2m\pi/L_i\right) \geq 0$ and $\left(K_0 - K_0 \sin\left(\theta^{\mathrm{inc}}\right) - 2m\pi/L_i\right) \geq 0$ should be analysed, so that the two conditions should be satisfied simultaneously:

$$K_0 + K_0 \sin\left(\theta^{\mathrm{inc}}\right) \geq -\frac{2m\pi}{L_i}; K_0 - K_0 \sin\left(\theta^{\mathrm{inc}}\right) \geq \frac{2m\pi}{L_i} \quad (5.64)$$

If $m \geq 0, K_0 + K_0 \sin\left(\theta^{\text{inc}}\right) \geq -\frac{2m\pi}{L_i}$ condition should be satisfied automatically. then:

$$K_0 - K_0 \sin\left(\theta^{\text{inc}}\right) \geq \frac{2m\pi}{L_i} \Rightarrow m \leq \frac{K_0 - K_0 \sin\left(\theta^{\text{inc}}\right)}{2\pi} L_i \tag{5.65}$$

On the contrary, If $m < 0, K_0 - K_0 \sin\left(\theta^{\text{inc}}\right) \geq \frac{2m\pi}{L_i}$ condition should be satisfied automatically. Then:

$$K_0 + K_0 \sin\left(\theta^{\text{inc}}\right) \geq -\frac{2m\pi}{L_i} \Rightarrow -\frac{K_0 + K_0 \sin\left(\theta^{\text{inc}}\right)}{2\pi} L_i \leq m \tag{5.66}$$

If $\left(K_0 + K_0 \sin\left(\theta^{\text{inc}}\right) + 2m\pi / L_i\right) < 0$ and $\left(K_0 - K_0 \sin\left(\theta^{\text{inc}}\right) - 2m\pi / L_i\right) < 0$, they cannot be satisfied no matter $m \geq 0$ or $m < 0$. Therefore, the condition for propagation real reflected mode m is obtained below:

$$-\frac{K_0 + K_0 \sin\left(\theta^{\text{inc}}\right)}{2\pi} L_i \leq m \leq \frac{K_0 - K_0 \sin\left(\theta^{\text{inc}}\right)}{2\pi} L_i \tag{5.67}$$

Since the incident wave angle θ^{inc} increases from 0 to 90 degrees, the maximum range of m is obtained, which is:

$$-\frac{2f}{c_0} L_i \leq m \leq \frac{f}{c_0} L_i \tag{5.68}$$

Therefore, the maximum number for different m is $\text{int}\,(2f/c_0 L_i) + \text{int}\,(f/c_0 L_i) + 1$, so that m changes with the frequency $f = nc_0/2L_i = nf_i^{\min}, n \in \mathbb{N}$. It also can lead a better condition for only $m = 0$ existed, which is $f < f_i^{\min}$. Because the pure negative refraction only happens when $f > f_i^{\min}$, the reflection wave $m = 0$ with $m = -1$ must appear as propagation waves during the pure negative refraction.

5.6.2 The unusual energy peak with pure negative refraction

The scattering coefficients have been obtained from matrix calculation in Chapter 3. Then, the normalised energy flux balance (3.28) is based on the scattering coefficients:

$$E = \sum_{i=0}^{mt} \left|\bar{T}_i\right|^2 \frac{K_y^{(i)} \bar{\mu}}{K_0 \cos(\theta^{\text{inc}})\, \mu_0} + \sum_{m}^{nr} \left|\bar{R}_m\right|^2 \frac{k_y^{(m)}}{K_0 \cos(\theta^{\text{inc}})} = 1$$

in which the two summations represent the normalized transmitted and reflected energies, respectively:

$$\text{trans}: \left|\bar{T}_i\right|^2 \frac{K_y^{(i)} \bar{\mu}}{K_0 \cos(\theta^{\text{inc}})\, \mu_0}, \quad \text{ref}: \left|\bar{R}_m\right|^2 \frac{k_y^{(m)}}{K_0 \cos(\theta^{\text{inc}})}$$

The values of the energy associated with each real mode can be plotted versus the angle of incidence θ^{inc} to appreciate the behaviour of the functions or, alternatively, versus the transverse

wavenumber $K_x L_i$. With the latter choice (preferred in the plots of Figure 5.16), it is easier to assess the behaviour of the energy flows when entering in the second Brillouin zone, for instance, $\pi < K_x L_i < 2\pi$.

Plots in Figure 5.16 display the energy landscape of all real transmitted and reflected modes available for the considered problem. In all cases, the scattering coefficients are calculated by assuming $N = 6$ in system (12 evanescent and one transmitted modes; 11 or 12 depending on the case evanescent reflected waves). The number of real transmitted modes is always equal to one ($\bar{T}_0$), while the reflected ones can be either one (i.e. $\bar{R}_0$) or two (i.e. $\bar{R}_0$ and $\bar{R}_{-1}$).

From the Figure 5.16, the pure negative refraction can be easily distinguished with the transverse wave number $K_x L_i > \pi$ instead of plot θ^{inc}. There exists a unusually peak of transmitted energy T_0 in Figure 5.16. (a) within pure negative refraction range, which means the transmission angle is negative with energy almost 0.52 of total energy, which is good enough for applications. The transmitted energy is decreased with the remaining 5 plots without peak. From Figure 5.17, the energy peak actually shows in a frequency range not only fixed frequency value. However, it disappears as another transmitted mode propagation as shown in Figure 5.17 (c). Moreover, as an additional note, in all plots of Figure 5.16, 5.17 and 5.18, the energy associated with the reflected mode R_{-1} is symmetric with respect to $K_x L_i = \pi$ at which the function is stationary. The observed symmetry is related to properties of Equation (5.63), with $m = -1$, as can be demonstrated quite easily:

$$K_0 L_i + K_0 \sin(\theta^{\text{inc}}) L_i = 2\pi \tag{5.69}$$

In addition, the initial positive transmitted energy is changed with the different substrates. It looks like the substrate material is more softer, the transmitted energy would be smaller with a minor incident wave angle. Moreover, the other three combinations with different substrate show unusually peaks in Figure 5.18. If the quasiperiodic generated laminates are used as a perfect acoustic lens for wave focusing, the pure negative transmitted wave must have enough energy. Thus, the unusually peak in Figure 5.16 (a) deserves to be further analysed in the future, specially in view of the assessment of the optimal performance of a particular choice of materials of the system.

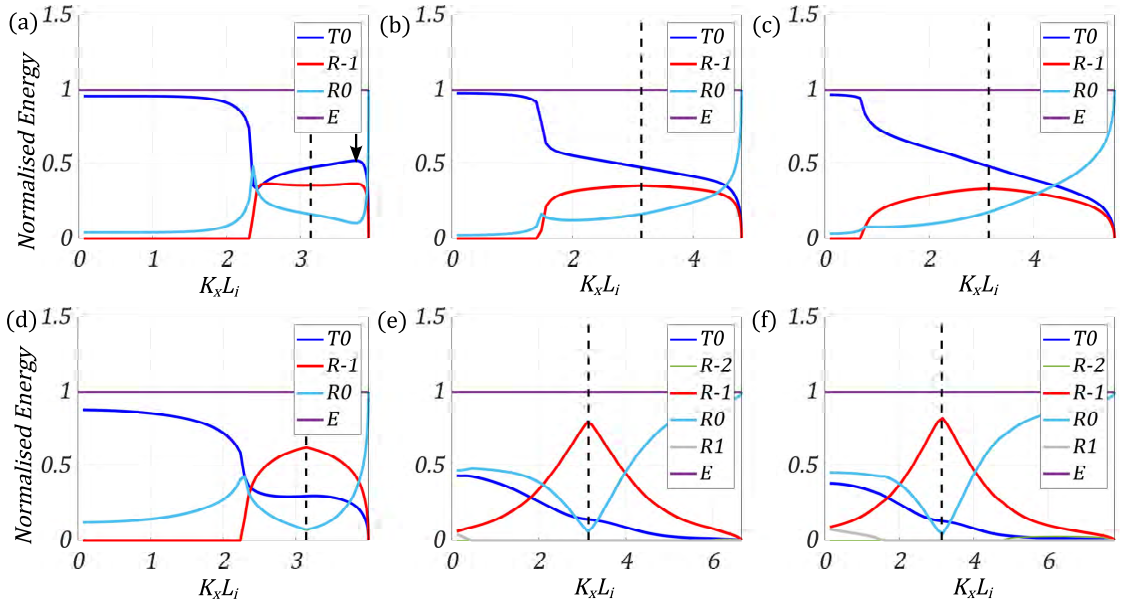

Figure 5.16. Normalised energy metrics for the transmitted and reflected propagation modes with material L PMMA and S steel, $L_2 = 4.3mm$, canonical ratio $C = 1$, frequency $f = f_2^{1bg} = 459.364kHz$. Black dash line associated with Brillouin zone edge $K_xL_i = \pi$. (a) with substrate Steel. (b). with substrate Iron. (c). with substrate Copper. (d). with substrate Aluminium. (e). with substrate Nylon. (f). with substrate PMMA.

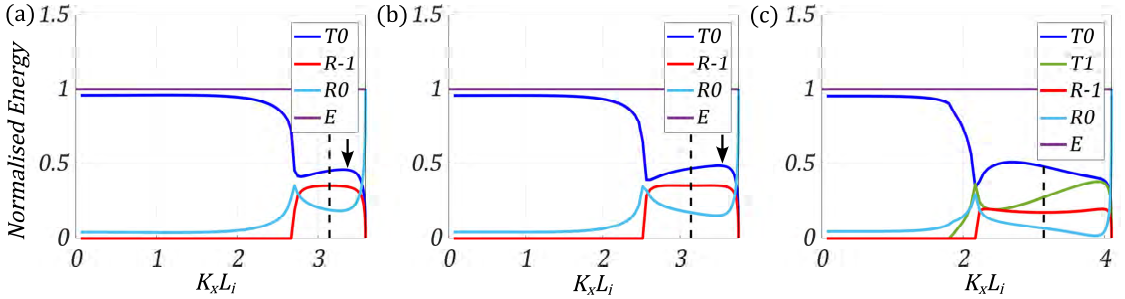

Figure 5.17. Normalised energy metrics for the transmitted and reflected propagation modes with material L PMMA and S steel with substrate Steel, $L_2 = 4.3mm$, canonical ratio $C = 1$. (a) $f = 420kHz$. (b) $f = 440kHz$. (c) $f = 480kHz$.

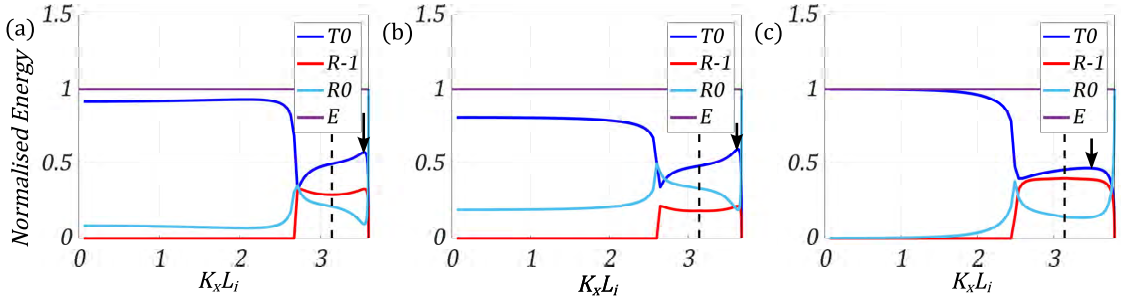

Figure 5.18. Normalised energy metrics for the transmitted and reflected propagation modes with different materials, $L_2 = 4.3mm$, canonical ratio $C = 1$. (a) $f = 420.98kHz$, material L Iron, S Aluminium, substrate Steel. (b) $f = 351.94kHz$, material L Aluminium, S Polyethylene, substrate Iron. (c) $f = 314.19kHz$, material L Iron, S Polyethylene, substrate Copper.

5.7 Conclusion and Remarks

A method to accomplish pure negative refraction for harmonic elastic anti-plane shear dynamics is wave transmission across an interface between a substrate and a composite laminate whose lamination direction is orthogonal to the interface. Previous studies have shown that the goal is achievable if the frequency of the impinging wave is compatible with propagation of the refracted wave within the second Brillouin zone of the laminate (this has been reviewed in Chapter 2). Therefore, the study of the dispersion properties of the composite is a fundamental task to be carried out in detail. The control of those properties is particularly easy for a special class of laminates, called canonical, that can be studied by considering sets of elementary cells generated by a quasicrystalline sequence (the Fibonacci GM sequence in this case). For waves propagating orthogonally to the lamination direction, canonical laminates display a periodic stop- and pass-band layout, the periodicity being governed by a special frequency called canonical frequency. The key features leading to the definition of such special configurations are (i): the recursive relationship (5.6) existing between three consecutive traces of transmission matrices; (ii): the existence of an invariant function (Kohmoto's invariant) and (iii): the nonlinear trace map (2.31) that can be written from the recursive rule: the canonical configurations correspond to periodic orbits of the trace map and this takes place at well-defined frequencies, namely, the canonical frequencies, which is shown in Chapter 4. The theory shows that there are three families of canonical laminates. In this Chapter, all results and conclusions are first found.

For the problem of pure negative refraction, the focus is on the first two pass bands of the spectrum that possess the same limits of the first two transition zones at low frequencies for the laminate if we consider wave propagation in any direction. The self-similar pattern displayed by them at increasing index of the sequence can be quantitatively described through a scaling factor that can be estimated by square root of the maximum eigenvalue from fixed point on Kohmoto's manifold, which is the golden ratio explained in Chapter 4. Through this parameter, the breadths of the two transition zones can be predicted by scaling backward and/or forward the corresponding values of a given configuration taken as a reference. It is also shown how the impedance mismatch β of the laminate affects the limits of the transition zones at constant canonical ratio and how to modify the dispersive properties of the elementary cell by changing its total length L_i.

In addition, the relevant frequencies can be predicted with linear approximation under specified conditions. This method comes from the periodic cycle points in the canonical structure. The numerical results are shown that for better prediction f_i^{1bg} and $\tilde{f}_i$ at same time, the canonical ratio 2 or $1/2$ can be chosen. The canonical ratio range for only predicting one of f_i^{1bg} and $\tilde{f}_i$ already is

shown in detailed. For better prediction f_i^{1st}, it depends on impedance mismatch β and canonical ratio C. If β is far away from 2, the better prediction with C should be approximation to 1. On the contrary, if β is close to 2, the better prediction with C should be far away from 1.

Moreover, the universal representation of the frequency spectrum based on the reduced torus allows us to study effectively how a change in canonical ratio affects the change in the frequencies relevant for negative refraction, namely, those at the limits of the first two transition zone. This representation provides a tool that can be exploited for optimization of the performance of the substrate-laminate system. To demonstrate it, we study analytically the cases F_2 and F_3 with the condition: $\rho_L > \rho_S, \mu_L > \mu_S$ or $\rho_L < \rho_S, \mu_L < \mu_S$.

For a linear relationship between longitudinal wavenumber and frequency, the Poynting vector indicating the direction of energy flow and then the transmission angle, can be calculated explicitly. With this closed-form solution, the properties of laminate and substrate, and the angle of incidence can be easily selected to achieve a particular direction of the negative refracted wave without solving numerically the whole coupled problem. Thus, the transmission angle can be controlled before considering frequency, substrate and incident wave angle. Moreover, if a vast transmission wave angle or small incident wave angle for pure negative refraction is needed, the substrate with small wave speed should be selected.

While, on the one hand, the possibility to achieve negative refraction can be analysed through an accurate selection of both materials and layouts of the unit cell, on the other, the amount of transmitted energy is an additional factor that should be duly considered as it may vary considerably at a change of the angle of incidence. We show here that, for a combination of materials of the substrate-laminate system, a peak in the energy of the only transmitted mode is found, whereas this feature is not present for several other configurations. This aspect must be taken into account in practical applications when the investigated prototype system is adopted.

For design system, which is composed by two phase quaiscrystalline laminate and homogenous substrate with fixed total length L_i, for having SH wave pure negative refraction is following steps:
(1): For having relative large incident wave angle's range for pure negative refraction, the material for substrate with slower phase speed c_0 should be chosen so that f_i^{min} is relative lower.
(2): For increasing three edge frequencies f_i^{1st}, f_i^{1bg} and $\tilde{f}_i$ (upper edge for pure negative refraction), the material with higher wave phase speed should be chosen as material A, the material with lower wave phase speed should be chosen as material B.
(3): If Fibonacci order for laminate is F_2 or F_3 and satisfied the condition $\rho_L > \rho_S, \mu_L > \mu_S$ or

$\rho_L < \rho_S, \mu_L < \mu_S$, the canonical ratio can be chosen as $C = 1$ or $C = 2$ for having local maximum value $\tilde{f}_i$ (upper edge for pure negative refraction), respectively.

(4): Three frequencies f_i^{1st}, f_i^{1bg} and $\tilde{f}_i$ can be predicted with linear approximation (lower Fibonacci order) $f_2^{1bg} \approx f - (2 + x_2)\frac{dx_2}{df}$, $\tilde{f}_2 \approx f + (2 - x_2)/\frac{dx_2}{df}$, $f_2^{1st} \approx f + (-2 - x_2)/\frac{dx_2}{df}$ or with transition zone scaling (higher Fibonacci order) using coefficients ϕ_g.

(5): The incident wave angle θ^{inc}, pure negative refraction angle θ^{trans} and incoming wave frequency f can be plotted on Figure analogy with 5.15 according equation $(\frac{1}{fL_i} - \nu)c_0 = \sin(\theta^{inc})$ to determine the relationship among them. Engineer can pick up two of these three terms to obtain another one.

Chapter 6 - Topological Interface State on Rods

Localized modes occurring at the interface between two quasicrystalline-generated rods are investigated in this Chapter. The general condition for the existence of the interface mode, based on the mismatch between the surface mechanical impedance of the two semi-infinite rods composing the system and related to the symmetry properties of the edge modes characterizing these rods, is introduced in Section 6.1. This explicit condition is exploited together with the concept of canonical configuration and the universal toroidal representation of the spectrum illustrated in previous Chapters in order to predict the presence of an interface mode avoiding the commonly performed calculation of the Zak phase and the associated complex numerical computations in Section 6.2. An explicit formula for the frequency of the interface mode is obtained considering the case of a system composed of one rod by canonical ratio and another by inverse of that canonical ratio in Section 6.3. Very good agreement is found between the analytical predictions provided by the newly developed approach and the numerical results and then this study provides new insights into rational design of systems providing an interface localized mode at a determined frequency.

6.1 Symmetric Properties of Band Edge-Mode

6.1.1 Dispersion relation of two phase quasiperiodic rod

A 1D quasiperiodic generated rod is composed of the two-phase material rods as shown in Figure 6.1. The fundamental cell is generated according to generalized Fibonacci GM sequence F_2 but we assume the centre of phase S as the centre of the whole elementary cell, where the length of the two segments L and S are indicated with l_L and l_S, while A_j, E_j and $\rho_j, (j \in L, S)$ denote the cross-section area of each rod as in Chapter 4, Young's modulus and mass density per unit volume respectively. The governing equation of harmonic axial waves has two solutions (2.9) and (2.10) and rewritten here.

$$u_X(z) = a\exp(\mathrm{i}\sqrt{\frac{\rho_X}{E_X}}\omega z) + b\exp(-\mathrm{i}\sqrt{\frac{\rho_X}{E_X}}\omega z) \tag{6.1}$$

$$u_X(z) = C_1\sin(\sqrt{\frac{\rho_X}{E_X}}\omega z) + C_2\cos(\sqrt{\frac{\rho_X}{E_X}}\omega z) \tag{6.2}$$

In order to exploit also in this Chapter the universal structure of the frequency spectrum, the normalized variable ξ_X on the universal torus and the impedance of the phase Z_X are reported

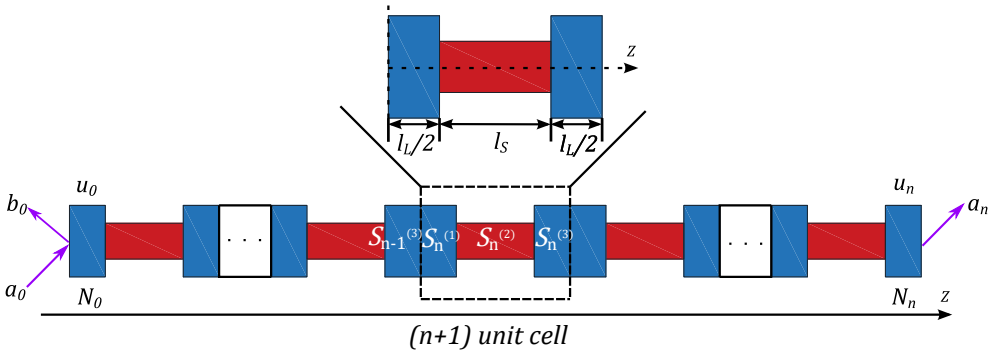

Figure 6.1. One dimension quasiperiodic rod with (n) unit cell, a_0, b_0 and a_n are incident, reflected and transmitted wave amplitude. $u_{0,n}$ and $N_{0,n}$ are displacements and the axial force on the boundary of the elementary cell, respectively

again below (Shmuel and Band 2016):

$$\xi_X = \sqrt{\frac{\rho_X}{E_X}}\omega l_X;\ \ Z_X = A_X\sqrt{E_X\rho_X}\ (X \in L,S)$$

The global transfer matrix referred to the general deduced from displacement solution (6.2) is denoted by T:

$$T = \begin{bmatrix} T_{11} & T_{12} \\ T_{21} & T_{22} \end{bmatrix}. \tag{6.3}$$

The transfer matrix is unimodular and relates the state vector in one unit cell to the adjacent one. The displacement and axial force terms $[u, N]^T$, and components are:

$$T_{11} = T_{22} = \cos(\xi_L)\cos(\xi_S) - \frac{(Z_L^2 + Z_S^2)\sin(\xi_L)\sin(\xi_S)}{2Z_SZ_L}$$

$$T_{12} = \frac{2Z_SZ_L\cos(\xi_S)\sin(\xi_L) + (Z_L^2 - Z_S^2 + (Z_L^2 + Z_S^2)\cos(\xi_L))\sin(\xi_S)}{2Z_L^2Z_S\omega}$$

$$T_{21} = -\omega\frac{2Z_SZ_L\cos(\xi_S)\sin(\xi_L) + (Z_S^2 - Z_L^2 + (Z_L^2 + Z_S^2)\cos(\xi_L))\sin(\xi_S)}{2Z_S} \tag{6.4}$$

The Floquet-Bloch theorem implies that transfer matrix has eigenvalues $\exp(\mathrm{i}KL_t)$, where L_t is the total length of the elementary cell which is $L_t = l_L + l_S$. Therefore, the dispersion equation is obtained:

$$\det[T - \exp(\mathrm{i}KL_t)\mathbf{E}] = 0 \tag{6.5}$$

The solution of equation (6.5) provides the Floquet-Bloch dispersion relation, which has the form reported in equation (2.26):

$$2\cos(\xi_L)\cos(\xi_S) - \beta\sin(\xi_L)\sin(\xi_S) = 2\cos(KL_t),\ \beta = (Z_L^2 + Z_S^2)/(Z_SZ_L) \tag{6.6}$$

The wave propagates when KL_t is a real number, whereas band gaps correspond to the ranges of frequencies where KL_t have imaginary parts (it is an evanescent wave). Combining the components in transfer matrix (6.4) together with the dispersion relation (6.6), we obtain $T_{11} = T_{22} = \cos(KL_t)$, so that the transfer matrix (6.3) can be rewritten as:

$$T = \begin{bmatrix} \cos(KL_t) & T_{12} \\ T_{21} & \cos(KL_t) \end{bmatrix} \tag{6.7}$$

The normalised Bloch wave number KL_t is 0 or π for frequencies at band edge. Thus, the eigenvalues are $e^{\mathrm{i}0} = 1 = \cos(0)$ or $e^{\mathrm{i}\pi} = -1 = \cos(\pi)$. Since the transfer matrix is unimodular, evaluating the determinant we obtain:

$$\det[T] = \cos^2(KL_t) - T_{12}T_{21} = 1 \;\Rightarrow\; T_{12}T_{21} = 0 \tag{6.8}$$

The global transfer matrix **F** referred to the solution of the wave equation in the form (6.1), the amplitude of incident and reflected waves $[a, b]^T$ at the beginning with those at the end of the cell. The matrix is given in the form:

$$\mathbf{F} = \begin{bmatrix} \mathbf{f}_{11} & \mathbf{f}_{12} \\ \mathbf{f}_{21} & \mathbf{f}_{22} \end{bmatrix}$$

$$\mathbf{f}_{11} = e^{(\mathrm{i}\xi_L)}[\cos(\xi_S) + \frac{\mathrm{i}}{2}(\frac{Z_S}{Z_L} + \frac{Z_L}{Z_S})\sin(\xi_S)]$$

$$\mathbf{f}_{12} = -\mathbf{f}_{21} = \frac{\mathrm{i}}{2}(\frac{Z_S}{Z_L} - \frac{Z_L}{Z_S})\sin(\xi_S).$$

$$\mathbf{f}_{22} = e^{(-\mathrm{i}\xi_L)}[\cos(\xi_S) - \frac{\mathrm{i}}{2}(\frac{Z_S}{Z_L} + \frac{Z_L}{Z_S})\sin(\xi_S)] \tag{6.9}$$

The axial force at $z = 0$ is $|N_0| = \omega Z_L|\mathrm{i}(a_0 - b_0)|$, where a_0 and b_0 are the amplitudes of the incident and reflected wave at $z = 0$, respectively. These quantities can be evaluated by using the components of the matrix (6.9) together with the dispersion relation (6.6):

$$a_0(z = 0) = \mathbf{f}_{12} = \frac{\mathrm{i}}{2}(\frac{Z_S}{Z_L} - \frac{Z_L}{Z_S})\sin(\xi_S)$$

$$b_0(z = 0) = e^{\mathrm{i}KL_t} - \mathbf{f}_{11} = e^{\mathrm{i}KL_t} - e^{(\mathrm{i}\xi_L)}[\cos(\xi_S) + \frac{\mathrm{i}}{2}(\frac{Z_S}{Z_L} + \frac{Z_L}{Z_S})\sin(\xi_S)] \tag{6.10}$$

Then, the axial force and displacement also at $z = 0$ become:

$$N_0 = \mathrm{i}\omega Z_L(a_0 - b_0) = -\omega\frac{2Z_SZ_L\cos(\xi_S)\sin(\xi_L) + (Z_S^2 - Z_L^2 + (Z_L^2 + Z_S^2)\cos(\xi_L))\sin(\xi_S)}{2Z_S} \tag{6.11}$$

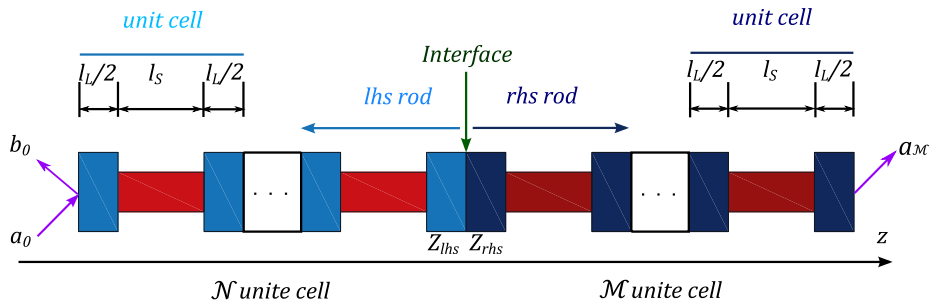

Figure 6.2. Two 1D quasiperiodic rods with $\mathcal{N}$ unit cells in the left and $\mathcal{M}$ unit cells in the right connections at the interface, a_0, b_0 and $a'_{\mathcal{M}}$ are incident, reflected and transmitted wave amplitude. lhs and rhs denote the left and right side quasiperiodic rod. Figure reproduced from Chen et al. (2021)

$$u_0 = a_0 + b_0 = -\frac{2iZ_SZ_L\cos(\xi_S)\sin(\xi_L) + i(Z_L^2 - Z_S^2 + (Z_L^2 + Z_S^2)\cos(\xi_L))\sin(\xi_S)}{2Z_SZ_L} \tag{6.12}$$

Remembering the expressions for the terms T_{12} and T_{21} in equation (6.4) and using them into (6.11) and (6.12), we obtain:

$$N_0 = T_{21};\ u_0 = -i\omega Z_L T_{12}. \tag{6.13}$$

6.1.2 Equivalence property in symmetric of band edge-mode

Let us consider a system composed of two dissimilar quasiperiodic rods whose elementary cell is generated according to F_2 GM Fibonacci sequence as illustrated in Figure 6.2. The condition for the presence of an interface mode is $Z_{\text{rhs}} + Z_{\text{lhs}} = 0$, where Z_{rhs} and Z_{lhs} are surface impedance corresponding to the right hand side and the left hand side rod, respectively. The surface impedance Z_j and the reflection coefficient r_j are related by: (Xiao et al. 2014) (2.73)

$$Z_j = \frac{1 + r_j}{1 - r_j} Z_0,\ (j \in \text{lhs}, \text{rhs})$$

where Z_0 is reference impedance. The equation for having interface state can be written as:

$$Z_{\text{rhs}} + Z_{\text{lhs}} = \text{Re}(Z_{\text{rhs}}) + \text{Re}(Z_{\text{lhs}}) + i(\text{Im}(Z_{\text{rhs}}) + \text{Im}(Z_{\text{lhs}})) = 0 \tag{6.14}$$

Considering a frequency inside a band gap for both the right and the left hand side rod, only the imaginary part of surface impedance is non zero, and then the relationship (6.14) becomes:

$$Z_{\text{rhs}} + Z_{\text{lhs}} = i(\text{Im}(Z_{\text{rhs}}) + \text{Im}(Z_{\text{lhs}})) = 0 \ \Rightarrow\ \text{Im}(Z_{\text{rhs}}) = -\text{Im}(Z_{\text{lhs}}) \tag{6.15}$$

Thus, the sign of the imaginary part of surface impedance $\varsigma_j = \text{Im}(Z_j)$ is crucial to predict the presence of an interface mode at a bandgap. A simple way to obtain an interface state is to design a system in which the sign of the imaginary part of the surface impedance (sign$[\varsigma_j]$) from two

quasicrystalline rods is opposite. Several studies have shown that the symmetric property of band-edge mode is related to sgn[ς] and band Zak phase (Xiao et al. 2014; Xiao et al. 2015; Meng et al. 2018; Chen et al. 2021; Muhammad et al. 2019). The band edge mode is the displacement u and axial force N solution for one periodic elementary cell at the normalised Bloch wave number $KL_t = 0, \pi$, because they are the edge between passband and stop band frequency. An antisymmetric (A) edge mode is associated with $N_0 = 0$, whereas a symmetric mode (S) corresponds to $N_0 \neq 0$ (the symmetric and antisymmetry is associated with wave field at the beginning of elementary cell). An illustrative example of the concept of symmetric and antisymmetric edge modes is shown in Figure 6.3 with $E_L = E_S = 70\text{GPa}$; $\rho_L = \rho_s = 2700\text{kgm}^{-3}$; $A_L = 2A_S = 2\times10^{-4}\text{m}^2$ total length $L_t = 0.15\text{m}$, $l_S = 0.05\text{m}$ and $l_L = 0.1\text{m}$ (it represents the canonical ratio $1/2$). Some

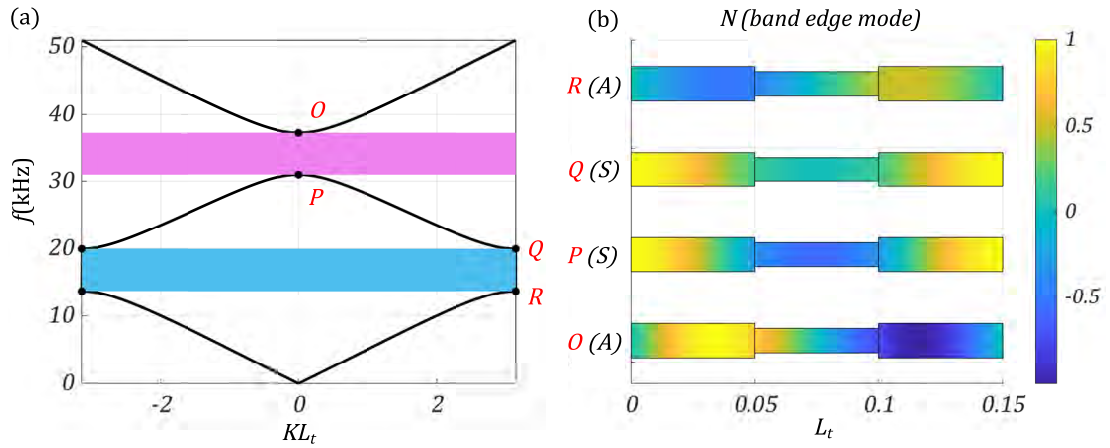

Figure 6.3. The value of the force field of initial R, Q, P and O band edge mode with the symmetric properties A, S, S, A and associated dispersion relation, the cyan and magenta shows the sign of ς negative or positive.

conditions are proved from the displacement function (6.1) and transfer matrix (6.3) (Xiao et al. 2010), and can be checked in Figure 6.3.

(1): The symmetric state must change from (S) to (A) or from (A) to (S) when the frequency passes through a bandgap.

(2): If the (A) state is at the lower edge and (S) state at the upper edge, then $\varsigma < 0$; otherwise, $\varsigma > 0$.

From equations (6.8) and (6.13), we can easily find the conditions for the vanishing of the axial force, which means only one of two terms T_{12} or T_{21} equal to 0. They cannot vanish simultaneously in that case the edge mode becomes undeterminable:

$$T_{12} = 0 \Rightarrow [u_0, N_0]^T = [0,1]^T, \text{ type (S)}; T_{21} = 0 \Rightarrow [u_0, N_0]^T = [1,0]^T, \text{ type (A)} \qquad (6.16)$$

In the next Sections, the condition (6.16) is used together with the notion of canonical structure introduced in Chapter 4 to predict the presence of an interface rods in systems as the one illustrated

in Figure 6.1.

6.2 Interface Modes in Systems Composed of Canonical Rods

6.2.1 The relationship between the sign of surface impedance and canonical period

The symmetry of edge mode determines the sign of surface impedance as frequency is inside a band gap. As anticipated in the previous Section, we will now use these symmetry properties together with the periodicity of the spectrum in order to study the presence of interface modes in a system composed of two canonical quasicrystalline rods. Two different cases are here considered of the two structures: (1): the system is composed of two structures one characterised by canonical ratio C and the other by the inverse $1/C$. (2): the canonical ratio the same but the two phases are swapped. The elementary cells for both case (1) and (2) are shown in Figure 6.4. Let us start by investigating case (1). Using the expressions (6.11) and (6.12) for the axial force and the displacement at $z = 0$ together with the definition of symmetric and antisymmetric mode, for a canonical rod which fundamental cell designed according to F_2 GM sequence and characterized by canonical ratio C, we obtain the conditions:

$$2Z_S Z_L \cos(\xi_S)\sin(\xi_L) + (Z_L^2 - Z_S^2 + (Z_L^2 + Z_S^2)\cos(\xi_L))\sin(\xi_S) = H_1, \text{ if } H_1 = 0: \text{ type (S)}$$

$$2Z_S Z_L \cos(\xi_S)\sin(\xi_L) + (Z_S^2 - Z_L^2 + (Z_L^2 + Z_S^2)\cos(\xi_L))\sin(\xi_S) = H_2, \text{ if } H_2 = 0: \text{ type (A)} \quad (6.17)$$

where H_1 and H_2 have relationship with T_{12} and T_{21}:

$$H_1 = 2Z_L^2 Z_S \omega T_{12};\ H_2 = -2Z_S T_{21}/\omega.$$

Considering a canonical structure which fundamental cell is also designed according to GM F_2 but with inverse canonical ratio $1/C$ we swap the position of ξ_S and ξ_L to derive symmetry conditions W_1 and W_2, which are counterparts of H_1 and H_2. This is possible as the two variables ξ_S and ξ_L are dimensionless and bandgap area is symmetric concerning diagonal on the representation of the universal torus for F_2 as shown in Figure 3.2. The conditions W_1 and W_2 are then:

$$2Z_S Z_L \cos(\xi_L)\sin(\xi_S) + (Z_L^2 - Z_S^2 + (Z_L^2 + Z_S^2)\cos(\xi_S))\sin(\xi_L) = W_1, \text{ if } W_1 = 0: \text{ type (S)}$$

$$2Z_S Z_L \cos(\xi_L)\sin(\xi_S) + (Z_S^2 - Z_L^2 + (Z_L^2 + Z_S^2)\cos(\xi_S))\sin(\xi_L) = W_2, \text{ if } W_2 = 0: \text{ type (A)} \quad (6.18)$$

In order to factorize the conditions (6.17) and (6.18), the following expressions are introduced:

$$Y_1 = Z_S\sin(\frac{\xi_L}{2})\cos(\frac{\xi_S}{2}) + Z_L\cos(\frac{\xi_L}{2})\sin(\frac{\xi_S}{2});\ Y_2 = Z_S\cos(\frac{\xi_L}{2})\cos(\frac{\xi_S}{2}) - Z_L\sin(\frac{\xi_L}{2})\sin(\frac{\xi_S}{2})$$

$$Y_3 = Z_L\sin(\frac{\xi_L}{2})\cos(\frac{\xi_S}{2}) + Z_S\cos(\frac{\xi_L}{2})\sin(\frac{\xi_S}{2});\ Y_4 = Z_L\cos(\frac{\xi_L}{2})\cos(\frac{\xi_S}{2}) - Z_S\sin(\frac{\xi_L}{2})\sin(\frac{\xi_S}{2}) \tag{6.19}$$

and then H_1, H_2, W_1 and W_2 become:

$$4Y_1Y_4 = H_1;\ 4Y_2Y_3 = H_2;\ 4Y_1Y_2 = W_2;\ 4Y_3Y_4 = W_1.$$

The following relationship is also obtained by dispersion relation (6.6):

$$4Y_1Y_3/(Z_LZ_S) = 2 - 2\cos(KL_t);\ 4Y_2Y_4/(Z_LZ_S) = 2\cos(KL_t) + 2 \tag{6.20}$$

Considering the band edge at the centre of Brillouin zone ($KL_t = 0$), we have $Y_1Y_3 = 0$, $Y_2Y_4 \neq 0$, as H_1 and H_2 cannot equal zero simultaneously. This condition is satisfied in two cases: (1). $Y_1 = 0, Y_3 \neq 0$, and then $H_1 = W_2 = 0$. (2). $Y_3 = 0, Y_1 \neq 0$, and then $H_2 = W_1 = 0$. Remembering the properties of the edge modes introduced in Section 6.1.2, the condition $H_1 = W_2 = 0$ corresponds to a symmetric mode at the lower edge of the considered band gap and an antisymmetric one at the upper edge for the structure with canonical ratio C ($\varsigma > 0$), whereas for the rod with ratio $1/C$ we have an antisymmetric mode at the lower edge and a symmetric one at the upper edge ($\varsigma < 0$). Similarly, $H_2 = W_1 = 0$ is associated with to an antisymmetric mode at the lower edge of the considered band gap and a symmetric one at the upper edge for the structure with canonical ratio C ($\varsigma < 0$), whereas for the rod with ratio $1/C$ we have a symmetric mode at the lower edge and an antisymmetric one at the upper edge ($\varsigma > 0$). Thus, the sign of ς is different in the two structures when band edge is the centre of Brillouin zone; The case where the band edge at the boundary of Brillouin zone ($KL_t = \pi$) corresponds to $Y_1Y_3 \neq 0$ and then $Y_2Y_4 = 0$. So there are two possibilities: (1). if $Y_2 = 0, Y_4 \neq 0$, then $H_2 = W_2 = 0$. (2). if $Y_4 = 0, Y_2 \neq 0$, and then $H_1 = W_1 = 0$. Both the conditions $H_2 = W_2 = 0$ and $H_1 = W_2 = 0$ are associated with cases where the symmetry properties of the modes at the lower and upper edge of the considered band gap are the same the structures with canonical ratio C and $1/C$. Thus, the sign of ς is the same in these two structures when band edge is the boundary of Brillouin zone. Consequently, if the two rods with canonical ration C and $1/C$ are connected, an interface mode can occur only inside the band gaps limited by edge mode at the centre of the Brillouin zone.

Let us investigate now the case where the two-phase are swapped, which the position of Z_L and

Z_S are changed because these two variables are symmetric concerning geometric formulation of elementary cell. It is easy to deduce that if the symmetry of band edge mode is fully inverse, then the condition for type(A) in the original structure is the type(S) in the swapped two-phase material structure. As a consequence, the sgn(ς) is inverse in every bandgap. If these two quasicrystalline rods are connected, the interface mode is found in every bandgap. Notice that the two conditions do not affect the dispersion relation, so that the shape for the dispersion spectra are the same. The two structures with one canonical ratio and another with inverse canonical ratio or two-phase material swapping shown in Figure 6.4 are considered and used together with the periodic properties of the spectrum to predict the presence of an interface mode inside an arbitrary band gap.

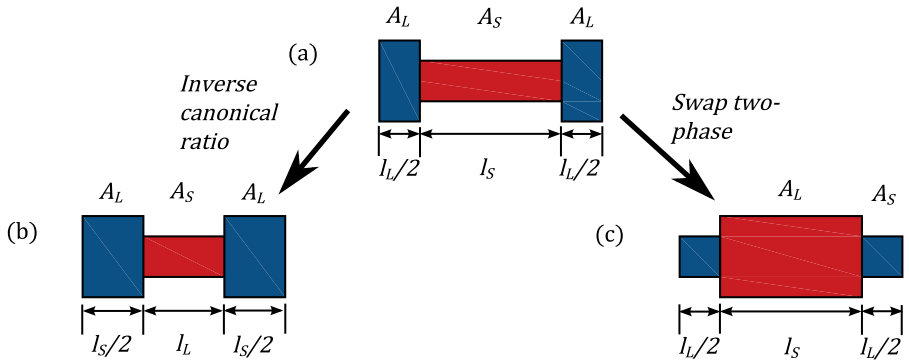

Figure 6.4. Elementary cell changing in this chapter. (a) original elementary cell. (b) inverse canonical ratio. (c) swapping two phases material. Notice that total length L_t is fixed, and for easy illustration, the density and Young's modulus in the two phases are the same.

6.2.2 The periodic property for the sign of surface impedance in canonical family no. 1

The variation of the symmetric properties of edge modes within a canonical period is now analysed using the explicit conditions (6.17) and (6.18), f_t and f_c are the period of the trace and the canonical frequency, respectively and $f_t = 4f_c$. Within a canonical period, two variables ξ_S and ξ_L changes simultaneously according to the values reported in the following table:

Table 6.1. ξ_S and ξ_L are changing with frequency increasing in family no. 1.

f	0	f_c	$2f_c$	f_t
ξ_S	0	$\frac{\pi}{2}(1+2j)$	$\pi(1+2j)$	$2\pi(1+2j)$
ξ_L	0	$\frac{\pi}{2}(1+2k)$	$\pi(1+2k)$	$2\pi(1+2k)$

Due to the periodicity of the symmetry conditions (6.17) and (6.18), it is easy to deduce that for $\xi_S' = \xi_S + 2\pi(1+2j)$ and $\xi_L' = \xi_L + 2\pi(1+2k)$ substituting into symmetric conditions (6.17) and (6.18), the values of H_1, H_2, W_1 and W_2 do not change and neither does the symmetry of modes on

the upper or lower edge of the band gap. The sign of ς keeps the same for band gaps translated by one canonical period. This property is detected for canonical structures of all the three families.

Assuming $\xi_S' = 2\pi(1+2j) - \xi_S$, $\xi_L' = 2\pi(1+2k) - \xi_L$ and substituting into symmetry conditions (6.17) and (6.18) the values still do not change. However, as we can observe in Figure 6.5 (a) and (b), where the edge points associated with this values of ξ_L and ξ_S are reported, the dispersion spectrum is symmetric with respect to the frequency value $f_t/2(2f_c)$. This means that if ξ_S and ξ_L are associated with an edge at the bottom of a band gap, then ξ_L' and ξ_S' correspond to an edge on the top, and vice versa, and similarly the symmetry properties of the edge modes do not change. As a consequence, the band gap corresponding to ξ_S, ξ_L and ξ_L' and ξ_S' have opposite sign of imaginary part of the impedance.

Substituting $\xi_S' = \pi(1+2j) - \xi_S$ and $\xi_L' = \pi(1+2k) - \xi_L$ into symmetry conditions (6.17) and (6.18) we detect that if an antisymmetric edge mode is associated with ξ_S and ξ_L, it becomes symmetric for ξ_S' and ξ_L' and vice versa. However, due to the antisymmetry with respect to the canonical frequency observed in Figure 6.5, the symmetry properties of the modes of the band gap corresponding to ξ_L, ξ_S and ξ_L', ξ_S' are the different, and consequently also same the sign of ς.

The results are illustrated in Figure 6.5, assuming material parameters $E_L = E_S = 70\text{GPa}$; $\rho_L = \rho_s = 2700\text{kgm}^{-3}$; $A_L = 2A_S = 2\times10^{-4}\text{m}^2$ total length $L_t = 0.15\text{m}$ with canonical ratios 3 ($j = 1, k = 0$) and $1/3$, ($j = 0, k = 1$). The Zak phase has been calculated by means of the method in Chapter 3 for verifying the predictions obtained through analysis of edge mode symmetries.

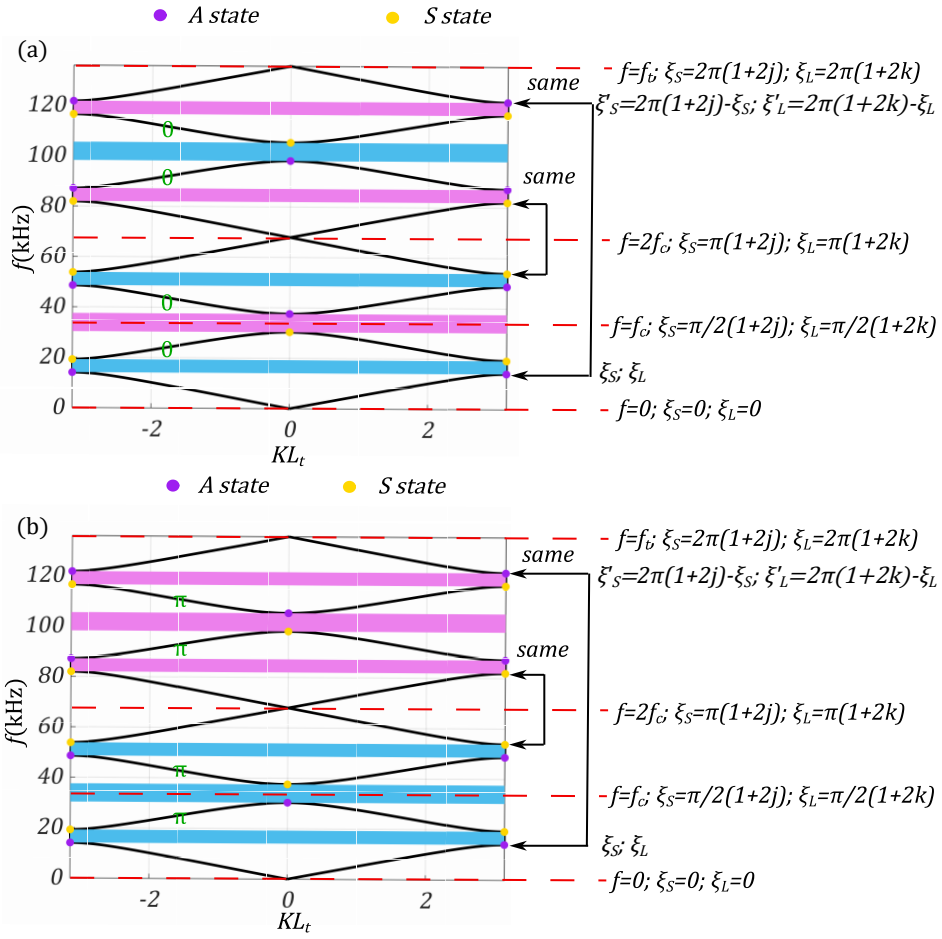

Figure 6.5. The dispersion spectrum (solid black line) of the quasiperiodic rod with canonical ratio $1/3$ *(a) and* 3 *(b). The material parameters are* $E_L = E_S = 70GPa$; $\rho_L = \rho_s = 2700kgm^{-3}$; $A_L = 2A_S = 2 \times 10^{-4}m^2$ *Total length* $L_t = 0.15m$. *The light magenta represents the gap with* $\varsigma > 0$, *while the cyan strip represents the gap* $\varsigma < 0$. *The Zak phase of each individual band is labeled in green. The solid purple circle is the A state at the band edge, and the yellow one is the S state, the black arrows target same symmetric properties for edge mode.*

Observing Figure 6.5, we can conclude that for family no. 1, the symmetry properties of band edge mode within a canonical period are symmetric with respect to the frequency $f = 2f_c$, while if we analyse an half-canonical period they are antisymmetric with respect to the canonical frequency f_c. It is also important to note that the structure with inverse canonical ratio possesses the same symmetry properties and then the same sign of the imaginary impedance for band gaps limited by points at the edge of the Brillouin zone, while opposite symmetry properties and then opposite sign[ς] for those limited by points at the centre of the Brillouin zone. This means that, according the condition (6.15), for a system composed of two canonical rods of family 1 corresponding to canonical ratios C and $1/C$, an interface mode can be found inside band gaps limited by points at the centre of Brillouin zone.

6.2.3 The periodic property for the sign of surface impedance in canonical families no. 2 and 3

Let us consider now a canonical rod of family no. two within a canonical period f_t, the two variables ξ_S and ξ_L change according to the values reported in the following table:

Table 6.2. ξ_S and ξ_L are changing with frequency increasing in family no. 2.

f	0	f_c	$2f_c$	f_t
ξ_S	0	$\frac{\pi}{2}(1+2j)$	$\pi(1+2j)$	$2\pi(1+2j)$
ξ_L	0	$\pi(q)$	$\pi(2q)$	$2\pi(2q)$

Substituting $\xi_S' = 2\pi(1+2j) - \xi_S$ and $\xi_L' = 2\pi(2q) - \xi_L$ into symmetry conditions (6.17) and (6.18) the values of H_1, H_2, W_1 and W_2 do not change. However, similarly to what we have observed in Figure 6.5 for canonical family no. 1 the dispersion spectrum is symmetric with respect to the frequency value $f = 2f_c$. This means that if ξ_S and ξ_L are associated with an edge at the bottom of a band gap, then ξ_L' and ξ_S' correspond to and edge on the top, and vice versa, and similarly the symmetry properties of the edge modes do not change. As a consequence, the band gap corresponding to ξ_L, ξ_S and ξ_L' and ξ_S' have opposite sign of imaginary part of the impedance.

Assuming $\xi_S' = \pi(1+2j) - \xi_S$ and $\xi_L' = \pi(2q) - \xi_L$ the values of the symmetric conditions (6.17) and (6.18) still do not change. However, as it is observed in Figure 6.6, also in this case if ξ_S and ξ_L are associated with an edge at the bottom of a band gap, then ξ_L' and ξ_S' correspond to and edge on the top, and vice versa, and similarly the symmetry properties of the edge modes do

not change, and sign[ς] is changed.

In family no. three, ξ_S and ξ_L evolve within a canonical period as follows:

Table 6.3. ξ_S and ξ_L are changing with frequency increasing in family no. 3.

f	0	f_c	$2f_c$	f_t
ξ_S	0	$\pi(q)$	$\pi(2q)$	$2\pi(2q)$
ξ_L	0	$\frac{\pi}{2}(1+2k)$	$\pi(1+2k)$	$2\pi(1+2k)$

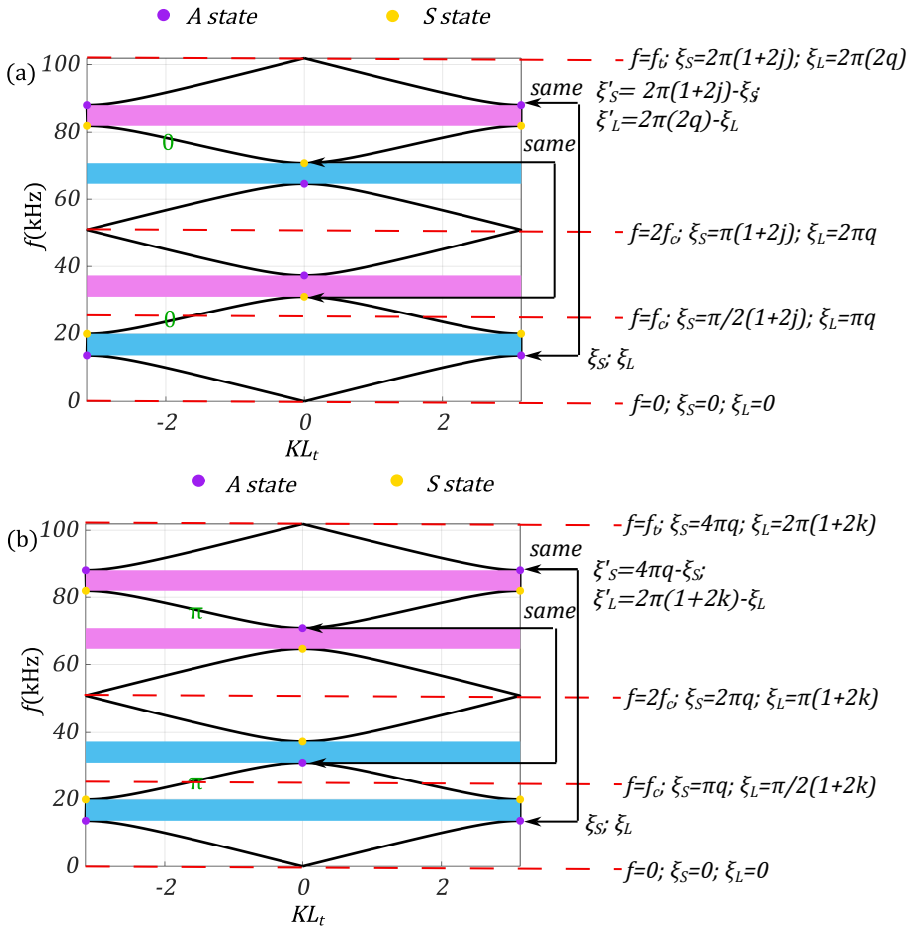

Figure 6.6. The dispersion spectrum (solid black line) of the quasiperiodic rod with canonical ratio 1/2 (a) and 2 (b). The material parameters are $E_L = E_S = 70GPa$; $\rho_L = \rho_s = 2700kgm^{-3}$; $A_L = 2A_S = 2 \times 10^{-4}m^2$ Total length $L_t = 0.15m$. The light magenta represents the gap with $\varsigma > 0$, while the cyan strip represents the gap $\varsigma < 0$. The Zak phase of each individual band is labeled in green. The solid purple circle is the A state at the band edge, and the yellow one is the S state, the black arrows target same symmetric properties for edge mode.

For family no. 3, the properties of the band edge modes possesses the same symmetry properties with respect f_c detected for family no. 2, and consequently also the sign of the imaginary part of the impedance changes similarly from a band gap to another one. In Figure 6.6 the spectra for two rods with the same geometrical and physical parameter of Figure 6.5 and canonical ratio 1/2 and

2 are shown (family no. 2 and 3).

Observing Figure 6.6, we can conclude that for families no. 2 and 3, the symmetry properties of band edge mode within a canonical period are symmetric with respect to the frequency $f = 2f_c$, while if we analyse an half-canonical period ($2f_c$) they are symmetric with respect to the canonical frequency f_c for family no. 2 and antisymmetric for family no. 3, respectively. It is also important to note that the structure with inverse canonical ratio possesses the same symmetry properties and then the same sign of the imaginary impedance for band gaps limited by points at the edge of the Brillouin zone ($KL_t = \pi$), while opposite symmetry properties and then opposite sign[ς] for those limited by points at the centre of the Brillouin zone ($KL_t = 0$). This means that, according the condition (6.15), for a system composed of two canonical rods of family 2 and 3 corresponding to canonical ratios C and $1/C$, an interface mode can be found inside band gaps as Bloch wave number is $KL_t = 0$.

The results of three canonical families are reported in the following table where the relationship between sign of ς detected in any band gap within the first canonical frequency ($f \in [0, f_c]$) compared with the cases in other bandgaps:

Table 6.4. The sign of ς in first canonical frequency $f \in [0, f_c]$ changing with different frequencies

	$f = f + f_c$	$f = f + 2f_c$	$f = f + f_t$
Family no. 1	ς same	ς opposite	ς same
Family no. 2	ς opposite	ς same	ς same
Family no. 3	ς same	ς opposite	ς same

6.2.4 Predicting the sign of impedance using the extended toroidal representation

The general representation of the spectrum on an universal toroidal surface illustrated in recent works (Shmuel and Band 2016, Morini et al. 2019b) is now used to predict the sign of the imaginary part of the impedance within a canonical period.

Assuming this general representation, for a canonical rod generated by Fibonacci F_2 cell, the boundary of the band gap subdomain on the reduced torus is given by the expression introduced for canonical laminates in Chapter 3:

$$\tan(\frac{\xi_L}{2}) = (\frac{\beta}{2} - \sqrt{\frac{\beta^2}{4} - 1})\cot(\frac{\xi_S}{2}) \tag{6.21}$$

where β is:

$$\beta = (Z_L^2 + Z_S^2)/(Z_S Z_L)$$

If a point (ξ_S, ξ_L) lies on the curve (6.21), it is associated with the edge of a band gap on the frequency spectrum. Using equation (6.21) together with the symmetry conditions (6.17), the following alternative expressions are obtained:

$$Z_L \cos(\frac{\xi_L}{2})\cos(\frac{\xi_S}{2}) - Z_S \sin(\frac{\xi_L}{2})\sin(\frac{\xi_S}{2}) = Y_2 = 0, (Z_S > Z_L);$$

$$Z_S \cos(\frac{\xi_L}{2})\cos(\frac{\xi_S}{2}) - Z_L \sin(\frac{\xi_L}{2})\sin(\frac{\xi_S}{2}) = Y_4 = 0, (Z_L > Z_S) \quad (6.22)$$

Due to the properties of the trigonometric functions, the first band gap is associated with $\cos(KL_t) < -1$. This means that, remembering the relationships $H_1 = 4Y_1Y_4$ and $H_2 = 4Y_2Y_3$ (see equation (6.20)), the condition (6.22) becomes:

$$(Z_L > Z_S) \Rightarrow H_2 = 0, \text{ type (A)}; \ (Z_S > Z_L) \Rightarrow H_1 = 0, \text{ type (S)} \quad (6.23)$$

Consequently, in cases where $Z_L > Z_S$, the lower band edge mode of the first bandgap is asymmetric, and then the sign of ς is always negative (cyan in the figure) inside the first bandgap. This result is in agreement with Xiao et al. (2014) ($\text{sgn}(\varsigma) = -\text{sgn}(1 - Z_S/Z_L)$). By using the periodicity of the spectrum the variables ξ_L and ξ_S are modulated by adding integer multiples of π, $\xi_L' = \xi_L + m\pi$ and $\xi_S' = \xi_S + n\pi$ ($m, n \in \mathbb{N}$), the m and n can be odd or even numbers. The values of the conditions (6.17) are analyzed for all possible combinations of odd and even numbers m and n, and then related to the symmetry of the band edge modes and the changes of sign[ς]. The results of this study are reported in the following table where the sign of ς detected in any band gap of the canonical period is compared with the first one:

Table 6.5. The sign of ς changing with different m and n

n: odd; m: odd	n: odd; m: even	n: even; m: odd	n: even; m: even
ς opposite	ς same	ς opposite	ς same

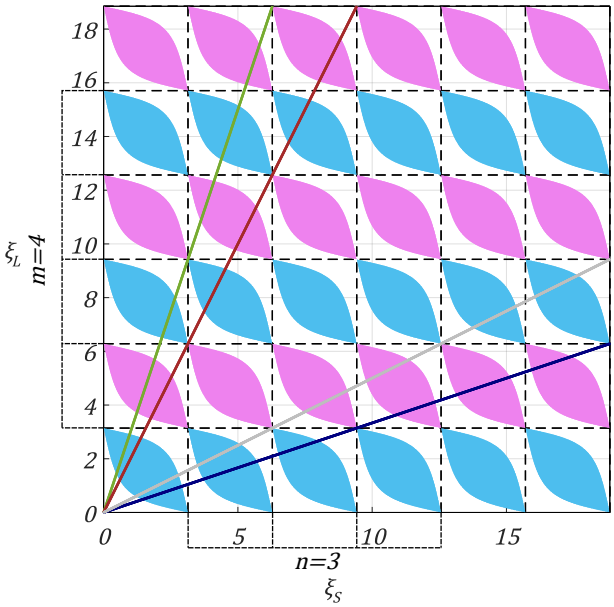

Figure 6.7. Extension torus with range of ξ_S and ξ_L are both 6π. The color domain represents the band gap, which light magenta is $\varsigma > 0$ while the cyan $\varsigma < 0$. There are four different flow lines, which are green (representing the $C = 1/3$), deep blue ($C = 3$), brown ($C = 1/2$), grey ($C = 2$).

The band gaps on the two-dimensional toroidal domain can be represented by different colours associated with $\varsigma > 0$ and $\varsigma < 0$. The ranges for ξ_L and ξ_S do not need to be reduced into π currently. For illustration, the ξ_L and ξ_S are increased to 6π as shown in Figure 6.7, which is called extension torus in this thesis. Magenta band gaps are associated with $\varsigma > 0$ while cyan correspond to $\varsigma < 0$. The slope of the flow line is the inverse of the canonical ratio.

The different slope flow lines in Figure 6.7 correspond to the dispersion spectra shown in Figures 6.5 and 6.6. Moreover, in case where the flow line pass through the transitional point the sign of ς can change. This is the so-called bandgap closeing and reopening process (band inversion). The plot in Figure 6.7 can help engineers to design topological interface states by varying the slope of the flow line in order to pass through the topological point in an arbitrary bandgap. Then, an interface state within the band gap for a particular combination of two quasicrystalline rods can be predicted. A plot similar to the one illustrated in Figure 6.7 can be used for non-canonical structures, associated with slope of flow line given by number.

The band crossing points can be determined quantitatively by means of the extended toroidal representation. The transitional point is associated with $(\xi_S, \xi_L) = (n\pi, m\pi)$, so that the frequency at the band crossing point is:

$$f = \frac{\mathcal{M}(n+m)}{2(l_L\sqrt{\rho_L/E_L} + l_S\sqrt{\rho_S/E_S})} \ (\mathcal{M} \in \mathbb{N}^+) \tag{6.24}$$

If the flow line passes through the band crossing point, then the structure is a canonical one, because in this case $\xi_S/\xi_L = n/m$ is a rational number. The number of the bandgaps in the canonical period for Fibonacci order F_2 can be determined by means of the extended torus. it is given by:

$$C^{(1)} : 4(j+k)+2;\ C^{(2)} : 4(j+q);\ C^{(3)} : 4(k+q) \tag{6.25}$$

where $C^{(1)}$, $C^{(2)}$, $C^{(3)}$ indicates canonical family no. 1, 2 and 3, respectively. The sign of imaginary part of impedance of arbitrary bandgap can be predicted by means of the extended torus and then this approach can be applied to create a system with two different structures to have a interface state as frequency is in bandgap. An exact formula for the frequency of the interface state is derived for a particular combination of two canonical rods in Section 6.3.

6.2.5 Condition for coincident dispersion in two quasicrystalline rods

In this section same two combinations of quasicrystalline rods introduced in Subsection 6.2.1 are considered: (1) a system composed of one rod with canonical ratio and other with inverse canonical ratios (2) another composed of two rods with the same canonical ratio and swapped two-phase materials. The condition for having identical dispersion spectrum for both combination (1) and (2) is now derived. First, the expressions for two variables of left hand side quasicrystalline rods (without inverse canonical ratio and without exchange two-phase material) are rewritten into:

$$\xi_L^{(o)} = \frac{l_L^{(o)}\omega^{(o)}}{c_L};\ \xi_S^{(o)} = \frac{l_S^{(o)}\omega^{(o)}}{c_S} \tag{6.26}$$

Superscript (o) denotes the original quasicrystalline rod expression. Remembering the total length of the fundamental cell is $l_L^{(o)} + l_S^{(o)} = L_t^{(o)}$, and using the canonical ratio, the frequency $\omega^{(o)}$ corresponding to $(\xi_L^{(o)}, \xi_S^{(o)})$ can be obtained:

$$\omega^{(o)} = \frac{\xi_L^{(o)}(c_L + Cc_S)}{L_t^{(o)}} = \frac{\xi_S^{(o)}(c_L + Cc_S)}{CL_t^{(o)}} \tag{6.27}$$

where C is canonical ratio. Similarly, for the right (other) quasicrystalline rod with inverse canonical ratio by the same two-phase material (case(1)), the two variables $\xi_L^{(i)}$, $\xi_S^{(i)}$ and frequency $\omega^{(i)}$ can be defined:

$$\xi_L^{(i)} = \frac{l_L^{(i)}\omega^{(i)}}{c_L};\ \xi_S^{(i)} = \frac{l_S^{(i)}\omega^{(i)}}{c_S} \tag{6.28}$$

$$\omega^{(i)} = \frac{\xi_L^{(i)}(Cc_L + c_S)}{CL_t^{(i)}} = \frac{\xi_S^{(i)}(Cc_L + c_S)}{L_t^{(i)}} \tag{6.29}$$

Superscript (i) denote the condition for the right quasicrystalline rod with inverse canonical ratio compared with the left (original) one. Moreover, duplicating the process into the right quasicrystalline rods with exchanging two phases material with fixed the same canonical ratio (case (2)), the two variables $\xi_L^{(e)}$, $\xi_S^{(e)}$ and frequency $\omega^{(e)}$ are introduced:

$$\xi_L^{(e)} = \frac{l_L^{(e)}\omega^{(e)}}{c_S};\ \xi_S^{(e)} = \frac{l_S^{(e)}\omega^{(e)}}{c_L} \tag{6.30}$$

$$\omega^{(e)} = \frac{\xi_L^{(e)}(Cc_L + c_S)}{L_t^{(e)}} = \frac{\xi_S^{(e)}(Cc_L + c_S)}{CL_t^{(e)}} \tag{6.31}$$

For the case of inverse canonical ratio, we have $\xi_L^{(i)} = \xi_S^{(o)}$ and $\xi_S^{(i)} = \xi_L^{(o)}$. If the two phases material are swapped, then the $\xi_L^{(e)} = \xi_L^{(o)}$ and $\xi_S^{(e)} = \xi_S^{(o)}$. Finally, conditions for frequency

$\omega^{(o)} = \omega^{(i)}$ and $\omega^{(o)} = \omega^{(e)}$ are:

$$\omega^{(o)} = \omega^{(i)} \rightleftharpoons \frac{L_t^{(i)}}{L_t^{(o)}} = \frac{Cc_L + c_S}{c_L + Cc_S};\ \omega^{(o)} = \omega^{(e)} \rightleftharpoons \frac{L_t^{(e)}}{L_t^{(o)}} = \frac{Cc_L + c_S}{c_L + Cc_S}; \tag{6.32}$$

Wave phase speed c_L, c_S and canonical ratio C are associated with the left quasicrystalline rods (original one). If conditions (6.32) are satisfied, then the dispersion spectra of left-hand side and right-hand side rod are identical. Therefore, the total length for the right quasicrystalline rods could be changed according to the expression (6.32). However, for the numerical examples considered in this thesis, because $c_L = c_S$, the frequency in dispersion relation is the same without changing total length.

6.3 Surface Impedance and Reflection Coefficients in Finite Rods

An exact formula for the frequency of the interface state mode is derived in this Section for the case of a system composed of two periodic rods with canonical ratio C and $1/C$. We consider two finite rods which elementary cell is generated according to Fibonacci F_2 cell, both composed of $\mathcal{N}$ unit cells and satisfying the condition for having the same dispersion spectrum (6.32).

6.3.1 Exact formula for frequency at the interface state

According to surface impedance expression (6.15), the explicit condition for interface state is:

$$\mathrm{Im}\left(\frac{1 + r_{\mathrm{lhs}}}{1 - r_{\mathrm{lhs}}}\right) + \mathrm{Im}\left(\frac{1 + r_{\mathrm{rhs}}}{1 - r_{\mathrm{rhs}}}\right) = 0 \tag{6.33}$$

Therefore, we need to evaluate the reflection coefficients for both left hand side and right hand side structure in order to determine the frequency for the interface state. Let us consider the finite quasicrystalline rods with $\mathcal{N}$ unit cell all information concerning the wave propagation are given by the transfer matrix is already shown in Chapter 3:

$$\begin{bmatrix} a_{\mathcal{N}} \\ b_{\mathcal{N}} \end{bmatrix} = \begin{bmatrix} \mathbf{f}_{11} & \mathbf{f}_{12} \\ \mathbf{f}_{21} & \mathbf{f}_{22} \end{bmatrix}^{\mathcal{N}} \begin{bmatrix} a_0 \\ b_0 \end{bmatrix} \equiv \mathbf{F}_t \begin{bmatrix} a_0 \\ b_0 \end{bmatrix} \tag{6.34}$$

where a_0 and b_0 are the amplitude coefficients of incident and reflected waves at the incident side of structure whereas $a_{\mathcal{N}}$ and $b_{\mathcal{N}}$ are the counterparts at the output side. $\mathbf{F}_t$ is the global transfer matrix previously introduced. In order to calculate the transmission coefficients for the finite quasicrystalline rods, the amplitude of the reflected wave at the output side is assumed to be

($b_{\mathcal{N}} = 0$). As a result, the wave reflection coefficient and transmission coefficient are:

$$r = -\frac{b_0}{a_0} = \frac{\mathbf{F}_t(2,1)}{\mathbf{F}_t(2,2)},\ t_{\mathcal{N}} = \left|\frac{a_{\mathcal{N}}}{a_0}\right|^2 = \left|\mathbf{F}_t(1,1) - \frac{\mathbf{F}_t(1,2)\mathbf{F}_t(2,1)}{\mathbf{F}_t(2,2)}\right|^2 \tag{6.35}$$

where $\mathbf{F}_t(i,j)$ are the components of the global transfer matrix. Since the $\mathbf{F}$ matrix is unimodular, the $\mathcal{N}$th power of this matrix can be expressed by Chebyshev's identity (Yeh et al. 1977):

$$\begin{bmatrix} \mathbf{f}_{11} & \mathbf{f}_{12} \\ \mathbf{f}_{21} & \mathbf{f}_{22} \end{bmatrix}^{\mathcal{N}} = \begin{bmatrix} \mathbf{f}_{11}U_{\mathcal{N}-1} - U_{\mathcal{N}-2} & \mathbf{f}_{12}U_{\mathcal{N}-1} \\ \mathbf{f}_{21}U_{\mathcal{N}-1} & \mathbf{f}_{22}U_{\mathcal{N}-1} - U_{\mathcal{N}-2} \end{bmatrix} \tag{6.36}$$

where $U_{\mathcal{N}} = \sin((\mathcal{N}+1)KL_t)/\sin(KL_t)$ and the KL_t is the normalised Floquet-Bloch wavenumber coming from dispersion relation (6.4). Then, the reflection coefficient becomes:

$$r = -\frac{b_0}{a_0} = -\frac{\frac{\mathrm{i}}{2}(\frac{Z_S}{Z_L} - \frac{Z_L}{Z_S})\sin(\xi_S)\sin(\mathcal{N}KL_t)}{e^{(-\mathrm{i}\xi_L)}(\cos(\xi_S) - \frac{\mathrm{i}}{2}(\frac{Z_S}{Z_L} + \frac{Z_L}{Z_S})\sin(\xi_S))\sin(\mathcal{N}KL_t) - \sin((\mathcal{N}-1)KL_t)} \tag{6.37}$$

The imaginary part of the ratio of the relative impedance Z/Z_0 can be derived by using equation (6.37). Substituting expression (6.37) in equation (6.33) and remembering that since we are considering a frequency inside a band gap the impedance Z_0 is Z_L, and $\sin(\mathcal{N}KL_t)$ are pure imaginary numbers and $H_1H_2 = 4Z_L^2Z_S^2\sin^2(KL_t)$ is a real number. $\mathrm{Im}(Z/Z_0)$ can be simplified as:

$$\mathrm{Im}(\frac{Z}{Z_0}) = \mathrm{Im}(\frac{1+r}{1-r}) = \frac{4Z_LZ_S\sin(\mathcal{N}KL_t)\cos(\mathcal{N}KL_t)\sin(KL_t)(Z_L^2 - Z_S^2)\sin(\xi_S)}{H_1^2 + 2\sin(\xi_S)H_1(Z_S^2 - Z_L^2)\cos^2(\mathcal{N}KL_t)} \tag{6.38}$$

and:

$$\mathrm{Re}(\frac{Z}{Z_0}) = \mathrm{Re}(\frac{1+r}{1-r}) = \frac{4Z_L^2Z_S^2\sin^2(KL_t)}{H_1^2 + 2\sin(\xi_S)H_1(Z_S^2 - Z_L^2)\cos^2(\mathcal{N}KL_t)}. \tag{6.39}$$

Let us consider KL_t corresponding to frequency inside a band gap:

$$KL_t = n\pi + i\overline{K} \tag{6.40}$$

where $\overline{K} > 0$ and describe the decay length inside the band gap (Xiao et al. 2014). Thus, the term $\cos^2(\mathcal{N}KL_t) = \cosh^2(\mathcal{N}\overline{K})$. As the number of unit cells $\mathcal{N}$ increases, the term $\cosh^2(\mathcal{N}\overline{K}) \approx \infty$ due to the properties of hyperbolic cosine function leading to $\mathrm{Re}(\frac{Z}{Z_0}) \approx 0$ and term H_1 is independent of number $\mathcal{N}$, in agreement with the definition of $\mathrm{Re}(\frac{Z}{Z_0}) = 0$ in semi-infinity rod theory for the case of a frequency inside a bandgap.

The same material parameters considered for the numerical examples shown Section 6.1 are chosen and the canonical ratio $1/3$ and 3 are assumed. The frequency range is canonical period as

shown in Figure 6.8. From the Figure 6.8, with the increasing number of unit cells $\mathcal{N}$, the abso-

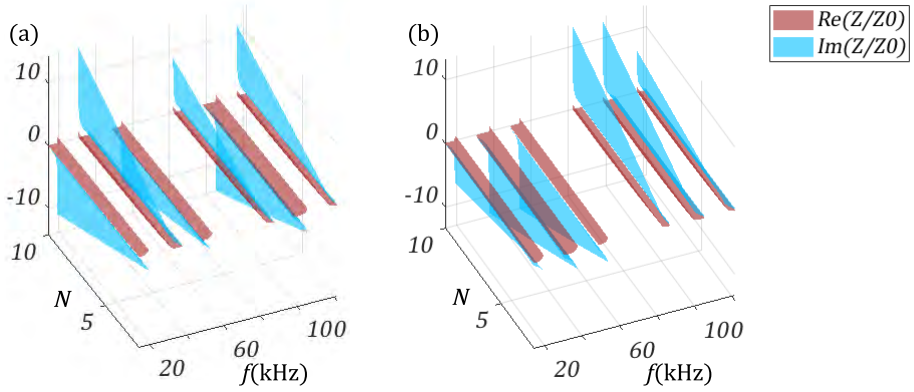

Figure 6.8. The real part and imaginary part of $\frac{Z}{Z_0}$ *in the bandgap, The brown and light blue represents the real and imaginary part of the quasiperiodic rod with canonical ratio* $1/3$ *(a) and* 3 *(b), respectively.*

lute value for the imaginary part of Z/Z_0 is decreased inside the bandgap, in agreement with the predictions of the monotonic decreasing from ∞ to 0 or 0 to $-\infty$ predicted by semi-infinite theory (Xiao et al. 2014). The real part keeps stable and close to 0, which is also consistent to what expected by the theory when the frequency is in a bandgap.

As we anticipated, the left-hand side and right-hand side rods satisfy the condition (6.32) for having the same the dispersion relation layouts, and consequently the normalised Bloch wave number KL_t is the same. Also the number of unit cells $\mathcal{N}$ in these two structures is same, then $\sin(\mathcal{N}KL_t)$, $\sin((\mathcal{N}-1)KL_t)$ and $\cos(KL_t)$ have the same value for these two configurations. Assuming that the equation (6.38) is associated with the left-hand side rod with canonical ratio C, we introduce another particular expression corresponding to the right hand side with ratio $1/C$ exchanging the position of ξ_S and ξ_L ($H_1 \Rightarrow W_1$):

$$\mathrm{Im}(\frac{Z}{Z_0}) = \mathrm{Im}(\frac{1+r}{1-r}) = \frac{4Z_L Z_S \sin(\mathcal{N}KL_t)\cos(\mathcal{N}KL_t)\sin(KL_t)(Z_L^2 - Z_S^2)\sin(\xi_L)}{W_1^2 + 2\sin(\xi_L)W_1(Z_S^2 - Z_L^2)\cos^2(\mathcal{N}KL_t)} \tag{6.41}$$

By summing up (6.38) and (6.41), we obtain:

$$H_1^2\sin(\xi_L) + W_1^2\sin(\xi_S) + (H_1 + W_1)(2\sin(\xi_L)\sin(\xi_S)(Z_S^2 - Z_L^2)\cos^2(\mathcal{N}KL_t)) = 0 \tag{6.42}$$

The frequency satisfying equation (6.42) is associated with the interface mode inside the band gap. From the results derived by (Xiao et al. 2014), if an interface state exists in these structure combination, equation (6.42) has only one solution. We can deduce that the unique solution is

given by the pair of values (ξ_S, ξ_L) satisfying:

$$\sin(\xi_S) = -\sin(\xi_L) \neq 0; \;\; \cos(\xi_S) = \cos(\xi_L) \tag{6.43}$$

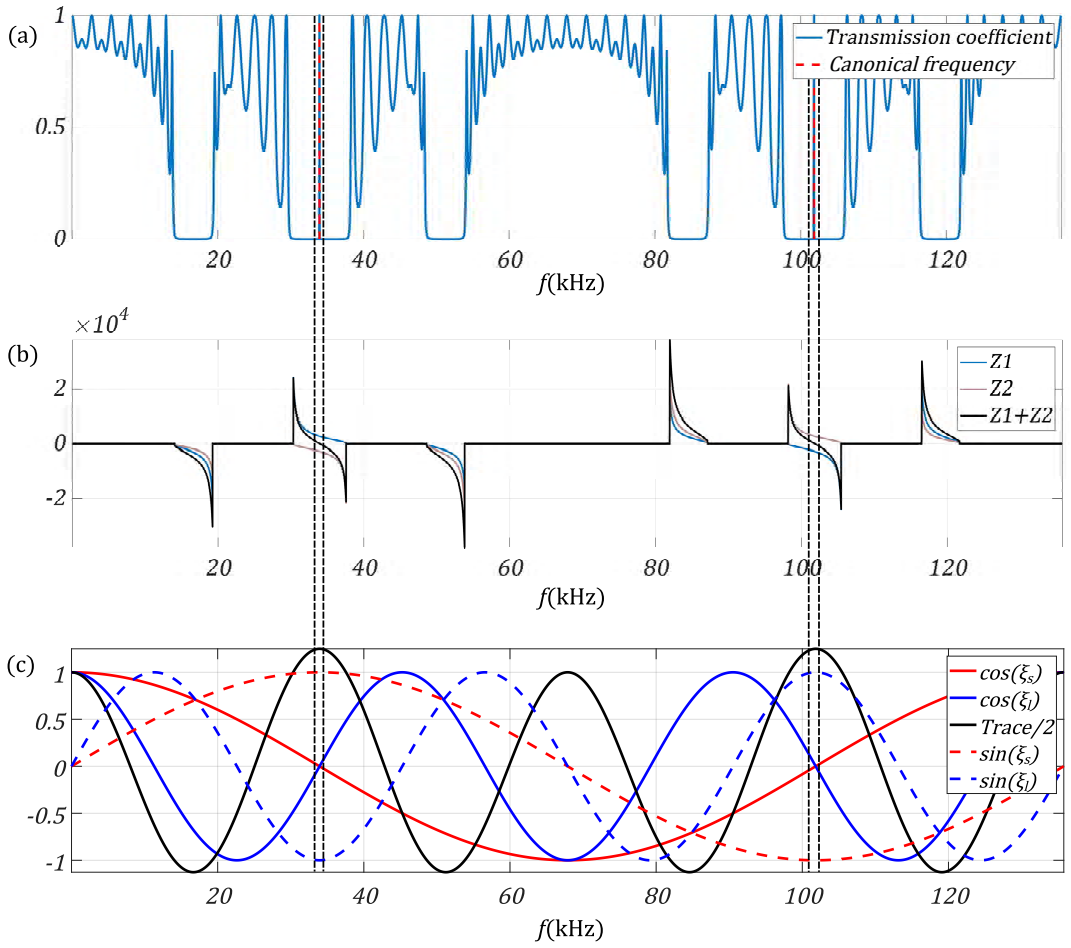

Figure 6.9. (a): The transmission spectrum of the system with canonical ratio $1/3$ *and* 3 *(left and right) with* 6 *unit cells, respectively. The interface state are coincident with canonical frequency. (b): The imaginary part of relative surface impedance of canonical rod of ratio* $1/3$ *(*$Z1$*, solid cyan line) and* 3 *(*$Z2$*, solid brown line), and the sum of the two (solid black line) inside the band gap region. (c): The plot of* $\cos(\xi_S)$*,* $\cos(\xi_L)$*,* $\sin(\xi_S)$*,* $\sin(\xi_L)$ *and half trace. The canonical ratio is* $1/3$*.*

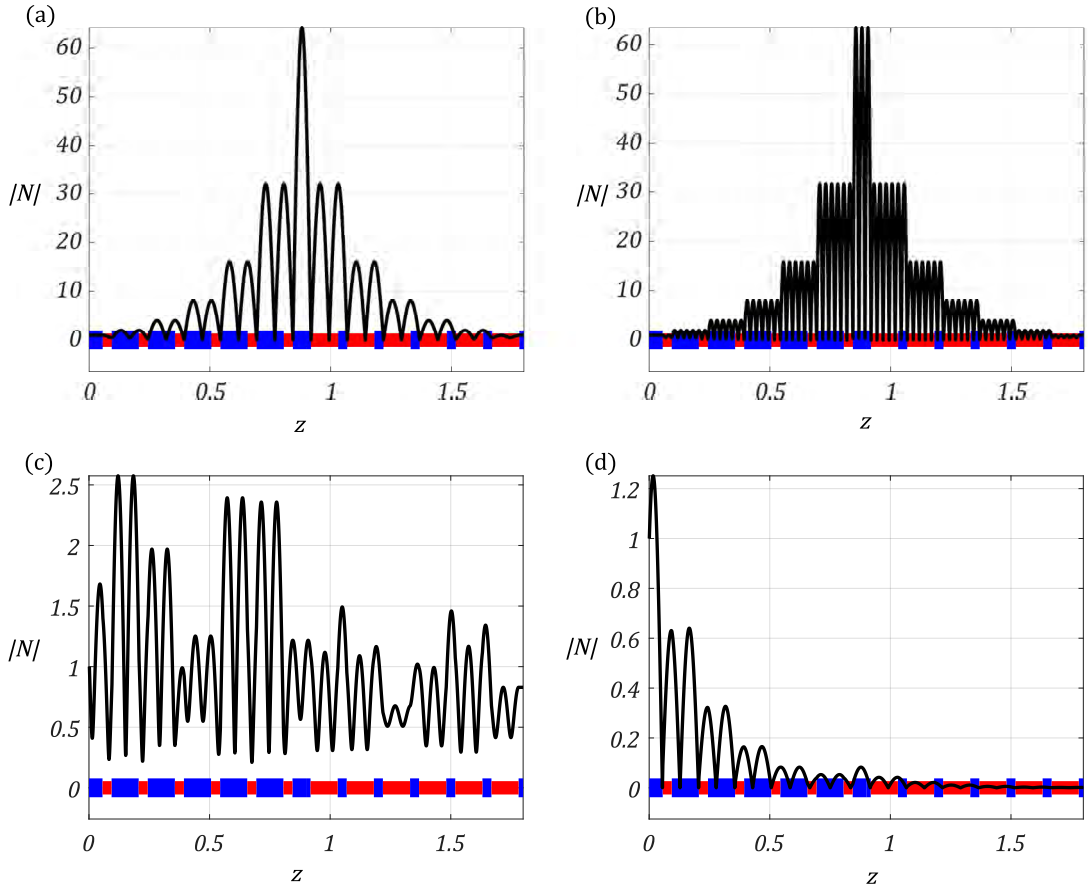

Figure 6.10. Numerical calculation of absolute value of the force field at the interface state associated with the system with canonical ratio 1/3 and 3 (left and right). The material parameters are same with Figure 6.9 (a)*:* $f = 33.945kHz$ *(interface state).* (b)*:* $f = 101.835kHz$ *(interface state).* (c)*:* $f = 40kHz$ *(passband).* (d)*:* $f = 33kHz$ *(bandgap).*

By means of trigonometric formulas, the equation (6.43) can be transformed in the coupled system:

$$\sin(\xi_S) + \sin(\xi_L) = 0 \Rightarrow 2\sin(\frac{\xi_S + \xi_L}{2})\cos(\frac{\xi_L - \xi_S}{2}) = 0 \tag{6.44}$$

$$\cos(\xi_S) - \cos(\xi_L) = 0 \Rightarrow 2\sin(\frac{\xi_S + \xi_L}{2})\sin(\frac{\xi_L - \xi_S}{2}) = 0 \tag{6.45}$$

The solution of coupled equations (6.44) and (6.45) is given by the values of ξ_S and ξ_L satisfying $\sin((\xi_S + \xi_L)/2) = 0$ and the corresponding frequency is:

$$f = \frac{n_1}{(1+C)l_L}\sqrt{\frac{E_L}{\rho_L}} = \frac{Cn_1}{(1+C)l_S}\sqrt{\frac{E_S}{\rho_S}},\ n_1 \in \mathbb{N} \tag{6.46}$$

Notice that $2n_1/(1+C)$ and $2Cn_1/(1+C)$ are not solutions of it because the $\sin(\xi_L) = \sin(\xi_S) = 0$ corresponds to passband. Also, the total length L_t of these two different rods must be adjusted in order to satisfy the condition for identical dispersion spectrum (equation (6.32)).

The exact formula (6.46) is valid under two conditions, (1). the two-phase material cannot be

changed. (2), the number of unit cells $\mathcal{N}$ must be identical in both left and right hand side rods. Figure 6.9 concerns a left quasicrystalline rods with canonical ratio with $C = 1/3$ and a right hand side $C = 3$. In the figure we report in part (a) the transmission coefficient for this whole system, in part (b) the imaginary part of impedance for these two different structures and whole system as frequency in bandgap and in part (c) the plot of $\cos(\xi_S)$, $\cos(\xi_L)$, $\sin(\xi_S)$, $\sin(\xi_L)$. The results from Figure 6.9 tell us that the frequency of interface state corresponds to transmission peak in transmission coefficients, zero value of summation of impedance for two structure $(Z_1 + Z_2)$ and the numerical value of the frequency of the interface mode is the one evaluated by formula (6.46). Figure 6.11 shows case for the combination of canonical ratio $C = 1/2$ and $C = 2$.

The axial force fields reported in Figure 6.10, calculated numerically for the values of the canonical ratios $C = 3$ and $C = 1/3$, are in good agreement with the theoretical predictions. The absolute value of the force field is localized at the interface between two quasicrystalline rods, and it decays dramatically towards the ends of mixed waveguides. This is an evident sign of the interface states due to the topological conflict of the distinct states. Moreover, the wave field for frequency which is in passband and bandgap are shown here for comparison, the axial force amplitude at the interface is 60 more times than the input signals. For the case for system combined with canonical ratio $C = 1/2$ and $C = 2$ we detected similar results with the force amplitude at the interface being 35 more times than the input signals.

6.3.2 The method to place the interface state at the centre of the bandgap

The frequency of an interface state for a system composed of two rods with canonical ratio C and $1/C$ is given by equation (6.43). We now determine the condition for having the interface state at the centre of bandgap. Let us assume that the $\xi_L - \delta$ and $\xi_S - C\delta$ correspond to the frequency at the edge of the bandgap. Remembering the dispersion relation (6.6): (Note: $\xi_S = C\xi_L$)

$$\cos(\xi_L - \delta)\cos(C(\xi_L - \delta)) - \frac{\beta}{2}\sin(\xi_L - \delta)\sin(C(\xi_L - \delta)) = \pm 1 \tag{6.47}$$

If the interface state is at the bandgap centre, the following additional dispersion relation should be satisfied:

$$\cos(\xi_L + \delta)\cos(C(\xi_L + \delta)) - \frac{\beta}{2}\sin(\xi_L + \delta)\sin(C(\xi_L + \delta)) = \pm 1 \tag{6.48}$$

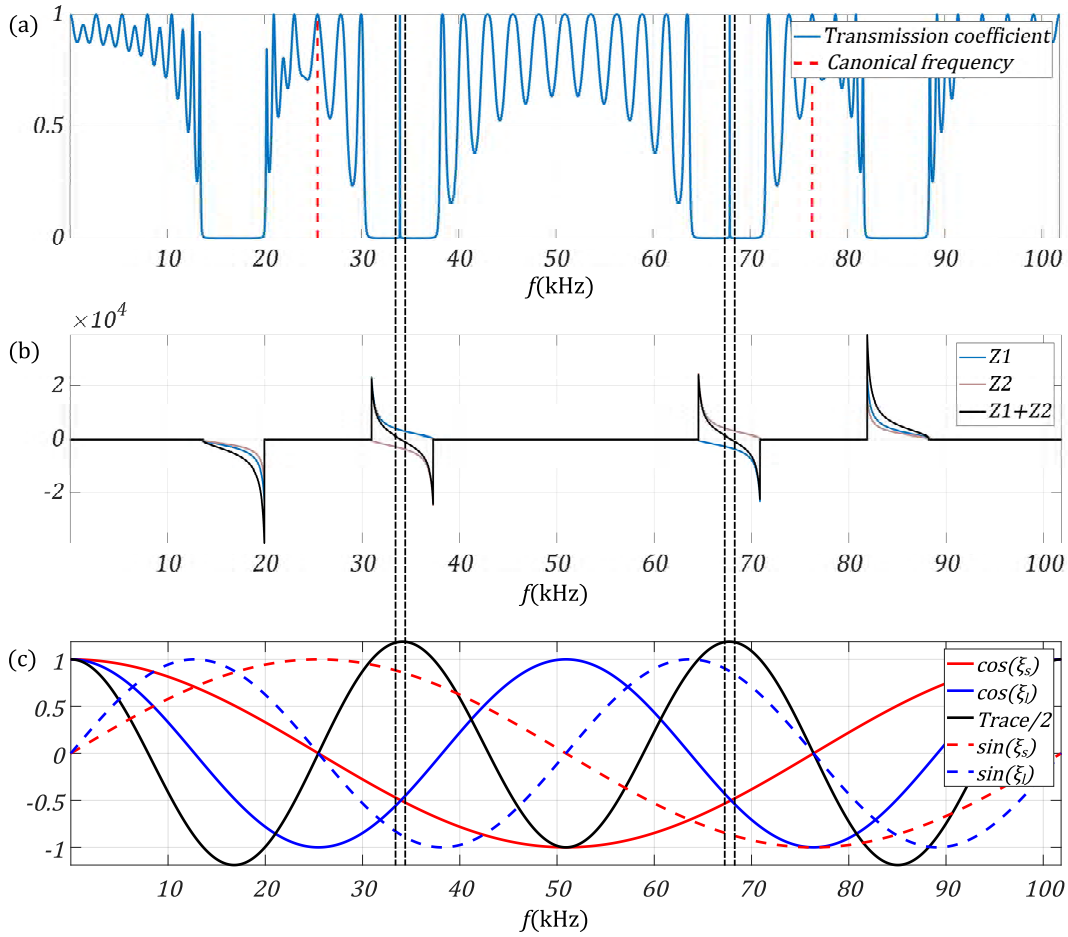

Figure 6.11. (a)*: The transmission spectrum of the system with canonical ratio* $1/2$ *and* 2 *(left and right) with* 6 *unit cells, respectively.* (b)*: The imaginary part of relative surface impedance of canonical rod of ratio* $1/2$ *(*$Z1$*, solid cyan line) and* 2 *(*$Z2$*, solid brown line), and the sum of the two (solid black line) inside the band gap region.* (c)*: The plot of* $cos(\xi_S)$*,* $cos(\xi_L)$*,* $sin(\xi_S)$*,* $sin(\xi_L)$ *and half trace. The canonical ratio is* $1/2$*.*

Subtracting equations (6.47) from (6.48) and using the interface state conditions $\sin(\xi_L) = -\sin(C\xi_L)$ and $\cos(\xi_L) = \cos(C\xi_L)$, the following equation is obtained:

$$2(\frac{\beta}{2} - 1)\sin((C-1)\delta)\sin(\xi_L)\cos(\xi_L) = 0 \tag{6.49}$$

If $\frac{\beta}{2} = 1$, the waveguide becomes homogenous. If β is close to 2, the interface state would be close to the centre of band gap. If the canonical ratio C is close to 1, the frequency of interface state would be close to the centre of band gap also. If the $\sin(\xi_L) = 0$, the frequency is at the passband. Consequently, only for $\cos(\xi_L) = 0$ equation (6.49) is satisfied and the interface state is at the centre of band gap. Note that from equation (6.43), $\cos(\xi_L) = \cos(\xi_S) = 0 \Rightarrow \sin(\xi_L) = -\sin(\xi_S) = \pm 1$. It represents the canonical frequency for family no. one, which is $\xi_L = \pi(1+2k)/2$ and $\xi_S = \pi(1+2j)/2$. Since the sign of $\sin(\xi_L)$ is different from the sign of $\sin(\xi_S)$, the $j+k$ must be an odd number, which let the $\cos(KL_t) = \beta/2 > 1$ at the canonical

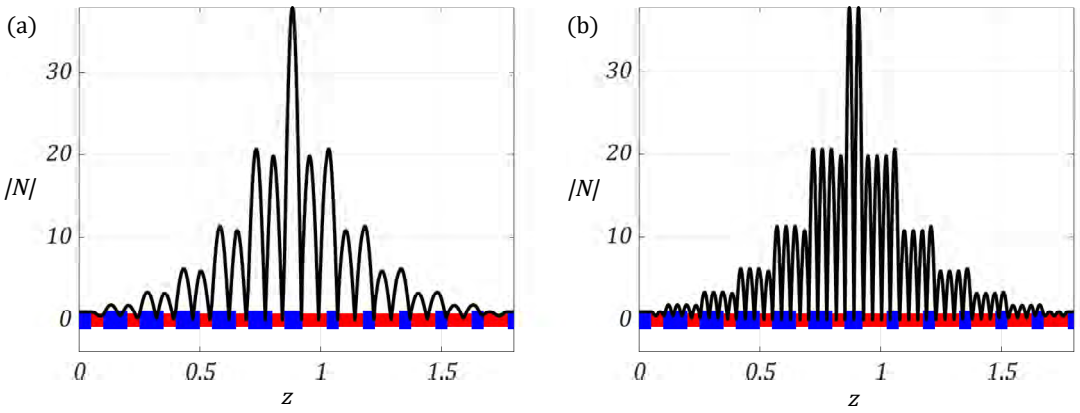

Figure 6.12. Numerical calculation of absolute value of the force field at the interface state with the system with canonical ratio 1/2 and 2 (left and right). The material parameters are same with Figure 6.11. (a)*:* $f = 33.945kHz$ *(interface state).* (b)*:* $f = 67.89kHz$ *(interface state).*

frequency according to dispersion relation (6.6). Thus, the canonical frequency is associated with the frequency of an interface state for family no. one when $j + k$ is odd number.

6.3.3 Determination of interface state frequency in system with swapped two-phases of the rods

Let us determine the frequency for the interface state in a system where the structure on the left and on the right have the same canonical ratio but the two phases composing the fundamental cells are swapped. This means that $Z_L \Rightarrow Z_S$ and $Z_S \Rightarrow Z_L$. The different topological phase of these two structures dose not come from the flow line passing through the topological transition point (bandgap close and reopen). In addition, the solution for the imaginary part of the surface impedance is more complicated than equation (6.46). Similar to equation (6.38), the right hand side structure with swapped two-phases of the rods is:

$$\mathrm{Im}(\frac{Z}{Z_0}) = \mathrm{Im}(\frac{1+r}{1-r}) = \frac{4Z_L Z_S \sin(\mathcal{N}KL_t)\cos(\mathcal{N}KL_t)\sin(KL_t)(Z_S^2 - Z_L^2)\sin(\xi_S)}{H_2^2 + 2\sin(\xi_S)H_2(Z_L^2 - Z_S^2)\cos^2(\mathcal{N}KL_t)} \tag{6.50}$$

If the interface state exists, the corresponding frequency should satisfy the following equation given by the sum of equations (6.38) and (6.50):

$$H_1^2 Z_S - H_2^2 Z_L + 2(Z_S^2 - Z_L^2)\cos^2(\mathcal{N}KL_t)(H_1 Z_S + H_2 Z_L) = 0 \tag{6.51}$$

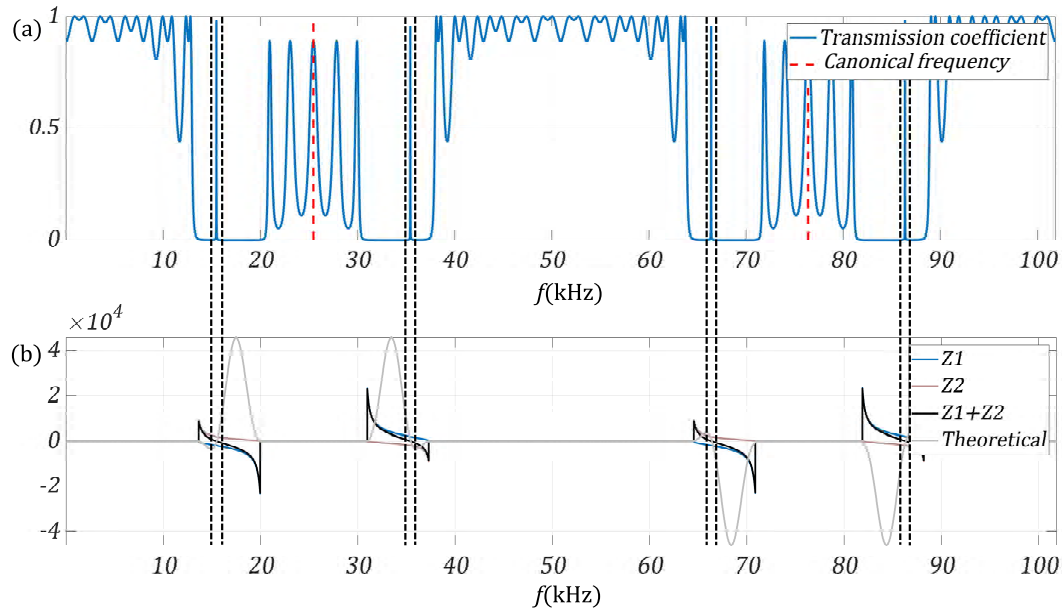

Figure 6.13. (a): The transmission spectrum of the system with canonical ratio $1/2$ *connected with rod changing the two-phase material (left and right) with* 6 *unit cells respectively. (b): The imaginary part of the relative surface impedance and the sum of the two (solid black line) inside the bandgap region. The solid grey line represents the solution from solution* (6.51)

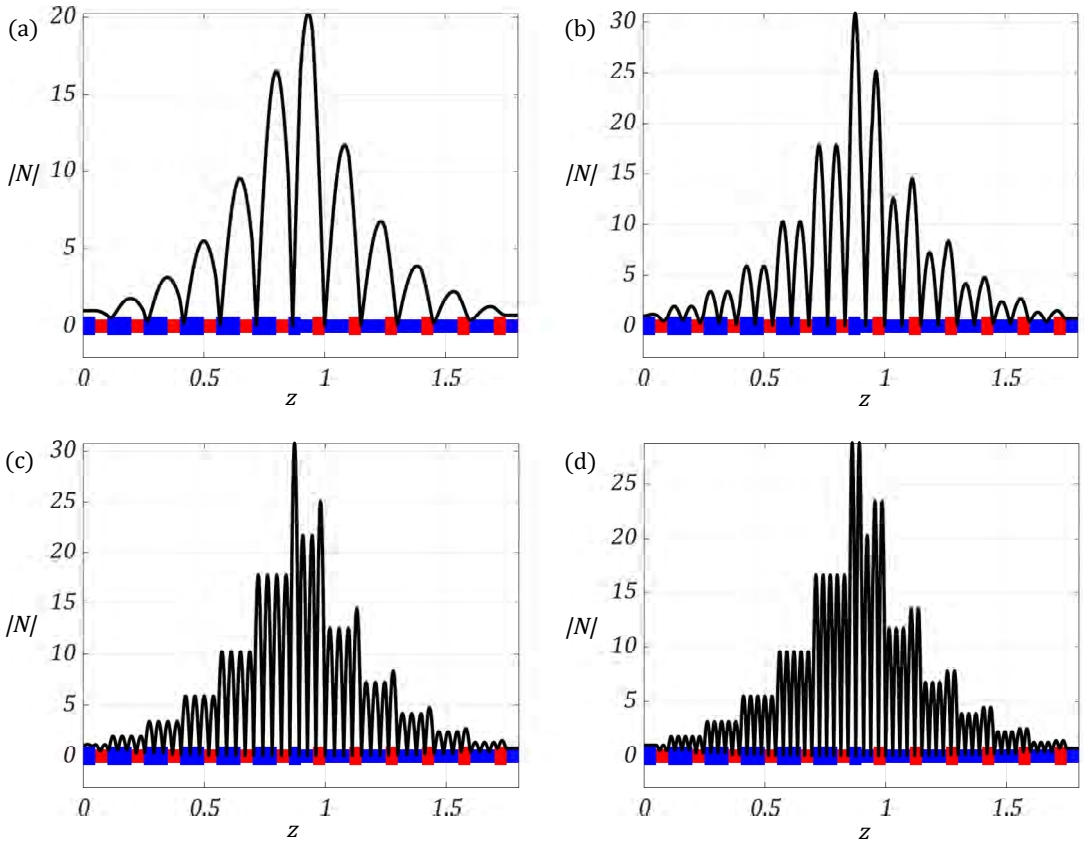

Figure 6.14. Numerical calculation of absolute value of the force field at the interface state. Material parameters same with case in Figure 6.13 (a)*:* $f = 15.481kHz$ *(interface state).* (b)*:* $f = 35.436kHz$ *(interface state).* (c)*:* $f = 66.399kHz$ *(interface state).* (d)*:* $f = 86.354kHz$ *(interface state).*

where H_1 and H_2 are the same terms of equation (6.17). Equation (6.43) is an implicit function which reveal the frequency at interface state within this configuration. The transmission coefficient and corresponding imaginary part of impedance are depicted in Figure 6.13 considering a system composed of two different periodic rods swapping the two-phase material with fixed canonical ratio $C = 1/2$. The grey line in Figure 6.13 (b) is the analytical solution (6.51), which is associated with zero value of summation of imaginary part of impedance $Z_1 + Z_2$ and the corresponding transmission peak in Figure 6.13 (a).

Observing Figure 6.14, it is easy to note that the absolute value of the force field is localized at the interface between two quasicrystalline rods, and it decays dramatically towards the ends of mixed waveguides. The results obtained in the section can also be extended to the non-canonical structure.

6.4 The Solution from Semi-Infinite Theory

The solution for a semi-infinite structure is now used to verify the analytical results obtained for a finite structure. Let us consider an axial wave $u = (ae^{\mathrm{i}k_0 z} + be^{-\mathrm{i}k_0 z})e^{\mathrm{i}\omega t}$ coming from a homogenous waveguide with impedance Z_0 incident into our semi-infinite rods. The velocity field and force field are:

$$V^- = \mathrm{i}\omega(ae^{\mathrm{i}k_0 z} + be^{-\mathrm{i}k_0 z}) \tag{6.52}$$

$$N^- = \mathrm{i}\omega Z_0(ae^{\mathrm{i}k_0 z} - be^{-\mathrm{i}k_0 z}) \tag{6.53}$$

The two fields inside the bandgap at $z = 0^+$ are given by equation (6.11):

$$V^+ = \omega(-\sin(KL_t) + \frac{H_1}{2Z_L Z_S}) \tag{6.54}$$

$$N^+ = Z_L\omega(\sin(KL_t) - \frac{H_2}{2Z_L Z_S}) \tag{6.55}$$

The mechanical impedance is defined as the ratio between the applied force and the resulting velocity at the point of excitation ($z = 0$). Thus, it is given by:

$$Z = \frac{N}{V} = Z_0\frac{a-b}{a+b} = Z_L\frac{(\sin(KL_t) - \frac{H_2}{2Z_L Z_S})}{(-\sin(KL_t) + \frac{H_1}{2Z_L Z_S})} \tag{6.56}$$

Force reflection coefficient is $r = -b/a$, so that the equation (6.56) becomes:

$$Z = Z_0 \frac{1+r}{1-r} \tag{6.57}$$

Equation (6.56) is identical to equation (2.73). Then, equation (6.57) can be simplified further:

$$\frac{Z}{Z_0} = \frac{2Z_L^2 Z_S \sin(KL_t)}{H_1} \tag{6.58}$$

The frequency solution at interface state is investigated for the same two conditions considered in previous Sections: (1) inverse canonical ratio, the equation (6.58) becomes:

$$\frac{Z}{Z_0} = \frac{2Z_L^2 Z_S \sin(KL_t)}{W_1} \tag{6.59}$$

(2) swapping of two-phase material, the equation (6.58) becomes:

$$\frac{Z}{Z_0} = \frac{2Z_S^2 Z_L \sin(KL_t)}{H_2} \tag{6.60}$$

It is easy to find the solution for case (1) is given by the condition given by the sum of equations (6.58) and (6.59):

$$H_1 + W_1 = 0 \tag{6.61}$$

Equation (6.61) is identical to equation (6.43). For case (2), the solution is determined by the sum of equations (6.58) and (6.60):

$$(H_1 Z_S + H_2 Z_L) = 0 \tag{6.62}$$

Equation (6.62) is due to the fact that term $\cos^2(\mathcal{N}KL_t)$ is dominated by the expression (6.51) and $(Z_S^2 - Z_L^2)$ cannot be zero with increasing of $\mathcal{N}$. The solution for the finite unit cell is in agreement with the results of semi-infinite theory solution and then our results are benchmarked.

6.5 Conclusion and Remarks

This chapter is concerning the study of interface state in a system composed of two periodic rods which fundamental cells are designed according to Fibonacci F_2 cell. In cases where the frequency is inside a bandgap, the localised mode occurs if the sign of imaginary part of surface impedance is opposite in the two rods composing the system. The sign of imaginary part of surface impedance is linked by symmetric properties of lower or upper band edge mode, for instance, the sign of impedance is negative as asymmetric band mode at lower band gap edge or vice versa. Thus, it provides a simple way to calculate the sign of imaginary part of impedance, which is easier than

Zak phase which is usually calculated through complex numerical integral.

Due to the fact that a canonical structure owns periodic and symmetric dynamic properties, the sign of the imaginary part of surface impedance has also these properties so that we can predict sign of surface impedance for all band gaps inside a canonical period. The sign of the imaginary part of surface impedance keeps the same if we translate a band gap of a canonical period, different in cases where we translate by half canonical period. Combining the condition of band edge symmetry with the extended toroidal representation of the sign of imaginary part of impedance in any bandgap can be predicted starting from the analysis of the first band gap. Thus, the new extended torus can be used to design the topological transition properties in quasicrystalline rods by studying the flow line passing through the topological transition point first time. The proposed novelty method can be used to design a system composed of two rods with different signs of imaginary part of impedance in the same bandgap region.

We derived an exact formula for the frequency of the interface state valid for the case where both the finite rods composing the systems have the same materials for the two phases and the same number of unitary cells, which is first time compare with previous research works. Two particular cases are considered: different structures with the inverse canonical ratio or swapping two-phase materials while fixed canonical ratio. The formula is derived by evaluating analytical expressions for the reflection coefficient and the imaginary part of surface impedance for the two rods, and using these expressions in the general condition for having a localised mode at the interface. The exact formula is benchmarked with numerical results. Moreover, a condition to let the interface state at the bandgap's centre is also obtained. If the structure belong to canonical family no. 1 and satisfied $j + k =$ odd number, the canonical frequency must be identical with frequency for the interface state and in the centre of the bandgap. In addition, the theoretical results obtained through the analysis of the semi-infinite rods are verified by a comparison with semi-infinite theory. The developed approach can be extended to the case of an interface between non-canonical structure.

The interface state and sign of the imaginary part of surface impedance are usually predicted by evaluating the Zak phase (Zak 1989) through a complicated integral introduced in Chapter 3. The results obtained in this chapter using symmetric properties of edge mode to analyse the sign of imaginary part of impedance for having interface state have been verified by a comparison with numerically calculated Zak phase in dispersion spectra.

For design system, which has two quasicrystalline-generated rods, for having interface state is following steps:

(1): Two structures with one canonical ratio C and another with inverse canonical ratio $1/C$ can be chosen. The interface state will happen only as wave number $KL_t = 0$. The frequency at interface state is $f = \frac{n_1}{(1+C)l_L}\sqrt{\frac{E_L}{\rho_L}} = \frac{Cn_1}{(1+C)l_S}\sqrt{\frac{E_S}{\rho_S}}$, $n_1 \in \mathbb{N}$. Thus, engineer can adjust material or length coefficients to obtain desire or target frequency. If this frequency coincide with canonical frequency, the interface state will be at the centre of bandgap.

(2): Two structures with two-phase material swapping each other can be chosen. The interface state will happen in every bnandgap. The frequency at interface state is $H_1^2 Z_S - H_2^2 Z_L + 2(Z_S^2 - Z_L^2)\cos^2(\mathcal{N}KL_t)(H_1 Z_S + H_2 Z_L) = 0$. Thus, engineer can adjust material or length coefficients to obtain desire or target frequency.

(3): If two wave speed in two phase material are different ($c_L \neq c_S$), the total unit cell length $L_t^{(i)}$ with canonical ratio $1/C$ or $L_t^{(e)}$ with two phase swapping should be adjusted according $L_t^{(i)} =$ (or $L_t^{(e)}$) $L_t^{(o)}\frac{Cc_L + c_S}{c_L + Cc_S}$, $L_t^{(o)}$ is original unit cell total length.

Chapter 7 - Conclusions and Further Work

7.1 Conclusions

In this thesis, we investigate the dynamical properties of a class of quasicrystalline-generated phononic structures whose elementary cells are designed using the Fibonacci golden mean substitution rules. We analyze in details several aspects concerning the propagation of harmonic axial waves in quasicrystalline rods and anti-plane shear waves in Fibonacci-generated laminates. Closed form exact solutions for the two one-dimensional problems allowed us to study and understand the following extraordinary properties of this class of structures: (i). self-similar layout of the dispersion spectra governed by analytically evaluated scaling factors; (ii). periodic stop/pass diagrams characterizing a sub-family of quasicrystalline-generated structures (the so-called canonical structures); (iii). pure negative refraction induced at an interface between an elastic substrate and a quasicrystalline laminate; (iv) topological localized modes obtained at the interface between two canonical quasicrystalline rods. The main results about these non-standard dynamical features, their physical interpretation and their possible technological applications are summarized in the next three sections.

7.1.1 Wave propagation in canonical rods

The dispersion relation for axial wave propagating in two-phase Fibonacci-generated periodic rods is obtained as a function of the trace of the transfer matrix corresponding to fundamental cells of any arbitrary order. Trace of transfer matrices of Fibonacci consecutive cells are related by recursive relationships so that the propagation properties of consecutive cells at any given frequency can be studied by means of nonlinear recursive maps. An invariant for these maps, i.e. Kohmoto's invariant and the relevant manifold, is investigated. For any arbitrary frequency, the traces of the transfer matrix corresponding to consecutive Fibonacci cells are associated with points on the Kohmoto's surface. Analyzing the trajectories of these points allow us to obtain a rigorous interpretation of the scaling effects and self-similarity observed in the stop/passband diagrams. Moreover, we have shown that there are six-saddle point closed orbits on Kohmoto's manifold corresponding to the so-called canonical frequencies. In order to have this phenomenon, the geometrical and physical properties of the two phases composing the rods must statisfy three alternative conditions associated with three families of canonical structures. If the structure is a canonical waveguide, the Floquet Bloch spectra, dynamic traces and Kohmoto's invariant are periodic with well defined special frequencies which are canonical frequencies. The relationships between canonical ratio and associated canonical frequencies are explained by several numerical

examples from initial three traces with dimensionless frequency. By using these relationships, the dynamic properties of canonical structure can be controlled modulating the material parameters of the two phases.

In addition, a close inspection of the associated trace map has revealed that there could be multiple periodic orbits at frequencies that differ from the canonical ones. The effect of scaling on the length of the bandgap (family no. one) and passbands (families no. two and three or other periodic orbits) have been examined in details with good accuracy. The validity of scaling increases with increasing index of Fibonacci order. The scaled passband and trace are symmetric between F_i and $F_{(i+p)}$ (p is number of periodic points) associated with the frequency with the positive maximum eigenvalue of Jacobian and are not symmetric as the maximum eigenvalue is negative one which means the increasing perturbation direction is the opposite comparing with initial direction through linearisation.

We studied scaling in linearizing nonlinear maps around periodic orbit and the eigenvalues of the linearized transformation are the scaling factors. Frequencies at half canonical period are the most exceptional examples. The maximum eigenvalue is not the scaling factor but the square root of it. According to the concept of linear approximation, the coefficients of the first-order term of the Taylor series becomes zero. Therefore, if we wish to employ the approximation method, the Taylor series must be extended to the second order, and then theory matchs numerical results. In addition, the generic formula for any traces x_i connected with periodic orbits and position in one canonical period are solved. The canonical configuration exploits the periodic features of the trigonometric functions (cosine and sine), resulting in a periodic trace and dispersion pattern, which is a particular solution of these systems. This approach can be used as a guideline for their potential use in the design of innovative construction metamaterials whose bandgap and passband topology may be easily regulated and controlled.

In principle, the canonical configuration takes advantage of the periodic properties of the trigonometric function, cosine and sine, leading to periodic trace and dispersion layouts, which is the particular solution of these systems. This is first time to show how the canonical configuration on rods to influence the effects for dispersion layout. In addition, the scaling effects concern periodic points are investigated in both positive, negative or square roots of eigenvalue comparing with previous research works.

For design dispersion spectrum in quasicrystalline-generated rods is following steps:
(1): The frequency at bandgap can be computed by canonical frequency $\omega_{cj} = \frac{\pi\sqrt{E_S}}{2l_S\sqrt{\rho_S}}(1+2j)(1+$

$2m) = \frac{\pi\sqrt{E_L}}{2l_L\sqrt{\rho_L}}(1+2k)(1+2m) = \omega_{ck}$ as structure belongs familiy no .1 at Fibonacci order F_2, F_5, F_8 (F_{2+3n}, $n \in \mathbb{N}$). Thus, engineer can design this system to forbidden desire frequency wave $\omega = \omega_c$.

(2): The bandgap length at Fibonacci order F_2, F_5, F_8 (F_{2+3n}, $n \in \mathbb{N}$) can be predicted by scaling technique with scaling factor ϑ^+ by using $\omega_{A*} - \omega_{B*} = \frac{\widetilde{\omega}_A - \widetilde{\omega}_B}{\vartheta^+}$ ($\omega_{A*} - \omega_{B*}$ assuming as bandgap length for F_i, $\omega_{A*} - \omega_{B*}$ is bandgap length for F_{i+6}) or with scaling factor λ^+ by using $\omega_{A*} - \omega_{B*} = \frac{\widetilde{\omega}_{A'} - \widetilde{\omega}_{B'}}{\lambda^+}$ ($\widetilde{\omega}_{A'} - \widetilde{\omega}_{B'}$ assuming as bandgap length for F_i, $\omega_{A*} - \omega_{B*}$ is bandgap length for F_{i+3}). Therefore, engineer can design a structure with very narrow bandgap at desire frequency.

7.1.2 Wave propagation in quasicrystalline and canonical laminates

A method to obtain pure negative refraction for harmonic elastic anti-plane shear (SH) dynamics is wave transmission across an interface between a substrate and a composite laminate whose lamination direction is orthogonal to the interface. The concept of transition zone is associated with a particular range of frequencies and the frequency inside transition zone could lead to a determined number of propagating waves transmitted from the substrate to the laminate. For instance, zero or one transmitted modes will be found in first transition zone, one or two in second transition zone, etc. Consequently, in order to have only one single negatively refracted mode transmitted at the interface (the so-called 'pure' negative refraction phenomenon), the frequency of the source should be lower than the upper limit of the second transition zone of the harmonic spectrum of the laminate. The rigorous conditions for pure negative refraction are derived by obtaining exact expressions with three edge frequencies, which are upper edge for first transition zone, lower and upper edge for second transition zone. In addition, an exact condition for total reflection is also obtained.

The rest conclusions in quasicrystalline laminates are novelty works comparing previous research papers. Canonical laminates are particularly suitable to tune the values of these three edge frequencies and then obtain pure negative refraction in a given range of frequencies. Canonical laminates display a periodic stop- and pass-band layout, the periodicity being governed by canonical frequency, which is similar to the rod problem in Chapter 4. For the problem of pure negative refraction, the focus is on the first two passbands of the spectrum that possess the same limits of the first two transition zones at low frequencies for the laminate if we consider wave propagation in any direction. The self-similar pattern displayed by them at increasing index of the sequence can be quantitatively described through a scaling factor that can be estimated by square root of the maximum eigenvalue from fixed point on Kohmoto's manifold, which is golden ratio. Through this parameter, the breadths of the first two transition zones can be predicted first time by scaling

backward and/or forward the corresponding values of a given configuration taken as a reference. It is also shown how the impedance mismatch inside dispersion relation of the laminate affect the limits of the transition zones at constant canonical ratio and how to modify the dispersive properties of the elementary cell by changing cell's total length.

Furthermore, the universal representation of the frequency spectrum based on the reduced torus enables us to properly investigate how a change in canonical ratio impacts the change in the frequencies relevant for negative refraction, specifically those at the boundaries of the first two transition zones. This depiction provides a tool that may be used to optimise the substrate-laminate system's performance. To demonstrate it, we study analytically the cases F_2 and F_3 whose have evident extreme value for edge frequencies concerning pure negative refraction.

Using a linear relationship between longitudinal wavenumber and frequency, it is possible to directly calculate the Poynting vector for a specific direction of energy flow and the transmission angle. With this closed-form solution, the parameters of the laminate and substrate, as well as the incidence angle, may be easily chosen to produce a certain direction of the negatively refracted wave without numerically solving the entire coupled problem. Therefore, the transmission angle can be selected on the basis of frequency, substrate, and incident wave angle considerations. If a large transmission wave angle or a small incident wave angle is required for pure negative refraction, a substrate with a relatively low wave speed should be chosen.

The possibility of achieving negative refraction can be analysed through the careful selection of both materials and layouts of the unit cell, the amount of transmitted energy is an additional factor that must be taken into account because it varies significantly with the angle of incidence. Here, we demonstrate that, for a particular combination of substrate and laminate materials, a peak in the energy of the only negative transmitted mode is found. When adopting the examined prototype system in practical applications, this factor must be considered. Pure negative refraction is an intriguing phenomena, but it is ineffective if the transmitted energy is relatively low.

For design system, which is composed by two phase quaiscrystalline laminate and homogenous substrate with fixed total length L_i, for having SH wave pure negative refraction is following steps:
(1): For having relative large incident wave angle's range for pure negative refraction, the material for substrate with slower phase speed c_0 should be chosen so that $f_i^{\min}$ is relative lower.
(2): For increasing three edge frequencies $f_i^{1\text{st}}$, $f_i^{1\text{bg}}$ and $\tilde{f}_i$ (upper edge for pure negative refraction), the material with higher wave phase speed should be chosen as material A, the material with lower wave phase speed should be chosen as material B.

(3): If Fibonacci order for laminate is F_2 or F_3 and satisfied the condition $\rho_L > \rho_S, \mu_L > \mu_S$ or $\rho_L < \rho_S, \mu_L < \mu_S$, the canonical ratio can be chosen as $C = 1$ or $C = 2$ for having local maximum value $\tilde{f}_i$ (upper edge for pure negative refraction), respectively.

(4): Three frequencies f_i^{1st}, f_i^{1bg} and $\tilde{f}_i$ can be predicted with linear approximation (lower Fibonacci order) $f_2^{1bg} \approx f - (2 + x_2)\frac{dx_2}{df}$, $\tilde{f}_2 \approx f + (2 - x_2)/\frac{dx_2}{df}$, $f_2^{1st} \approx f + (-2 - x_2)/\frac{dx_2}{df}$ or with transition zone scaling (higher Fibonacci order) using coefficients ϕ_g.

(5): The incident wave angle θ^{inc}, pure negative refraction angle θ^{trans} and incoming wave frequency f can be plotted on Figure analogy with 5.15 according equation $(\frac{1}{fL_i} - v)c_0 = \sin(\theta^{inc})$ to determine the relationship among them. Engineer can pick up two of these three terms to obtain another one.

7.1.3 Topological interface state in periodic rods

The system considered to study interface modes is composed of two periodic rods which fundamental cells are designed according to Fibonacci F_2 cell. We considered harmonic axial wave propagation through this system. The localised mode occurs as an opposite sign of surface impedance when frequency is in bandgap of each two structures combined. The sign of surface impedance can be obtained by the geometric topological phase-Zak phase for each passband, which is calculated through complex numerical integrals. However, since the periodic cell of rods is 1D and holds inversion symmetry, the sign of surface impedance can be linked by symmetric properties of lower or upper band edge mode, for instance, the sign of impedance is negative as asymmetric band mode at lower band edge or vice versa.

The case of an interface between two canonical F_2 rods is considered. Due to the fact that a canonical structure owns periodic and symmetric properties, the sign of surface impedance has also these properties so that we can predict sign of surface impedance if the cases in first canonical frequency range are obtained. In addition, the representation of extended torus can be used in the bandgap domain with the different sign of surface impedance only depending on the boundary line of the first bandgap. Thus, with an easy analytical derivation, the novel extended torus can be used to construct the periodic rods with topological phase transitions and we can first predict sign of surface impedance in an arbitrary bandgap. These two predicting tools can be easily used to create a system with two rods in the same bandgap area that have opposite signs of surface impedance for interface state formulation.

Moreover, we derived an exact frequency formula for the interface state under conditions with same two-phase material and number of unit cell under two combinations, which are two different

structures with the inverse canonical ratio or swapping two-phase materials while fixed canonical ratio, which is first time because previous study do not mention exact frequency solution. The solution is based on the reflection coefficient and the imaginary part of surface impedance for these two rods, respectively. The numerical calculations confirm the exact formula validity as it is shown in plots of the transmission spectra, trace plots and wave fields at interface state. We finally propose a method to generate an interface mode at the centre of the bandgap, whose frequency coincides with canonical frequency. The theoretical investigations of the periodic semi-infinite rods validated the solution of finite unit cell. In addition, all results can be extended to non-canonical structures.

For design system, which has two quasicrystalline-generated rods, for having interface state is following steps:

(1): Two structures with one canonical ratio C and another with inverse canonical ratio $1/C$ can be chosen. The interface state will happen only as wave number $KL_t = 0$. The frequency at interface state is $f = \frac{n_1}{(1+C)l_L}\sqrt{\frac{E_L}{\rho_L}} = \frac{Cn_1}{(1+C)l_S}\sqrt{\frac{E_S}{\rho_S}}$, $n_1 \in \mathbb{N}$. Thus, engineer can adjust material or length coefficients to obtain desire or target frequency. If this frequency coincide with canonical frequency, the interface state will be at the centre of bandgap.

(2): Two structures with two-phase material swapping each other can be chosen. The interface state will happen in every bnandgap. The frequency at interface state is $H_1^2 Z_S - H_2^2 Z_L + 2(Z_S^2 - Z_L^2)\cos^2(\mathcal{N}KL_t)(H_1 Z_S + H_2 Z_L) = 0$. Thus, engineer can adjust material or length coefficients to obtain desire or target frequency.

(3): If two wave speed in two phase material are different ($c_L \neq c_S$), the total unit cell length $L_t^{(i)}$ with canonical ratio $1/C$ or $L_t^{(e)}$ with two phase swapping should be adjusted according $L_t^{(i)} =$ (or $L_t^{(e)}$) $L_t^{(o)}\frac{Cc_L+c_S}{c_L+Cc_S}$, $L_t^{(o)}$ is original unit cell total length.

7.2 Further Developments

We found a new class of waveguides, the so-called canonical structures, that are associated with periodic dynamical spectrum. The possibility of realizing a period spectrum is connected to the purely harmonic solution of the Helmholtz-type equation describing the propagation of axial waves in these type of structures. In Euler-Bernoulli beam theory (which might be generalised to other beam theories, e.g. Timoshenko beam), with or without prestress, the displacement solution for each phase may contain the non-periodic hyperbolic functions cosh and sinh. In order to apply the concept of canonical configuration to flexural beams and 2D and 3D lattices more

research is needed as a theory for the extension to the new problems is still lacking.

As SH waves propagate through laminates, the unusual normalised energy peak for pure negative refraction can be explored in further detail. As illustrated in Figure 5.16, it appears that the unusual energy peaks are related to the substrate properties and incoming wave frequency. However, it is difficult to develop a theoretical solution from normalised energy because of the scattering coefficients obtained through the approximated equation set (3.23), regardless of whether the mode decomposition method or the Lagrange multiplier technique is used. Negative refraction requires the transmission of a relevant sufficient amount of energy, so for potential future research, the principle underlying an unusual energy peak can be investigated using other methods, such as machine learning (neural networks) that can find the potential law of this phenomenon based on a large number of numerical results. In future, negative refraction with damping in viscoelastic multilayered composites may also be investigated.

The exact frequency for the interface state in a 1D system is derived in Chapter 6. Evaluating the topological invariant determining the existence of localized modes in 2D systems implies very challenging numerical computations. Similarly to the method presented in this thesis also in 2D systems, the state of the topological interface can be induced by two distinct systems with the same dispersion relation. This could be an innovative method for tackling 2D system issues. In addition, the results and conclusions of this thesis can be applied to acoustic and electromagnetic wave guides and structures with minor modifications.

Appendix A Main MATLAB code

Change Font Size and Style in MATLAB Plot

If we required a unique plot font size and style, these codes would be helpful in each figure code.

```
figure_FontSize=16; % change font size
set(get(gca,'XLabel'),'FontSize',figure_FontSize,'Vertical','top');
set(get(gca,'YLabel'),'FontSize',figure_FontSize,'Vertical','middle');
set(findobj('FontSize',10),'FontSize',figure_FontSize);
set(gca,'FontName','Cambria Math'); % change font
set(gca,'FontAngle','Italic'); % change font style
set(gcf, 'color', [1 1 1]);% setting edge of figure white axis tight% axis will be tight with vectors
```

One-Dimensional Quasicrystalline Canonical Rods

The main programme for trace and passband layouts

```
El=152943.700000000; Es=152943.700000000;pl=1.3; ps=1.3;% change here according material
Ll1=0.03*2; Ls1=0.08; As=0.000530929158456675; Al=0.00090792027688745; % change here
according material
j=2; k=0; q=0; % change here according canonical parameters
calcustep=1E0; % calculation accuracy
[rtio,period1,fam]=ratios(j,k,q);[Ll,Ls]=keepthicnesssame(Ll1,Ls1,2,cl,cs,rtio);
Ql=(pl/El); Qs=(ps/Es); cl=sqrt(El/pl); cs=sqrt(Es/ps);
[n,n2]=periodforf(r,fam,1/sqrt(Ql),1/sqrt(Qs),Ll,Ls,j,k,q);
[trans,bandg,fl,trM,Koho,trT3,trB3]=bandgapforaxially(n,El,Es,Ll,Ls,Al,As,pl,ps,rtio,calcustep);
limitKoho=max(Koho); limittracemax=max(trM(3,:)); limittracemin=min(trM(3,:)); % setting limit
for Kohmoto invariant and trace plot
figure(1)
for jc=3:9
   plot(fl,trans(jc,:),'Color',[0 0 1],'LineWidth',20),grid; % passband layoutshold on;
end
hold on;fck0=(n)/4*1e-3; fck1=(n*3)/4*1e-3;
plot([fck0,fck0],[-18,-2],'r','LineWidth',2),grid on; % canonical frequencyhold on;
plot([fck1,fck1],[-18,-2],'r','LineWidth',2),grid on; % canonical frequencytitle('Passband');
figure(2); % dispersion for traces
plot(fl,trM(1,:),'k','LineWidth',3),grid; % change here for different order tracehold on;
plot(fl,trM(2,:),'m–','LineWidth',3),grid; hold on;
plot(fl,trM(3,:),'b-.','LineWidth',3),grid; hold on;
plot([fck0,fck0],[limittracemin,limittracemax],'r','LineWidth',2.5),grid on; hold on;
plot([fck1,fck1],[limittracemin,limittracemax],'r','LineWidth',2.5),grid on;title('trace diagram');
figure(3); % plot of Kohmoto's invariant
plot(fl,Koho,'k','LineWidth',3),grid on;hold on;
plot([fck0,fck0],[-1,limitKoho],'b','LineWidth',2.5),grid on; hold on;
plot([fck1,fck1],[-1,limitKoho],'b','LineWidth',2.5),grid on;title('Kohomoto invariant');

%%
fck2=17.5; % change here which is point in small frequency range
deltl=3; % change here the intervalfll=fck2-deltl; fu=fck2+deltl;
```

```
calcustep1=1E-2; % change here the calculation accuracy
[transsmal,bandgsmal,flsmal,trMlimt,Kohosmal]=bandgapforaxiallysmall(n,El,Es,Ll,Ls,Al,As,pl,
ps,r,calcustep1,fll,fu);
[passglbandg]=passglengthsaxalliymall(fll,fu,trMlimt,fck2,calcustep1);
figure(4) % plot small frequency range passband layouts
for jc=3:12
   plot(flsmal,transsmal(jc,:),'Color',[0 0 1],'LineWidth',20),grid;hold on;
end
plot([fck2,fck2],[-24,2],'r','LineWidth',2.5),grid on;title('Passband diagram small interval');
figure(5); % plot small frequency range traces
plot(flsmal,trMlimt(1,:),'k','LineWidth',3),grid;hold on;
plot(flsmal,trMlimt(2,:),'m–','LineWidth',3),grid;hold on;
plot(flsmal,trMlimt(3,:),'b-.','LineWidth',3),grid;title('trace diagram');
figure(6); % plot small frequency Kohmoto's invariant
plot(flsmal,Kohosmal,'k','LineWidth',3),grid on;title('Kohomoto invariant');
```

Subprogramme for trace and passband layouts

```
function [rtio,period,fam]=ratios(j,k,q)%canonical ratio and percoid, family
if q==0
   l=gcd(1+2*j,1+2*k);rtio=(1+2*j)/(1+2*k);k1=((1+2*k)/l-1)/2;period=2*(1+2*k1);fam=1;
   else if k==0
      l=gcd(1+2*j,2*q);rtio=(1+2*j)/(2*q);q1=(2*q)/(2*l);period=4*q1;fam=2;
   else rtio=(2*q)/(1+2*k);
      l=gcd(1+2*j,2*q);k1=((1+2*k)/l-1)/2;period=2*(1+2*k1);fam=3;
   end
end

function [hA,hB,Li,nA,nB]=keepthicnesssame(hA1,hB1,fii,cA,cB,r)%keep total length or thick-
ness same
[Li, ,nA,nB]=LFibonacci(fii,hA1,hB1);hA=(Li/(nA+nB*r*cB/cA));hB=hA*r*cB/cA;

function [n1,n2]=periodforf(r,fam,cA,cB,hA,hB,j,k,q)
if fam==1
   n1=(cA/hA*(1+2*k));n2=(cB/hB*(1+2*j));
end
if fam==2
   n1=(cA/hA*(2*q));n2=(cB/hB*(1+2*j));
end
if fam==3
   n1=(cA/hA*(1+2*k));n2=(cB/hB*(2*q));
end

function [trans,bandg,fl,trM,Koho]=bandgapforaxially(n,El,Es,Ll,Ls,Al,As,pl,ps,r,
calcustep)%passband layout
F=0:calcustep:n;fl=F.*1e-3;
Koho(1:1:length(F))=0;trM(1:9,1:length(F))=0;trans(1:9,1:length(F))=0;bandg(1:9,1:length(F))=0;
for ic=1:length(F)
   f=F(ic);
   if F(ic)==0
      trM(1,ic)=2;trM(2,ic)=2;trM(3,ic)=2;trM(4,ic)=trM(4-2,ic)*trM(4-1,ic)-trM(4-3,ic);
```

```
        trM(5,ic)=trM(5-2,ic)*trM(5-1,ic)-trM(5-3,ic);trM(6,ic)=trM(6-2,ic)*trM(6-1,ic)-trM(6-3,ic);
        trM(7,ic)=trM(7-2,ic)*trM(7-1,ic)-trM(7-3,ic);trM(8,ic)=trM(8-2,ic)*trM(8-1,ic)-trM(8-3,ic);
        trM(9,ic)=trM(9-2,ic)*trM(9-1,ic)-trM(9-3,ic);Koho(ic)=0;
    else
        [MB]=axiallmatrix(ps,Es,As,f*2*pi,Ls);[MA]=axiallmatrix(pl,El,Al,f*2*pi,Ll);
        [Kinv,kgp,kgm]=Kohmotoinvaxially(pl,El,Al,Ll,ps,Es,As,Ls,f*2*pi);Koho(ic)=Kinv;
        trM(1,ic)=trace(M0);trM(2,ic)=trace(M1);trM(3,ic)=trace(M2);
        trM(4,ic)=trM(4-2,ic)*trM(4-1,ic)-trM(4-3,ic);trM(5,ic)=trM(5-2,ic)*trM(5-1,ic)-trM(5-3,ic);
        trM(6,ic)=trM(6-2,ic)*trM(6-1,ic)-trM(6-3,ic);trM(7,ic)=trM(7-2,ic)*trM(7-1,ic)-trM(7-3,ic);
        trM(8,ic)=trM(8-2,ic)*trM(8-1,ic)-trM(8-3,ic);trM(9,ic)=trM(9-2,ic)*trM(9-1,ic)-trM(9-3,ic);
    end
    for jc=1:12
        [trans(jc,ic),bandg(jc,ic)]= transtionf(trM(jc,ic),jc);
    end
end

function [T]=axiallmatrix(p,E,A,w,L)%transfer matrix
T(1:2,1:2)=0;EA=E*A;Q=p/E;
T(1,1)=cos(sqrt(Q)*w*L);T(1,2)=sin(sqrt(Q)*w*L)/(EA*sqrt(Q)*w);
T(2,1)=-sin(sqrt(Q)*w*L)*(EA*sqrt(Q)*w);T(2,2)=cos(sqrt(Q)*w*L);

function [Kinv,kgp,kgm]=Kohmotoinvaxially(pl,El,Al,Ll,ps,Es,As,Ls,w)%Kohmoto
Qs=ps/Es;Ql=pl/El;
peita=(Al*El/(As*Es)*sqrt(pl*Es/(ps*El))+As*Es/(Al*El)*sqrt(ps*El/(pl*Es)));
Kinv=(peita^2-4)*sin(sqrt(Qs)*w*Ls)^2*sin(sqrt(Ql)*w*Ll)^2;
kgp=0.25*(sqrt(4+(4+Kinv)^2)+4+Kinv)^2;
kgm=0.25*(sqrt(4+(4+Kinv)^2)-4-Kinv)^2;

function [trans,bandg]= transtionf(trM,jc)
if abs(trM)-2<=0
    trans=-(jc-1)*2;bandg=nan;
else
    bandg=-(jc-1)*2;trans=nan;
end
```

Function bandgapforaxiallysmall is very similar to function bandgapforaxially so we do not show here.

```
function [passglbandg]=passglengthsaxalliymall(fll,fu,trM,fck1,calcustep1)%detect bandgap
fll1=floor(fll*1e3/calcustep1);fu1=floor(fu*1e3/calcustep1);
nwc1=floor(fck1*1e3/calcustep1)+1-fll1;
for m=3:9
    for iln=nwc1:-1:2
        if (abs(trM(m,iln-1))-2)*(abs(trM(m,iln))-2)<=0
            break;
        end
    end
    for iun=nwc1:fu1-fll1-1
        if (abs(trM(m,iun+1))-2)*(abs(trM(m,iun))-2)<=0
            iu=iu+1;
        else
            break;
```

```
    end
  end
  passglbandg(m)=(iun-iln+1)*calcustep1*1e-3;
end
```

Wave Transmission and Reflection in Laminate

The method for plotting transition zone is similar to passband layout in axially wave propagation in rods problem. However, for simplicity, we do not show it here.

The main programme for analysis angle and energy

```
u0=80e9; p0=8000; % material parameters for substrate
uA=3e9; uB=80e9; pA=1180; pB=8000; % material parameters for two phase
hA1=0.003; hB1=0.0013; %original thicknessj=0; k=0; q=0; %canonical ratio coefficients
[rtio,period1,fam]=ratios(j,k,q); r=rtio; Fi=2; %Fibonacci order
KyLi=45; %calculation limit for wavenumber KyLi
stepforwave=1e-4; %calculation accuracy for KyLi
ewaven=13; %number of evanescent taking into consideration
lenstep=1e-6; %calculation accuracy for modeshape w
c0=(sqrt(u0/p0)); cA=(sqrt(uA/pA)); cB=(sqrt(uB/pB));
[Li,ni,nA,nB]=LFibonacci(Fi,hA1,hB1);[hA,hB, ]=keepthicnesssame(hA1,hB1,Fi,cA,cB,r);
[n1, ]=periodforf(r,fam,cA,cB,hA,hB,j,k,q);f=200; %frequency (kHz)
w=(2*pi*f*1000); %circular frequencyK0=w/c0; %wavenumber in substrate
inciang=60; %incident angle (degree)realKxLi=K0*sind(inciang)*Li; %wavenumber KxLi
Kx=realKxLi/Li;uaverage=(uA*nA*hA+uB*nB*hB)/Li; %average shear modules
[aimKxLi]=waveinfirst(realKxLi);
[rKxLi,solution,iKxLi,fix,p,isolution,ifix]=generKxLiparfo(w,uA,cA,hA,uB,cB,hB,KyLi,
stepforwave,Fi,Li,realKxLi);
[suresolu,countnum,co,co2,suresolu2,countnum2,bounddis,u,usuresolu,isuresolu2,ibounddis,
iusuresolu,ico2,iu,wanumbangle,n360,error,ierror]=smallfindKyLi(solution,fix,realKxLi,w,uA,cA,
hA,uB,cB,hB,Fi,Li,stepforwave,isolution,ifix,realKxLi);
[N]=ensureN(co2,ewaven);
[wvampn,lengn,bouncodi,n,C,loc,iwvampn,uvamp,duvamp,bounddis,ibounddis,normalized,
intgdispla,intgdisplanew,uwvamp,iuvamp]=waveamptde(Li,Fi,w,uA,cA,hA,uB,cB,hB,lenstep,
usuresolu,realKxLi,bounddis,iusuresolu,ibounddis,ckn,uaverage,realKyLi);
[rflewvam, kyn,propkyn,evankyn]=waveamfrel(c0,w,Li,lenstep,N,inciang);
[cvecinte,qmatrixintenew,dvecintenew,conditinum]=matrixcalcintenew(usuresolu,iusuresolu,C,loc,
Fi,uA,uB,w,c0,inciang,hA,hB,N,u0,Li,nbounddis,nibounddis,realKxLi,cA,cB,ewaven,co2,
normalized,uaverage);
[poyntintex,poyntinteynew,tranangintenew]=poyntvectorinte(C,loc,Fi,uA,uB,w,usuresolu,hA,hB,
Li,cA,cB,bounddis); %transmission angle
[energyme,e,et,er,energratio,evantotal]=energemetrix(usuresolu,iusuresolu,C,loc,Fi,uA,uB,w,c0,
inciang,hA,hB,N,u0,Li,bounddis,cA,cB,cvecinte,ewaven,co2,ibounddis,qmatrixintenew);
%energy
figure(1) %dispersion relation with two wavenumber
plot(rKxLi,p,'b–','LineWidth',2.5),grid on;hold on
plot(irKxLi,p,'m–','LineWidth',2.5),grid on;hold on
plot([aimKxLi,aimKxLi],[0,KyLi],'k–','LineWidth',2.5),grid on;hold on
```

```
xlabel('KxLi');ylabel('KyLi')
figure(2) %modeshape for real Ky
plot(leng(1:length(leng)-2),real(wvamp(1,(1:length(leng)-2))),'k','LineWidth',2.5),grid on;
%change number in wvamp hold on
plot(leng(1:length(leng)-2),imag(wvamp(1,(1:length(leng)-2))),'k–','LineWidth',2.5),grid on;
xlabel('x');ylabel('w(x) for Ky');
figure(3) %modeshape for evanescent iKy
plot(leng(1:length(leng)-2),real(iwvamp(1,(1:length(leng)-2))),'k–','LineWidth',2.5),grid on;
%change number in iwvamp xlabel('x');ylabel('w(x) for iKy');
```

Subprogramme for angle and energy

```
function [aimKxLi,ckn]=waveinfirst(realKxLi) %translate KxLi into first Brillouin zone
n2pi=floor(realKxLi/2/pi);
if (realKxLi-n2pi*2*pi-pi)*(realKxLi-n2pi*2*pi)==0
   aimKxLi=0;ckn=2;
else
   if (realKxLi-n2pi*2*pi-pi)*(realKxLi-n2pi*2*pi)>0
      aimKxLi=2*pi-realKxLi+n2pi*2*pi;ckn=1;
   else
      aimKxLi=realKxLi-n2pi*2*pi;ckn=2;
   end
end

function [rKxLi,irKxLi,solution,fix,p,isolution,ifix]=generKxLiparfo(w,uA,cA,
hA,uB,cB,hB,KyLi,stepforwave,Fi,Li,aimKxLi)%generated KxLi and KyLi
fix=0;ifix=0;numco=floor(KyLi/stepforwave)+1;
rKxLi(1:numco+1)=0;irKxLi(1:numco+1)=0;p(1,1:numco+1)=0;
parfor j1=1:numco+1
   Ky=(j1-1)/Li*stepforwave;iKy=i*(j1-1)/Li*stepforwave;
   [MA,]=shearmatrix(w,uA,cA,Ky,hA);[MB]=shearmatrix(w,uB,cB,Ky,hB);
   [~,trMi]=MFibonacci(MA,MB,Fi);
   [iMA,]=shearmatrix(w,uA,cA,iKy,hA);[iMB]=shearmatrix(w,uB,cB,iKy,hB);
   [~,triMi]=MFibonacci(iMA,iMB,Fi);
   rKxLi(j1)=real(acos(trMi/2));irKxLi(j1)=real(acos(triMi/2));p(j1)=(j1-1)*stepforwave;
end
for i1=1:numco+1
   if abs(trMin(i1)-2*cos(aimKxLi))<=1e-1
      fix=fix+1;solution(1,fix)=(i1-1)*stepforwave;solution(2,fix)=rKxLi(i1);
   end
   if abs(triMin(i1)-2*cos(aimKxLi))<=1e-1
      ifix=ifix+1;isolution(1,ifix)=(i1-1)*stepforwave;isolution(2,ifix)=irKxLi(i1);
   end
end

function [suresolu,countnum,co,co2,suresolu2,countnum2,bounddis,u,usuresolu,isuresolu2,
ibounddis,iusuresolu,ico2,iu,wanumbangle,n2pi,error,ierror]=smallfindKyLi(solution,fix,aimKxLi,
w,uA,cA,hA,uB,cB,hB,Fi,Li,stepforwave,isolution,ifix,realKxLi);%Newton method and inverse it-
eration
i1=0; ij1=0; fix2=0; ifix2=0;[suresolu,countnum,co]=smallfind2KyLinew(solution,fix,aimKxLi);
[isuresolu, ,ico]=smallfind2KyLinew(isolution,ifix,aimKxLi);
```

```
for k=1:co
   for j1=suresolu(k,1):stepforwave*1e-4:suresolu(k,2)
      i1=i1+1;Ky=j1/Li;
      [MA]=shearmatrix(w,uA,cA,Ky,hA);[MB]=shearmatrix(w,uB,cB,Ky,hB);
      [~,trMi]=MFibonacci(MA,MB,Fi);trMin(i1)=trMi;rKxLi(i1)=real(acos(trMi/2));
      if abs(trMi-2*cos(aimKxLi))<=1e-4
         fix2=fix2+1;solution2(1,fix2)=j1;solution2(2,fix2)=rKxLi(i1);solution2(3,fix2)=trMin(i1);
      end
   end
end
for ik=1:ico
   for ij=isuresolu(ik,1):stepforwave*1e-4:isuresolu(ik,2)
      ij1=ij1+1;iKy=ij*i/Li;
      [iMA]=shearmatrix(w,uA,cA,iKy,hA);[iMB]=shearmatrix(w,uB,cB,iKy,hB);
      [~,triMi]=MFibonacci(iMA,iMB,Fi);triMin(ij1)=triMi;irKxLi(ij1)=real(acos(triMi/2));
      if abs(triMi-2*cos(aimKxLi))<=1e-4
         ifix2=ifix2+1;isolution2(1,ifix2)=ij;isolution2(2,ifix2)=irKxLi(ij1);
         isolution2(3,ifix2)=triMin(ij1);
      end
   end
end
[suresolu2,countnum2,co2]=smallfind2KyLinew(solution2,fix2,aimKxLi);
[isuresolu2,~,ico2]=smallfind2KyLinew(isolution2,ifix2,aimKxLi);
[bounddis,u,usuresolu,error]=inverseitertionlamina(suresolu2,co2,w,uA,cA,hA,uB,cB,hB,Fi,Li,
realKxLi);
[ibounddis,iu,iusuresolu,ierror]=inverseitertionlaminaiky(isuresolu2,ico2,w,uA,cA,hA,uB,cB,hB,
Fi,Li,aimKxLi);wanumbangle(1:length(usuresolu))=0;
for j1=1:length(usuresolu)
   wanumbangle(j1)=atand(realKxLi/usuresolu(j1));n2pi=floor(wanumbangle(j1)/360);
   wanumbangle(j1)=wanumbangle(j1)-n2pi*360;
end

function [suresolu,countnum,co]=smallfind2KyLinew(solution,fix,aimKxLi);
suresolu(1:30,1:2)=0;%The number of row can be changedcountnum(1:30,1:2)=0;
cosKxLi=2*cos(aimKxLi);j1=0;
for i1=2:fix
   if abs(solution(1,i1)-solution(1,i1-1))<=1e-2
      if (solution(3,i1)-cosKxLi)*(solution(3,i1-1)-cosKxLi)<=0
         j1=j1+1;suresolu(j1,1)=solution(1,i1-1);suresolu(j1,2)=solution(1,i1);
         countnum(j1,1)=solution(2,i1-1);countnum(j1,2)=solution(2,i1);
      end
   end
end
co=j1;

function [M,q]=shearmatrix(w,u,c,Ky,h);
q=(sqrt((w/c)^2-Ky^2))
if w==0
   M(1,1)=1;M(1,2)=0;M(2,1)=h/u;M(2,2)=1;
else
   M(1,1)=(cos(q*h));M(1,2)=(-u*q*sin(q*h));M(2,1)=(sin(q*h)/(u*q));M(2,2)=M(1,1);
```

```
end

function [Mi,trMi,Mc]=MFibonacci(MA,MB,Fi);
Mc=eye(2);trM(1:Fi+1)=0;trM(1)=trace(MB);trM(2)=trace(MA);trM(3)=trace(MB*MA);
[C,loc]=vectorFibon(Fi);
for i1=1:C(1,Fi+1)
   if loc(i1,Fi+1)==1
      Mc=MA*Mc;
   else
      Mc=MB*Mc;
   end
end
M(1:2,1:(Fi+1)*2)=0;M(1:2,1:2)=MB;M(1:2,3:4)=MA;
for i=2:Fi
   M(1:2,2*i+1:2*i+2)=M(1:2,2*(i-2)+1:2*(i-2)+2)*M(1:2,2*(i-1)+1:2*(i-1)+2);
end
Mi=M(1:2,Fi*2+1:Fi*2+2);trMi=trace(Mi);

function [bounddis,u,usuresolu,error]=inverseitertionlamina(suresolu2,co2,w,uA,cA,hA,uB,cB,
hB,Fi,Li,aimKxLi)
eim(1,1)=exp(-i*aimKxLi);eim(1,2)=0;eim(2,1)=0;eim(2,2)=eim(1,1);
bounddis(1:2,1:co2)=0;u(1:co2)=0;usuresolu(1:co2)=0;
for i1=1:co2
   Kyl=suresolu2(i1,1)/Li;Kyu=suresolu2(i1,2)/Li;Kym=(Kyl+Kyu)/2;
   [MAl,qAl]=shearmatrix(w,uA,cA,Kyl,hA);[MBl,qBl]=shearmatrix(w,uB,cB,Kyl,hB);
   [Mil,trMil]=MFibonacci(MAl,MBl,Fi);
   [MAu,qAl]=shearmatrix(w,uA,cA,Kyu,hA);[MBu,qBl]=shearmatrix(w,uB,cB,Kyu,hB);
   [Miu,trMil]=MFibonacci(MAu,MBu,Fi);
   [MAm,qAl]=shearmatrix(w,uA,cA,Kym,hA); [MBm,qBl]=shearmatrix(w,uB,cB,Kym,hB);
   [Mim,trMil]=MFibonacci(MAm,MBm,Fi);
   Mm=Mim-eim;Mu=Miu-eim;Ml=Mil-eim;inver=(Mm)\(Mu-Ml);
   j1(1:2,1:1000)=0;lamda(1:1000)=0;j1(1:2,1)=rand(2,1);
   for k=2:1e7
      j1(1:2,k)=inver*j1(1:2,k-1);[mx,id]=max(abs(j1(1:2,k)));lamda(k)=j1(id,k);
      j1(1:2,k)=j1(1:2,k)/j1(id,k);
      if abs(j1(id,k)-j1(id,k-1))<=1e-40
         break
      end
   end
   error(i1,1)=abs(j1(id,k)-j1(id,k-1));bounddis(1:2,i1)=((j1(1:2,k)));
   u(i1)=real(1/lamda(k));usuresolu(i1)=((Kym-u(i1)*(Kyu-Kyl)))*Li;
end

function [N]=ensureN(co2,ewaven)
if mod(co2(1,1)+ewaven-1,2)==0
   N=(co2(1,1)+ewaven-1)/2;
else
   N=(co2(1,1)+ewaven-2)/2;
end

function [C,loc]=vectorFibon(Fi) % vectorising Fibonacci sequence
C(1,1:Fi+1)=0;C(1,1:2)=1;
```

```
for jp=2:Fi
   C(1,jp+1)=C(1,jp)+C(1,jp-1);
end
loc(1:C(1,Fi+1),1:Fi+1)=0;loc(1,1)=2;loc(1,2)=1;
for j1=2:Fi
   loc(:,j1+1)=loc(:,j1);putjl=find(loc(:,j1)==0);putjm=find(loc(:,j1-1)==0);
   loc(putjl(1):putjl(1)+putjm(1)-2,j1+1)=loc(1:putjm(1)-1,j1-1);
end

function [wvampn,lengn,bouncodi,n,C,loc,iwvampn,uvamp,duvamp,bounddis,ibounddis,
normalized,intgdispla,intgdisplanew,uwvamp,iuvamp]=waveamptde(Li,Fi,w,uA,cA,hA,uB,cB,hB,
lenstep,usuresolu,aimKxLi,bounddis,iusuresolu,ibounddis,ckn,uaverage,realKyLi);
[C,loc]=vectorFibon(Fi);intgdispla(1:length(usuresolu)+length(iusuresolu))=0;
intgdisplanew(1:length(usuresolu)+length(iusuresolu))=0;intgdis(1:4,1)=0;Kx=aimKxLi/Li;
leng=0:lenstep:Li;
wvamp(1:length(usuresolu),1:length(leng))=0;iwvamp(1:length(iusuresolu),1:length(leng))=0;
uvamp(1:length(usuresolu),1:length(leng))=0;iuvamp(1:length(iusuresolu),1:length(leng))=0;
duvamp(1:length(usuresolu),1:length(leng))=0;uwvamp(1:length(usuresolu),1:length(leng))=0;
bouncodi(1:2,1:length(usuresolu))=0;ibouncodi(1:2,1:length(iusuresolu))=0;
nbounddis(1:2,1:length(usuresolu))=0;nibounddis(1:2,1:length(usuresolu))=0;
bound(1:2,1:length(leng))=0;ibound(1:2,1:length(leng))=0;
for ic=1:length(usuresolu)
   Ky=usuresolu(ic)/Li;
   [MA,qA]=shearmatrix(w,uA,cA,Ky,hA);[MB,qB]=shearmatrix(w,uB,cB,Ky,hB);
   bouncodi(1:2,ic)=bounddis(1:2,ic);start=0;k=1;wvamp(ic,1)=(bouncodi(2,ic));
   for i1=1:C(1,Fi+1)
      if loc(i1,Fi+1)==1
         for x=lenstep:lenstep:hA
            k=k+1; [MAs]=shearmatrix(w,uA,cA,Ky,x);bound(1:2,k)=MAs*bouncodi(1:2,ic);
            wvamp(ic,k)=bound(2,k)*exp(i*Kx*(x+start));uwvamp(ic,k)=uA*wvamp(ic,k);
            uvamp(ic,k)=(bound(2,k));
            duvamp(ic,k)=real(cos(qA*x)/uA*bouncodi(1,ic)-qA*sin(qA*x)*bouncodi(2,ic));
         end
         intgdis(1)=abs(bouncodi(1,ic))^2/(uA*qA^3)*(qA*hA/2-sin(2*qA*hA)/4);
         intgdis(2)=conj(bouncodi(2,ic))*bouncodi(1,ic)/(qA^2)/2*sin(qA*hA)^2;
         intgdis(3)=conj(bouncodi(1,ic))*bouncodi(2,ic)/(qA^2)/2*sin(qA*hA)^2;
         intgdis(4)=uA/qA*abs(bouncodi(2,ic))^2*(qA*hA/2+sin(2*qA*hA)/4);
         intgdisplanew(ic)=intgdisplanew(ic)+sum(intgdis);start=start+hA;
         bouncodi(1:2,ic)=MA*bouncodi(1:2,ic);
      else
         for x=lenstep:lenstep:hB
            k=k+1;[MBs, ]=shearmatrix(w,uB,cB,Ky,x);bound(1:2,k)=MBs*bouncodi(1:2,ic);
            wvamp(ic,k)=bound(2,k)*exp(i*Kx*(x+start));uwvamp(ic,k)=uB*wvamp(ic,k);
            uvamp(ic,k)=(bound(2,k));
            duvamp(ic,k)=real(cos(qB*x)/uB*bouncodi(1,ic)-qB*sin(qB*x)*bouncodi(2,ic));
         end
         intgdis(1)=abs(bouncodi(1,ic))^2/(uB*qB^3)*(qB*hB/2-sin(2*qB*hB)/4);
         intgdis(2)=conj(bouncodi(2,ic))*bouncodi(1,ic)/(qB^2)/2*sin(qB*hB)^2;
         intgdis(3)=conj(bouncodi(1,ic))*bouncodi(2,ic)/(qB^2)/2*sin(qB*hB)^2;
         intgdis(4)=uB/qB*abs(bouncodi(2,ic))^2*(qB*hB/2+sin(2*qB*hB)/4);
         intgdisplanew(ic)=intgdisplanew(ic)+sum(intgdis);start=start+hB;
```

```
        bouncodi(1:2,ic)=MB*bouncodi(1:2,ic);
      end
    end
end
for ii=1:length(iusuresolu)
   iKy=iusuresolu(ii)/Li;
   [iMA,iqA]=shearmatrix(w,uA,cA,iKy,hA);[iMB,iqB]=shearmatrix(w,uB,cB,iKy,hB);
   ibouncodi(1:2,ii)=ibounddis(1:2,ii);start=0;ik=1;iwvamp(ii,1)=(ibouncodi(2,ii));
   for i1=1:C(1,Fi+1)
      if loc(i1,Fi+1)==1
         for x=lenstep:lenstep:hA
            ik=ik+1;[iMAs]=shearmatrix(w,uA,cA,iKy,x);ibound(1:2,ik)=iMAs*ibouncodi(1:2,ii);
            iwvamp(ii,ik)=(ibound(2,ik)*exp(i*Kx*(x+start)));iuvamp(ii,ik)=(ibound(2,ik));
         end
         intgdis(1)=abs(ibouncodi(1,ii))^2/(uA*iqA^3)*(iqA*hA/2-sin(2*iqA*hA)/4);
         intgdis(2)=conj(ibouncodi(2,ii))*ibouncodi(1,ii)/(iqA^2)/2*sin(iqA*hA)^2;
         intgdis(3)=conj(ibouncodi(1,ii))*ibouncodi(2,ii)/(iqA^2)/2*sin(iqA*hA)^2;
         intgdis(4)=uA/iqA*abs(ibouncodi(2,ii))^2*(iqA*hA/2+sin(2*iqA*hA)/4);
         intgdisplanew(ii+length(usuresolu))=intgdisplanew(ii+length(usuresolu))+sum(intgdis);
         start=start+hA;ibouncodi(1:2,ii)=iMA*ibouncodi(1:2,ii);
      else
         for x=lenstep:lenstep:hB
            ik=ik+1;[iMBs, ]=shearmatrix(w,uB,cB,iKy,x);ibound(1:2,ik)=iMBs*ibouncodi(1:2,ii);
            iwvamp(ii,ik)=(ibound(2,ik)*exp(i*Kx*(x+start)));iuvamp(ii,ik)=(ibound(2,ik));
         end
         intgdis(1)=abs(ibouncodi(1,ii))^2/(uB*iqB^3)*(iqB*hB/2-sin(2*iqB*hB)/4);
         intgdis(2)=conj(ibouncodi(2,ii))*ibouncodi(1,ii)/(iqB^2)/2*sin(iqB*hB)^2;
         intgdis(3)=conj(ibouncodi(1,ii))*ibouncodi(2,ii)/(iqB^2)/2*sin(iqB*hB)^2;
         intgdis(4)=uB/iqB*abs(ibouncodi(2,ii))^2*(iqB*hB/2+sin(2*iqB*hB)/4);
         intgdisplanew(ii+length(usuresolu))=intgdisplanew(ii+length(usuresolu))+sum(intgdis);
         start=start+hB;ibouncodi(1:2,ii)=iMB*ibouncodi(1:2,ii);
      end
   end
end
normalized=sqrt(intgdisplanew/(uaverage*Li));
for i1=1:length(usuresolu)
   wvamp(i1,:)=(wvamp(i1,:)/normalized(i1));uvamp(i1,:)=(uvamp(i1,:)/normalized(i1));
   uwvamp(i1,:)=uwvamp(i1,:)/normalized(i1);bounddis(:,i1)=(bounddis(:,i1)/normalized(i1));
end
for j1=1:length(iusuresolu)
   iwvamp(j1,:)=(iwvamp(j1,:)/normalized(j1+length(usuresolu)));
   ibounddis(:,j1)=(ibounddis(:,j1)/normalized(j1+length(usuresolu)));
   iuvamp(j1,:)=(iuvamp(j1,:)/normalized(j1+length(usuresolu)));
end

function [rflewvam, kyn,propkyn,evankyn]=waveamfrel(c0,w,Li,lenstep,N,inciang);
kyn(1:2*N+1,1)=0;leng=0:lenstep:Li;rflewvam(1:2*N+1,1:length(leng))=0;
K0=w/c0;ic=0;j1=0;
for i1=-N:1:N
   kyn(i1+N+1)=sqrt(K0^2-(K0*sind(inciang)+2*i1*pi/Li)^2);
   if imag(kyn(i1+N+1))==0
```

```
        ckn=0;ic=ic+1;propkyn(ic,1)=i1;propkyn(ic,2)=kyn(i1+N+1);
    else
        ckn=1;j1=j1+1;evankyn(j1,1)=i1;evankyn(j1,2)=kyn(i1+N+1)*(-1)^ckn;
    end
    kyn(i1+N+1)=kyn(i1+N+1)*(-1)^ckn;
    for jc=1:length(leng)
        rflewvam(i1+N+1,jc)=exp(i*2*i1*pi*(jc-1)*lenstep/Li);
    end
end

function [cvecinte,qmatrixintenew,dvecintenew,conditinum]=matrixcalcintenew(usuresolu,
iusuresolu,C,loc,Fi,uA,uB,w,c0,inciang,hA,hB,N,u0,Li,bounddis,ibounddis,realKxLi,cA,cB,
ewaven,co2,normalized,uaverage)%scattering coefficients
usuresolu(co2+1:co2+ewaven)=iusuresolu(1,1:ewaven);Kx=realKxLi/Li;K0=w/c0;
bounddis(1:2,co2+1:co2+ewaven)=ibounddis(1:2,1:ewaven);
boundcodij(1:2,1:co2+ewaven)=0;cboundcodij(1:2,1:co2+ewaven)=0;
dvecintenew(1:4*N+2,1)=0;qmatrixintenew(1:4*N+2,1:4*N+2)=0;
for ic=1:2*N+1
    iKy=(usuresolu(ic)/Li);qmatrixintenew(ic,ic)=uaverage*Li;
    [iMA,iqA]=shearmatrix(w,uA,cA,iKy,hA);[iMB,iqB]=shearmatrix(w,uB,cB,iKy,hB);
    qmatrixintenew(ic+2*N+1,ic)=qmatrixintenew(ic,ic)*iKy;
    for jc=1:2*N+1
        start=0;boundcodij(1:2,ic)=bounddis(1:2,ic);cboundcodij(1:2,ic)=conj(boundcodij(1:2,ic));
        m=(jc-N-1);xigma=1/(-i*(Kx+2*m*pi/Li));
        if real(sqrt(K0.^2-(K0.*sind(inciang)+2.*(jc-N-1).*pi./Li).^2))==0
            ckn=1;
        else
            ckn=0;
        end
        for i1=1:C(1,Fi+1)
            if loc(i1,Fi+1)==1
                M22(1)=((xigma*sin(iqA*hA)/uA/iqA*exp(-i*(Kx+2*m*pi/Li)*(hA+start))-xigma^2/
                uA*cos(iqA*hA)*exp(-i*(Kx+2*m*pi/Li)*(hA+start))+xigma^2/uA*exp(-i*(Kx+2*m*
                pi/Li)*(start)))*cboundcodij(1,ic)/(1+xigma^2*iqA^2));
                M22(2)=((xigma*cos(iqA*hA)*exp(-i*(Kx+2*m*pi/Li)*(hA+start))-xigma*exp(-i*(
                Kx+2*m*pi/Li)*start)+xigma^2*iqA*sin(iqA*hA)*exp(-i*(Kx+2*m*pi/Li)*
                (hA+start)))*cboundcodij(2,ic)/(1+xigma^2*iqA^2));
                qmatrixintenew(ic,jc+2*N+1)=qmatrixintenew(ic,jc+2*N+1)-uA*(sum(M22));
                qmatrixintenew(ic+2*N+1,jc+2*N+1)=qmatrixintenew(ic+2*N+1,jc+2*N+1)+u0*(-1)^
                ckn*sqrt(K0^2-(K0*sind(inciang)+2*m*pi/Li)^2)*(sum(M22));start=start+hA;
                boundcodij(1:2,ic)=iMA*boundcodij(1:2,ic);cboundcodij(1:2,ic)=conj(boundcodij(1:2,ic));
            else
                M22(1)=((xigma*sin(iqB*hB)/uB/iqB*exp(-i*(Kx+2*m*pi/Li)*(hB+start))-xigma^2/
                uB*cos(iqB*hB)*exp(-i*(Kx+2*m*pi/Li)*(hB+start))+xigma^2/uB*exp(-i*(Kx+2*m*
                pi/Li)*(start)))*cboundcodij(1,ic)/(1+xigma^2*iqB^2));
                M22(2)=((xigma*cos(iqB*hB)*exp(-i*(Kx+2*m*pi/Li)*(hB+start))-xigma*exp(-i*(
                Kx+2*m*pi/Li)*start)+xigma^2*iqB*sin(iqB*hB)*exp(-i*(Kx+2*m*pi/Li)*
                (hB+start)))*cboundcodij(2,ic)/(1+xigma^2*iqB^2));
                qmatrixintenew(ic,jc+2*N+1)=qmatrixintenew(ic,jc+2*N+1)-uB*(sum(M22));
                qmatrixintenew(ic+2*N+1,jc+2*N+1)=qmatrixintenew(ic+2*N+1,jc+2*N+1)+u0*(-1)^
                ckn*sqrt(K0^2-(K0*sind(inciang)+2*m*pi/Li)^2)*(sum(M22));start=start+hB;
```

```
            boundcodij(1:2,ic)=iMB*boundcodij(1:2,ic);
            cboundcodij(1:2,ic)=conj(boundcodij(1:2,ic));
        end
    end
  end
end
dvecintenew(1:2*N+1,1)=-qmatrixintenew(1:2*N+1,3*N+2);
dvecintenew(2*N+2:4*N+2,1)=qmatrixintenew(2*N+2:4*N+2,3*N+2);
cvecinte=qmatrixintenew\dvecintenew;conditinum=cond(qmatrixintenew);

function [poyntintex,poyntinteynew,tranangintenew]=poyntvectorinte(C,loc,Fi,uA,uB,w,usuresolu,
hA,hB,Li,cA,cB,bounddis)%transmission wave angle
poyntintex(1:length(usuresolu))=0;poyntinteynew(1:length(usuresolu))=0;
tranangintenew(1:length(usuresolu))=0;bouncodi(1:2,1:length(usuresolu))=0;
for ic=1:length(usuresolu)
  Ky=usuresolu(ic)/Li;poyntinteynew(ic)=1/2*w*Ky*uaverage;
  [MA,qA]=shearmatrix(w,uA,cA,Ky,hA);[MB,qB]=shearmatrix(w,uB,cB,Ky,hB);
  bouncodi(1:2,ic)=bounddis(1:2,ic);
  for i1=1:C(1,Fi+1)
    if loc(i1,Fi+1)==1
      px4=(imag(bouncodi(2,ic)*conj(bouncodi(1,ic)))*hA/2/Li*w);
      poyntintex(ic)=poyntintex(ic)+sum(px4);bouncodi(1:2,ic)=MA*bouncodi(1:2,ic);
    else
      px4=(imag(bouncodi(2,ic)*conj(bouncodi(1,ic)))*hB/2/Li*w);
      poyntintex(ic)=poyntintex(ic)+sum(px4);bouncodi(1:2,ic)=MB*bouncodi(1:2,ic);
    end
  end
  tranangintenew(ic)=atand(poyntintex(ic)/poyntinteynew(ic));
end

function [energyme,e,et,er,energratio,evantotal]=energemetrix(usuresolu,iusuresolu,C,loc,Fi,
uA,uB,w,c0,inciang,hA,hB,N,u0,Li,bounddis,cA,cB,cvecinte,ewaven,co2,ibounddis,qmatrixinte)
energyme(1:2*N+1,1:2)=0;K0=w/c0;e=0.5*u0*K0*cosd(inciang)*w*Li;
energratio(1:3,1)=0;er(1:2*N+1)=0;et(1:2*N+1)=0;
if inciang==90
  energyme(N+1,2)=1;
else
  for ic=1:2*N+1
    energyme(ic,2)=(real(sqrt(K0^2-(K0*sind(inciang)+2*pi*(ic-1-N)/Li)^2))*
    abs(cvecinte(ic+2*N+1))^2)/(K0*cosd(inciang));
    er(ic)=0.5*w*(real(sqrt(K0^2-(K0*sind(inciang)+2*pi*(ic-1-N)/Li)^2))*
    abs(cvecinte(ic+2*N+1))^2)*u0*Li;
    et(ic)=0.5*w*abs(cvecinte(ic))^2*real(qmatrixinte(ic+2*N+1,ic));
    energyme(ic,1)=abs(cvecinte(ic))^2*real(qmatrixinte(ic+2*N+1,ic))/(u0*K0*cosd(inciang)*Li);
    energratio(1)=energratio(1)+energyme(ic,1);energratio(2)=energratio(2)+energyme(ic,2);
    evantotal=(-imag(sqrt(K0^2-(K0*sind(inciang)+2*pi*(ic-1-N)/Li)^2))*
    abs(cvecinte(ic+2*N+1))^2)/(K0*cosd(inciang))+abs(cvecinte(ic))^2
    *imag(qmatrixinte(ic+2*N+1,ic))/(u0*K0*cosd(inciang)*Li);
  end
end
energratio(3)=energratio(1)/energratio(2);
```

Topological Interface State

The main programme for the sign of Impedance and the Zak phase

```
ps=2700; pl=2700; El=70e9; Es=70e9; b=0.01; hs=0.01; hl=0.02;%material and geometric
As=hs*b; Al=hl*b; Fi=3;N=6;%number of unit cellsKLpi=pi; KLZERO=0;
cl=sqrt(El/pl); cs=sqrt(Es/ps); rl=sqrt(Al/pi); rs=sqrt(As/pi);
Ll1=0.025*2; Ls1=0.1;%original length of rods Lm=Ll1*2+Ls1;
j=1; k=0; q=3;%canonical ratio[rtio,period1,fam]=ratios(j,k,q);
Ltimes=(cs+(1/rtio)*cl)/(cl+(1/rtio)*cs);
[Ll2,Ls]=keepthicnesssame(Ll1*Ltimes,Ls1*Ltimes,2,cl,cs,rtio);
[n,n2]=periodforf(rtio,fam,cl,cs,Ll2,Ls,j,k,q);Ll=Ll2/2;calcustep=5e-3;%calculation accuracy
linstep=1e-6;%calculation accuracy for wave field
expizak=1-Al^2*El*pl/Es/ps/As^2;%Zak phase for passband 0
f=calcustep:calcustep:(n/3)*1e-3; trTi(1:3,1:length(f))=0;BlochK(1:length(f))=0;fix=0;Ofix=0;
for ic=1:length(f)
    fi=f(ic);[Ts]=axiallmatrix(ps,Es,As,fi*2*pi*1000,Ls);
    [Tl]=axiallmatrix(pl,El,Al,fi*2*pi*1000,Ll);[Ti,trTi(3,ic), ]=MFibonacci(Tl,Ts,Fi);
    BlochK(ic)=(acos(trTi(3,ic)/2));
end
for j1=1:length(f)
    if abs(trTi(3,j1)-2*cos(KLpi))<=1e-1
        fix=fix+1;solutionpi(1,fix)=(j1-1)*calcustep;
        solutionpi(2,fix)=BlochK(j1);solutionpi(3,fix)=trTi(3,j1);
    end
    if abs(trTi(3,j1)-2*cos(KLZERO))<=1e-1
        Ofix=Ofix+1;solutionzero(1,Ofix)=(j1-1)*calcustep;
        solutionzero(2,Ofix)=BlochK(j1);solutionzero(3,Ofix)=trTi(3,j1);
    end
end
zvecto(1:length(f))=0; blocksurf=-pi:pi/200:pi;
[suresolupi,countnumpi,copi]=smallfind2KyLinew(solutionpi,fix,KLpi);
[suresoluzero,countnumzero,cozero]=smallfind2KyLinew(solutionzero,Ofix,KLZERO);
[bounddispi,upi,usuresolupi,errorpi]=inverseitertionrod(suresolupi,copi,ps,pl,Ll,As,Al,Ls,El,Es,
Fi,Lm,KLpi);
[bounddiszero,uzero,usuresoluzero,errorzero]=inverseitertionrod(suresoluzero,cozero,ps,pl,Ll,As,
Al,Ls,El,Es,Fi,Lm,KLZERO);
[Blockband,fband]=numericalbandproblem(BlochK,f);
[wzero,Pzero,xcordzero,bounddisnewzero,intePzero,boundnewzero]=displacementrod(
bounddiszero,usuresoluzero,KLZERO,linstep,ps,pl,Ll,As,Al,Ls,El,Es,Fi,Lm,rl,rs);
[wpi,Ppi,xcordpi,bounddisnewpi,intePpi,boundnewpi]=displacementrod(bounddispi,usuresolupi,
KLpi,linstep,ps,pl,Ll,As,Al,Ls,El,Es,Fi,Lm,rl,rs);
[negaimp,postiimp,surfaceimpepi,surfaceimpezero,aspi,aszero]=surfaceimpedanceother(
bounddisnewpi,bounddisnewzero,ps,Es,As,Ls,pl,El,Al,Ll,usuresolupi,usuresoluzero,f,blocksurf,
calcustep);
[eigenu,Blockbandc,fbandc]=eigenfucntionrod(Blockband,fband,ps,Es,As,Ls,pl,El,Al,Ll,Fi,rl,rs,
boundnewzero,usuresoluzero,boundnewpi,usuresolupi);
[thetaZako,thetaZak,Impro]=numericalZakphase(ps,pl,Es,El,rs,rl,As,Al,Ll,Ls,Blockbandc,fbandc,
Fi,eigenu,Lm);
xcord2=(length(xcordpi)+1)/2; xcorf=length(xcordpi); Lmd2=Lm/2;
figure(1);
plot3(real(BlochK),f,zvecto,'k','LineWidth',2),grid on;hold on
```

```
plot3(-real(BlochK),f,zvecto,'k','LineWidth',2),grid on;hold on
surf(blocksurf,f,postiimp,'EdgeColor','none','FaceColor',[0.93333 0.5098 0.93333]),grid on;
hold on
surf(blocksurf,f,negaimp,'EdgeColor','none','FaceColor',[0.3010 0.7450 0.9330]),grid on;
view([0,0,1]);
figure(2);
plot(xcordpi(1:xcord2),real(wpi(1,1:xcord2)),'k','LineWidth',2.5),grid on;hold on
plot(xcordpi(xcord2:xcorf)-Lm,-real(wpi(1,xcord2:xcorf)),'k','LineWidth',2.5),grid on;
xlabel('x');ylabel('u(x) for band edge pi');
figure(3);
plot(xcordpi(1:xcord2),real(wzero(1,1:xcord2)),'k','LineWidth',2.5),grid on;hold on
plot(xcordpi(xcord2:xcorf)-Lm,real(wzero(1,xcord2:xcorf)),'k','LineWidth',2.5),grid on;
xlabel('x');ylabel('u(x) for band edge 0');
```

Subprogramme for the sign of Impedance and the Zak phase

We do not show inverse iteration and Newton method and wave filed due to similar to method in obtaining KyLi and modeshape w in SH wave propagation in laminate.

```
function [Blockband,fband]=numericalbandproblem(BlochK,f)
Blockband(1,1)=0;fband(1,1)=0;countband=1;fstart=0;
for ic=1:length(f)-1
   if imag(BlochK(ic))==0
      Blockband(countband,ic-fstart)=BlochK(ic);fband(countband,ic-fstart)=f(ic);
   else
      fstart=ic;
   end
   if imag(BlochK(ic))==0 && imag(BlochK(ic+1)) =0
      countband=countband+1;
   end
   if imag(BlochK(ic)) =0 && imag(BlochK(ic+1))==0
      countband=countband+1;
   end
end
```

```
function [negaimp,postiimp,surfaceimpepi,surfaceimpezero,aspi,aszero]=surfaceimpedanceother
(bounddisnewpi,bounddisnewzero,ps,Es,As,Ls,pl,El,Al,Ll,usuresolupi,usuresoluzero,f,blocksurf,
calcustep)
totalpiband=floor(length(usuresolupi)/2);totalzeroband=floor(length(usuresoluzero)/2);
aspi(length(usuresolupi))=0;aszero(length(usuresolupi))=0;
negaimp(1:length(f),1:length(blocksurf))=nan;postiimp(1:length(f),1:length(blocksurf))=nan;
surfaceimpepi(1:totalpiband,1)=0;surfaceimpezero(1:totalzeroband,1)=0;
for ic=1:totalpiband
   lopf=usuresolupi(2*ic-1);bouncodi=bounddisnewpi(1:2,2*ic-1);
   [Tsco]=axiallmatrix(ps,Es,As,lopf*2*pi*1000,Ls/2);
   [Tlco]=axiallmatrix(pl,El,Al,lopf*2*pi*1000,Ll);answer=Tsco*Tlco*bouncodi;
   if abs(answer(2))>=1.1e-2
      locl=floor(usuresolupi(2*ic-1)/calcustep);locu=floor(usuresolupi(2*ic)/calcustep);
      surfaceimpepi(ic,1)=-1;negaimp(locl:locu,1:length(blocksurf))=1;
      aspi(2*ic-1)=-1;aspi(2*ic)=1;
   else
```

```
        locl=floor(usuresolupi(2*ic-1)/calcustep);locu=floor(usuresolupi(2*ic)/calcustep);
        postiimp(locl:locu,1:length(blocksurf))=1;surfaceimpepi(ic,1)=1;
        aspi(2*ic-1)=1;aspi(2*ic)=-1;
    end
end
for ic=1:totalzeroband
    lopf=usuresoluzero(2*ic-1);bouncodi=bounddisnewzero(1:2,2*ic-1);
    [Tsco]=axiallmatrix(ps,Es,As,lopf*2*pi*1000,Ls/2);
    [Tlco]=axiallmatrix(pl,El,Al,lopf*2*pi*1000,Ll);answer=Tsco*Tlco*bouncodi;
    if abs(answer(2))>=1.1e-2
        locl=floor(usuresoluzero(2*ic-1)/calcustep);locu=floor(usuresoluzero(2*ic)/calcustep);
        postiimp(locl:locu,1:length(blocksurf))=1;surfaceimpezero(ic,1)=1;
        aszero(2*ic-1)=1;aszero(2*ic)=-1;
    else
        locl=floor(usuresoluzero(2*ic-1)/calcustep);locu=floor(usuresoluzero(2*ic)/calcustep);
        negaimp(locl:locu,1:length(blocksurf))=1;surfaceimpezero(ic,1)=-1;
        aszero(2*ic-1)=-1;aszero(2*ic)=1;
    end
end

function [eigenu,Blockbandc,fbandc]=eigenfucntionrod(Blockband,fband,ps,Es,As,Ls,pl,El,Al,
Ll,Fi,rl,rs,bounddisnewzero,usuresoluzero,bounddisnewpi,usuresolupi)
numbr=mod(length(Blockband(:,1)),2);counttotal=(length(Blockband(:,1))+numbr)/2;
eigenu(1:2*counttotal,1:2*length(Blockband(1,:))+3)=0;
Blockbandc(1:counttotal,1:2*length(Blockband(1,:))+3)=0;
fbandc(1:counttotal,1:2*length(Blockband(1,:))+3)=0;pin=length(usuresolupi);
zeron=length(usuresoluzero);[C,loc]=vectorFibon(Fi);
for count=1:counttotal
    for ic=1:length(Blockband(1,:))
        if Blockband(2*count-1,ic)>0
            [Ts]=axiallmatrix(ps,Es,As,fband(2*count-1,ic)*2*pi*1000,Ls);
            [Tl]=axiallmatrix(pl,El,Al,fband(2*count-1,ic)*2*pi*1000,Ll);
            [Ti]=MFibonacci(Tl,Ts,Fi);[eigenf,eigenv]=eig(Ti);sum=0;bouncodi(1:2,1)=eigenf(1:2,1);
            for i1=1:C(1,Fi+1)
                if loc(i1,Fi+1)==1
                    [Tl]=axiallmatrix(pl,El,Al,fband(2*count-1,ic)*2*pi*1000,Ll);
                    theint=@(x) 1./2./El.*rl.*abs(cos(sqrt(pl./El).*fband(2*count-1,ic).*2.*pi.*1000.*x).*
                    bouncodi(2,1)-sin(sqrt(pl./El).*fband(2*count-1,ic).*2.*pi.*1000.*x).*El.*Al.*sqrt(
                    pl./El).*(fband(2*count-1,ic).*2.*pi.*1000).*bouncodi(1,1)).^2;
                    inttheint=integral(theint,0,Ll);sum=sum+inttheint;bouncodi(1:2,1)=Tl*bouncodi(1:2,1);
                else
                    [Ts]=axiallmatrix(ps,Es,As,fband(2*count-1,ic)*2*pi*1000,Ls);
                    theint=@(x) 1./2./Es.*rs.*abs(cos(sqrt(ps./Es).*fband(2*count-1,ic).*2.*pi.*1000.*x).*
                    bouncodi(2,1)-sin(sqrt(ps./Es).*fband(2*count-1,ic).*2.*pi.*1000.*x).*Es.*As.*sqrt(
                    ps./Es).*(fband(2*count-1,ic).*2.*pi.*1000).*bouncodi(1,1)).^2;
                    inttheint=integral(theint,0,Ls);sum=sum+inttheint;bouncodi(1:2,1)=Ts*bouncodi(1:2,1);
                end
            end
            eigenf=eigenf/sqrt(sum);
            if imag(eigenv(1,1))>=0
                if mod(2*count-1,4)==1
```

```
            Blockbandc(count,length(Blockband(1,:))+2+ic)=Blockband(2*count-1,ic);
            Blockbandc(count,length(Blockband(1,:))+2-ic)=-Blockband(2*count-1,ic);
            eigenu(2*count-1:2*count,length(Blockband(1,:))+2+ic)=eigenf(1:2,1);
            eigenu(2*count-1:2*count,length(Blockband(1,:))+2-ic)=eigenf(1:2,2);
            fbandc(count,length(Blockband(1,:))+2+ic)=fband(2*count-1,ic);
            fbandc(count,length(Blockband(1,:))+2-ic)=(fband(2*count-1,ic));
        end
        if mod(2*count-1,4)==3
            ind=find(Blockband(2*count-1,:)==0);differ=ind(length(ind))-ind(1)+1;
            Blockbandc(count,2*length(Blockband(1,:))-differ-ic+3)=Blockband(2*count-1,ic);
            Blockbandc(count,ic+differ+1)=-Blockband(2*count-1,ic);
            eigenu(2*count-1:2*count,2*length(Blockband(1,:))+3-differ-ic)=eigenf(1:2,1);
            eigenu(2*count-1:2*count,ic+differ+1)=eigenf(1:2,2);
            fbandc(count,2*length(Blockband(1,:))+3-differ-ic)=(fband(2*count-1,ic));
            fbandc(count,ic+differ+1)=(fband(2*count-1,ic));
        end
        else
            if mod(2*count-1,4)==1
            Blockbandc(count,length(Blockband(1,:))+2+ic)=Blockband(2*count-1,ic);
            Blockbandc(count,length(Blockband(1,:))+2-ic)=-Blockband(2*count-1,ic);
            eigenu(2*count-1:2*count,length(Blockband(1,:))+2+ic)=eigenf(1:2,2);
            eigenu(2*count-1:2*count,length(Blockband(1,:))+2-ic)=eigenf(1:2,1);
            fbandc(count,length(Blockband(1,:))+2+ic)=fband(2*count-1,ic);
            fbandc(count,length(Blockband(1,:))+2-ic)=(fband(2*count-1,ic));
        end
        if mod(2*count-1,4)==3
            ind=find(Blockband(2*count-1,:)==0);differ=ind(length(ind))-ind(1)+1;
            Blockbandc(count,2*length(Blockband(1,:))+3-differ-ic)=Blockband(2*count-1,ic);
            Blockbandc(count,ic+1+differ)=-Blockband(2*count-1,ic);
            eigenu(2*count-1:2*count,2*length(Blockband(1,:))+3-differ-ic)=eigenf(1:2,2);
            eigenu(2*count-1:2*count,ic+1+differ)=eigenf(1:2,1);
            fbandc(count,2*length(Blockband(1,:))+3-differ-ic)=(fband(2*count-1,ic));
            fbandc(count,ic+1+differ)=fband(2*count-1,ic);
        end
      end
    end
  end
end
eigenzerosum=0;
for i1=1:C(1,Fi+1)
  if loc(i1,Fi+1)==1
    eigenzerosum=eigenzerosum+rl*Ll/El/2;
  else
    eigenzerosum=eigenzerosum+rs*Ls/Es/2;
  end
end
eigenzero(1,1)=0;eigenzero(2,1)=0;
eigenu(1:2,(length(eigenu)+1)/2)=eigenzero;Blockbandc(1,length(Blockbandc(1,:)))=pi;
Blockbandc(1,1)=-pi;fbandc(1,length(Blockbandc(1,:)))=(usuresolupi(1));
fbandc(1,1)=((usuresolupi(1)));eigenu(1:2,length(Blockbandc(1,:)))=real(bounddisnewpi(1:2,1));
eigenu(1:2,1)=real(bounddisnewpi(1:2,1));
```

```
for ipi=2:pin
   if mod(2*ipi-1,4)==1
      ind=find(Blockband(2*ipi-1,:)==0);differ=ind(length(ind))-ind(1)+1;
      Blockbandc(ipi,length(Blockbandc(1,:))-differ)=pi;Blockbandc(ipi,differ+1)=-pi;
      fbandc(ipi,length(Blockbandc(1,:))-differ)=real(usuresolupi(ipi));
      fbandc(ipi,differ+1)=real(usuresolupi(ipi));
      eigenu(2*ipi-1:2*ipi,length(Blockbandc(1,:))-differ)=real(bounddisnewpi(1:2,ipi));
      eigenu(2*ipi-1:2*ipi,differ+1)=real(bounddisnewpi(1:2,ipi));
   end
   if mod(2*ipi-1,4)==3
      ind=find(Blockband(2*ipi-1,:)==0);differ=ind(length(ind))-ind(1)+1;
      Blockbandc(ipi,length(Blockbandc(1,:))-differ)=pi;Blockbandc(ipi,differ+1)=-pi;
      fbandc(ipi,length(Blockbandc(1,:))-differ)=real(usuresolupi(ipi));
      fbandc(ipi,differ+1)=real(usuresolupi(ipi));
      eigenu(2*ipi-1:2*ipi,length(Blockbandc(1,:))-differ)=real(bounddisnewpi(1:2,ipi));
      eigenu(2*ipi-1:2*ipi,differ+1)=real(bounddisnewpi(1:2,ipi));
   end
end
for izero=1:zeron
   Blockbandc(izero+1,(length(Blockbandc(1,:))+1)/2)=0;
   fbandc(izero+1,(length(Blockbandc(1,:))+1)/2)=usuresoluzero(izero);
   eigenu(2*(izero+1)-1:2*(izero+1),(length(Blockbandc(1,:))+1)/2)=real(bounddisnewzero
   (1:2,izero));
end
evennum=floor(length(Blockbandc(:,1))/2);midloc=length(Blockband)+2;
zeroloc1(1:2,1:length(Blockbandc(:,1)))=0;
for chekczero=1:evennum
   for jce=1:floor(length(Blockbandc(1,:))/2)
      if Blockbandc(2*chekczero,midloc-jce)<0
         break;
      end
   end
   for jcb=1:floor(length(Blockbandc(1,:))/2)
      if Blockbandc(2*chekczero,jcb)<0
         break;
      end
   end
   Blockbandc(2*chekczero,jcb+jce-1:midloc-1)=Blockbandc(2*chekczero,jcb:midloc-jce);
   Blockbandc(2*chekczero,midloc+1:2*midloc-jce-jcb)=Blockbandc(2*chekczero,midloc+jce:
   length(Blockbandc(1,:))-jcb);Blockbandc(2*chekczero,1:jcb+jce-2)=0;
   Blockbandc(2*chekczero,2*midloc-jce-jcb+1:length(Blockbandc(1,:)))=0;
   fbandc(2*chekczero,jcb+jce-1:midloc-1)=fbandc(2*chekczero,jcb:midloc-jce);
   fbandc(2*chekczero,midloc+1:2*midloc-jce-jcb)=fbandc(2*chekczero,midloc+jce:length(
   Blockbandc(1,:))-jcb);fbandc(2*chekczero,1:jcb+jce-2)=0;
   fbandc(2*chekczero,2*midloc-jce-jcb+1:length(Blockbandc(1,:)))=0;
   eigenu(2*(2*chekczero)-1:2*(2*chekczero),jcb+jce-1:midloc-1)=eigenu(2*(2*chekczero)-1:2*
   (2*chekczero),jcb:midloc-jce);
   eigenu(2*(2*chekczero)-1:2*(2*chekczero),midloc+1:2*midloc-jce-jcb)=eigenu(2*(2*chekczero)-
   1:2*(2*chekczero),midloc+jce:length(Blockbandc(1,:))-jcb);
   eigenu(2*(2*chekczero)-1:2*(2*chekczero),1:jcb+jce-2)=0;
   eigenu(2*(2*chekczero)-1:2*(2*chekczero),2*midloc-jce-jcb+1:length(Blockbandc(1,:)))=0;
```

```
end

function [thetaZako,thetaZak]=numericalZakphase(ps,pl,Es,El,rs,rl,As,Al,Ll,Ls,Blockbandc,
fbandc,Fi,eigenu,Lm)
thetaZak(1:length(Blockbandc(:,1)),1)=0;thetaZako(1:length(Blockbandc(:,1)),1)=0;
[C,loc]=vectorFibon(Fi);
for count=1:length(fbandc(:,1))
   for ic=1:length(fbandc(1,:))-1
      bouncodi(1:2,1)=0;bouncodip(1:2,1)=0;
      if fbandc(count,ic) =0
         if fbandc(count,ic+1) =0
            start=0;inttheint(1:C(1,Fi+1))=0;bouncodi(1:2,1)=eigenu(2*count-1:2*count,ic);
            bouncodip(1:2,1)=eigenu(2*count-1:2*count,ic+1);
            K=Blockbandc(count,ic)/Lm;Kp=Blockbandc(count,ic+1)/Lm;
            for i1=1:C(1,Fi+1)
               if loc(i1,Fi+1)==1
                  [Tli]=axiallmatrix(pl,El,Al,fbandc(count,ic)*2*pi*1000,Ll);
                  [Tlip]=axiallmatrix(pl,El,Al,fbandc(count,ic+1)*2*pi*1000,Ll);
                  theint=@(x) 1./2./El.*rl.*conj(cos(sqrt(pl./El).*fbandc(count,ic).*2.*pi.*1000.*
                  x).*bouncodi(2,1)-sin(sqrt(pl./El).*fbandc(count,ic).*2.*pi.*1000.*x).*El.*Al.*
                  sqrt(pl./El).*(fbandc(count,ic).*2.*pi.*1000).*bouncodi(1,1)).*exp(i.*K.*(x+
                  start)).*(cos(sqrt(pl./El).*fbandc(count,ic+1).*2.*pi.*1000.*x).*bouncodip(2,1)-
                  sin(sqrt(pl./El).*fbandc(count,ic+1).*2.*pi.*1000.*x).*El.*Al.*sqrt(pl./El).*(
                  fbandc(count,ic+1).*2.*pi.*1000).*bouncodip(1,1)).*exp(-i.*Kp.*(x+start));
                  inttheint(i1)=integral(theint,0,Ll);start=start+Ll;
                  bouncodi(1:2,1)=Tli*bouncodi(1:2,1);bouncodip(1:2,1)=Tlip*bouncodip(1:2,1);
               else
                  [Tsi]=axiallmatrix(ps,Es,As,fbandc(count,ic)*2*pi*1000,Ls);
                  [Tsip]=axiallmatrix(ps,Es,As,fbandc(count,ic+1)*2*pi*1000,Ls);
                  theint=@(x) 1./2./Es.*rs*conj(cos(sqrt(ps./Es).*fbandc(count,ic).*2.*pi.*1000.*
                  x).*bouncodi(2,1)-sin(sqrt(ps./Es).*fbandc(count,ic).*2.*pi.*1000.*x).*Es.*As.*
                  sqrt(ps./Es).*(fbandc(count,ic).*2.*pi.*1000).*bouncodi(1,1)).*exp(i.*K.*(x+
                  start)).*(cos(sqrt(ps./Es).*fbandc(count,ic+1).*2.*pi.*1000.*x).*bouncodip(2,1)-
                  sin(sqrt(ps./Es).*fbandc(count,ic+1).*2.*pi.*1000.*x).*Es.*As.*sqrt(ps./Es).*(
                  fbandc(count,ic+1).*2.*pi.*1000).*bouncodip(1,1)).*exp(-i.*Kp.*(x+start));
                  inttheint(i1)=integral(theint,0,Ls);start=start+Ls;
                  bouncodi(1:2,1)=Tsi*bouncodi(1:2,1);bouncodip(1:2,1)=Tsip*bouncodip(1:2,1);
               end
            end
            thetaZako(count,1)=thetaZako(count,1)-angle(sum(inttheint));
         end
      end
   end
end
for l1=1:length(thetaZako)
   pinum=round(thetaZako(l1)/pi);
   if mod(pinum,2)==1
      thetaZak(l1)=pi;
   else
      thetaZak(l1)=0;
   end
```

```
end
```

The main programme for transmission and reflection coefficients

```
Es1=70e9; El1=70e9; pl1=2700; ps1=2700; %material parameters for rod1
As1=0.01*0.01; Al1=0.01*0.02; Ll1o=0.025*2; Ls1o=0.1; %geometric parameters for rod1
cl1=sqrt(El1/pl1); cs1=sqrt(Es1/ps1); Fi=3;j1=1; k1=0; q1=3; %canonical parameters for rod1
calcustep=5E0; %calculating accuracy for coefficients [rtio1,period11,fam1]=ratios(j1,k1,q1);
[tLl1,Ls1]=keepthicnesssame(Ll1o,Ls1o,2,cl1,cs1,rtio1);Ll1=tLl1/2;
[L31]=LFibonacci(Fi,Ll1,Ls1);N1=6; Linterface=L31*N1; %number of unit cells for rod1
El2=70e9; Es2=70e9; pl2=2700; ps2=2700; %material parameters for rod2
As2=0.01*0.02; Al2=0.01*0.01; Ll2o=0.025*2; Ls2o=0.1; %geometric parameters for rod2
cl2=sqrt(El2/pl2); cs2=sqrt(Es2/ps2);Ltimes=(cs1+(rtio1)*cl1)/(cl1+(rtio1)*cs1);
j2=1; k2=0; q2=3; %canonical parameters for rod2[rtio2,period12,fam2]=ratios(j2,k2,q2);
[tLl2,Ls2]=keepthicnesssame(Ll2o*Ltimes,Ls2o*Ltimes,2,cl2,cs2,rtio2);Ll2=tLl2/2;
[L32]=LFibonacci(Fi,Ll2,Ls2);
N2=6; Linterface2=L32*N2; Ltotal=Linterface+Linterface2;%number of unit cells for rod2
[n1,n2]=periodforf(rtio2,fam2,cl2,cs2,tLl2,Ls2,j2,k2,q2);n=n1/3;%frequency range
[fl,relfec1,relfec2,trans1,trans2,transt,sufaceimpe1,sufaceimpe2]=totaltransmisionfullyaxilly(n,
El2,Es2,Ll2,Ls2,Al2,As2,pl2,ps2,calcustep,N2,El1,Es1,Ll1,Ls1,Al1,As1,pl1,ps1,N1,Fi);
figure(1)
plot(fl,(trans1),'r','LineWidth',2.5),grid on;hold on
plot(fl,(trans2),'–','LineWidth',2.5,'Color',[0 0 0]),grid on;hold on
xlabel('Frequency'); ylabel('tn');
figure(2)
plot(fl,(transt),'LineWidth',2.5,'Color',[0 0.4470 0.7410]),grid on;hold on
plot([n/4/1000,n/4/1000],[0,1],'r–','LineWidth',2.5),grid on;hold on;
plot([n/4/1000*3,n/4/1000*3],[0,1],'r–','LineWidth',2.5),grid on;xlabel('Frequency'); ylabel('t');
figure(3)
plot(fl,imag(sufaceimpe1),'LineWidth',2,'Color',[0 0.4470 0.7410]),grid on;hold on
plot(fl,imag(sufaceimpe2),'LineWidth',2,'Color',[0.73725 0.56078 0.56078]),grid on;hold on
plot(fl,imag(sufaceimpe1+sufaceimpe2),'LineWidth',2,'Color',[0 0 0]),grid on;
xlabel('Frequency'); ylabel('rn');
%%
ftest=47.805*1e3;%wave field at determined frequency Tgnew=eye(2);
[Tinew1]=newaxiallytransfemateriinver(El1,Es1,Ll1,Ls1,Al1,As1,pl1,ps1,ftest*2*pi);
[Tinew2]=newaxiallytransfemateriinver(El2,Es2,Ll2,Ls2,Al2,As2,pl2,ps2,ftest*2*pi);
for k=1:N1
   Tgnew=Tinew1*Tgnew;
end
Ticha(1,1)=-sqrt(El1*pl1)*Al1/(sqrt(El2*pl2)*Al2)-1;
Ticha(1,2)=sqrt(El1*pl1)*Al1/(sqrt(El2*pl2)*Al2)-1;
Ticha(2,1)=sqrt(El1*pl1)*Al1/(sqrt(El2*pl2)*Al2)-1;
Ticha(2,2)=-sqrt(El1*pl1)*Al1/(sqrt(El2*pl2)*Al2)-1;
Tgnew=(Ticha.*(-1/2))*Tgnew;
for jc=1:N2
   Tgnew=Tinew2*Tgnew;
end
[P,inteP,xcord,Lvecol1,Lvecos1,Lvecol2,Lvecos2,w,boun]=interfacedisplacmentnew(lenstep,El2,
Es2,Ll2,Ls2,Al2,As2,pl2,ps2,N2,El1,Es1,Ll1,Ls1,Al1,As1,pl1,ps1,N1,ftest,K,Linterface,Tgnew);
figure(4)
```

```
plot(xcord,abs(P),'k','LineWidth',2.5),grid on;xlabel('x'); ylabel('[N]');
```

Subprogramme for transmission and reflection coefficients

```
function [fl,relfec1,relfec2,trans1,trans2,transt,sufaceimpe1,sufaceimpe2]=totaltransmisionfullyax-
illy(n,El2,Es2,Ll2,Ls2,Al2,As2,pl2,ps2,calcustep,N2,El1,Es1,Ll1,Ls1,Al1,As1,pl1,ps1,N1,Fi)
F=calcustep:calcustep:n;fl=F.*1e-3;
relfec1(1:1:length(F))=0;relfec2(1:1:length(F))=0;
sufaceimpe1(1:1:length(F))=nan;sufaceimpe2(1:1:length(F))=nan;
transt(1:1:length(F))=0;trans1(1:1:length(F))=0;trans2(1:1:length(F))=0;
l1=Al1*sqrt(El1*pl1);l2=Al2*sqrt(El2*pl2);s1=As1*sqrt(Es1*ps1);s2=As2*sqrt(Es2*ps2);
for ic=1:length(F)
   f=F(ic);[Tinew1]=newaxiallytransfemateriinver(El1,Es1,Ll1,Ls1,Al1,As1,pl1,ps1,f*2*pi);
   [Tinew2]=newaxiallytransfemateriinver(El2,Es2,Ll2,Ls2,Al2,As2,pl2,ps2,f*2*pi);
   Tgnew=eye(2);Tgnew1=eye(2);Tgnew2=Tinew2;
   for k=1:N1
      Tgnew1=Tinew1*Tgnew1;Tgnew=Tinew1*Tgnew;
   end
   Ticha(1,1)=-sqrt(El1*pl1)*Al1/(sqrt(El2*pl2)*Al2)-1;
   Ticha(1,2)=sqrt(El1*pl1)*Al1/(sqrt(El2*pl2)*Al2)-1;
   Ticha(2,1)=sqrt(El1*pl1)*Al1/(sqrt(El2*pl2)*Al2)-1;
   Ticha(2,2)=-sqrt(El1*pl1)*Al1/(sqrt(El2*pl2)*Al2)-1;Tgnew=Tinew2*(Ticha.*(-1/2))*Tgnew;
   for j=2:N2
      Tgnew2=Tinew2*Tgnew2;Tgnew=Tinew2*Tgnew;
   end
   relfec1(ic)=Tgnew1(2,1)/Tgnew1(2,2);relfec2(ic)=Tgnew2(2,1)/Tgnew2(2,2);
   trans1(ic)=abs((Tgnew1(1,1)-Tgnew1(1,2)*Tgnew1(2,1)/Tgnew1(2,2)))^2;
   trans2(ic)=abs((Tgnew2(1,1)-Tgnew2(1,2)*Tgnew2(2,1)/Tgnew2(2,2)))^2;
   transt(ic)=abs((Tgnew(1,1)-Tgnew(1,2)*Tgnew(2,1)/Tgnew(2,2)))^2*l2/l1;
   if abs(trace(Tinew1))-2>0
      sufaceimpe1(ic)=(1+(relfec1(ic)))/(1-(relfec1(ic)))*l1;
   end
   if abs(trace(Tinew2))-2>0
      sufaceimpe2(ic)=(1+(relfec2(ic)))/(1-(relfec2(ic)))*l2;
   end
end

function [P,inteP,xcord,w,bounddis]=interfacedisplacmentnew(lenstep,El2,Es2,Ll2,Ls2,Al2,As2,
pl2,ps2,N2,El1,Es1,Ll1,Ls1,Al1,As1,pl1,ps1,N1,ftest,K,Linterface,Tgnew,Tinew1,Tinew2)
k=1; sum=0;Lm1=2*Ll1+Ls1;Lm2=2*Ll2+Ls2;start=Lm1*N1+Lm2*N2;
xcord(1)=Lm1*N1+Lm2*N2;
rl1=sqrt(Al1/pi);rs1=sqrt(As1/pi);rl2=sqrt(Al2/pi);rs2=sqrt(As2/pi);
bounddis(1,1)=0;bounddis(2,1)=-Tgnew(2,1)*Tgnew(1,2)/Tgnew(1,1)+Tgnew(2,2);
[A1,B1,C1,D1,k11,k21]=trnsmissionmatrixnew(El1,Es1,Ll1,Ls1,Al1,As1,pl1,ps1,ftest*2*pi);
[A2,B2,C2,D2,k12,k22]=trnsmissionmatrixnew(El2,Es2,Ll2,Ls2,Al2,As2,pl2,ps2,ftest*2*pi);
w(k)=bounddis(1)*exp(i*k12*(0))+bounddis(2)*exp(-i*k12*(0));
P(k)=i*Al2*k12*El2*(bounddis(1)*exp(i*k12*(0))-bounddis(2)*exp(-i*k12*(0)));
for ic=1:N2
   bouncodi2=B2\A2*bounddis;bouncodi1=C2\D2*bouncodi2;
   for x=lenstep:lenstep:Ll2
      k=k+1;xcord(k)=start-x;
```

```
        w(k)=bounddis(1)*exp(i*k12*(xcord(k)-N1*Lm1-(N2-ic+1)*Lm2))+bounddis(2)*exp(-i*
        k12*(xcord(k)-N1*Lm1-(N2-ic+1)*Lm2));
        P(k)=i*Al2*k12*El2*(bounddis(1)*exp(i*k12*(xcord(k)-N1*Lm1-(N2-ic+1)*Lm2))-
        bounddis(2)*exp(-i*k12*(xcord(k)-N1*Lm1-(N2-ic+1)*Lm2)));
    end
    theint=@(x) 1./2./El2.*rl2.*abs(bounddis(1).*exp(i.*k12.*(x+start-N1*Lm1-(N2-ic+1)*Lm2))+
    bounddis(2).*exp(-i.*k12.*(x+start-N1*Lm1-(N2-ic+1)*Lm2))).^2;
    start=start-Ll2;inttheint=integral(theint,0,Ll2);sum=sum+inttheint;
    for x=lenstep:lenstep:Ls2
        k=k+1;xcord(k)=start-x;
        w(k)=bouncodi2(1)*exp(i*k22*(xcord(k)-N1*Lm1-(N2-ic+1)*Lm2))+bouncodi2(2)*exp(-i*
        k22*(xcord(k)-N1*Lm1-(N2-ic+1)*Lm2));
        P(k)=i*As2*k22*Es2*(bouncodi2(1)*exp(i*k22*(xcord(k)-N1*Lm1-(N2-ic+1)*Lm2))-
        bouncodi2(2)*exp(-i*k22*(xcord(k)-N1*Lm1-(N2-ic+1)*Lm2)));
    end
    theint=@(x) 1./2./Es2.*rs2.*abs(bouncodi2(1).*exp(i.*k22.*(x+start-N1*Lm1-(N2-ic+1)*
    Lm2))+bouncodi2(2).*exp(-i.*k22.*(x+start-N1*Lm1-(N2-ic+1)*Lm2))).^2;
    start=start-Ls2;inttheint=integral(theint,0,Ls2);sum=sum+inttheint;
    for x=lenstep:lenstep:Ll2
        k=k+1;xcord(k)=start-x;
        w(k)=bouncodi1(1)*exp(i*k12*(xcord(k)-N1*Lm1-(N2-ic+1)*Lm2))+bouncodi1(2)*exp(-i*
        k12*(xcord(k)-N1*Lm1-(N2-ic+1)*Lm2));
        P(k)=i*Al2*k12*El2*(bouncodi1(1)*exp(i*k12*(xcord(k)-N1*Lm1-(N2-ic+1)*Lm2))-
        bouncodi1(2)*exp(-i*k12*(xcord(k)-N1*Lm1-(N2-ic+1)*Lm2)));
    end
    theint=@(x) 1./2./El2.*rl2.*abs(bouncodi1(1).*exp(i.*k12.*(x+start-N1*Lm1-(N2-ic+1)*
    Lm2))+bouncodi1(2).*exp(-i.*k12.*(x+start-N1*Lm1-(N2-ic+1)*Lm2))).^2;
    inttheint=integral(theint,0,Ll2);start=start-Ll2;sum=sum+inttheint;bounddis=Tinew2\bounddis;
end
Ticha(1,1)=-sqrt(El1*pl1)*Al1/(sqrt(El2*pl2)*Al2)-1;
Ticha(1,2)=-sqrt(El1*pl1)*Al1/(sqrt(El2*pl2)*Al2)+1;
Ticha(2,1)=-sqrt(El1*pl1)*Al1/(sqrt(El2*pl2)*Al2)+1;
Ticha(2,2)=-sqrt(El1*pl1)*Al1/(sqrt(El2*pl2)*Al2)-1;
bounddis=Ticha.*(-(sqrt(El2*pl2)*Al2)/(sqrt(El1*pl1)*Al1)/2)*bounddis;
for jc=1:N1
    bouncodi2=B1\A1*bounddis;bouncodi1=C1\D1*bouncodi2;
    for x=lenstep:lenstep:Ll1
        k=k+1;xcord(k)=start-x;
        w(k)=bounddis(1)*exp(i*k11*(xcord(k)-(N1-jc+1)*Lm1))+bounddis(2)*exp(-i*k11*(
        xcord(k)-(N1-jc+1)*Lm1));
        P(k)=i*Al1*k11*El1*(bounddis(1)*exp(i*k11*(xcord(k)-(N1-jc+1)*Lm1))-bounddis(2)*
        exp(-i*k11*(xcord(k)-(N1-jc+1)*Lm1)));
    end
    theint=@(x) 1./2./El1.*rl1.*abs(bounddis(1).*exp(i.*k11.*(x+start-(N1-jc+1)*Lm1))+
    bounddis(2).*exp(-i.*k11.*(x+start-(N1-jc+1)*Lm1))).^2;
    start=start-Ll1;inttheint=integral(theint,0,Ll1);sum=sum+inttheint;
    for x=lenstep:lenstep:Ls1
        k=k+1;xcord(k)=start-x;
        w(k)=bouncodi2(1)*exp(i*k21*(xcord(k)-(N1-jc+1)*Lm1))+bouncodi2(2)*exp(-i*k21*(
        xcord(k)-(N1-jc+1)*Lm1));
        P(k)=i*As1*k21*Es1*(bouncodi2(1)*exp(i*k21*(xcord(k)-(N1-jc+1)*Lm1))-bouncodi2(2)*
```

```
        exp(-i*k21*(xcord(k)-(N1-jc+1)*Lm1)));
    end
    theint=@(x) 1./2./Es1.*rs1.*abs(bouncodi2(1).*exp(i.*k21.*(x+start-(N1-jc+1)*Lm1))+
    bouncodi2(2).*exp(-i.*k21.*(x+start-(N1-jc+1)*Lm1))).^2;
    start=start-Ls1;inttheint=integral(theint,0,Ls1);sum=sum+inttheint;
    for x=lenstep:lenstep:Ll1
        k=k+1;xcord(k)=start-x;
        w(k)=bouncodi1(1)*exp(i*k11*(xcord(k)-(N1-jc+1)*Lm1))+bouncodi1(2)*exp(-i*k11*(
        xcord(k)-(N1-jc+1)*Lm1));
        P(k)=i*Al1*k11*El1*(bouncodi1(1)*exp(i*k11*(xcord(k)-(N1-jc+1)*Lm1))-bouncodi1(2)*
        exp(-i*k11*(xcord(k)-(N1-jc+1)*Lm1)));
    end
    theint=@(x) 1./2./El1.*rl1.*abs(bouncodi1(1).*exp(i.*k11.*(x+start-(N1-jc+1)*Lm1))+
    bouncodi1(2).*exp(-i.*k11.*(x+start-(N1-jc+1)*Lm1))).^2;
    inttheint=integral(theint,0,Ll1);start=start-Ll1;sum=sum+inttheint;bounddis=Tinew1\bounddis;
end
inteP(1)=sqrt(sum); P=P/inteP(1);

function [Ti]=newaxiallytransfemateriinver(El,Es,Ll,Ls,Al,As,pl,ps,w)
k1=w/sqrt(El/pl);k2=w/sqrt(Es/ps);Z1=w*sqrt(El*pl)*Al;Z2=w*sqrt(Es*ps)*As;
Ti(1,1)=exp(i*k1*2*Ll)*(cos(k2*Ls)+i/2*(Z2/Z1+Z1/Z2)*sin(k2*Ls));
Ti(1,2)=-i/2*(Z1/Z2-Z2/Z1)*sin(k2*Ls);Ti(2,1)=-Ti(1,2);
Ti(2,2)=exp(-i*k1*2*Ll)*(cos(k2*Ls)-i/2*(Z2/Z1+Z1/Z2)*sin(k2*Ls));

function [A,B,C,D,k1,k2]=trnsmissionmatrixnew(El,Es,Ll,Ls,Al,As,pl,ps,w)
k1=w*sqrt(pl/El);k2=w*sqrt(ps/Es);Z1=w*sqrt(El*pl)*Al;Z2=w*sqrt(Es*ps)*As;
A(1,1)=exp(-i*k1*Ll);A(1,2)=exp(i*k1*Ll);A(2,1)=Z1/Z2*exp(-i*k1*Ll);A(2,2)=-conj(A(2,1))
B(1,1)=exp(-i*k2*Ll);B(1,2)=exp(i*k2*Ll);B(2,1)=exp(-i*k2*Ll);B(2,2)=-exp(i*k2*Ll);
C(1,1)=exp(-i*k1*(Ll+Ls));C(1,2)=conj(C(1,1));C(2,1)=exp(-i*k1*(Ll+Ls));C(2,2)=-conj(C(2,1));
D(1,1)=exp(-i*k2*(Ll+Ls));D(1,2)=exp(i*k2*(Ll+Ls));
D(2,1)=Z2/Z1*exp(-i*k2*(Ll+Ls));D(2,2)=-Z2/Z1*exp(i*k2*(Ll+Ls));
```

Appendix B

Another Way to Prove the Recursion Rule Equation (2.25)

The recursive rule (2.25) can be verified by using this way:

$$trT_{i+1} = trT_{i-1}trT_i - trT_{i-2}$$

$$T_i = T_{i-2}T_{i-1}, T_{i+1} = T_{i-1}T_i = T_{i-1}T_{i-2}T_{i-1}$$

Thus, the original formula become:

$$tr(T_{i-1}T_{i-2}T_{i-1}) = tr(T_{i-1})tr(T_{i-2}T_{i-1}) - tr(T_{i-2})$$

If assumed:

$$T_{i-1} = a = \begin{bmatrix} A_1 & A_2 \\ A_3 & A_4 \end{bmatrix}, T_{i-2} = b = \begin{bmatrix} B_1 & B_2 \\ B_3 & B_4 \end{bmatrix}$$

Then:

$$tr\,(T_{i-2}T_{i-1}) = B_1A_1 + B_2A_3 + B_3A_2 + B_4A_4 = tr\,(T_{i-1}T_{i-2}) \Leftrightarrow tr\,(ba) = tr\,(ab)$$

Thus, this formula should be verified:

$$tr(a^2b) = tr(a)tr(ab) - tr(b)$$

It is not hard to find:

$$tr\left(a^2b\right) = A_1^2B_1 + A_2A_3B_1 + A_1A_2B_3 + A_2A_4B_3 + A_1A_3B_2 + A_3A_4B_2 + A_2A_3B_4 + A_4^2B_4$$

$$tr\,(ab) = B_1A_1 + B_2A_3 + B_3A_2 + B_4A_4;\ tr\,(a) = A_1 + A_4,\ tr\,(b) = B_1 + B_4$$

The determinant for matrix a is one, which means $A_1A_4 - A_2A_3 = 1$, the equation (2.25) is proved.

Impedance for Laminate Problem When Antiplane Shear Wave Propagation

Mechanical impedance is the ratio of the applied force to the resulting velocity at the excitation ($x = 0$) point. To determine the impedance of a laminates, consider that the semi-infinite laminate is excited by the stress $\sigma_{xz}(x,t)$ at the end of the laminate:

$$u_z(x,t) = a(\exp(\mathrm{i}\sqrt{\frac{\rho}{\mu}}\omega x))e^{\mathrm{i}\omega t}$$

Differentiating with respect to space and time, respectively, results in:

$$\frac{\partial u_z(x,t)}{\partial x} = \mathrm{i}\sqrt{\frac{\rho}{\mu}}\omega u_z(x,t)$$

$$\frac{\partial u_z(x,t)}{\partial t} = \mathrm{i}\omega u_z(x,t)$$

And then, the impedance is:

$$\frac{\sigma_{xz}(0,t)}{V(0,t)} = \frac{\mu\mathrm{i}\sqrt{\frac{\rho}{\mu}}\omega u_z(0,t)}{\mathrm{i}\omega u_z(0,t)} = \sqrt{\rho\mu}$$

Jacobian for Silver and Bronze Mean Sequence

Defining $t_i = tr(T_{i-2}T_{i-1})$, for silver means sequence ($\mathrm{m} = 2$ and $\mathrm{l} = 1$), the pair of equations are determined:

$$x_{i+1} = x_i t_{i+1} - x_{i-1}$$

$$t_{i+1} = x_i x_{i-1} - t_i, \text{ with } i \geq 2$$

Similarly, for bronze mean sequence ($\mathrm{m} = 3$ and $\mathrm{l} = 1$):

$$x_{i+1} = (x_i^2 - 1)t_{i+1} - x_i x_{i-1}$$

$$t_{i+1} = (x_i - t_i)x_{i-1} + x_{i-2}, \text{ with } i \geq 2$$

According to these equations, the Jacobian matrix can be derived:

$$J_s = \frac{\partial(\tilde{x}_{i+1}, \tilde{y}_{i+1}, \tilde{z}_{i+1})}{\partial(\tilde{x}_i, \tilde{y}_i, \tilde{z}_i)} = \begin{bmatrix} \tilde{y}_i^2 - 1 & 2\tilde{x}_i\tilde{y}_i - \tilde{z}_i & -\tilde{y}_i \\ \tilde{y}_i & \tilde{x}_i & -1 \\ 0 & 1 & 0 \end{bmatrix}$$

$$J_b = \frac{\partial(\tilde{x}_{i+1}, \tilde{y}_{i+1}, \tilde{z}_{i+1})}{\partial(\tilde{x}_i, \tilde{y}_i, \tilde{z}_i)} = \begin{bmatrix} \tilde{y}_i^3 - 2\tilde{y}_i & 3\tilde{x}_i\tilde{y}_i^2 - 2\tilde{y}_i\tilde{z}_i - 2\tilde{x}_i & 1 - \tilde{y}_i^2 \\ \tilde{y}_i^2 - 1 & 2\tilde{x}_i\tilde{y}_i - \tilde{z}_i & -\tilde{y}_i \\ 0 & 1 & 0 \end{bmatrix}$$

They have the same determinant which is $\det J_{s,b} = -1$ and Kohmoto's invariant is still the equation (2.35). In addition, the matrix $\mathbf{A}_s$ and $\mathbf{A}_b$ which are Jacobian, (For silver mean sequence, the number of iterations is 4):

$$\mathbf{A}_s = \begin{bmatrix} 2I(\omega)^2 + 12I(\omega) + 17 & 2(2 + I(\omega))(3 + I(\omega))\sqrt{4 + I(\omega)} & 0 \\ 2(3 + I(\omega))\sqrt{4 + I(\omega)} & 2I(\omega)^2 + 12I(\omega) + 17 & 0 \\ 0 & 0 & 1 \end{bmatrix}$$

$$\mathbf{A}_b = \begin{bmatrix} \mathbf{A}_{b11} & \mathbf{A}_{b12} & 0 \\ \mathbf{A}_{b21} & \mathbf{A}_{b22} & 0 \\ 0 & 0 & 1 \end{bmatrix}$$

$$\mathbf{A}_{b11} = 469 + I(\omega)(721 + I(\omega)(399 + 94I(\omega) + 8I(\omega)^2))$$

$$\mathbf{A}_{b12} = (4 + I(\omega))^{3/2}(9 + 4I(\omega))(15 + 2I(\omega)(6 + I(\omega)))$$

$$\mathbf{A}_{b21} = (4 + I(\omega))^{3/2}(5 + 2I(\omega))(9 + 4I(\omega))$$

$$\mathbf{A}_{b22} = 829 + I(\omega)(1079 + 2I(\omega)(257 + I(\omega)(53 + 4I(\omega))))$$

Thus, two pair eigenvalues for linearised transformation are obtained, which are (subscript s, b denoted SM and BM chain):

$$\vartheta_s^{\pm}(\omega) = (\sqrt{(3 + I(\omega))^2 - 1} \pm (3 + I(\omega)))^2$$

$$\vartheta_b^{\pm}(\omega) = \frac{1}{4}(\sqrt{4 + (4 + I(\omega))^2 (9 + 4I(\omega))^2} \pm (4 + I(\omega))(9 + 4I(\omega)))^2$$

Complex Function Time Average Proof

Made assumption:

$$\sigma = (a + \mathrm{i}b)e^{\mathrm{i}\omega t},\ U = (c + \mathrm{i}d)e^{\mathrm{i}\omega t}$$

In here, coefficients a, b, c and d are pure real numbers. Thus, U differential to time t is:

$$\dot{U} = \mathrm{i}\omega(c + \mathrm{i}d)e^{\mathrm{i}\omega t}$$

The conjugate of $\dot{U}^*$ is:

$$\dot{U}^* = -\mathrm{i}\omega(c - \mathrm{i}d)e^{-\mathrm{i}\omega t}$$

Therefore:

$$\frac{1}{2}\mathrm{Re}(\sigma\dot{U}^*) = \frac{1}{2}\mathrm{Re}(-\mathrm{i}\omega(c - \mathrm{i}d)(a + \mathrm{i}b)) = \frac{1}{2}\mathrm{Re}(-\mathrm{i}\omega(ac - \mathrm{i}ad + \mathrm{i}bc + bd)) = \frac{1}{2}(bc - ad)\omega$$

Then, taking the real part of σ and $\dot{U}$:

$$\mathrm{Re}(\sigma) = a\cos(\omega t) - b\sin(\omega t),\ \mathrm{Re}(\dot{U}) = -\omega(c\sin(\omega t) + d\cos(\omega t))$$

With time average:

$$\frac{1}{T}\int_0^T \mathrm{Re}[\sigma]\mathrm{Re}[\dot{U}]dt = -\frac{1}{T}\int_0^T (a\cos(\omega t) - b\sin(\omega t)\omega(c\sin(\omega t) + d\cos(\omega t)))dt$$

Finally:

$$\frac{1}{T}\int_0^T \mathrm{Re}[\sigma]\mathrm{Re}[\dot{U}]dt = \frac{1}{2}(bc - ad)\omega = \frac{1}{2}\mathrm{Re}(\sigma\dot{U}^*)$$

The Orthogonality of Eigenvectors in Jacobian

When the scaling factor concerning periodic orbit and associated Jacobian matrix analysed, for instance, $\mathbf{A}_g$ for Fibonacci GM sequence, they have the forms similar to the matrix (also in SM and BM sequence):

$$\mathbf{A} = \begin{bmatrix} a & b & d \\ b & c & e \\ 0 & 0 & 1 \end{bmatrix}$$

It is not hard to find that it has an eigenvalue $\vartheta^0 = 1$ and eigenvector associated with $\psi^0 = (0, 0, 1)^T$. The eigenfunction is solved in this way:

$$\mathbf{A} - \vartheta\mathbf{E} = \begin{bmatrix} a - \vartheta & b & d \\ b & c - \vartheta & e \\ 0 & 0 & 1 - \vartheta \end{bmatrix}$$

Because of $\vartheta \neq 1$ currently, the elimination on the column can be performed, the matrix becomes without changing determinant:

$$\begin{bmatrix} a - \vartheta & b & 0 \\ b & c - \vartheta & 0 \\ 0 & 0 & 1 - \vartheta \end{bmatrix}$$

Thus, the other two eigenvalues are that:

$$\vartheta^{\pm} = \frac{(a + c) \pm \sqrt{(a + c)^2 - 4ac + 4b^2}}{2}$$

where two associated eigenvectors:

$$(-\frac{-a + c + \sqrt{a^2 + 4b^2 - 2ac + c^2}}{2b}, 1, 0)^T,\ (-\frac{-a + c - \sqrt{a^2 + 4b^2 - 2ac + c^2}}{2b}, 1, 0)^T$$

With little knowledge, these two eigenvectors are orthogonal with ψ^0.

Elementary Transfer Matrix for Prestressed Euler-Bernoulli Beam Theory

Considering an Euler beam with pressure axially force N, constant crossing area A, stiffness for bending EI and density per volume ρ, the governing equation of lateral deflection v is fourth-order ordinary differential equations in each elementary beam:

$$EI\frac{d^4v}{dx^4} + N\frac{d^2v}{dx^2} - \rho A\omega^2 v = 0$$

The general solution v in trigonometric function is:

$$v(x) = C_1\sin(\gamma x) + C_2\cos(\gamma x) + C_3\sinh(\varepsilon x) + C_4\cosh(\varepsilon x)$$

where $\gamma = \sqrt{\frac{N}{2EI} + \sqrt{\frac{N^2}{4E^2I^2} + \frac{\rho A\omega^2}{EI}}}$, $\varepsilon = \sqrt{-\frac{N}{2EI} + \sqrt{\frac{N^2}{4E^2I^2} + \frac{\rho A\omega^2}{EI}}}$.

With the same process from the quasicrystalline rods (laminates), the general displacements is deflection v and rotation φ, general forces are bending moment M and shear force Q. The relationship among them in Euler beam theory is following:

$$\varphi = \frac{dv}{dx};\ M = -EI\frac{d^2v}{dx^2};\ Q = -EI\frac{d^3v}{dx^3}$$

The elementary transfer matrix for prestressed Euler beam is (assuming length of the elementary beam is L):

$$\begin{bmatrix} v(L) \\ \varphi(L) \\ M(L) \\ Q(L) \end{bmatrix} = \begin{bmatrix} B_{11} & B_{12} & B_{13} & B_{14} \\ B_{21} & B_{22} & B_{23} & B_{24} \\ B_{31} & B_{32} & B_{33} & B_{34} \\ B_{41} & B_{42} & B_{43} & B_{44} \end{bmatrix} \begin{bmatrix} v(0) \\ \varphi(0) \\ M(0) \\ Q(0) \end{bmatrix}$$

where terms in elementary transfer matrix are (where $\alpha = EI\varepsilon\gamma(\varepsilon^2 + \gamma^2)$, $\beta = EI(\varepsilon^2 + \gamma^2)$):

$$B_{11} = EI\frac{\varepsilon^2\cos(\gamma L) + \gamma^2\cosh(\varepsilon L)}{\alpha};\ B_{12} = EI\frac{\varepsilon^3\sin(\gamma L) + \gamma^3\sinh(\varepsilon L)}{\beta};$$

$$B_{13} = \frac{\cosh(\varepsilon L) - \cos(\gamma L)}{\alpha};\ B_{14} = \frac{\gamma\sinh(\varepsilon L) - \varepsilon\sin(\gamma L)}{\beta}$$

$$B_{21} = EI\frac{\gamma^2\varepsilon\sinh(\varepsilon L) - \varepsilon^2\gamma\sin(\gamma L)}{\alpha};\ B_{22} = EI\frac{\varepsilon^3\gamma\cos(\gamma L) + \gamma^3\varepsilon\cosh(\varepsilon L)}{\beta};$$

$$B_{23} = \frac{\varepsilon\sinh(\varepsilon L) + \gamma\sin(\gamma L)}{\alpha};\ B_{24} = \frac{\gamma\varepsilon\cosh(\varepsilon L) - \gamma\varepsilon\cos(\gamma L)}{\beta}$$

$$B_{31} = E^2I^2\frac{\varepsilon^2\gamma^2\cosh(\varepsilon L) - \gamma^2\varepsilon^2\cos(\gamma L)}{\alpha};\ B_{32} = E^2I^2\frac{\varepsilon^2\gamma^3\sinh(\varepsilon L) - \varepsilon^3\gamma^2\sin(\gamma L)}{\beta};$$

$$B_{33} = EI\frac{\varepsilon^2\cosh(\varepsilon L) + \gamma^2\cos(\gamma L)}{\alpha};\ B_{34} = EI\frac{\gamma^2\varepsilon\sin(\gamma L) + \varepsilon^2\gamma\sinh(\varepsilon L)}{\beta}$$

$$B_{41} = E^2I^2\frac{\gamma^2\varepsilon^3\sinh(\varepsilon L) - \varepsilon^2\gamma^3\sin(\gamma L)}{\alpha};\ B_{42} = E^2I^2\frac{\varepsilon^3\gamma^3\cosh(\varepsilon L) - \varepsilon^3\gamma^3\cos(\gamma L)}{\beta};$$

$$B_{43} = EI\frac{\gamma^3\sin(\gamma L) + \varepsilon^3\sinh(\varepsilon L)}{\alpha};\ B_{44} = EI\frac{\gamma^3\varepsilon\cos(\gamma L) + \gamma\varepsilon^3\cosh(\varepsilon L)}{\beta}$$

Elementary Transfer Matrix for Laminates as In-Plane Wave Problem

Similar to the transfer matrix as SH wave propagation into the laminates, the solutions of displacement u_x and u_y in each n^{th} layer for in-plane wave problem (coupled P and SV wave) are investigated using Naiver-Lamé equations:

$$(\lambda+2\mu)\frac{d^2u_x}{dx^2}+(\lambda+\mu)\frac{d^2u_y}{dxdy}+\mu\frac{d^2u_x}{dy^2}=\rho\ddot{u}_x$$

$$(\lambda+2\mu)\frac{d^2u_y}{dy^2}+(\lambda+\mu)\frac{d^2u_x}{dxdy}+\mu\frac{d^2u_y}{dx^2}=\rho\ddot{u}_y$$

where λ is the first Lamé constant and μ is the shear modulus. The Helmholtz decomposing is employed into in-plane components of (u_x, u_y) in terms of scalar potential ϕ and ψ, which are:

$$u_x=\frac{d\phi}{dx}+\frac{d\psi}{dy},\ u_y=\frac{d\phi}{dy}+\frac{d\psi}{dx}$$

Thus, two equations similar to (2.39) should be solved:

$$\left(\frac{\partial^2\phi}{\partial x^2}+\frac{\partial^2\phi}{\partial y^2}\right)=\frac{1}{c_L^2}\frac{\partial^2\phi}{\partial t^2}$$

$$\left(\frac{\partial^2\psi}{\partial x^2}+\frac{\partial^2\psi}{\partial y^2}\right)=\frac{1}{c_S^2}\frac{\partial^2\psi}{\partial t^2}$$

where $c_L=\sqrt{\frac{\lambda+2\mu}{\rho}}$ longitudinal wave speed and $c_S=\sqrt{\frac{\mu}{\rho}}$ shear wave speed. Therefore, the two solutions are achieved:

$$\phi=N_{L1}e^{\mathrm{i}(\omega t+q_Lx-K_yy)}+N_{L2}e^{\mathrm{i}(\omega t-q_Lx-K_yy)}$$

$$\psi=N_{S1}e^{\mathrm{i}(\omega t+q_Sx-K_yy)}+N_{S2}e^{\mathrm{i}(\omega t-q_Sx-K_yy)}$$

where coefficients $q_L^2=\omega^2/c_L^2-K_y^2$ and $q_S^2=\omega^2/c_S^2-K_y^2$. Combined with boundary condition to eliminate the coefficients $N_{L,S}$, the 4×4 transfer matrix is obtained: (assuming thickness is for each phase is h)

$$\begin{bmatrix}u_x(h)\\u_y(h)\\\sigma_{xx}(h)\\\tau_{xy}(h)\end{bmatrix}=\begin{bmatrix}N_{11}&N_{12}&N_{13}&N_{14}\\N_{21}&N_{22}&N_{23}&N_{24}\\N_{31}&N_{32}&N_{33}&N_{34}\\N_{41}&N_{42}&N_{43}&N_{44}\end{bmatrix}\begin{bmatrix}u_x(0)\\u_y(0)\\\sigma_{xx}(0)\\\tau_{xy}(0)\end{bmatrix}$$

where terms in elementary transfer matrix are:

$$N_{11}=A_1q_L\cos(q_Lh)-\mathrm{i}K_yA_3\cos(q_Sh);\ N_{12}=-A_5q_L\sin(q_Lh)-\mathrm{i}K_yA_7\sin(q_Sh);$$

$$N_{13}=-A_6q_L\sin(q_Lh)-\mathrm{i}K_yA_8\sin(q_Sh);\ N_{14}=A_2q_L\cos(q_Lh)-\mathrm{i}K_yA_4\cos(q_Sh);$$

$$N_{21}=A_3q_S\sin(q_Sh)-\mathrm{i}K_yA_1\sin(q_Lh);\ N_{22}=-A_7q_S\cos(q_Sh)-\mathrm{i}K_yA_5\cos(q_Lh);$$

$$N_{23}=-A_8q_S\cos(q_Sh)-\mathrm{i}K_yA_6\cos(q_Lh);\ N_{24}=A_4q_S\sin(q_Sh)-\mathrm{i}K_yA_2\sin(q_Lh);$$

$$N_{31}=-A_1((\lambda+2\mu)q_L^2+\lambda K_y^2)\sin(q_Lh)+(2\mathrm{i}K_yq_S\mu)A_3\sin(q_Sh);$$

$$N_{32}=-A_5((\lambda+2\mu)q_L^2+\lambda K_y^2)\cos(q_Lh)-(2\mathrm{i}K_yq_S\mu)A_7\cos(q_Sh);$$

$$N_{33}=-A_6((\lambda+2\mu)q_L^2+\lambda K_y^2)\cos(q_Lh)-(2\mathrm{i}K_yq_S\mu)A_8\cos(q_Sh);$$

$$N_{34}=-A_2((\lambda+2\mu)q_L^2+\lambda K_y^2)\sin(q_Lh)+(2\mathrm{i}K_yq_S\mu)A_4\sin(q_Sh);$$

$$N_{41}=A_3\mu(q_S^2-K_y^2)\cos(q_Sh)-2\mathrm{i}K_y\mu A_1q_L\cos(q_Lh);$$

$$N_{42} = A_7\mu(q_S^2 - K_y^2)\sin(q_S h) + 2\mathrm{i}K_y\mu A_5 q_L \sin(q_L h);$$
$$N_{43} = A_8\mu(q_S^2 - K_y^2)\sin(q_S h) + 2\mathrm{i}K_y\mu A_6 q_L \sin(q_L h);$$
$$N_{44} = A_4\mu(q_S^2 - K_y^2)\cos(q_S h) - 2\mathrm{i}K_y\mu A_2 q_L \cos(q_L h);$$

where coefficients A_i are:

$$A_1 = \frac{\omega^2\rho - 2\mu K_y^2}{\omega^2\rho q_L};\ A_2 = \frac{\mathrm{i}K_y}{\omega^2\rho q_L};\ A_3 = \frac{2\mathrm{i}K_y\mu}{\omega^2\rho};\ A_4 = \frac{1}{\omega^2\rho}$$

$$A_5 = \frac{2\mu\mathrm{i}K_y}{\omega^2\rho};\ A_6 = -\frac{1}{\omega^2\rho};\ A_7 = -\frac{\omega^2\rho - 2\mu K_y^2}{\omega^2\rho q_S};\ A_8 = \frac{\mathrm{i}K_y}{\omega^2\rho q_S}$$

Appendix C Plotting Kohmoto's Invariant in Mathematica

Iω = 0

```
Khomotobandg =Plot3D[{x*y/2 + Sqrt[Iω + 4 - x^2 - y^2 + x^2*y^2/4], x*y/2 - Sqrt[Iω + 4 - x^2 - y^2 + x^2*y^2/4]}, {x, -4, 4}, {y, -4, 4}, AxesLabel -> Automatic, Mesh -> None, ColorFunction -> Function[{x, y, z}, RGBColor[1, 0.5, 0]], RegionFunction -> Function[{x, y, z}, x < -2 || x > 2 || y < -2 || y > 2 || z < -2 || z > 2], PlotRange -> {-5, 5}, AxesLabel -> {x̃, ỹ, z̃}, PlotPoints -> 100, AxesStyle -> {Directive[Black, 14], Directive[Black, 14], Directive[Black, 14]}]
```

```
Khomotopassb =Plot3D[{x*y/2 + Sqrt[Iω + 4 - x^2 - y^2 + x^2*y^2/4], x*y/2 - Sqrt[Iω + 4 - x^2 - y^2 + x^2*y^2/4]}, {x, -2, 2}, {y, -2, 2}, AxesLabel -> Automatic, Mesh -> None,ColorFunction -> Function[{x, y, z}, RGBColor[1, 1, 0]],PlotPoints -> 100,RegionFunction ->Function[{x, y, z}, -2 < x < 2 && -2 < y < 2 && -2 < z < 2], AxesLabel -> {x̃, ỹ, z̃}, AxesStyle -> {Directive[Black, 14], Directive[Black, 14], Directive[Black, 14]}]
```

```
Koh = Show[Khomotobandg, Khomotopassb]
```

References

Achenbach, J. 2012. *Wave Propagation in Elastic Solids*. Amsterdam: Elsevier Science.

Arnold, V. Vogtmann, K. and Weinstein, A. 2013. *Mathematical Methods of Classical Mechanics*. 2^{ed}ed. New York: Springer.

Asboth, J. Oroszlany, L. and Palyi, A. 2015. *A Short Course on Topological Insulators*. New York: Springer.

Atala, M. Aidelsburger, M. Barreiro, J. Abanin, D. Kitagawa, T. Demler, E. and Bloch, I. 2013. Direct measurement of the Zak phase in topological Bloch bands. *Nature Physics* 9(12), pp. 795-800. doi: 10.1038/nphys2790

Band, R. and Berkolaiko, G. 2013. Universality of The Momentum Band Density of Periodic Networks. *Physical Review Letters* 111(13). doi: 10.1103/physrevlett.111.130404

Barra, F. and Gaspard, P. 2000. On the level spacing distribution in quantum graphs. *Journal of Statistical Physics* 101(1/2), pp. 283-319. doi: 10.1023/a:1026495012522

Berkolaiko, G. and Winn, B. 2010. Relationship between scattering matrix and spectrum of quantum graphs. *Transactions of the American Mathematical Society* 362(12), pp. 6261-6261. doi: 10.1090/s0002-9947-2010-04897-4

Bernevig, B. Hughes, T. and Zhang, S. 2006. Quantum Spin Hall Effect and Topological Phase Transition in HgTe Quantum Wells. *Science* 314(5806), pp. 1757-1761. doi: 10.1126/science.1133734

Bloch, F. 1929. Über die Quantenmechanik der Elektronen in Kristallgittern. *Zeitschrift für Physik* 52(7-8), pp. 555-600. doi: 10.1007/bf01339455

Boland, R. Galla, T. and McKane, A. 2009. Limit cycles, complex Floquet multipliers, and intrinsic noise. *Physical Review* E 79(5). doi: 10.1103/physreve.79.051131

Brillouin, L. 1946. *Wave propagation in periodic structures*. New York and London: McGraw-Hill.

Brun, M. Guenneau, S. and Movchan, A. 2009. Achieving control of in-plane elastic waves. *Applied Physics Letters* 94(6), p. 061903. doi: 10.1063/1.3068491

Brun, M. Guenneau, S. Movchan, A. and Bigoni, D. 2010. Dynamics of structural interfaces: Filtering and focussing effects for elastic waves. *Journal of the Mechanics and Physics of Solids* 58(9), pp. 1212-1224. doi: 10.1016/j.jmps.2010.06.008

Buckingham, M. Berknout, B. and Glegg, S. 1992. Imaging the ocean with ambient noise. *Nature* 356(6367), pp. 327-329. doi: 10.1038/356327a0

Chen, Y. and Ye, Z. 2001. Theoretical analysis of acoustic stop bands in two-dimensional periodic scattering arrays. *Physical Review E* 64(3). doi: 10.1103/physreve.64.036616

Chen, Y. Hu, G. and Huang, G. 2017. A hybrid elastic metamaterial with negative mass density and tunable bending stiffness. *Journal of the Mechanics and Physics of Solids* 105, pp. 179-198. doi: 10.1016/j.jmps.2017.05.009

Chen, Y. Wu, B. Li, J. Rudykh, S. and Chen, W. 2021. Low-frequency tunable topological interface states in soft phononic crystal cylinders. *International Journal of Mechanical Sciences* 191, p. 106098. doi: 10.1016/j.ijmecsci.2020.106098

Colquitt, D. Brun, M. Gei, M. Movchan, A. Movchan, N. and Jones, I. 2014. Transformation elastodynamics and cloaking for flexural waves. *Journal of the Mechanics and Physics of Solids* 72, pp. 131-143. doi: 10.1016/j.jmps. 2014.07.014

Colquitt, D. Colombi, A. Craster, R. Roux, P. and Guenneau, S. 2017. Seismic metasurfaces: Sub-wavelength resonators and Rayleigh wave interaction. *Journal of the Mechanics and Physics of Solids* 99, pp. 379-393. doi: 10.1016/j.jmps. 2016.12.004

Cui, T. Smith, R. and Liu, R. 2010. *Metamaterials*. New York: Springer.

Demir, A. Mehrotra, A. and Roychowdhury, J. 2000. Phase noise in oscillators: a unifying theory and numerical methods for characterization. *IEEE Transactions on Circuits and Systems I: Fundamental Theory and Applications* 47(5), pp. 655-674. doi: 10.1109/81.847872

Dong, X. and Liu, C. 2016. Classification of topological crystalline insulators based on representation theory. *Physical Review B* 93(4). doi: 10.1103/physrevb.93.045429

Ewing, W. Jardetzky, W. Press, F. and Beiser, A. 1957. Elastic Waves in Layered Media. *Physics Today* 10(12), pp. 27-28. doi: 10.1063/1.3060203

Edward Ott. 1993. Chaos in Dynamical Systems, Cambridge University Press . *Bulletin of Mathematical Biology* 57(6), pp. 943-944. doi: 10.1016/s0092-8240(95)80010-7

Fan, J. and Huang, H. 2021. Topological states in quasicrystals. *Frontiers of Physics* 17(1). doi: 10.1007/s11467-021-1100-y

Farhat, M. Guenneau, S. Enoch, S. and Movchan, A. 2009. Cloaking bending waves propagating in thin elastic plates. *Physical Review B* 79(3). doi: 10.1103/physrevb.79.033102

Farzbod, F. and Leamy, M. 2011. Analysis of Blochs Method and the Propagation Technique in Periodic Structures. *Journal of Vibration and Acoustics* 133(3). doi: 10.1115/1.4003202

Fatemi, M. 1998. Ultrasound-Stimulated Vibro-Acoustic Spectrography. *Science* 280(53 60), pp. 82-85. doi: 10.1126/science.280.5360.82

Floquet, G. 1883. Sur les équations différentielles linéaires à coefficients périodiques. *Annales scientifiques de l'École normale supérieure* 12, pp. 47-88. doi: 10.24033/asens.220

Frenzel, T. David Brehm, J. Bückmann, T. Schittny, R. Kadic, M. and Wegener, M. 2013. Three-dimensional labyrinthine acoustic metamaterials. *Applied Physics Letters* 103(6), 061907. doi: 10.1063/1.4817934

Frenzel, T. Kadic, M. and Wegener, M. 2017. Three-dimensional mechanical metamaterials with

a twist. *Science* 358(6366), 1072-1074. doi:10.1126/science.aao4640

Gammaitoni, L. Hänggi, P. Jung, P. and Marchesoni, F. 1998. Stochastic resonance. *Reviews of Modern Physics* 70(1), pp. 223-287. doi: 10.1103/revmodphys.70.223

Gao, W. Xiao, M. Chen, B. Pun, E. Chan, C. and Tam, W. 2017. Controlling interface states in 1D photonic crystals by tuning bulk geometric phases. *Optics Letters* 42(8), p. 1500. doi: 10.1364/ol.42.001500

Gaponenko, S. Zhukovsky, S. Lavrinenko, A. and Sandomirskii, K. 2002. Propagation of waves in layered structures viewed as number recognition. *Optics Communications* 205(1-3), pp. 49-57. doi: 10.1016/s0030-4018(02)01318-4

García-Pablos, D. Sigalas, M. Montero de Espinosa, F. Torres, M. Kafesaki, M. and García, N. 2000. Theory and Experiments on Elastic Band Gaps. *Physical Review Letters* 84(19), pp. 4349-4352. doi: 10.1103/physrevlett.84.4349

Gei, M. 2010. Wave propagation in quasiperiodic structures: stop/pass band distribution and prestress effects. *International Journal of Solids and Structures* 47(22-23), pp. 3067-3075. doi: 10.1016/j.ijsolstr.2010.07.008

Gei, M. Chen, Z. Bosi, F. and Morini, L. 2020. Phononic canonical quasicrystalline waveguides. *Applied Physics Letters* 116(24), p. 241903. doi: 10.1063/5.0013528

Graff, K.F. 1975. *Wave Motion in Elastic Solids*. Oxford: Oxford University Press.

Guckenheimer, J. Holmes, P. and Slemrod, M. 1984. Nonlinear Oscillations Dynamical Systems, and Bifurcations of Vector Fields. *Journal of Applied Mechanics* 51(4), pp. 947-947. doi: 10.1115/1.3167759

Guenneau, S. Movchan, A. Pétursson, G. and Anantha Ramakrishna, S. 2007. Acoustic metamaterials for sound focusing and confinement. *New Journal of Physics* 9(11), pp. 399-399. doi: 10.1088/1367-2630/9/11/399

Gumbs, G. and Ali, M. 1988. Dynamical maps, Cantor spectra, and localization for Fibonacci and related quasiperiodic lattices. *Physical Review Letters* 60(11), pp. 1081-1084. doi: 10.1103/physrevlett.60.1081

Haldane, F. and Raghu, S. 2008. Possible Realization of Directional Optical Waveguides in Photonic Crystals with Broken Time-Reversal Symmetry. *Physical Review Letters* 100(1). doi: 10.1103/physrevlett.100.013904

Hasan, M. and Kane, C. 2010. Colloquium: Topological insulators. *Reviews of Modern Physics* 82(4), pp. 3045-3067. doi: 10.1103/revmodphys.82.3045

Hatsugai, Y. 1993. Chern number and edge states in the integer quantum Hall effect. *Physical Review Letters* 71(22), pp. 3697-3700. doi: 10.1103/physrevlett.71.3697

Hatsugai, Y. Fukui, T. and Aoki, H. 2006. Topological analysis of the quantum Hall effect in graphene: Dirac-Fermi transition across van Hove singularities and edge versus bulk quantum numbers. *Physical Review B* 74(20). doi: 10.1103/physrevb.74.205414

Heeger, A. Kivelson, S. Schrieffer, J. and Su, W. 1988. Solitons in conducting polymers. *Reviews of Modern Physics* 60(3), pp. 781-850. doi: 10.1103/revmodphys.60.781

Hegemier, G. and Nayfeh, A. 1973. A Continuum Theory for Wave Propagation in Laminated CompositesCase 1: Propagation Normal to the Laminates. *Journal of Applied Mechanics* 40(2), pp. 503-510. doi: 10.1115/1.3423013

Holzer, M. 1988. Nonlinear dynamics of localization in a class of one-dimensional quasicrystals. *Physical Review B* 38(8), pp. 5756-5759. doi: 10.1103/physrevb.38.5756

Hodgkinson, I. Weiglhofer, WS. and Lakhtakia, A. 2001. *Complex mediums II*. Bellingham: SPIE.

Holzer, M. 1988. Three classes of one-dimensional, two-tile Penrose tilings and the Fibonacci Kronig-Penney model as a generic case. *Physical Review B* 38(3), pp. 1709-1720. doi: 10.1103/physrevb.38.1709

Hou, Z. and Assouar, B. 2008. Modeling of Lamb wave propagation in plate with two-dimensional phononic crystal layer coated on uniform substrate using plane-wave-expansion method. *Physics Letters A* 372(12), pp. 2091-2097. doi: 10.1016/j.physleta.2007.10.080

Hsu, J. and Wu, T. 2006. Efficient formulation for band-structure calculations of two-dimensional phononic-crystal plates. *Physical Review B* 74(14). doi: 10.1103/physrevb.74.144303

Huang, D. Gumbs, G. and Kolář, M. 1992. Localization in a one-dimensional Thue-Morse chain. *Physical Review B* 46(18), pp. 11479-11486. doi: 10.1103/physrevb.46.11479

Hussein, M. Hulbert, G. and Scott, R. 2007. Dispersive elastodynamics of 1D banded materials and structures: Design. *Journal of Sound and Vibration* 307(3-5), pp. 865-893. doi: 10.1016/j.jsv.2007.07.021

Hussein, M. Leamy, M. and Ruzzene, M. 2014. Dynamics of Phononic Materials and Structures: Historical Origins, Recent Progress, and Future Outlook. *Applied Mechanics Reviews* 66(4). doi: 10.1115/1.4026911

Jones, I. Movchan, A. and Gei, M. (2010). 2010. Waves and damage in structured solids with multi-scale resonators. *Proceedings of the Royal Society A: Mathematical, Physical and Engineering Sciences* 467(2128), pp. 964-984. doi: 10.1098/rspa.2010.0319

Jounior, L, V. and Savi, A, M. 2016. *Dynamics of Smart Systems and Structures: Concepts and Applications*. Switzerland: Springer.

Kadic, M. Milton, G. Van Hecke, M. and Wegener, M. 2019. 3D metamaterials. *Nature Reviews Physics* 1(3), pp. 198-210. doi: 10.1038/s42254-018-0018-y.

Kane, C. and Lubensky, T. 2013. Topological boundary modes in isostatic lattices. *Nature Physics* 10(1), pp. 39-45. doi: 10.1038/nphys2835

Kenneth, M. Golden, Geoffrey R. Grimmett, Richard D. James, Graeme W. and Milton, Pabitra N. 2012. *Mathematics of Multiscale Materials*. New York: Springer.

Khelif, A. Deymier, P. Djafari-Rouhani, B. Vasseur, J. and Dobrzynski, L. 2003. Two-dimensional phononic crystal with tunable narrow pass band: Application to a waveguide with selective frequency. *Journal of Applied Physics* 94(3), pp. 1308-1311. doi: 10.1063/1.1557776

King, P. and Cox, T. 2007. Acoustic band gaps in periodically and quasiperiodically modulated waveguides. *Journal of Applied Physics* 102(1), p. 014902. doi: 10.1063/1.2749483

Kohn, W. 1959. Analytic Properties of Bloch Waves and Wannier Functions. *Physical Review* 115(4), pp. 809-821. doi: 10.1103/physrev.115.809

Kolář, M. and Ali, M. 1989. Attractors of some volume-nonpreserving Fibonacci trace maps. *Physical Review A* 39(12), pp. 6538-6544. doi: 10.1103/physreva.39.6538

Kolář, M. and Ali, M. 1989. Generalized Fibonacci superlattices, dynamical trace maps, and magnetic excitations. *Physical Review B* 39(1), pp. 426-432. doi: 10.1103/physrevb.39.426

Kolář, M. and Nori, F. 1990. Trace maps of general substitutional sequences. *Physical Review B* 42(1), pp. 1062-1065. doi: 10.1103/physrevb.42.1062

Kolář, M. 1993. New class of one-dimensional quasicrystals. *Physical Review B* 47(9), pp. 5489-5492. doi: 10.1103/physrevb.47.5489

Kohmoto, M. and Oono, Y. 1984. Cantor spectrum for an almost periodic Schrödinger equation and a dynamical map. *Physics Letters A* 102(4), pp. 145-148. doi: 10.1016/0375-9601(84)90928-9

Kohmoto, M. Kadanoff, L. and Tang, C. 1983. Localization Problem in One Dimension: Mapping and Escape. *Physical Review Letters* 50(23), pp. 1870-1872. doi: 10.1103/physrevlett.50.1870

Kohmoto, M. Sutherland, B. and Tang, C. 1987. Critical wave functions and a Cantor-set spectrum of a one-dimensional quasicrystal model. *Physical Review B* 35(3), pp. 1020-1033. doi: 10.1103/physrevb.35.1020

Korringa, J. 1947. On the calculation of the energy of a Bloch wave in a metal. *Physica* 13(6-7), pp. 392-400. doi: 10.1016/0031-8914(47)90013-x

Kushwaha, M. and Halevi, P. 1996. Giant acoustic stop bands in twodimensional periodic arrays of liquid cylinders. *Applied Physics Letters* 69(1), pp. 31-33. doi: 10.1063/1.118108

Kushwaha, M. Halevi, P. Dobrzynski, L. and Djafari-Rouhani, B. (1993). Acoustic band structure of periodic elastic composites. *Physical Review Letters* 71(13), pp. 2022-2025. doi: 10.1103/physrevlett.71.2022

Laruelle, F. and Etienne, B. 1988. Fibonacci invariant and electronic properties of GaAs/Ga 1xAlxAs quasiperiodic superlattices. *Physical Review B* 37(9), pp. 4816-4819. doi: 10.1103/physrevb.37.4816

Lee, J. Singer, J. and Thomas, E. 2012. Micro-/Nanostructured Mechanical Metamaterials. *Advanced Materials* 24(36), pp. 4782-4810. doi: 10.1002/adma.201201644

Levine, D. and Steinhardt, P. 1984. Quasicrystals: A New Class of Ordered Structures. *Physical*

Review Letters 53(26), pp. 2477-2480. doi: 10.1103/physrevlett.53.2477

Li, X. Meng, Y. Wu, X. Yan, S. Huang, Y. Wang, S. and Wen, W. 2018. Su-Schrieffer-Heeger model inspired acoustic interface states and edge states. *Applied Physics Letters* 113(20), p. 203501. doi: 10.1063/1.5051523

Liboff, R. 1992. *Introductory quantum mechanics*. 4^th. Reading: Addison-Wesley.

Lin, Y. 1962. Free vibrations of a continuous beam on elastic supports. *International Journal of Mechanical Sciences* 4(5), pp. 409-423. doi: 10.1016/s0020-7403(62)80027-7

Liu, Z. Zhang, X. Mao, Y. Zhu, Y. Yang, Z. Chan, C. and Sheng P. 2000. Locally Resonant Sonic Materials. *Science* 289(5485), pp. 1734-1736. doi: 10.1126/science.289.5485.1734

Lustig, B. and Shmuel, G. 2018. On the band gap universality of multiphase laminates and its applications. *Journal of the Mechanics and Physics of Solids* 117, pp. 37-53. doi: 10.1016/j.jmps.2018.04.008

Lustig, B. Elbaz, G. Muhafra, A. and Shmuel, G. 2019. Anomalous energy transport in laminates with exceptional points. *Journal of the Mechanics and Physics of Solids* 133, p. 103719. doi: 10.1016/j.jmps.2019.103719

Maldovan, M. 2013. Sound and heat revolutions in phononics. *Nature* 503(7475), pp. 209-217. doi: 10.1038/nature12608

Mei, J. Liu, Z. Shi, J. and Tian, D. 2003. Theory for elastic wave scattering by a two-dimensional periodical array of cylinders: An ideal approach for band-structure calculations. *Physical Review B* 67(24). doi: 10.1103/physrevb.67.245107

Meng, Y. Wu, X. Zhang, R. Li, X. Hu, P. Ge, L. and Wen, W. (2018). 2018. Designing topological interface states in phononic crystals based on the full phase diagrams. *New Journal of Physics* 20(7), p. 073032. doi: 10.1088/1367-2630/aad136

Milton, G. Briane, M. and Willis, J. 2006. On cloaking for elasticity and physical equations with a transformation invariant form. *New Journal of Physics* 8(10), pp. 248-248. doi: 10.1088/1367-2630/8/10/248

Milton, W. 1995. *The Theory of Composite*. Cambridge: Cambridge press.

Mokhtari, A. Lu, Y. Zhou, Q. Amirkhizi, A. and Srivastava, A. 2020. Scattering of in-plane elastic waves at metamaterial interfaces. *International Journal of Engineering Science* 150, p. 103278. doi: 10.1016/j.ijengsci.2020.103278

Morini, L. and Gei, M. 2018. Waves in one-dimensional quasicrystalline structures: dynamical trace mapping, scaling and self-similarity of the spectrum. *Journal of the Mechanics and Physics of Solids* 119, pp. 83-103. doi: 10.1016/j.jmps.2018.06.007

Morini, L. Gokay Tetik, Z. Shmuel, G. and Gei, M. 2019. On the universality of the frequency spectrum and band-gap optimization of quasicrystalline-generated structured rods. *Philosophical Transactions of the Royal Society A: Mathematical, Physical and Engineering Sciences* 378(2162), pp. 20190240. doi: 10.1098/rsta. 2019.0240

Morini, L. Eyzat, Y. and Gei, M. 2019. Negative refraction in quasicrystalline multilayered metamaterials. *Journal of the Mechanics and Physics of Solids* 124, pp. 282-298. doi: 10.1016/j.jmps.2018.10.016

Morvan, B. Tinel, A. Hladky-Hennion, A. Vasseur, J. and Dubus, B. 2010. Experimental demonstration of the negative refraction of a transverse elastic wave in a two-dimensional solid phononic crystal. *Applied Physics Letters* 96(10), p. 101905. doi: 10.1063/1.3302456

Moskalets, M. and Büttiker, M. 2002. Floquet scattering theory of quantum pumps. *Physical Review* B 66(20). doi: 10.1103/physrevb.66.205320

Muhammad. Zhou, W. and Lim, C. (2019). 2019. Topological edge modeling and localization of protected interface modes in 1D phononic crystals for longitudinal and bending elastic waves. *International Journal of Mechanical Sciences* 159, pp. 359-372. doi: 10.1016/j.ijmecsci.2019.05.020

Nemat-Nasser, S. 1972. Harmonic Waves in Layered Composites. *Journal of Applied Mechanics* 39(3), pp. 850-852. doi: 10.1115/1.3422814

Nemat-Nasser, S. 2015a. Anti-plane shear waves in periodic elastic composites: band structure and anomalous wave refraction. *Proceedings of the Royal Society A: Mathematical, Physical and Engineering Sciences* 471(2180), p. 20150152. doi: 10.1098/rspa.2015. 0152

Nemat-Nasser, S. 2015b. Refraction characteristics of phononic crystals. *Acta Mechanica Sinica* 31(4), pp. 481-493. doi: 10.1007/s10409-015-0454-1

Nemat-Nasser, S. Fu, F. and Minagawa, S. 1975. Harmonic waves in one-, two- and three-dimensional composites: Bounds for eigenfrequencies. *International Journal of Solids and Structures* 11(5), pp. 617-642. doi: 10.1016/0020-7683(75)90034-7

Norris, A. 2008. Acoustic cloaking theory. *Proceedings of the Royal Society A: Mathematical, Physical and Engineering Sciences* 464(2097), pp. 2411-2434. doi: 10.1098/rspa. 2008.0076

Pankratov, O. Pakhomov, S. and Volkov, B. 1987. Supersymmetry in heterojunctions: Band-inverting contact on the basis of Pb1xSnxTe and Hg1xCdxTe. *Solid State Communications* 61(2), pp. 93-96. doi: 10.1016/0038-1098(87)90934-3

Parnell, W. Norris, A. and Shearer, T. 2012. Employing pre-stress to generate finite cloaks for antiplane elastic waves. *Applied Physics Letters* 100(17), p. 171907. doi: 10.1063/1.4704566

Pennec, Y. Vasseur, J. Djafari-Rouhani, B. Dobrzyski, L. and Deymier, P. 2010. Two-dimensional phononic crystals: Examples and applications. *Surface Science Reports* 65(8), pp. 229-291. doi: 10.1016/j.surfrep.2010.08.002

Penrose, R. 1974. The role of aesthetics in pure and applied mathematical research. *Bulletin - Institute of Mathematics and its Applications* 10, pp. 266-271.

Poddubny, A. and Ivchenko, E. 2010. Photonic quasicrystalline and aperiodic structures. *Physica E: Low-dimensional Systems and Nanostructures* 42(7), pp. 1871-1895. doi: 10.1016/j.physe.2010.02.020

Poddubny, A. Pilozzi, L. Voronov, M. and Ivchenko, E. 2009. Exciton-polaritonic quasicrystalline and aperiodic structures. *Physical Review B* 80(11). doi: 10.1103/physrevb.80.115314

Raghu, S. and Haldane, F. 2008. Analogs of quantum-Hall-effect edge states in photonic crystals. *Physical Review A* 78(3). doi: 10.1103/physreva.78.033834

Raman, A. and Fan, S. 2010. Photonic Band Structure of Dispersive Metamaterials Formulated as a Hermitian Eigenvalue Problem. *Physical Review Letters* 104(8). doi: 10.1103/physrevlett.104.087401

Regnault, N. and Bernevig, B. 2011. Fractional Chern Insulator. *Physical Review X* 1(2). doi: 10.1103/physrevx.1.021014

Roberts, R. Achenbach, J. Ko, R. Adler, L. Jungman, A. and Quentin, G. 1983. Beam splitting at the reflection of elastic waves by a periodic surface profile. *The Journal of the Acoustical Society of America* 74(5), pp. 1638-1640. doi: 10.1121/1.390129

Roberts, R. Achenbach, J. Ko, R. Adler, L. Jungman, A. and Quentin, G. 1985. Reflection of a beam of elastic waves by a periodic surface profile. *Wave Motion* 7(1), pp. 67-77. doi: 10.1016/0165-2125(85)90027-7

Romanoni, M. Gonella, S. Apetre, N. and Ruzzene, M. 2009. Two-dimensional periodic actuators for frequency-based beam steering. *Smart Materials and Structures* 18(12), p. 125023. doi: 10.1088/0964-1726/18/12/125023

Rudner, M. Lindner, N. Berg, E. and Levin, M. 2013. Anomalous Edge States and the Bulk-Edge Correspondence for Periodically Driven Two-Dimensional Systems. *Physical Review X* 3(3). doi: 10.1103/ physrevx.3.031005

Rudykh, S. and Boyce, M. 2014. Transforming Wave Propagation in Layered Media via Instability-Induced Interfacial Wrinkling. *Physical Review Letters* 112(3). doi: 10.1103/ physrevlett.112.034 301

Schneider, K. 1985. Haken, H.: Advanced Synergetics. Springer-Verlag, Berlin Heidelberg New York 1983. XV, 356 S., 105 Abb., DM 98,-. *Biometrical Journal* 27(4), pp. 384-384. doi: 10.1002/bimj.4710270405

Shirley, J. 1965. Solution of the Schrödinger Equation with a Hamiltonian Periodic in Time. *Physical Review* 138(4B), pp. B979-B987. doi: 10.1103/physrev.138.b979

Shmuel, G. and Band, R. 2016. Universality of the frequency spectrum of laminates. *Journal of the Mechanics and Physics of Solids* 92, pp. 127-136. doi: 10.1016/j.jmps.2016 .04.001

Sigalas, M. and Economou, E. 1992. Elastic and acoustic wave band structure. *Journal of Sound and Vibration* 158(2), pp. 377-382. doi: 10.1016/0022-460x(92)90059-7

Srivastava, A. 2015. Elastic metamaterials and dynamic homogenization: a review. *International Journal of Smart and Nano Materials* 6(1), pp. 41-60. doi: 10.1080/19475411. 2015.1017779

Srivastava, A. 2016. Metamaterial properties of periodic laminates. *Journal of the Mechanics and*

Physics of Solids 96, pp. 252-263. doi: 10.1016/j.jmps.2016.07.018

Srivastava, A. and Nemat-Nasser, S. 2014. On the limit and applicability of dynamic homogenization. *Wave Motion* 51(7), pp. 1045-1054. doi: 10.1016/j.wavemoti.2014.04.003

Srivastava, A. and Willis, J. 2017. Evanescent wave boundary layers in metamaterials and sidestepping them through a variational approach. *Proceedings of the Royal Society A: Mathematical, Physical and Engineering Sciences* 473(2200), p. 20160765. doi: 10.1098/rspa.2016.0765

Sukhovich, A. Jing, L. and Page, J. 2008. Negative refraction and focusing of ultrasound in two-dimensional phononic crystals. *Physical Review B* 77(1). doi: 10.1103/physrevb.77.0143 01

Steurer, W. 2004. Twenty years of structure research on quasicrystals. Part I. Pentagonal, octagonal, decagonal and dodecagonal quasicrystals. *Zeitschrift für Kristallographie - Crystalline Materials* 219(7), pp. 391-446. doi: 10.1524/zkri.219.7.391.35643

Steurer, W. and Sutter-Widmer, D. 2007. Photonic and phononic quasicrystals. *Journal of Physics D: Applied Physics* 40(13), pp. R229-R247. doi: 10.1088/0022-3727/40/13/r01

Strang, G. 2021. *Introduction to Linear Algebra*. 5^{th}ed. Wellesley-Cambridge Press.

Su, W. Schrieffer, J. and Heeger, A. 1979. Solitons in Polyacetylene. *Physical Review Letters* 42(25), pp. 1698-1701. doi: 10.1103/physrevlett.42.1698

Su, W. Schrieffer, J. and Heeger, A. 1980. Soliton excitations in polyacetylene. *Physical Review B* 22(4), pp. 2099-2111. doi: 10.1103/physrevb.22.2099

Sun, C. Achenbach, J. and Herrmann, G. 1968. Time-Harmonic Waves in a Stratified Medium Propagating in the Direction of the Layering. *Journal of Applied Mechanics* 35(2), pp. 408-411. doi: 10.1115/1.3601212

Tamura, S. and Nori, F. 1989. Transmission and frequency spectra of acoustic phonons in Thue-Morse superlattices. *Physical Review B* 40(14), pp. 9790-9801. doi: 10.1103/physrevb.40.9790

Tan, W. Sun, Y. Chen, H. and Shen, S. 2014. Photonic simulation of topological excitations in metamaterials. *Scientific Reports* 4(1). doi: 10.1038/srep03842

Thomson, W. 1950. Transmission of Elastic Waves through a Stratified Solid Medium. *Journal of Applied Physics* 21(2), pp. 89-93. doi: 10.1063/1.1699629

Timoshenko, S. 1970. *Theory of elasticity*. 3^{rd}ed. Auckland: McGraw-Hill.

Traversa, F. and Bonani, F. 2011. Oscillator Noise: A Nonlinear Perturbative Theory Including Orbital Fluctuations and Phase-Orbital Correlation. *IEEE Transactions on Circuits and Systems I: Regular Papers* 58(10), pp. 2485-2497. doi: 10.1109/tcsi.2011.2123531

Traversa, F. and Bonani, F. 2011. Asymptotic stochastic characterization of phase and amplitude noise in free running oscillators. *Fluctuation and Noise Letters* 10(02), pp. 207-221. doi: 10.1142/s021947751100048x

Valsakumar, M. and Kumar, V. 1986. Diffraction from a quasi-crystalline chain. *Pramana* 26(3),

pp. 215-221. doi: 10.1007/bf02845262

Veselago, V. 1968. The Electrodynamics of Substances with Simultaneously Negative Values of ϵ and μ. *Soviet Physics Uspekhi* 10(4), pp. 509-514. doi: 10.1070/pu1968v010n 04abeh003699

Vines, R. Wolfe, J. and Every, A. 1999. Scanning phononic lattices with ultrasound. *Physical Review B* 60(17), pp. 11871-11874. doi: 10.1103/physrevb.60.11871

Wang, G. Yu, D. Wen, J. Liu, Y. and Wen, X. 2004. One-dimensional phononic crystals with locally resonant structures. *Physics Letters A* 327(5-6), pp. 512-521. doi: 10.1016/j.physleta.2004.05.047

Wang, H. Liu, D. Fang, W. Lin, S. Liu, Y. and Liang, Y. 2020. Tunable topological interface states in one-dimensional extended granular crystals. *International Journal of Mechanical Sciences* 176, p. 105549. doi: 10.1016/j.ijmecsci.2020.105549

Willis, J. 2016. Negative refraction in a laminate. *Journal of the Mechanics and Physics of Solids* 97, pp. 10-18. doi: 10.1016/j.jmps.2015.11.004

Wu, L. Wu, M. and Chen, L. 2008. The narrow pass band filter of tunable 1D phononic crystals with a dielectric elastomer layer. *Smart Materials and Structures* 18(1), p. 015011. doi: 10.1088/0964-1726/18/1/015011

Xiao, D. Chang, M. and Niu, Q. 2010. Berry phase effects on electronic properties. *Reviews of Modern Physics* 82(3), pp. 1959-2007. doi: 10.1103/revmodphys.82.1959

Xiao, M. Ma, G. Yang, Z. Sheng, P. Zhang, Z. and Chan, C. 2015. Geometric phase and band inversion in periodic acoustic systems. *Nature Physics* 11(3), pp. 240-244. doi: 10.1038/nphys3228

Xiao, M. Zhang, Z. and Chan, C. 2014. Surface Impedance and Bulk Band Geometric Phases in One-Dimensional Systems. *Physical Review X* 4(2). doi: 10.1103/physrevx.4.021017

Yang, S. Page, J. Liu, Z. Cowan, M. Chan, C. and Sheng, P. 2004. Focusing of Sound in a 3D Phononic Crystal. *Physical Review Letters* 93(2). doi: 10.1103/physrevlett.93.024301

Yariv, A. and Yeh, P. 2003. *Optical waves in crystals*. New York: Wiley.

Yeh, P. Yariv, A. and Hong, C. 1977. Electromagnetic propagation in periodic stratified media I General theory*. *Journal of the Optical Society of America* 67(4), p. 423. doi: 10.1364/josa.67.000423

Yilmaz, C. Hulbert, G. and Kikuchi, N. 2007. Phononic band gaps induced by inertial amplification in periodic media. *Physical Review B* 76(5). doi: 10.1103/physrevb.76.054309

Yin, J. Ruzzene, M. Wen, J. Yu, D. Cai, L. and Yue, L. 2018. Band transition and topological interface modes in 1D elastic phononic crystals. *Scientific Reports* 8(1). doi: 10.1038/s41598-018-24952-5

Yuan, S. Ye, K. and Williams, F. 2004. Second order mode-finding method in dynamic stiffness matrix methods. *Journal of Sound and Vibration* 269(3-5), pp. 689-708. doi: 10.1016/s0022-460x(03)00126-3

Zak, J. 1985. Symmetry criterion for surface states in solids. *Physical Review B* 32(4), pp. 2218-2226. doi: 10.1103/physrevb.32.2218

Zak, J. 1989. Berry's phase for energy bands in solids. *Physical Review Letters* 62(23), pp. 2747-2750. doi: 10.1103/physrevlett.62.2747

Zhang, X. and Liu, Z. 2004. Negative refraction of acoustic waves in two-dimensional phononic crystals. *Applied Physics Letters* 85(2), pp. 341-343. doi: 10.1063/1.1772854

Zhao, D. Wang, W. Liu, Z. Shi, J. and Wen, W. 2007. Peculiar transmission property of acoustic waves in a one-dimensional layered phononic crystal. *Physica B: Condensed Matter* 390(1-2), pp. 159-166. doi: 10.1016/j.physb. 2006.08.009

Zhao, M. Xie, Y. Zhang, X. and Gao, J. 2013. Band gaps of Lamb waves propagating in one-dimensional periodic and nesting Fibonacci superlattices thin plates. *Thin Solid Films* 546, pp. 439-442. doi: 10.1016/j.tsf.2013. 05.044

Zhao, Y. Zhao, F. and Yuan, L. 2008. Study on interface guided mode of 2D heterostructures dislocation defect phononic crystal. *Journal of Physics D: Applied Physics* 41(13), p. 135116. doi: 10.1088/0022-3727/41/13/135116

Zhou, X. Wang, Y. and Zhang, C. 2009. Effects of material parameters on elastic band gaps of two-dimensional solid phononic crystals. *Journal of Applied Physics* 106(1), p. 014903. doi: 10.1063/1.3159644

Zhu, R. Liu, X. Hu, G. Sun, C. and Huang, G. 2014. Negative refraction of elastic waves at the deep-subwavelength scale in a single-phase metamaterial. *Nature Communications* 5(1). doi: 10.1038/ncomms6510